Fall 2018

PHYSICS-BASED MODELING FRAMEWORK INCORPORATING MICROSTRUCTURAL EVOLUTION FOR PREDICTING DEFORMATION AND RECRYSTALLIZATION OF METALLIC MATERIALS

Miroslav Zecevic
University of New Hampshire, Durham

A PHYSICS-BASED MODELING FRAMEWORK INCORPORATING
MICROSTRUCTURAL EVOLUTION FOR PREDICTING DEFORMATION
AND RECRYSTALLIZATION OF METALLIC MATERIALS

BY

MIROSLAV ZECEVIC

BS in Mechanical Engineering, University of Novi Sad, 2010
MS in in Mechanical Engineering, University of Novi Sad, 2012

DISSERTATION

Submitted to the University of New Hampshire
in Partial Fulfillment of
the Requirements for the Degree of

Doctor of Philosophy
in
Mechanical Engineering

September, 2018

DISSERTATION COMMITTEE PAGE

This dissertation has been examined and approved in partial fulfillment of the requirements for the degree of Doctor of Philosophy in Mechanical Engineering by:

Marko Knezevic, Assistant Professor, (Mechanical Engineering)

Brad Kinsey, Professor (Mechanical Engineering)

Ricardo A. Lebensohn, Scientist, Los Alamos National Laboratory (Theoretical Division)

Rodney J. McCabe, Scientist, Los Alamos National Laboratory (Materials Science and Technology Division)

Igor Tsukrov Professor (Mechanical Engineering)

On 8/2/2018

Original approval signatures are on file with the University of New Hampshire Graduate School.

DEDICATION

This work is dedicated to my family and friends.

ACKNOWLEDGEMENTS

TABLE OF CONTENTS

ABSTRACT

A PHYSICS-BASED MODELING FRAMEWORK INCORPORATING

MICROSTRUCTURAL EVOLUTION FOR PREDICTING DEFORMATION AND

RECRYSTALLIZATION OF METALLIC MATERIALS

by

Miroslav Zecevic

University of New Hampshire, September, 2018

Large number of metallic parts is produced from the raw materials by a set of mechanical shaping and heating operations. Considering the need for metallic components in the modern industry, the field of thermo-mechanical processing of metallic materials is of immense importance. Even modest improvements of the existing thermo-mechanical processes could potentially result in great savings of time, recourses and energy. Finite element modeling of the forming and heating operations introduced in the past decades has allowed for the optimization of the thermo-mechanical processes and has thus resulted in significant advancements. However, due to the limitations of the presently used constitutive models, certain aspects of the process and effects of the process parameters on the component properties cannot be simulated accurately. Work presented in this dissertation is a contribution to the development of a physics-based crystal plasticity model capable of accurately simulating both the mechanical shaping and heating portions of the process and their effect on the microstructure of the component. The well-established visco-plastic self-consistent polycrystal plasticity (VPSC) model is advanced in several aspects in an effort to develop a coupled deformation-recrystallization model. First, different numerical implementation of the VPSC constitutive model into the finite element

framework is developed. In addition, two methods for the accurate representation of the material rate sensitivity within the finite element framework are proposed. The proposed models are verified on Taylor impact tests of Zr and Ta cylinders. Next, an algorithm for statistical description of intragranular fluctuations of crystallographic orientation is developed. The effects of the fluctuations of crystallographic orientation within the grains on the fluctuations of stress and rotation rates are considered as well. The developed model is applied to compression and plane strain compression of fcc material and verified by direct comparison with experimental measurements and full-field predictions. Finally, a physics-based recrystallization model coupled with the developed VPSC model capable of predicting intragranular crystallographic orientation fluctuations is proposed. The coupled deformation-recrystallization model is applied to the recrystallization of fcc and bcc materials and reasonable agreement is observed. Combination of different models proposed in this dissertation allows for the simulation of both shaping and heating portions of the thermo-mechanical process.

INTRODUCTION

Metal forming has been present for thousands of years and has greatly influenced the development of our civilization. Throughout the history, blacksmiths followed a sequence of heating and mechanical shaping operations (thermo-mechanical process) in order to successfully produce a part of desired shape and properties, without any understanding of the underlying physical phenomena. In the past century, due to rapid development of material science and mechanics, the microstructural and mechanical consequences of the applied thermo-mechanical conditions have been understood. Consequently, the field of metal forming has significantly advanced as well and today it represents an important part of the modern manufacturing industry.

Design of a thermo-mechanical process involves a large number of costly and time consuming tests. In the past several decades, computational modeling of the metal forming operations resulted in the reduction of the number of actual tests performed during the design phase and thus significant savings in time and resources. Furthermore, computational modeling allows for determination of the influence of numerous process parameters on the thermo-mechanical process and thus facilitates its optimization.

Forming operations of complex metallic parts involve complicated boundary conditions and constitutive behavior and thus the initial boundary value problem usually has to be solved numerically. Finite element method (FEM) has become the most widely used numerical technique for solving the initial boundary value problems in metal forming. The constitutive models utilized within the FEM framework are predominantly phenomenological, based on the yield surfaces which describe the functional dependence of deviatoric stress and plastic strain during plastic deformation in a computationally efficient manner. These models have been quite successful in predicting the mechanical behavior of less anisotropic cubic materials which

deform by slip only. However, more anisotropic hexagonal and orthorhombic metals deform by multiple slip and twinning modes. Modeling of those metals using the phenomenological constitutive models based on the yield surfaces is substantially more involved and less accurate. In addition, phenomenological constitutive models do not provide any insight into the development of the microstructure which directly determines the properties of the finished part. Finally, modeling of heating operations of thermo-mechanical process is usually oversimplified and reduces to removing the hardening history of the material.

Crystal plasticity models calculate the constitutive response of the material based on the underlying physics of the single crystalline plastic deformation and are thus substantially more complex and computationally demanding than the phenomenological models. Each single crystalline grain is assumed to deform by a set of slip and twinning systems defined by the crystal lattice structure of the material. Consequently, the anisotropic constitutive response of the single crystalline grain is determined by the set of activate slip and twinning systems and their resistances. The mechanical response of the aggregate of the single crystalline grains is obtained by homogenization of the single crystalline responses. Therefore, the crystallographic orientations of grains, grain shapes and resistances to slip and twinning within the grains completely determine the mechanical response of the polycrystal. Consequently, the anisotropy of the material is determined by the single crystal lattice structure and the microstructure of the specimen and is thus accurately captured in a physical way. During plastic deformation of a polycrystal, the crystallographic orientations of grains rotate, the grain shapes evolve and the slip and twin resistances increase. Consequently, the change of the material anisotropy naturally follows from the microstructural evolution and there is no need for introduction of a large number of fitting parameters as in the phenomenological constitutive models. In addition, since

the microstructure of the component determines its properties, the crystal plasticity models enable prediction of properties of the finished part and thus allow tailoring of the thermo-mechanical process for the optimal component properties. Finally, the predicted deformed microstructure can serve as an input for the physics based recrystallization model capable of predicting the microstructure after the heating operation which in turn affects the following forming operation.

Considering the strengths and weaknesses of the phenomenological and crystal plasticity constitutive models, it follows that they complement each other and that both should be used jointly for modeling of the thermo-mechanical processes. The phenomenological constitutive models are less accurate but very computationally efficient and can thus be used for determination of the approximate process parameter values. On the other hand, the crystal plasticity constitutive models are far more computationally expensive and should be used for verification of the results of the phenomenological models and prediction of the component microstructure.

In this dissertation, a contribution to the development of a polycrystal plasticity model capable of simulating an arbitrary thermo-mechanical process is presented. The polycrystal plasticity model used as the basis for the development is the widely used vsico-plastic self-consistent (VPSC) model developed by Ricardo A. Lebensohn and Carlos N. Tomé. The dissertation is manuscript based with each chapter representing a research article which describes an advancement of the VPSC model with the final goal of developing a unified deformation and recrystallization model within implicit finite elements.

Chapters 1 and 2 present improvements to the implementation of the VPSC into implicit finite elements and two methods for accurate description of material rate sensitivity. First,

numerical method for coupling of VPSC with implicit finite elements is developed in Chapter 1. In addition, an approach for the macroscopic reduction of the artificial rate sensitivity, coming from the visco-plastic flow rule, is presented. The proposed model is applied to the Taylor impact of Zr cylinder. In Chapter 2 a different method for accurate description of material rate sensitivity is explored. The artificial rate sensitivity coming from the visco-plastic flow rule is completely removed using the rate insensitive approach and the true rate sensitivity of the material is described through the slip resistance. Consequently, an implicit integration of the slip resistances had to be implemented. In this case, the proposed model is applied to the Taylor impact of Ta cylinder.

Chapter 3 and 4 present a method for statistical description of intragranular crystallographic orientation fluctuations within VPSC which is a prerequisite for subsequent recrystallization modeling. First, Chapter 3 describes an algorithm for integration of the fluctuations of rotation rates within the grains. The proposed model is verified by comparison with the experiments and full field calculations obtained by the VPFFT model. In chapter 4 the effect of the intragranular crystallographic orientation fluctuations on the intragranular stress and rotation rate distributions at higher strains is added to the model developed in Chapter 3. In addition, a grain fragmentation model based in the orientation space is proposed. The predictions are compared with experiments and VPFFT calculations and reasonable agreement is achieved.

Chapter 5 presents a recrystallization model initialized with the deformed state predicted by the VPSC model capable of calculating the intragranular crystallographic orientation fluctuations (model developed in Chapters 3 and 4). Both grain boundary and transition band nucleation mechanisms are considered. The transition band nucleation is assumed to take place in the grains with fragmented crystallographic orientation while the grain boundary nuclei form in the grains

with highest strain energy. The model predictions are compared with experiments and acceptable agreement is observed.

In conclusion, the improvements of the implementation of VPSC into finite elements and methods for accurate representation of rate sensitivity (Chapters 1 and 2) facilitate simulations of the mechanical shaping operations. On the other hand, the method for calculation of intragranular crystallographic orientation fluctuations (Chapters 3 and 4) and the recrystallization model (Chapter 5) enable modeling of the thermal operations of the thermo-mechanical process. Therefore, combination of the models proposed in this dissertation would allow modeling of an arbitrary thermo-mechanical process. Merging the proposed improvements of the VPSC into a single model and application of the combined model to a thermo-mechanical process is left for future work.

In addition to the work presented in this dissertation, I have also worked on two separate projects during my PhD studies at University of New Hampshire. The main goal of the first project was development of a computationally efficient crystal plasticity finite element model for face-centered cubic materials. To this end, the spectral crystal plasticity (SCP) method developed by Marko Knezevic and Surya R. Kalidindi was coupled with implicit finite elements. The proposed constitutive model successfully simulated several different forming operations including rolling and ECAP. Description of the coupling of the SCP with implicit finite elements and the main modeling results can be found in the following two publications:

- Zecevic Miroslav, Rodney J. McCabe, and Marko Knezevic, "A new implementation of the spectral crystal plasticity framework in implicit finite elements", Mechanics of Materials 84 (2015): 114-126

- Zecevic Miroslav, Rodney J. McCabe, and Marko Knezevic, "Spectral database solutions to elasto-viscoplasticity within finite elements: application to a cobalt-based FCC superalloy", International Journal of Plasticity 70 (2015): 151-165.

In the second project, the relation between the slip activity and texture evolution was investigated using the self-consistent modeling. Shear rate on a slip system causes a reorientation rate of the crystal lattice in the direction perpendicular to the slip plane normal and slip direction. Therefore, crystal orientations of grains and the set of activated slip systems determine the texture evolution of a polycrystal. By analyzing the reorientation trends of different slip modes for crystal orientations present in the initial texture and by comparing the results with the measured experimental textures, the slip activity of different modes can be inferred. Reorientation trends and slip activity of Uranium and Magnesium under different loading conditions were investigated and the results were published in:

- Zecevic Miroslav, Marko Knezevic, Irene J. Beyerlein, and Rodney J. McCabe, "Texture formation in orthorhombic alpha-uranium under simple compression and rolling to high strains", Journal of Nuclear Materials 473 (2016): 143-156

- Zecevic Miroslav, Marko Knezevic, Irene J. Beyerlein, and Rodney J. McCabe, "Origin of texture development in orthorhombic uranium", Materials Science and Engineering: A 665 (2016): 108-124

- Zecevic Miroslav, Irene J. Beyerlein, and Marko Knezevic, "Activity of pyramidal I and II< c+ a> slip in Mg alloys as revealed by texture development", Journal of the Mechanics and Physics of Solids 111 (2018): 290-307.

These two projects represent separate, self-sufficient studies which do not directly contribute to the main goal of this dissertation and are hence not included in this dissertation.

Chapter 1: Transitioning rate sensitivities across multiple length scales: Microstructure-property relationships in the Taylor cylinder impact test on zirconium

This chapter was published as: "Transitioning rate sensitivities across multiple length scales: microstructure-property relationships in the Taylor cylinder impact test on zirconium", Zecevic, Miroslav, Irene J. Beyerlein, Rodney J. McCabe, Brandon A. McWilliams, and Marko Knezevic, International Journal of Plasticity 84 (2016): 138-159. My contribution to this chapter was:

- development and implementation of a numerical approach for coupling of visco-plastic self-consistent model with implicit finite elements

- development and implementation of the approach for reduction of rate sensitivity at the macroscopic level

- finite element modeling of Taylor impact of Zr cylinder using the proposed polycrystal plasticity constitutive model and comparison of results with experiments

- writing the modeling sections in this chapter.

Transitioning rate sensitivities across multiple length scales: Microstructure-property relationships in the Taylor cylinder impact test on zirconium

Miroslav Zecevic[a], Irene J. Beyerlein[b], Rodney J. McCabe[c], Brandon A. McWilliams[d], Marko Knezevic[a]

[a] Department of Mechanical Engineering, University of New Hampshire, Durham, NH 03824, USA
[b] Theoretical Division, Los Alamos National Laboratory, Los Alamos, NM 87545, USA
[c] Materials Science and Technology Division, Los Alamos National Laboratory, Los Alamos, NM 87545, USA
[d] Weapons and Materials Research Directorate, US Army Research Laboratory, Aberdeen Proving Ground, MD 21005, USA

Abstract

A finite-element based plasticity model is developed for polycrystals deformed to high-strain-rates. The model is multiscale, covering from thermally activated dislocation motion on a specific crystallographic slip system (*nm*), to single crystal plasticity (*μm*), to polycrystalline aggregate plasticity (*mm*), and ultimately heterogeneous deformation of the macroscale test sample (*m*). Within the model, the rate dependence in macroscale response arises solely from the microscopic characteristic stress to activate dislocation motion. This is accomplished by introduction of a novel methodology, used at the intermediate length scales, to relax the extraneous rate dependencies occurring as a result of the visco-plastic rate sensitive flow rule commonly associated with single crystal plasticity formulations. The multi-scale model developed here also permits simulations to be carried out in stress-imposed, strain-rate imposed, and mixed stress/strain-rate-imposed boundary conditions, another advancement over previous techniques. Simulation results are presented for the deformation of high-purity Zr in a Taylor impact cylinder test. The variation in sample shape changes, texture evolution, and deformation twin fraction after the test are experimentally examined. These same quantities are calculated with the model and good agreement is achieved in all aspects. We show that without adjustment of material parameters that the thermally activated hardening model applies to much higher

strain-rates (10^4 /s-10^5 /s) than the strain-rates used previously to characterize it. This model can be broadly applied to understanding microstructure-property relationships in high-strain-rate deformation processes that generate spatially and temporarily heterogeneous mechanical fields.

Keywords: A Microstructures; B Elastic-viscoplastic material; B Rate-dependent material; C Impact testing; C Finite elements

1   Introduction

Zirconium (Zr) and its alloys are of great significance in a number of structural applications in the nuclear industry due to its low absorption cross-section of thermal neutrons and excellent corrosion resistance (Lemaignan and Motta, 2006; Nielsen, 2000). In the interest of designing bulk metal forming and shaping processes for Zr, it is important to understand its deformation behavior over a wide range of strain-rates and temperatures. It has been shown in many studies that the response of Zr is plastically anisotropic and sensitive to changes in strain-rate and temperature (Capolungo et al., 2009). Much of this complication originates from its low-symmetry crystal structure. Zr has a hexagonal close packed (HCP) crystal structure and it plastically deforms via a number of possible slip and twinning modes. Unlike metals with a higher symmetry cubic structure, the deformation response cannot be understood or predicted without knowledge of the crystallography of the predominant slip and twinning systems, their contribution, and the texture. As a result, both elastic and plastic behavior grossly deviate from isotropy.

The deformation response of Zr, like other HCP metals, depends sensitively on which slip and twinning modes are activated throughout the history of deformation. Each mode acts on a particular slip or twinning plane and in a specific direction. Over the temperature and strain-rate regimes of interest, slip is carried by the motion of dislocations, and this motion is thermally activated (Knezevic et al., 2015b). Thus, the stresses needed for these mechanisms depend on strain-rate and temperature, and evolve with strain level as dislocations interact and become stored in the crystal. As the structural characteristics of the dislocations are different, it is known that each mode will have its own separate evolution law with strain, strain-rate, and temperature.

A Taylor impact cylinder test was first devised for efforts to determine dynamic yield stresses of a materials (Taylor, 1948) and later utilized to verify constitutive laws for polycrystalline metals over a wide range of strain-rates, strains, and stresses accessible by the single test (Hawkyard, 1969; Lee and Tupper, 1954; Maudlin et al., 1999b). This deceptively simple test involves propelling a cylindrical specimen at a rigid-as-possible target and measuring the changes in sample shape and microstructure after the test. The resulting strain-rate and stress fields vary along the cylinder axis and can vary over several orders of magnitude depending on the sample size, material, and parameters of the test. Heterogeneous deformation in both time and space can result in gradients in the plastic deformation response and underlying microstructural evolution. For a metal such as Ta, with a high symmetry body center cubic (BCC) crystal structure, a finite element model employing simple constitutive laws based on yield surfaces was sufficient to understand and model the shape changes resulting from the test (Maudlin et al., 1999a). For a low symmetry HCP metal such as Zr, it was pointed out that similar modeling approaches were not sufficient and that it is necessary to account for the evolution of texture and the specific deformation mechanisms underlying plastic deformation (Maudlin et al., 1999b). They also emphasized the importance of deformation twinning in the high-strain-rate response of Zr. Texture and twinning cause the material to be plastically anisotropic and to exhibit tension-compression asymmetry. The importance of accounting for these effects in Taylor impact tests was recently highlighted in a study on high-purity titanium (Ti), another HCP metal (Revil-Baudard et al., 2015). In that work, a continuum anisotropic yield surface specifically developed to account for plastic anisotropy and tension-compression asymmetry in high-purity Ti was incorporated into a finite element framework rather than

11

explicitly accounting for texture and twinning. The model successfully predicted the deformation and geometric changes of the Taylor impact specimens after testing (Revil-Baudard et al., 2015).

The prediction of which slip and twinning systems are active at any given material point and any given time in the deformation path is a complex problem. Determining the predominant slip and twinning systems is challenging via experimentation alone. Slip trace analysis of images taken in a scanning electron microscope (SEM), electron backscattered diffraction (EBSD) and transmission electron microscopy (TEM) is usually performed post-mortem and only indicate which dislocations were stored (Akhtar and Teghtsoonian, 1971; Bieler et al., 2014; Obara et al., 1973). Also, the volume of the material studied is too small to provide statistically significant assessment. In-situ X-ray or neutron diffraction can provide data more representative of the volume, but de-coupling the activities of different slip and twinning modes is a challenge (Li et al., 2012; Lind et al., 2014; Ungár et al., 2007; Ungár et al., 2015). It has been shown in many studies that simultaneous experiment and modeling of the constitutive response and microstructural evolution is necessary for the determination of active deformation modes (Abdolvand et al., 2015; Ardeljan et al., 2014; Carpenter et al., 2015; Fromm et al., 2009; Knezevic et al., 2013b; Knezevic and Landry, 2015; Knezevic et al., 2010; Knezevic et al., 2014e; Knezevic et al., 2015a; Lentz et al., 2015a; Lentz et al., 2015b; Zecevic et al., 2015a). The combination allows for a larger representative volume of the material to be probed. This method, however, relies on the model to be dependable at multiple scales; that is, to have a physically based hardening law, rigorous micromechanics, representative mechanical fields across the sample, and the same boundary conditions as in the test.

Many efforts have been devoted to developing multiscale constitutive models to meet these demands. Difficulty can arise when modeling the strain-rate dependency of the constitutive

response because rate sensitivity can enter into the calculation via the formulae used at different length scales. It is clearly desirable for the rate dependence in the macroscale response to arise solely due to the rate dependence of dislocation motion on individual slip systems at the microscale (Kocks and Mecking, 2003; Mecking and Kocks, 1981). However, additional rate sensitivities can emerge as a result of the implementation or formulation. Oftentimes, for instance, a rate-sensitive hardening law is implemented into a polycrystal plasticity code in efforts to link the evolution of the macroscopic responses and texture to rate-sensitive dislocation motion (Knezevic et al., 2013a; Knezevic et al., 2014a; Knezevic et al., 2014b; Knezevic et al., 2013e). The polycrystal code is then used to relate the response of the aggregate of grains to the response of each constituent grain. The grain response, in turn, is linked with the active slip and twinning systems via crystal plasticity theory. This theory may employ a visco-plastic rate-dependent flow rule to determine which slip and twinning systems are active given the current state of stress and strain-rate in the grain. The flow rule has a power-law form that introduces an exponent n that is often called or related to the rate sensitivity of the material (Asaro and Needleman, 1985; Hutchinson, 1976). In general the power-law expression with fixed exponent n can only be accurate for a small range of strain-rates (Kok et al., 2002). Varying this exponent from 1 to 100 can have a marked effect on the macroscale response. The value of n selected, particularly in the case of HCP materials, would not have an obvious connection to the actual material rate sensitivity and could undermine any attempts to develop a reliable, physically based rate-sensitive hardening law.

The objective of this study is to develop a multi-scale finite element (FE) based model for the rate-sensitive constitutive response of metals that deform by solely crystallographic slip as well as by multiple slip and twinning modes. We introduce a formulation that relaxes the rate

sensitivity that enters via the exponent, *n*, while still retaining the visco-plastic flow rule. As such, all the rate sensitivity can be embodied in the characteristic activation stresses for the individual slip and twinning systems. The formulation is applied to simulate a Taylor impact test on Zr. To this end, experimental post-test specimen geometry and evolution of texture and twin volume fraction as a function of axial position are measured and compared with the calculations. Very good agreement between the calculations and the experiments is realized in every aspect of the comparison.

2   Visco-plastic polycrystal modeling background

2.1   *Summary of VPSC*

The objective of a polycrystal model, such as visco-plastic self-consistent (VPSC) model, is to relate the deformation of an aggregate to the deformation of its constituent grains. In the VPSC model, a polycrystal is represented by a number of grains, each with an assigned crystallographic orientation, shape and volume fraction. In VPSC, elastic deformation is neglected. To calculate its interaction with the other grains in the polycrystal, each grain is treated as a visco-plastic inclusion embedded in a homogeneous effective medium (HEM) that has the average properties of the polycrystalline aggregate. This elementary inclusion problem is solved using a Green's function approach (Lebensohn and Tomé, 1993; Lebensohn et al., 2016). Each inclusion (or representative grain) may deform via a combination of crystallographic slip and twinning. Single crystal visco-plasticity is then used to relate the deformation of the grain to its active crystallographic slip and twinning systems. In this framework, active slip or twinning systems are selected by the following power-law relationship (Asaro and Needleman, 1985; Hutchinson, 1976):

14

$$\dot{\gamma}^{sc} = \dot{\gamma}_0 \left(\frac{|\boldsymbol{\sigma}'^c \cdot \mathbf{m}^{sc}|}{\tau_c^{sc}} \right)^n sign(\boldsymbol{\sigma}'^c \cdot \mathbf{m}^{sc}), \qquad (1)$$

where $\dot{\gamma}^{sc}$ is the shearing rate on a slip or twin system, s. In Eq. (1), $\boldsymbol{\sigma}'^c$ is the Cauchy stress deviator of a grain c, τ_c^{sc} is a slip or twin resistance, $\dot{\gamma}_0$ is the reference value of the shearing rate usually taken as unity, n is the rate sensitivity exponent, $\mathbf{m}^{sc}$ is the Schmid tensor for slip or twinning system, s, calculated as $0.5(\mathbf{b}^{sc} \otimes \mathbf{n}^{sc} + \mathbf{n}^{sc} \otimes \mathbf{b}^{sc})$, where, $\mathbf{b}^{sc}$ is the Burgers vector and $\mathbf{n}^{sc}$ is the slip plane normal.

The deviatoric strain-rate, $\dot{\boldsymbol{\varepsilon}}_{vp}$, is related to $\boldsymbol{\sigma}'^c$ through the following rate equation:

$$\dot{\boldsymbol{\varepsilon}}_{vp}^c = \dot{\gamma}_0 \sum_s \mathbf{m}^{sc} \left(\frac{|\boldsymbol{\sigma}'^c \cdot \mathbf{m}^{sc}|}{\tau_c^{sc}} \right)^n sign(\boldsymbol{\sigma}'^c \cdot \mathbf{m}^{sc}). \qquad (2)$$

Note that, $\dot{\varepsilon} = |\dot{\boldsymbol{\varepsilon}}_{vp}|$, $tr(\dot{\boldsymbol{\varepsilon}}_{vp}^c) = 0$, and $tr(\dot{\boldsymbol{\varepsilon}}_{vp}) = 0$. For every grain, the nonlinear relation in Eq. (2) can be linearized via:

$$\dot{\boldsymbol{\varepsilon}}_{vp}^c = \mathbf{M}^c \cdot \boldsymbol{\sigma}'^c + \dot{\boldsymbol{\varepsilon}}^{0c}, \qquad (3)$$

where $\mathbf{M}^c(\boldsymbol{\sigma}'^c)$ and $\dot{\boldsymbol{\varepsilon}}^{0c}$ are the grain scale visco-plastic compliance and back-extrapolated strain-rate, respectively. In VPSC, different choices are possible for the linearized behavior at the grain scale: (1) the upper bound secant approximation, which approaches an iso-strain state known to provide a stiff response (the Taylor model) (Hutchinson, 1976; Taylor, 1938), (2) the lower bound tangent approximation, which tends to a uniform stress state known to provide a compliant response (the Sachs model) (Lebensohn and Tomé, 1993; Sachs, 1929), (3) the affine approximation (Masson et al., 2000), and (4) the n^{eff} approximation (usually $n^{eff} = 10$, which gives a similar response to affine) (Lebensohn et al., 2007). The (1) and (2) are rarely used. The latter two linearization approaches are usually used and are referred to as intermediate because they are

between the bounds. Depending on the chosen linearization assumption, $\mathbf{M}^c$ and $\dot{\boldsymbol{\varepsilon}}^{0c}$ can be evaluated differently. For example, making use of the affine approximation:

$$\mathbf{M}^c = n\dot{\gamma}_0 \sum_s \frac{\mathbf{m}^{sc} \otimes \mathbf{m}^{sc}}{\tau_c^{sc}} \left(\frac{\left| \boldsymbol{\sigma'}^c \cdot \mathbf{m}^{sc} \right|}{\tau_c^{sc}} \right)^{n-1} \text{ and } \dot{\boldsymbol{\varepsilon}}^{0c} = (1-n)\dot{\boldsymbol{\varepsilon}}_{vp}^c . \tag{4}$$

The solution to Eq. (2) is the deviatoric stress of the Cauchy stress tensor, $\boldsymbol{\sigma'}^c$, consisting of five independent deviatoric stress components. The deviatoric components can be evaluated by solving Eq. (2) using the Newton-Raphson (NR) scheme after applying a strain-rate tensor $\dot{\boldsymbol{\varepsilon}}_{vp}^c$.

Arriving at a solution is computationally challenging because of the need to iteratively solve the set of highly non-linear, extremely stiff equations (exhibiting poor convergence characteristics), for every constituent crystal at each trial strain increment. The higher the exponent n in Eq. (1), the numerically stiffer these equations become and hence, the more difficult they are to solve. Treating numerical stiffness usually involves modifying the standard Newton-Raphson scheme to include a selective reduction of the correction term based on the Armijo method (Armijo, 1966) or involves using non-iterative spectral solvers (Al-Harbi et al., 2010; Kalidindi et al., 2006; Knezevic et al., 2009; Knezevic and Kalidindi, 2007; Knezevic et al., 2008a; Knezevic et al., 2008b; Shaffer et al., 2010).

The behavior of the polycrystalline aggregate takes on a similar linear relationship:

$$\dot{\boldsymbol{\varepsilon}}_{vp} = \mathbf{M} \cdot \boldsymbol{\sigma'} + \dot{\boldsymbol{\varepsilon}}^0, \tag{5}$$

where $\boldsymbol{\sigma'}$ is the effective stress deviator, $\mathbf{M}$ is the visco-plastic compliance, and $\dot{\boldsymbol{\varepsilon}}^0$ is the back-extrapolated strain-rate of the polycrystalline aggregate. The SC method then iteratively calculates the deviatoric stress and visco-plastic strain-rate for every ellipsoidal grain with moduli $\mathbf{M}^c$ and $\dot{\boldsymbol{\varepsilon}}^{0c}$ embedded in a polycrystalline aggregate of moduli $\mathbf{M}$ and $\dot{\boldsymbol{\varepsilon}}^0$.

After the solution procedure, shearing rates $\dot{\gamma}^{sc}$ are used to calculate the lattice rotation-rates associated with each grain. The lattice spin tensor, $\mathbf{W}^{*c}$, is defined as:

$$\mathbf{W}^{*c} = \mathbf{W} + \mathbf{\Pi}^c - \mathbf{W}^{pc} \tag{6}$$

where $\mathbf{W}$ is the applied spin, $\mathbf{\Pi}^c$ is the contribution from the antisymmetric part of the Eshelby tensor per ellipsoidal domain (Lebensohn and Tomé, 1993), and $\mathbf{W}^{pc}$ is the plastic spin in a grain due to crystallographic slip. The plastic spin is calculated from the shearing rates as:

$$\mathbf{W}^{pc} = 0.5 \sum_s \dot{\gamma}^{sc} (\mathbf{b}^{sc} \otimes \mathbf{n}^{sc} - \mathbf{n}^{sc} \otimes \mathbf{b}^{sc}). \tag{7}$$

The above anti-symmetric portion of the dyadic product of the two unit vectors is for the Burgers vector, $\mathbf{b}^{sc}$, and the slip plane normal, $\mathbf{n}^{sc}$. Equation (6) is used for the evolution of crystal orientations with strain.

2.2 Hardening law

The constitutive response requires a hardening model for τ_c^s that dictates how slip resistances evolve. Ideally the slip resistance should evolve with not only strain but also temperature (T) and strain-rate ($\dot{\varepsilon}$). In all calculations here, we employ a recently developed dislocation density-based hardening law where $\tau_c^s(\dot{\varepsilon}, T)$ is governed by thermally-activated rate laws for dislocation storage. The value of strain rate, $\dot{\varepsilon}$, used in the hardening law is the effective norm of the applied strain rate in the current time increment i.e. $\dot{\varepsilon} = \sqrt{\frac{2}{3}} |\dot{\boldsymbol{\varepsilon}}|$. The twin resistances are not a function of temperature and strain-rate directly but only indirectly through twin-slip interactions. The complete details and associated material parameters can be found in (Knezevic et al., 2015b) and for completeness of the present paper are repeated here as well. An added reason is, since the model presented here differs in handling the rate sensitivity, we found it

necessary to slightly adjust a few of parameters. Table 1 and 2 show the complete list of material

parameters. In the interest of space, the parameters are not further discussed. Detailed discussion

can be found in (Knezevic et al., 2015b), while the main equations of the model are given in the

appendix.

Table 1. Slip system characteristics and material parameters for the evolution of slip system resistances.

	$\alpha = 1, \{\bar{1}100\}\langle\bar{1}\bar{1}20\rangle$	$\alpha = 2, \{10\bar{1}1\}\langle\bar{1}\bar{1}23\rangle$	$\alpha = 3, \{0001\}\langle\bar{1}\bar{1}20\rangle$
$b^\alpha [m]$	3.231 x 10^{-10}	6.0771 x 10^{-10}	3.231 x 10^{-10}
$\tau_0^\alpha [MPa]$	$\tau_0^\alpha = A^\alpha \left(1 + B^\alpha \log\left(\frac{\dot{\varepsilon}}{\dot{\varepsilon}_{ref}}\right)\right) \exp\left(-\frac{T}{C^\alpha}\right)\left(1 + E^\alpha lognormal(\sigma^\alpha, v^\alpha)\right)$		
HP^α	0.1	0.17	0.1
$k_1^\alpha [m^{-1}]$	5.3 x 10^8	2.0 x 10^9	9.7 x 10^8
g^α	0.002	0.005	0.002
$D^\alpha [MPa]$	700	1400	1400
q^α	$12 \log(1 + T/30)$	0.1	$12 \log(1 + T/30)$
$A^\alpha [MPa]$	23.5	350	2500
B^α	0.04	0.02	N/A
$C^\alpha [K]$	235	190	150
E^α	6900	36000	N/A
v^α	7.2	7.45	N/A
σ^α	0.5	0.5	N/A

The possible slip and twinning deformation modes for Zr have been identified previously

(Akhtar, 1973a, b, 1975a, b), and these same families are made available in the present

calculations. For slip, these are prismatic $\{\bar{1}100\}\langle\bar{1}\bar{1}20\rangle$ slip, pyramidal type I $\{10\bar{1}1\}\langle\bar{1}\bar{1}23\rangle$

slip, and basal $\{0001\}\langle\bar{1}\bar{1}20\rangle$ slip. These are listed in order of easiest to hardest to activate at

ambient conditions. The possible twinning modes are $\{10\bar{1}2\}\langle10\bar{1}\bar{1}\rangle$, $\{11\bar{2}2\}\langle11\bar{2}\bar{3}\rangle$, and

$\{10\bar{1}1\}\langle10\bar{1}\bar{2}\rangle$. The former is the most commonly observed twin mode in most HCP metals and it accommodates extension of the c-axis, whereas the latter two accommodate contraction of the c-axis in Zr. Since in the hardening law each slip mode has its own separate dependencies on strain, temperature, and strain-rate, the modes are not all expected to act simultaneously or in the same relative amounts in all test conditions. The hardening law was validated on compression and tension tests over a broad range of strain-rates, from 0.001 /s to 4500 /s, and over a broad range of temperatures, from 76 K to 673 K. Particular changes in the flow stress behavior and anisotropy with several orders of magnitude increases in strain-rate have been linked to transitions in the predominant slip mode and twinning mode (Knezevic et al., 2015b).

3   A new formulation for relaxing the power-law flow rule imposed strain-rate sensitivity

In modeling the macroscale deformation response, it is physical and thus desirable to account for the strain-rate dependence solely with a functional dependence of $\tau_c^s(\dot{\varepsilon})$ on strain-rate $\dot{\varepsilon}$. However, in visco-plastic single crystal plasticity, rate sensitivity also enters via the power-law flow rule and its parameter n in Eq (1). Commonly used values for the exponent, n, lie in the range of 1 to 20 in VPSC. With these values, the flow rule can have a significant, superfluous effect on the strain-rate sensitivity of the macroscale response (Asaro and Needleman, 1985; Hutchinson, 1976; Kalidindi et al., 1992). In principle, the larger the exponent, n, the smaller the rate sensitivity. Only in the limit of n approaching infinity ($n \rightarrow \infty$) can a power-law rate-insensitive response be achieved, and only then will the rate sensitivity in material response be a consequence of solely the rate dependence of the slip resistance $\tau_c^s(\dot{\varepsilon})$, which is usually desired for metallic materials. In contrast, it is also possible to use slip resistance that does not depend on the strain rate and to capture the rate sensitivity solely with

exponent n determined from the experimental data for particular material. Achieving this numerically is challenging, however, due to the numerical stiffness of the equations involved.

Table 2. Twin system characteristics and material parameters for the evolution of twin resistances.

	$\beta = 1, \{10\bar{1}2\}\langle10\bar{1}\bar{1}\rangle$	$\beta = 2, \{11\bar{2}2\}\langle11\bar{2}\bar{3}\rangle$	$\beta = 3, \{10\bar{1}1\}\langle10\bar{1}\bar{2}\rangle$
b^β [m]	6.33 x 10^{-11}	9.24 x 10^{-11}	3.0796 x 10^{-11}
S^β	0.167	0.225	0.104
τ^β_{crit} [MPa]	100	230	350
τ^β_{prop} [MPa]	5	230	50
HP^β [MPa$\sqrt{m}$]	0.135	0.1	0.1
$C^{1\beta}$	N/A	$1300 - 100\log\left(\dfrac{\dot{\varepsilon}}{\dot{\varepsilon}_{ref}}\right)$	N/A
$C^{2\beta}$	100	10	N/A
$C^{3\beta}$	N/A	$1300 - 100\log\left(\dfrac{\dot{\varepsilon}}{\dot{\varepsilon}_{ref}}\right)$	N/A

Figure 1 shows the effect of the exponent n=10 on the stress-strain response of Zr when compressed through the thickness of the sheet. The value of n=10 was used in all previous reports involving the FE-VPSC calculations (Knezevic et al., 2013d; Segurado et al., 2012). These calculations involve repeating the uniaxial test at different strain-rates from 0.001/s to 10/s and using the same rate-dependent hardening law for $\tau^s_c(\dot{\varepsilon})$. By simply increasing n, the rate dependencie is expected to reduce. The values of slip/twin resistance used to generate the stress-strain curves shown in Fig. 1 were fixed to correspond to deformation at room temperature and a strain-rate, $\dot{\varepsilon}$, equal to unity. Therefore there was no contribution to the rate sensitivity from $\tau^s_c(\dot{\varepsilon})$.

Based on the analysis of material response at different strain-rates it was determined that a rate sensitivity of n approximately 400 ($m \approx 0.0025$, $n=1/m$) would be sufficient to reduce the rate dependence of stress to a negligible level.
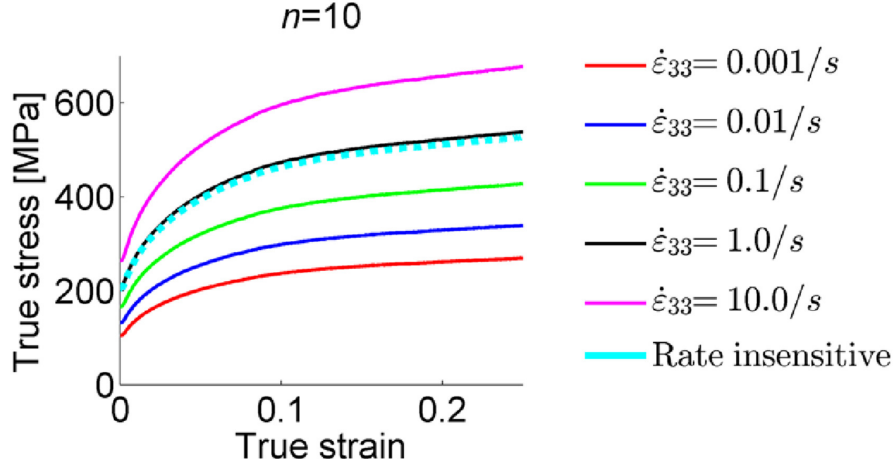
Fig. 1. Effect of $n =10$ on the room temperature mechanical response of Zr in through-thickness compression as a function of imposed strain rate. The rate insensitive strain rate corresponds to $|\dot{\varepsilon}| = 1.0 \ /s$.

This problem has been recognized and two methods are commonly used to remove the extraneous rate sensitivity arising from the visco-plastic power-law form (Knezevic et al., 2009; Kok et al., 2002). The first method involves simply increasing n to high values. However, this method is not efficient because increasing n could result in convergence problems since the non-linear equations become too stiff and prohibitively challenging for the Newton-Raphson numerical schemes to solve.

The second method involves setting the reference shear rate $\dot{\gamma}_0$, equal to the norm of the applied macroscopic strain-rate: $\dot{\gamma}_0 = |\dot{\varepsilon}_{vp}|$, which removes the dependence of grain stresses and macroscopic stress upon the norm of the applied strain rate absolutely. To this end, when $\dot{\varepsilon}_{vp}$ is applied, the relation between σ'^c and $\dot{\varepsilon}_{vp}^c$ is given by the following rate equation:

$$\dot{\boldsymbol{\varepsilon}}_{vp}^c = \left|\dot{\boldsymbol{\varepsilon}}_{vp}\right| \sum_s \mathbf{m}^{sc} \left(\frac{\left|\boldsymbol{\sigma}'^c \cdot \mathbf{m}^{sc}\right|}{\tau_c^{sc}}\right)^n sign(\boldsymbol{\sigma}'^c \cdot \mathbf{m}^{sc}). \tag{8}$$

Any applied strain-rate that scales the given value $\dot{\boldsymbol{\varepsilon}}_{vp}$ by λ, i.e. $\lambda\dot{\boldsymbol{\varepsilon}}_{vp}$, is realized similarly through the following rate equation:

$$\lambda\dot{\boldsymbol{\varepsilon}}_{vp}^c = \left|\lambda\dot{\boldsymbol{\varepsilon}}_{vp}\right| \sum_s \mathbf{m}^{sc} \left(\frac{\left|\boldsymbol{\sigma}'^c \cdot \mathbf{m}^{sc}\right|}{\tau_c^{sc}}\right)^n sign(\boldsymbol{\sigma}'^c \cdot \mathbf{m}^{sc}). \tag{9}$$

Note that λ only changes the magnitude of the applied strain rate and not the sense of loading. The stress $\boldsymbol{\sigma}'^c$ will remain unchanged provided that τ_c^s does not change with strain-rate making the response rate independent. Therefore, this method achieved the complete rate independence. In summary, scaling the applied strain rate $\lambda\dot{\boldsymbol{\varepsilon}}_{vp}$ will make the grain strain rates also scale since $\dot{\boldsymbol{\varepsilon}}_{vp} = \langle\dot{\boldsymbol{\varepsilon}}_{vp}^c\rangle \rightarrow \lambda\dot{\boldsymbol{\varepsilon}}_{vp} = \langle\lambda\dot{\boldsymbol{\varepsilon}}_{vp}^c\rangle$, but will not alter the grain stress and the overall polycrystal stress provided that $\dot{\gamma}_0 = \left|\lambda\dot{\boldsymbol{\varepsilon}}_{vp}\right|$. In contrast, if the reference value of shear rate was not set to be equal to the norm of the scaled applied macroscopic strain rate but kept to be $\dot{\gamma}_0 = \left|\dot{\boldsymbol{\varepsilon}}_{vp}\right|$, scaling the applied strain rate would result in scaling the solution grain stress by $\lambda^{\frac{1}{n}}\boldsymbol{\sigma}'^c$ according to:

$$\lambda\dot{\boldsymbol{\varepsilon}}_{vp}^c = \left|\dot{\boldsymbol{\varepsilon}}_{vp}\right| \sum_s \mathbf{m}^{sc} \left(\frac{\left|\lambda^{\frac{1}{n}}\boldsymbol{\sigma}'^c \cdot \mathbf{m}^{sc}\right|}{\tau_c^{sc}}\right)^n sign\left(\lambda^{\frac{1}{n}}\boldsymbol{\sigma}'^c \cdot \mathbf{m}^{sc}\right).$$ Similarly, the overall polycrystal

stress would also be scaled.

There is an issue with the second method when it comes to an FE implementation of the rate independent Eq. 9. Here, the five-component deviatoric stress, $\boldsymbol{\sigma}'^c$, is no longer a function of the norm of the applied visco-plastic strain rate, $\left|\dot{\boldsymbol{\varepsilon}}_{vp}\right|$, but a function of only four independent components of the normalized visco-plastic strain rate. Consequently, the solution for deviatoric stress contains five *dependent* deviatoric stress components. This further implies that the Cauchy

stress, required by Abaqus, will only have five independent components, representing a hyper-surface in six-dimensional stress space. This leads to difficulties when attempting to solve for this Cauchy stress within the FE framework since many matrices that need to be inverted within the UMAT numerical procedure will be singular.

In light of the issues faced by the two traditional methods, we propose an alternative method to eliminate the power-law rate-sensitivity introduced via the power-law exponent n. To this end, we return to the power-law rate-sensitive VPSC where the five deviatoric stress components are guaranteed to be independent. The aim is to reduce the power-law rate sensitivity of the deviatoric stress as much as possible by increasing n as much as possible. We first modify the Newton-Raphson method for solving the visco-plastic Eq. (2) per grain in VPSC by adding a loop that will use the solution obtained for a value of $n = 20$ as the initial guess for a higher value, say $n = 50$. The scheme can be repeated, such that the solution for $n = 50$ can be used as an initial guess for solving for the stress associated with a higher n like 80 or 100. With this method, the numerical scheme remains stable for every crystal orientation for $n<100$. We refer to this approach as the incremental-n method. As mentioned earlier, we have determined that the desired value of n sufficient to relax the rate sensitivity is 400. However, while with the incremental-n method we can access higher values of n, we find that this method substantially increases the computation time involved in simulations. The power-law equation is solved for every crystal at every trial time increment and thus a small increase in the number of iteration to solve for grain stress has a significant effect on overall computational time. After performing a trade of convergence and computational efficiency study, it was determined that the modified Newton-Raphson method works the best for $n=50$. Here, the added second loop was really entered by only a few crystals.

The proposed algorithm, called the *k*-modification method, achieves the best compromise between the speed and accuracy. We first define a VPSC rate-sensitive macroscopic constitutive function, **g**, for relating the macroscopic stress, **σ′**, and applied macroscopic strain rate, $\dot{\boldsymbol{\varepsilon}}_{vp}^{app}$, via:

$$\boldsymbol{\sigma}' = \mathbf{g}(\dot{\boldsymbol{\varepsilon}}_{vp}^{app}). \tag{10}$$

The key idea in this method is to modify the applied strain rate before evaluating the visco-plastic constitutive function, **g**. In place of the original rate $\dot{\boldsymbol{\varepsilon}}_{vp}^{app}$, we use a modified strain rate, $\dot{\boldsymbol{\varepsilon}}_{vp}$, whose norm is the $(k+1)^{\text{th}}$ root of $\dot{\boldsymbol{\varepsilon}}_{vp}^{app}$, i.e.:

$$\dot{\boldsymbol{\varepsilon}}_{vp} = \frac{\dot{\boldsymbol{\varepsilon}}_{vp}^{app}}{\left|\dot{\boldsymbol{\varepsilon}}_{vp}^{app}/\dot{\varepsilon}_{ref}\right|} \left|\dot{\boldsymbol{\varepsilon}}_{vp}^{app}/\dot{\varepsilon}_{ref}\right|^{\frac{1}{k+1}}. \tag{11}$$

Here, $\dot{\varepsilon}_{ref}$ represents a reference strain rate, which is used to normalize the applied strain rate ensuring that the expression raised to the power is dimensionless. In the current implementation $\dot{\varepsilon}_{ref}$ is set to be $\dot{\varepsilon}_{ref} = 1 \ /\text{s}$. It can be readily shown that the inverse relationship is:

$$\dot{\boldsymbol{\varepsilon}}_{vp}^{app} = \dot{\boldsymbol{\varepsilon}}_{vp}\left|\dot{\boldsymbol{\varepsilon}}_{vp}/\dot{\varepsilon}_{ref}\right|^{k}. \tag{12}$$

Finally, the macroscopic visco-plastic constitutive function for the modified $\dot{\boldsymbol{\varepsilon}}_{vp}$ is evaluated as:

$$\boldsymbol{\sigma}' = \mathbf{g}(\dot{\boldsymbol{\varepsilon}}_{vp}). \tag{13}$$

Relationships 11 and 12 assure that $\left|\dot{\boldsymbol{\varepsilon}}_{vp}\right|$ approaches unity with increasing *k*. Macroscopic stress, **σ′**, can now be calculated after imposing the applied strain rate, $\dot{\boldsymbol{\varepsilon}}_{vp}$, which is less rate sensitive than the original $\dot{\boldsymbol{\varepsilon}}_{vp}^{app}$, provided that we set $k > 0$. As a result, the rate sensitivity is now characterized by both the power-law exponent, n, and the additional exponent k. By analogy to Eq. 9, suppose that the applied strain rate, $\dot{\boldsymbol{\varepsilon}}_{vp}^{app}$, is scaled such that $\lambda\dot{\boldsymbol{\varepsilon}}_{vp}^{app}$ is applied.

Then from Eq. 11 the *k*-modified imposed strain rate would be $\lambda^{\frac{1}{k+1}}\dot{\boldsymbol{\varepsilon}}_{vp}$. Similar to the discussion

after Eq. 9, the grain strain rate changes according to: $\dot{\boldsymbol{\varepsilon}}_{vp} = \langle\dot{\boldsymbol{\varepsilon}}_{vp}^{C}\rangle \rightarrow \lambda^{\frac{1}{k+1}}\dot{\boldsymbol{\varepsilon}}_{vp} = \langle\lambda^{\frac{1}{k+1}}\dot{\boldsymbol{\varepsilon}}_{vp}^{C}\rangle$.

Finally, the grain stress and macroscopic stress change according to: $\boldsymbol{\sigma}' = \langle\boldsymbol{\sigma}'^{C}\rangle \rightarrow \lambda^{\frac{1}{(k+1)n}}\boldsymbol{\sigma}' =$

$\langle\lambda^{\frac{1}{(k+1)n}}\boldsymbol{\sigma}'^{C}\rangle$. The power-law exponent is now multiplied by $k+1$, which has the direct effect of

decreasing the overall rate sensitivity effect ($m=1/((k+1)n)$), provided again that $k > 0$. Removing

the rate dependence introduced by the power-law exponent *n* is the key achievement of the *k*-

modification method. A notable advantage is that this method does not increase the

computational time of VPSC calculations.

To demonstrate the effect, Fig. 2 compares the stress-strain response for the same conditions

as presented in Fig. 1.It can be seen that the *k*-modification method for $n = 50$ and $k+1=8$

effectively relaxes the power-law imposed rate sensitivity. Therefore, the rate sensitivity can be

embedded solely in $\tau_c^s(\dot{\varepsilon})$.

The *k*-modification method is effective at removing the rate sensitivity introduced by *n*,

while still enabling the formulation to retain the visco-plastic power-law flow rule. We will use

the *k*-modification method with a value of $n(k+1) = 400$ in all remaining calculations of the FE-

VPSC model. This value added negligible small computational cost compared to calculations

with $k=0$.
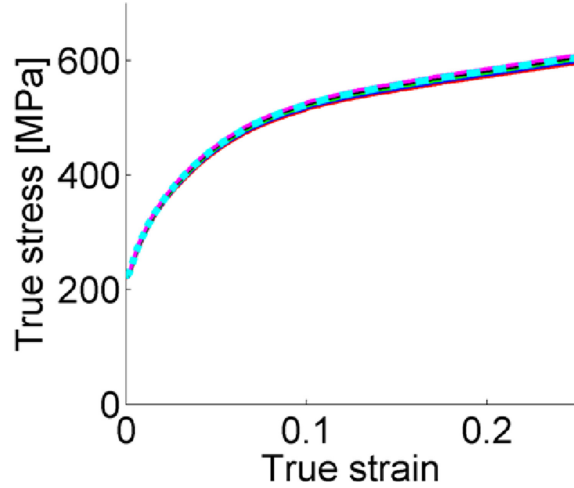
Fig. 2. Effect of a combination of $n = 50$ and $k + 1 = 8$ on removing the power-law imposed strain-rate sensitivity of the mechanical response of Zr in through-thickness compression as a function of imposed strain rate. The legend here is the same as the one in Fig. 1.

It should be noted that there is a fundamental difference between the proposed *k*-modification approach and the approach that involves solely increasing the exponent *n* when arriving at the grain stress solution. The effect of increasing *n* is illustrated on the Fig. 3, where a shear stress tensor has been applied to a Zr single crystal oriented in such a way as to activate only one prismatic slip system. A relative contribution of each deformation system has been calculated and the normalized values ($\dot{\gamma}^s / \sum_s \dot{\gamma}^s$) plotted versus the exponent *n*. Figure 3 shows that the relative contribution of individual slip/twin systems changes the *n*, which in turn will cause changes in both the magnitude and direction of the macroscale plastic strain rate. Low values of *n* cause the slip and twinning systems to be active over a relatively wide range of stresses, making the results smooth with respect to a change in stress. As illustrated, even if the stress tensor is favorable for slip on only one system, several systems can be active for low values of the exponent *n*. In contrast, high values of *n* bring the resolved shear stress closer to the critical resolved shear stress for each active system making the range of stresses to reduce and correspond to a particular slip system. In addition to making the activation threshold sharper, it also makes the direction of strain rate very sensitive to changes in stress.

26
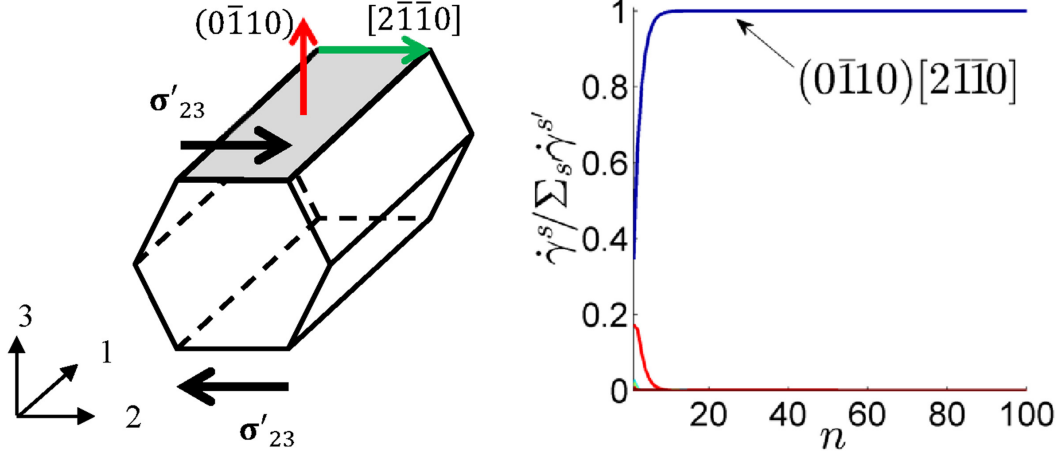
Fig. 3. Predicted activity of deformation systems in a single crystal of Zr oriented to activate only $(0\bar{1}10)[2\bar{1}\bar{1}0]$ slip system during pure shear as a function of the exponent n.

While the magnitude of strain rate is defined by both n and k, the increase in k does not affect the relative contribution of deformation systems that are active but only affects the scaling of the norm of strain rate with the norm of stress. As a result, the direction of strain rate is defined solely by n meaning that the unrealistic smoothing associated with lower values of n can be present in the k-modification approach. However smoothing is not expected to cause any appreciable differences in the response and especially in the macroscopic-level response, as long a sufficiently high value of n is used. For example, the macroscopic stresses in the compression test of Zr calculated using $n=400$, on one hand, and using the k-modification approach with $k=7$ and $n=50$, on the other hand, are predicted to be about 1% different from each other.

4   FE formulation of the power-law relaxed strain-rate sensitivity VPSC capable of handling the strain-rate imposed boundary conditions

Elastic and plastic strain rates can develop heterogeneously in a mechanical test. Furthermore, bulk metal forming processes typically impose non-monotonic boundary conditions on the sample (Bhattacharyya et al., 2015; Hosford and Caddell, 2011; Jahedi et al., 2015b; Jahedi et al., 2015c; Jahedi et al., 2014; Smith et al., 2016; Zecevic et al., 2016c). For these

reasons, a polycrystal code, like VPSC, has been integrated into an FE framework, where every integration point is a VPSC polycrystal. A strategy for embedding the VPSC model at the meso-scale level in an implicit FE analysis tools was first described in (Segurado et al., 2012) and later advanced in (Knezevic et al., 2013d). Since then, the FE-VPSC model has been successfully applied to simulate bi-metallic tube extrusion (Knezevic et al., 2014d), bending of beams (Knezevic et al., 2013c), rolling of sheets (Zecevic et al., 2016a, b) and integrity of structural components (Knezevic et al., 2016). However, while stand-alone VPSC works for strain-rate-imposed, stress-imposed, or mixed boundary conditions, the earlier versions of the FE-VPSC techniques were based on *stress-imposed boundary conditions*. This approach caused the model to be numerically unstable as n increases above 10. To resolve this problem and test the convergence properties in strain rate space, we formulate below an alternative version of FE-VPSC, which is based on *strain-rate-imposed boundary conditions*.

Within the former FE-VPSC UMAT algorithm with *stress-imposed boundary conditions*, the VPSC model begins under the Sachs assumption of a uniform stress enforced on all its constituent grains, i.e., $\boldsymbol{\sigma}'^{c} = \boldsymbol{\sigma}'$. From this initial guess, the corresponding single crystal visco-plastic strain-rate, $\dot{\boldsymbol{\varepsilon}}_{vp}^{c}$, as well as the single crystal viscoplastic compliance, $\mathbf{M}^{c}$, and back-extrapolated strain-rate, $\dot{\boldsymbol{\varepsilon}}^{0c}$, can be readily calculated. Next, initial guesses for the polycrystal compliance, $\mathbf{M}$, and the polycrystal back-extrapolated strain-rate, $\dot{\boldsymbol{\varepsilon}}^{0}$, are obtained by assuming that they are equal to simple volume averages of the local moduli. With these initial guesses, and the applied stress, $\boldsymbol{\sigma}'$, the initial guess for the polycrystal strain-rate, can be obtained using Eq. (5). At this point, the Eshelby tensor can be computed and the rest of the standard self-consistent (SC) iterative procedure can be performed (Eshelby, 1957; Lebensohn and Tomé, 1993; Lebensohn et al., 2007). In the SC iterations, new estimates of the grain stress and strain-rate are

calculated as well as the average polycrystalline values. The procedure continues until the recalculated average grain stresses are within a certain tolerance of the input values at the beginning of every iteration.

In the proposed FE-VPSC UMAT algorithm for *the strain-rate-imposed boundary conditions*, the VPSC model in the first increment starts with an initial guess for grain stresses derived from an iso-strain or Taylor model, where a uniform strain-rate is imposed over all constituent grains embedded at an FE integration point, i.e., $\dot{\boldsymbol{\varepsilon}}_{vp}^{c} = \dot{\boldsymbol{\varepsilon}}_{vp}$, from which the corresponding single crystal stresses, $\boldsymbol{\sigma}'^{c}$, are calculated. From this point onward, the SC iterations run as described above. In every subsequent increment, the initial guess is the solution from the previous increment. An added benefit of a *strain-rate-imposed boundary conditions* FE-VPSC implementation is that it can run with a Taylor-type homogenization through, which is faster than the SC homogenization. The new FE-VPSC model can also run as the CPFE code (Ardeljan et al., 2015b; Jahedi et al., 2015a; Knezevic et al., 2014c), where every integration point represents a single crystal. All the results reported in this paper are obtained using the SC homogenization.

4.1 *Constitutive equation and its time integration procedure within the UMAT*

To couple the new FE-VPSC framework in the implicit FE framework, we rely on the rate constitutive equation for stress and integration procedure used in (Zecevic et al., 2015b, c). Here, the rate of Cauchy stress (Asaro, 1979; Asaro and Needleman, 1985; Asaro and Rice, 1977; Hill, 1966; Hill and Rice, 1972; Peirce et al., 1982a; Peirce et al., 1982b) is defined at every FE integration point as a time derivative of the stress averaged over the polycrystal (Hill's condition $\boldsymbol{\sigma} = \langle \boldsymbol{\sigma}^{c} \rangle$) in the global frame as:

$$\dot{\boldsymbol{\sigma}} = \langle \dot{\boldsymbol{\sigma}}^c \rangle = \langle \hat{\boldsymbol{\sigma}}^c \rangle + \langle \mathbf{W}^{*c}\boldsymbol{\sigma}^c - \boldsymbol{\sigma}^c\mathbf{W}^{*c} \rangle = \langle \mathbf{C}^c \cdot \dot{\boldsymbol{\varepsilon}}_{el}^c \rangle + \langle \mathbf{W}^{*c}\boldsymbol{\sigma}^c - \boldsymbol{\sigma}^c\mathbf{W}^{*c} \rangle, \qquad (14)$$

where $\langle \cdot \rangle$ denotes the volumetric average, $\hat{\boldsymbol{\sigma}}^c$ is the Jaumann stress rate for each crystal rotating with the lattice, and $\mathbf{W}^{*c}$ is the lattice spin as defined in Eq. 6. Next we proceed with the integration of the rate form of the constitutive equation following (Hughes and Winget, 1980; Zecevic et al., 2015b, c) as:

$$\boldsymbol{\sigma}^{t+\Delta t} - \boldsymbol{\sigma}^t = \langle \mathbf{C}^c \cdot \Delta\boldsymbol{\varepsilon}_{el}^c \rangle + \int_t^{t+\Delta t} \langle \mathbf{W}^{*c}\boldsymbol{\sigma}^c - \boldsymbol{\sigma}^c\mathbf{W}^{*c} \rangle d\tau. \qquad (15)$$

We decouple the self-consistent determination of the polycrystalline elastic and visco-plastic responses as done in (Mercier and Molinari, 2009), thus neglecting the elastic anisotropy of individual grains. This means that we can separately treat the elastic properties of the polycrystal without consideration of the visco-plastic properties and assume that we have applied a $\Delta\boldsymbol{\varepsilon}_{el}$ to an elastic polycrystal. This permits calculation of the self-consistent elastic stiffness of the HEM satisfying: $\langle \mathbf{C}^c \cdot \Delta\boldsymbol{\varepsilon}_{el}^c \rangle = \mathbf{C} \cdot \Delta\boldsymbol{\varepsilon}_{el}$. The integrated constitutive equation then becomes:

$$\boldsymbol{\sigma}^{t+\Delta t} = \mathbf{C} \cdot \Delta\boldsymbol{\varepsilon}_{el} + \langle \boldsymbol{\sigma}^{c,t} + \int_t^{t+\Delta t} (\mathbf{W}^{*c}\boldsymbol{\sigma}^c - \boldsymbol{\sigma}^c\mathbf{W}^{*c}) d\tau \rangle = \mathbf{C} \cdot \Delta\boldsymbol{\varepsilon}_{el} + \langle \Delta\mathbf{R}^{*c}\boldsymbol{\sigma}^{c,t}\Delta\mathbf{R}^{*c^T} \rangle, \quad (16)$$

where $\Delta\mathbf{R}^{*c} = (\mathbf{I} - \beta\mathbf{W}^{*c}\Delta t)^{-1}(\mathbf{I} + (1-\beta)\mathbf{W}^{*c}\Delta t)$ (Hughes and Winget, 1980). $\Delta\mathbf{R}^{*c}$ is evaluated explicitly based on the spin, $\mathbf{W}^{*c}$, at the start of the time increment. The integration parameter, β, can be selected in the range from zero to one. In our calculations, it is taken to be 0.5. Due to the explicit integration procedure chosen in evaluating $\Delta\mathbf{R}^{*c}$, the time step should be carefully chosen since it can have some small influence on the solution for cases involving large rotations. Since the hydrostatic stress, σ_m^t, is invariant to rotation we can separate it and express Eq. (16) as follows:

$$\boldsymbol{\sigma}^{t+\Delta t} = \mathbf{C} \cdot \Delta\boldsymbol{\varepsilon}_{el} + \langle \Delta\mathbf{R}^{*c}(\boldsymbol{\sigma}'^{c,t} + \mathbf{I}\sigma_m^{c,t})\Delta\mathbf{R}^{*c^T} \rangle = \mathbf{C} \cdot \Delta\boldsymbol{\varepsilon}_{el} + \langle \Delta\mathbf{R}^{*c}\boldsymbol{\sigma}'^{c,t}\Delta\mathbf{R}^{*c^T} \rangle + \mathbf{I}\sigma_m^t. \quad (17)$$

As an aside, the elastic strain increment is readily determined if $\dot{\boldsymbol{\varepsilon}}_{vp}$ is known, that is, $\Delta\boldsymbol{\varepsilon}_{el} = \Delta\boldsymbol{\varepsilon} - \dot{\boldsymbol{\varepsilon}}_{vp}^{t+\Delta t}\Delta t$. The rate $\dot{\boldsymbol{\varepsilon}}_{vp}^{t+\Delta t}$ (in what follows we drop the superscript $t + \Delta t$: $\dot{\boldsymbol{\varepsilon}}_{vp}^{t+\Delta t} = \dot{\boldsymbol{\varepsilon}}_{vp}$), in turn, is related to the deviatoric stress of the polycrystalline aggregate through the visco-plastic self-consistent formalism. Finally, the expression for stress that is returned to Abaqus is:

$$\boldsymbol{\sigma}^{t+\Delta t} = \boldsymbol{\sigma}^{t,rot} + \Delta\boldsymbol{\sigma} \tag{18}$$

where $\Delta\boldsymbol{\sigma} = \hat{\boldsymbol{\sigma}}\Delta t = \mathbf{C} \cdot (\Delta\boldsymbol{\varepsilon} - \dot{\boldsymbol{\varepsilon}}_{vp}\Delta t)$ and $\boldsymbol{\sigma}^{t,rot} = \langle\Delta\mathbf{R}^{*c}\boldsymbol{\sigma}'^{c,t}\Delta\mathbf{R}^{*cT}\rangle + \mathbf{I}\sigma_m^t$.

It is worth noting that Eqs. (17) and (18) are different than those presented in a prior FE-VPSC implementation (Knezevic et al., 2013d; Segurado et al., 2012). The difference lies in the use of $\Delta\mathbf{R}^{*c}$ in the current formulation. In contrast, in the previous one, this was not considered. There, the rate form of the constitutive equation was defined in the corrotational material frame (subscript mat) rotating with the material spin, $\mathbf{W}$, as $\hat{\boldsymbol{\sigma}}_{mat} = \mathbf{C}_{mat} \cdot (\dot{\boldsymbol{\varepsilon}}_{mat} - \dot{\boldsymbol{\varepsilon}}_{vp,mat})$, then integrated in the corrotational frame as $\boldsymbol{\sigma}_{mat}^{t+\Delta t} = \mathbf{C}_{mat} \cdot (\Delta\boldsymbol{\varepsilon}_{mat} - \dot{\boldsymbol{\varepsilon}}_{vp,mat}\Delta t) + \boldsymbol{\sigma}_{mat}^t$. In the global frame this equation corresponds to: $\boldsymbol{\sigma}^{t+\Delta t} = \mathbf{C} \cdot (\Delta\boldsymbol{\varepsilon} - \dot{\boldsymbol{\varepsilon}}_{vp}\Delta t) + \Delta\mathbf{R}\boldsymbol{\sigma}^t\Delta\mathbf{R}^T$, where $\boldsymbol{\sigma}^t = \mathbf{R}^t\boldsymbol{\sigma}_{mat}^t\mathbf{R}^{t^T}$.

4.2 Solution procedure

The above defined system of equations (Eq. 16 or 17) is solved using Newton's method. We define a residue in the vector form as follows. The final expression for stress (Eq. 17) is first decoupled into its deviatoric, $\mathbf{s}^{t+\Delta t}$, and hydrostatic , $\sigma_m^{t+\Delta t}$, portions and then written in a vector form as:

$$\mathbf{s}^{t+\Delta t} - \mathbf{s}^{t,rot} - \mathbf{C}'_{5x6}\left(\Delta\boldsymbol{\varepsilon} - |\dot{\boldsymbol{\varepsilon}}_{vp}/\dot{\varepsilon}_{ref}|^k \mathbf{P}_{6x5}\dot{\mathbf{e}}_{vp}\Delta t\right) = 0, \tag{19a}$$

$$\sigma_m^{t+\Delta t} - \sigma_m^t - \frac{1}{3}\mathrm{tr}\left[\mathbf{C}\left(\Delta\boldsymbol{\varepsilon} - |\dot{\boldsymbol{\varepsilon}}_{vp}/\dot{\varepsilon}_{ref}|^k \mathbf{P}_{6x5}\dot{\mathbf{e}}_{vp}\Delta t\right)\right] = 0. \tag{19b}$$

In doing so, we organize the variables in Eq. (19) in a vector form to consist of five independent deviatoric components as $\dot{\mathbf{e}}_{vp} = \{\dot{\varepsilon}_{vp,11}, \dot{\varepsilon}_{vp,22}, \dot{\varepsilon}_{vp,12}, \dot{\varepsilon}_{vp,13}, \dot{\varepsilon}_{vp,23}\}$ and $\mathbf{s}^{t+\Delta t} = \{\sigma'^{t+\Delta t}_{11}, \sigma'^{t+\Delta t}_{22},$ $\sigma'^{t+\Delta t}_{12}, \sigma'^{t+\Delta t}_{13}, \sigma'^{t+\Delta t}_{23}\}$. $\mathbf{s}^{t,rot}$ is a vector representation of $\langle \Delta\mathbf{R}^{*c}\boldsymbol{\sigma}'^{c,t}\Delta\mathbf{R}^{*cT}\rangle$. Note that $\Delta\boldsymbol{\varepsilon}$ is imposed by Abaqus as a six dimensional vector i.e. $\Delta\boldsymbol{\varepsilon} = \{\Delta\varepsilon_{11}, \Delta\varepsilon_{22}, \Delta\varepsilon_{33}, 2\Delta\varepsilon_{12}, 2\Delta\varepsilon_{13}, 2\Delta\varepsilon_{23}\}$. Additionally, $\mathbf{C}'_{5\times6}$ is a matrix representation (with removed third row) of $C'_{ijkl} = C_{ijkl} - \frac{1}{3}C_{mnkl}\delta_{mn}\delta_{ij}$, which is the fourth-rank elastic stiffness tensor that gives the deviatoric stress increment when multiplied by the elastic strain increment tensor. $\mathbf{P}_{6\times5}$ is defined as the matrix that transforms a five dimensional $\dot{\mathbf{e}}_{vp}$ vector form of the $\dot{\boldsymbol{\varepsilon}}_{vp}$ tensor into a six dimensional vector form as dictated by $\Delta\boldsymbol{\varepsilon}$:

$$\mathbf{P}_{6\times5} = \begin{bmatrix} 1 & 0 & 0 & 0 & 0 \\ 0 & 1 & 0 & 0 & 0 \\ -1 & -1 & 0 & 0 & 0 \\ 0 & 0 & 2 & 0 & 0 \\ 0 & 0 & 0 & 2 & 0 \\ 0 & 0 & 0 & 0 & 2 \end{bmatrix} \tag{20}$$

The elastic stiffness tensor, $\mathbf{C}$, is calculated based on texture and the invariant elastic single crystal constants (Fast et al., 2008; Landry and Knezevic, 2015; Wu et al., 2007). For Zr, these are: $C_{11} = 143{,}500$ MPa, $C_{33} = 164{,}900$ MPa, $C_{12} = 72{,}500$ MPa, $C_{13} = 65{,}400$ MPa, $C_{44} = 32{,}100$ MPa and $C_{66} = 35{,}500$ MPa (Meyers and Chawla, 1998).

Equation (19a) represents a system of five equations and five unknowns, where the unknowns are the five components of the visco-plastic strain rate $\dot{\mathbf{e}}_{vp}$. The rate $\dot{\mathbf{e}}_{vp}$ is the solution at the UMAT level, which is used to interrogate VPSC operating with the *strain-rate-imposed boundary conditions*. VPSC returns the deviatoric stress, which enables calculation of $\mathbf{s}^{t+\Delta t}$ and $\sigma_m^{t+\Delta t}$ and finally $\boldsymbol{\sigma}^{t+\Delta t}$ for Abaqus.

To solve for $\dot{\mathbf{e}}_{vp}$ in the UMAT, we define the following residual in the vector form:

$$\mathbf{F}(\dot{\mathbf{e}}_{vp}) = \mathbf{s}^{t+\Delta t}(\dot{\mathbf{e}}_{vp}) - \mathbf{s}^{t,rot} - \mathbf{C'}_{5x6}\left(\Delta\boldsymbol{\varepsilon} - \mathbf{P}_{6x5}\dot{\mathbf{e}}_{vp}\left|\dot{\boldsymbol{\varepsilon}}_{vp}/\dot{\varepsilon}_{ref}\right|^{k}\Delta t\right) = 0, \qquad (21)$$

where $\mathbf{s}^{t+\Delta t}(\dot{\mathbf{e}}_{vp})$ represents the stress calculated based on the VPSC model (where VPSC essentially represents a function $\mathbf{s}^{t+\Delta t}(\dot{\mathbf{e}}_{vp})$ at this level). This system of equations is then solved iteratively using Newton's method, where the Jacobian is:

$$\frac{\partial\mathbf{F}(\dot{\mathbf{e}}_{vp})}{\partial\dot{\mathbf{e}}_{vp}}\bigg|_{5x5} = \frac{\partial\mathbf{s}^{t+\Delta t}}{\partial\dot{\mathbf{e}}_{vp}} + \mathbf{C'}_{5x6}\mathbf{P}_{6x5}\left|\frac{\dot{\boldsymbol{\varepsilon}}_{vp}}{\dot{\varepsilon}_{ref}}\right|^{k}\Delta t + \mathbf{C'}_{5x6}(\mathbf{P}_{6x5}\dot{\mathbf{e}}_{vp})\Delta tk\left|\frac{\dot{\boldsymbol{\varepsilon}}_{vp}}{\dot{\varepsilon}_{ref}}\right|^{k-2}\dot{\mathbf{e}}_{vp}^{T}\mathbf{Q}_{6x5}^{T}\mathbf{P}_{6x5}, \quad (22)$$

where: $\frac{\partial\mathbf{s}^{t+\Delta t}}{\partial\dot{\mathbf{e}}_{vp}} = \mathbf{M}^{-1}$ and $\mathbf{Q}_{6x5}$ is analogous to $\mathbf{P}_{6x5}$ only without doubling the shears. Starting from an initial guess for $\dot{\mathbf{e}}_{vp}$ (which is usually taken as the solution of the previous time increment), every subsequent value of $\dot{\mathbf{e}}_{vp}$ is iteratively obtained using:

$$^{i+1}\dot{\mathbf{e}}_{vp} = {}^{i}\dot{\mathbf{e}}_{vp} - \left(\frac{\partial\mathbf{F}}{\partial\dot{\mathbf{e}}_{vp}}({}^{i}\dot{\mathbf{e}}_{vp})\right)^{-1}\mathbf{F}({}^{i}\dot{\mathbf{e}}_{vp}). \qquad (23)$$

Recall that the old FE-VPSC based on *the stress-imposed boundary condition* involves a solution procedure at the UMAT level for total stress (six components) and not visco-plastic strain rate (five components). Therefore, the corresponding residual equation is different than that given in Eq. (20) (Knezevic et al., 2013d; Segurado et al., 2012).

4.3 Jacobian for global FE solver

As a very last step, we define the Jacobian matrix required by the Abaqus global solver (2013) for the UMAT level constitutive equation: $\boldsymbol{\sigma}^{t+\Delta t} = \mathbf{C}\left(\Delta\boldsymbol{\varepsilon} - \left|\dot{\boldsymbol{\varepsilon}}_{vp}/\dot{\varepsilon}_{ref}\right|^{k}\dot{\boldsymbol{\varepsilon}}_{vp}\Delta t\right) + \boldsymbol{\sigma}^{t,rot}$, where $\Delta\boldsymbol{\varepsilon}$ is an independent and $\boldsymbol{\sigma}^{t+\Delta t}$ is a dependent variable. After differentiation of the constitutive equation, the fully analytical expression for the Jacobian is:

$$\frac{\partial \boldsymbol{\sigma}^{t+\Delta t}}{\partial \Delta \boldsymbol{\varepsilon}}\bigg|_{6x6} = \left\{ \mathbf{I}_{6x6} + \mathbf{C} \left[\mathbf{I}_{6x6} \left| \frac{\dot{\boldsymbol{\varepsilon}}_{vp}}{\dot{\varepsilon}_{ref}} \right|^{k} \Delta t + \mathbf{P}_{6x5}\dot{\mathbf{e}}_{vp}\Delta t k \left| \frac{\dot{\boldsymbol{\varepsilon}}_{vp}}{\dot{\varepsilon}_{ref}} \right|^{k-2} \dot{\mathbf{e}}_{vp}^{T}\mathbf{Q}_{6x5}^{T} \right] \mathbf{P}_{6x5}\mathbf{M}\frac{\partial \mathbf{s}}{\partial \boldsymbol{\sigma}} \right\}^{-1} \mathbf{C}. \quad (24)$$

The size of the last three matrices within the curly brackets in the chain are 6x5, 5x5, and

5x6. The only undefined term is $\frac{\partial \mathbf{s}}{\partial \boldsymbol{\sigma}}$, which is the derivative of the Cauchy deviatoric stress with

respect to the Cauchy stress and is defined as

$$\frac{\partial \mathbf{s}}{\partial \boldsymbol{\sigma}} = \begin{bmatrix} 2/3 & -1/3 & -1/3 & 0 & 0 & 0 \\ -1/3 & 2/3 & -1/3 & 0 & 0 & 0 \\ 0 & 0 & 0 & 1 & 0 & 0 \\ 0 & 0 & 0 & 0 & 1 & 0 \\ 0 & 0 & 0 & 0 & 0 & 1 \end{bmatrix}, \quad (25a)$$

with,

$$\boldsymbol{\sigma}'_{11} = \frac{2}{3}\boldsymbol{\sigma}_{11} - \frac{1}{3}\boldsymbol{\sigma}_{22} - \frac{1}{3}\boldsymbol{\sigma}_{33}, \boldsymbol{\sigma}'_{22} = \frac{2}{3}\boldsymbol{\sigma}_{22} - \frac{1}{3}\boldsymbol{\sigma}_{11} - \frac{1}{3}\boldsymbol{\sigma}_{33}, \boldsymbol{\sigma}'_{12} = \boldsymbol{\sigma}_{12},$$

$$\boldsymbol{\sigma}'_{13} = \boldsymbol{\sigma}_{13}, \boldsymbol{\sigma}'_{23} = \boldsymbol{\sigma}_{23} \quad (25b)$$

The elastic stiffness $\mathbf{C}$ is calculated at the beginning of each deformation increment, meaning

that texture changes are taken into account. If the deformation is elastic, the stress tensor and the

Jacobian for Abaqus are directly available from the elastic SC response without the need to

determine a visco-plastic strain rate, which in this case is zero. The procedure is fully implicit in

terms of the stress-strain measures, where internal equilibrium is checked at every iteration.

However, the plastic spin used for the integration of stress rotation is calculated based on shear

rates from the previous time increment and is assumed to be constant in the iterations for solving

current visco-plastic strain rate. The internal variables such as grain orientations, dislocation

densities, etc. are updated at the end of the increment. It should also be noted that the new

UMAT facilitates that each FE integration point in an FE mesh can be associated with either a

single crystal or a polycrystalline VPSC material point. In the former case, the overall response

of the polycrystalline material is obtained by the micromechanical FE homogenization while in the latter case is multiscale and involves a combination of the mesoscale VPSC homogenization followed by the FE overall homogenization.

5   Results

5.1   Validation of FE-VPSC using a single-element model

Before moving forward to the application of a Taylor impact test, we first test the FE-VPSC UMAT to make sure that it is capable of exactly reproducing results attainable using a stand-alone VPSC code (SA-VPSC). Toward this end, we compare results of texture and stress-strain response in a sheet of Zr from the FE-VPSC code with the corresponding predictions from the SA-VPSC. We consider two types of tests: compression in one of the in-plane directions of the sheet (called IPC2) under a strain rate of 3500/s and in-plane simple shear (in the in-plane/through-thickness directions) under a strain rate of 0.001/s. The former is chosen in order to check if twinning is treated properly while the latter is selected to make sure the macroscopically imposed spin due to simple shear deformation is accounted for correctly. Figure 4 presents the stress–strain curves and pole figures at the end of deformation for both tests. The agreement is excellent and provides confidence in the UMAT developed here, such that we can progress to the more complex problem of a Taylor impact test for which stand-alone VPSC would not apply.

In addition to the validation against the SA VPSC code, we have performed a simple shear test on a single crystal by imposing $\dot{\varepsilon}_{23}$ as shown in Fig. 3 to further test the validity of our rotation treatment. As illustrated, only one prismatic slip system $(0\bar{1}10)[2\bar{1}\bar{1}0]$ is active for values of n greater than 20 and the crystal orientation remains stable during deformation to large

strain levels. The hardening was turned off since the slip resistance of the active slip system would increase, allowing for unphysical activation of other slip systems.
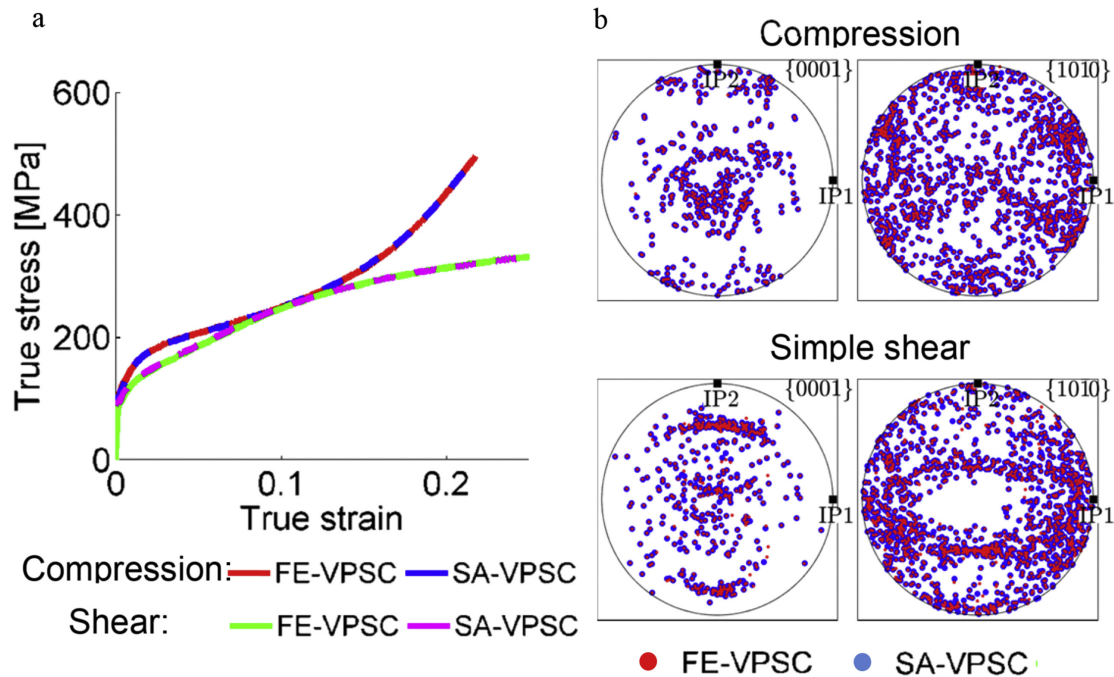
Fig. 4. (a) Predictions for the stress-strain response and (b) texture development at the end of deformation for Zr from the FE-VPSC UMAT developed here and the stand-alone VPSC code (SA-VPSC) for in-plane compression in the IPC2 direction under a strain rate of 3500/s and simple shear in IP2-TT direction under a strain rate of 0.001/s. Results from the two codes are indistinguishable.

5.2   Application case study: the Taylor impact test of Zr

The FE-VPSC model is applied to calculate the deformation of high-purity Zr in a Taylor impact test. It is known that the strain rate distribution generated during this test is highly heterogeneous, giving rise to variation in the plastic deformation response and microstructural evolution throughout the sample (Maudlin et al., 1999a). This test has been a challenge to model comprehensively and across many scales from the macroscale response to the underlying microscopic deformation mechanisms (Maudlin et al., 1999b). We show here that the new multi-scale FE-VPSC is well suited to model such a test and in turn, this test represents a good check for the model.
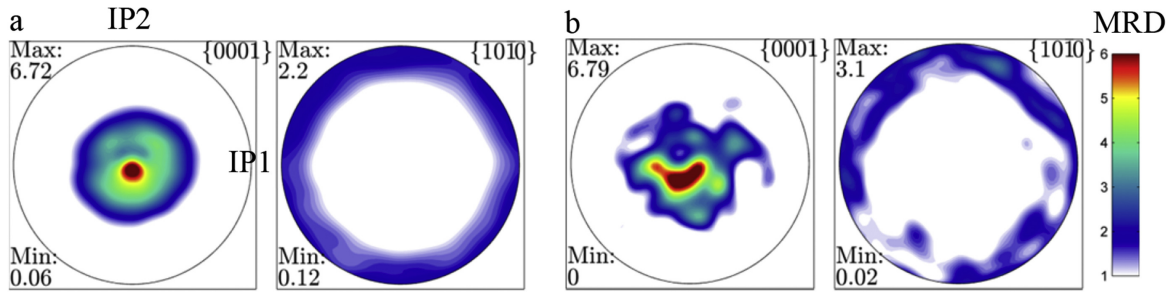
Fig. 5. Pole figures showing the initial texture of the clock-rolled and recrystallized zirconium plate: (a) measured by X-ray diffraction and (b) approximated measure texture using 150 weighted orientations used in modeling.

The material used is the same one that has been examined in several prior studies and the complete details can be found in (Ardeljan et al., 2015a; Bingert et al., 2002; Kaschner and Gray III, 2000; Knezevic et al., 2015b). It is a clock-rolled and fully recrystallized plate of Zr with the following chemical composition (wt. ppm): O < 50, C < 22, N < 20, Fe < 50, Al < 20, V < 50, Hf 35, Ti<25 and Zr balance. As a result of the clock rolling process, the material has a strong in-plane isotropic basal texture. The initial texture is presented using pole figures in Fig. 5a. Figure 5b shows an approximated texture to the texture shown in Fig. 5a that is represented using 150 weighted orientations. It achieves reasonable consistency. Some second-order differences are seen. Particularly, some asymmetries in the experimental texture are not captured by the approximate texture. Nonetheless, the important strong basal pole alignment with the normal direction of the sheet and the nearly random in-plane distribution of the prismatic poles are captured. The approximated texture is used in the FE simulations where every FE integration point is initialized by embedding the same 150 weighted orientations. Figure 6 shows comparisons of true stress-true strain compressive response under several deformation conditions along the in plane (IPC) and through-thickness (TTC) between measurements and predictions using the measured texture (Fig. 6a) and the approximated texture (Fig. 6b). It can be seen that texture in Fig. 5b is representative in terms of capturing the material response.

37
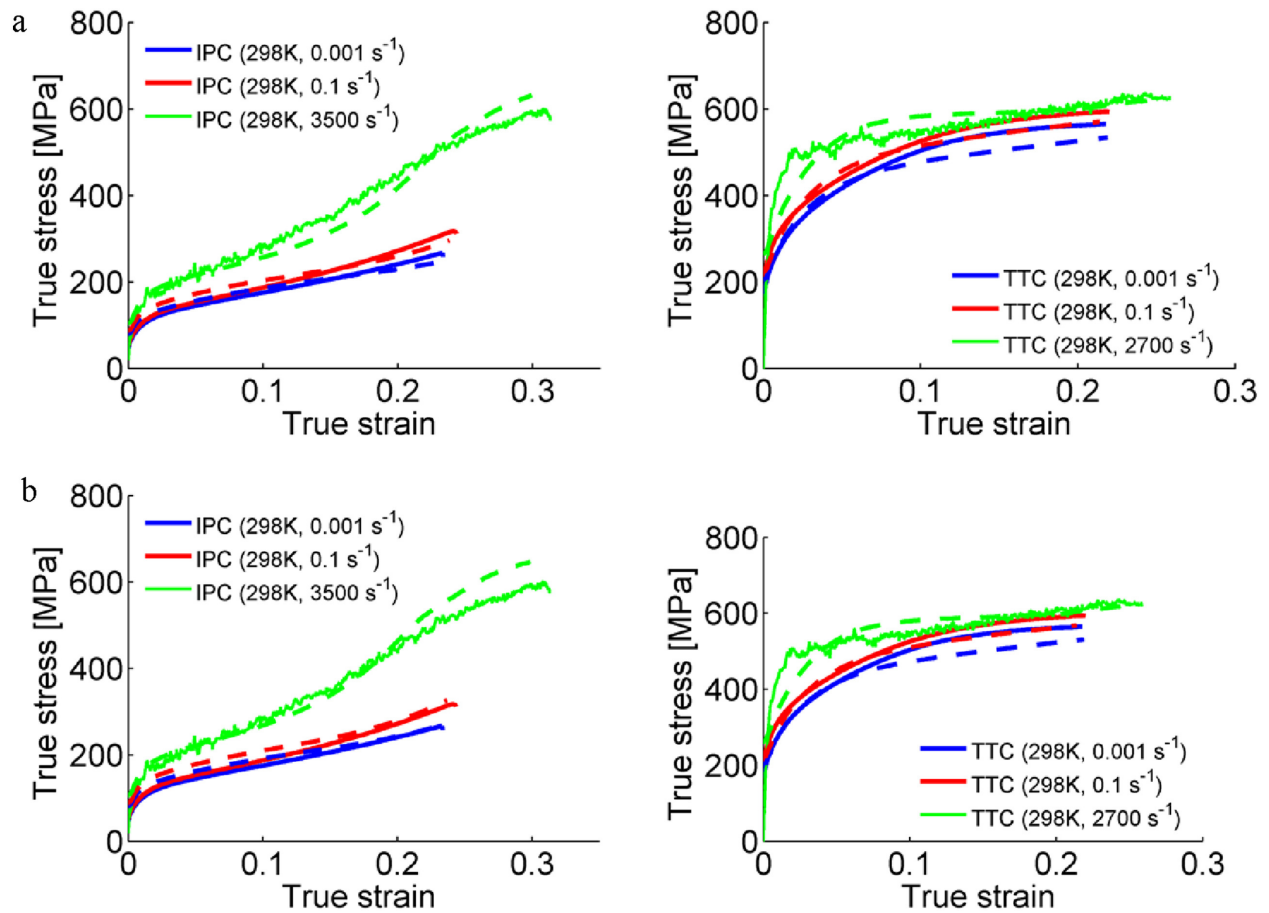
Fig. 6. Predictions based on the parameters in Table 1 and 2 and using: (a) the full measured texture containing many orientations and (b) approximated texture using 150 weighted orientations. The solid lines represent experimentally measured stress strain curve while the dashed lines represent the predictions.

Taylor cylinder specimens were machined from the clock-rolled Zr plate such that the cylinder axis aligned with the IP2 direction of the plate. The length and diameter of the cylindrical specimens were 50.8 mm and 7.62 mm, respectively. The cylinders are launched as a projectile toward a steel target. The velocity of the shot studied here was 100 m/s. More experimental details on the Taylor impact cylinder test method can be found in (Maudlin et al., 1999a; Maudlin et al., 1999b).

Figure 7 shows the 3D FE model set up for simulating the Taylor impact cylinder test. As shown, only one-quarter of the cylinder is modeled, taking advantage of symmetry in the model

geometry, material response and boundary conditions. This quarter cylinder model used 405 elements of the type C3D8. The element aspect ratio varied from being approximately 1 in the foot region to approximately 2.8 at the tail of the cylinder. There was no appreciable effect of the mesh on the results according to mesh sensitivity study performed. An initial velocity field of 100 m/s was applied to the cylinder. The wall was modeled as a fixed rigid plane.
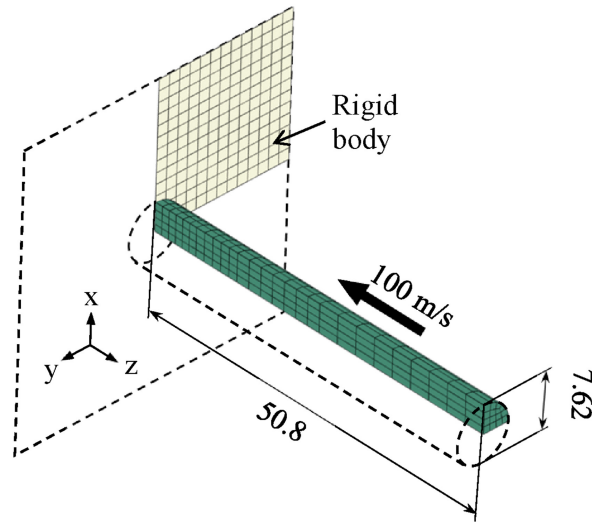
Fig. 7. Simulation set up for the Zr Taylor impact simulation. The initial FE model is the ¼ cylinder, which consists of 405 C3D8 (continuum 3D 8 node) elements.

To perform the dynamic impact simulation, we use the dynamic implicit FE code called ABAQUS STANDARD dynamic. A density value for Zr of $\rho = 6520$ kg/m^3 was used to account for inertia effects in simulating the impact tests. In the literature an explicit solver is generally used for conducting FE simulations in the dynamic regime (Cerreta et al., 2013; Maudlin et al., 1999b). Within the implicit dynamic analyses an acceleration that balances the residual force is calculated on the nodes while enforcing the linear momentum balance equation. The difference between the implicit and explicit dynamic analysis is that the former analyses assume that the stress waves have communicated information across multiple elements whereas the latter

analyses propagate information over a distance that is less than one element per time step. Therefore, to more accurately simulate the change in shape of the Zr specimen and the evolution
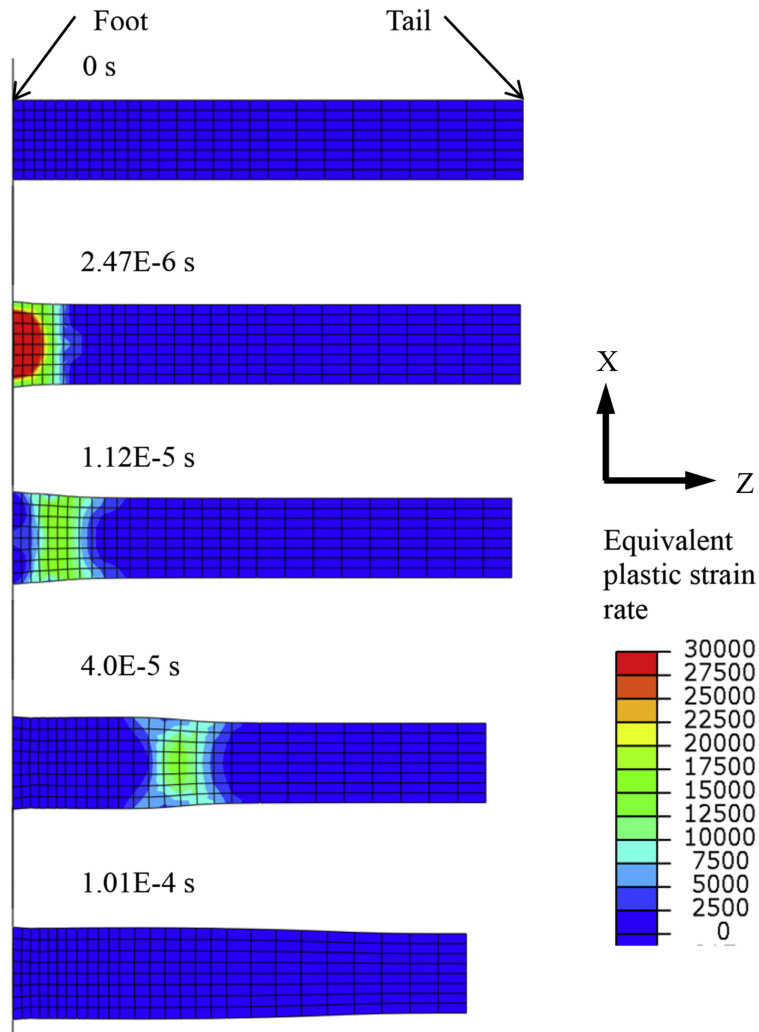
Fig. 8. Contours of the equivalent plastic strain-rate over the sample cross-sectional area at times indicated in the figure during the impact test.

of texture and twin volume fraction during the impact, we decided to use the implicit solver for which we developed the new UMAT. As described above, every FE integration point was represented by a VPSC polycrystal with 150 orientations, which is a smaller number than is typically used in stand-alone VPSC calculations. However, in FE, there is the additional concern that computational time increases with number of orientations (Knezevic et al., 2016), which can

be relaxed by reducing the number of orientations embedded at integration points or by the development of high-performance applications (Knezevic and Savage, 2014; Mihaila et al., 2014; Savage and Knezevic, 2015). The former approach is used here.
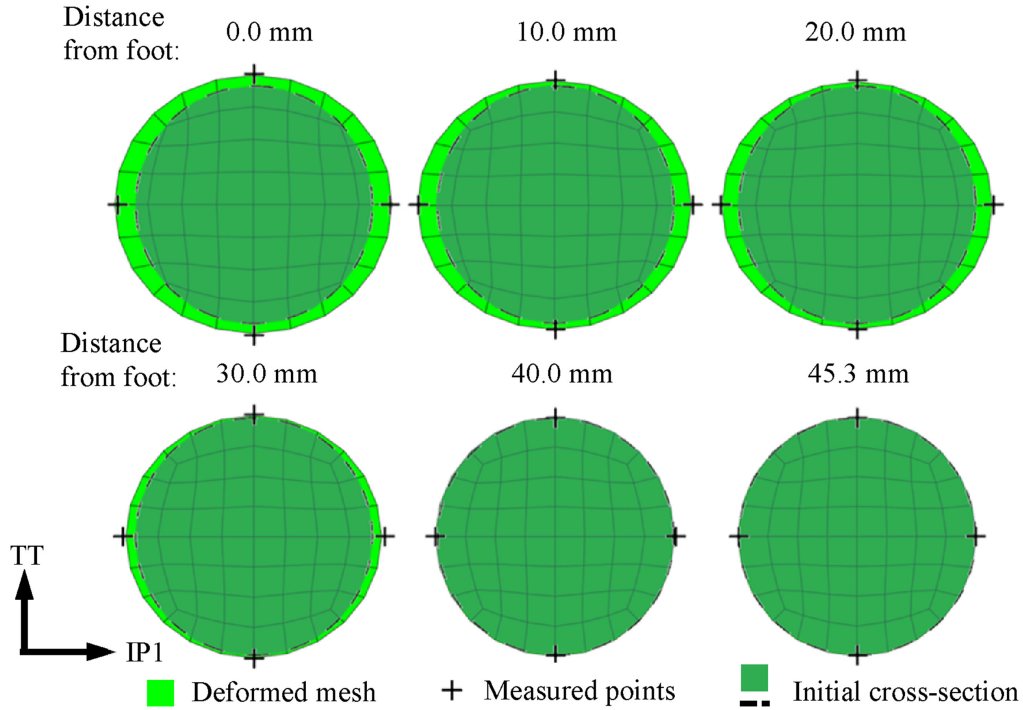
Fig. 9. Cross-sections of the Zr Taylor cylinder after the impact as a function of the distance from the foot predicted by FE-VPSC along with the experimentally measured points superimposed over the FE mesh. The initial cross-sectional geometry is shown to illustrate the extend of plastic deformation from the foot towards the tail. It can be seen that the cross-sections 40 mm and 45.1 (the actual tail cross-section) from the foot do not show any permanent shape change.

Figure 8 shows the time evolution of the equivalent plastic strain rate that develops during the simulation over the time period simulated (1.01E-4 s). The calculations indicate that the strain rate develops heterogeneously along the sample length, with peak rates rising substantially to excess of 10^4/s. The peak position travels from the foot, where impact first occurs, to the tail of the sample. During its excursion, the sample deforms elasto-plastically until the peak decreases in intensity to cause only elastic deformation to no deformation.
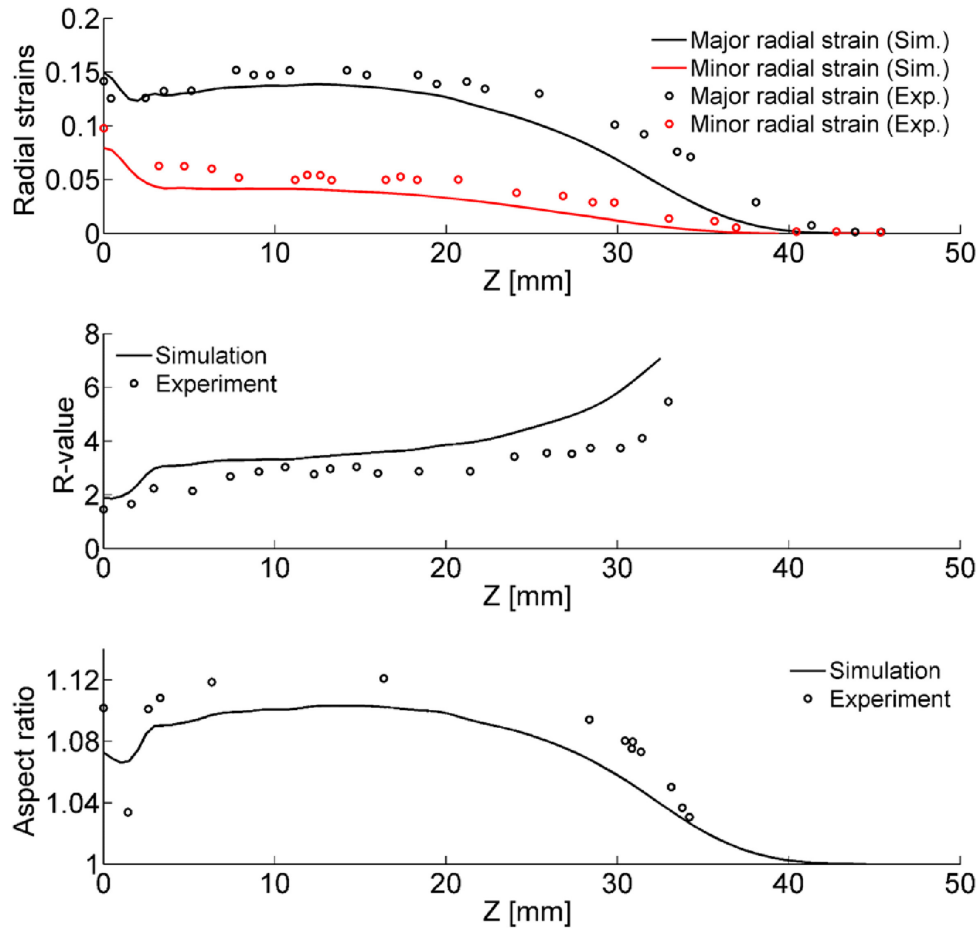
Fig. 10. Comparison between measured and simulated geometrical changes of the Zr Taylor cylinder after the impact. An elliptical cross-sectional shape from the foot to about 40 mm from the foot is evident from the major and minor radial strain plot. The R-value plot presents the ratio between the major radial strain and the minor radial strain. The aspect ratio plot depicts the ratio between the major and minor axis of the cylinder.

When such variable plastic deformation occurs, it can be expected that the sample will have incurred non-uniform plastic distortions. Three-dimensional post-impact specimen shapes were digitized using the procedure described in (Maudlin et al., 1999b) in order to estimate the distribution of strains. The cylinder cross-section changed shape from a circle to an ellipse and for Zr, these changes typically vary non-linearly along the cylinder axis. Figure 9 shows the cross-sections for the sample at different points from the foot of the sample. Such permanent distortions are commonly quantified as the radial strains in the major and minor axes, their ratio or the so-called r-value, and the aspect ratio of the ellipse. Figure 10 presents these quantities as

a function of position from the foot of the sample. From the comparison between the calculations and the corresponding measurements, we observe that the model is capable of capturing reasonably well the variation in the radial strains, r-values, and aspect ratios. It is also worth noting that these good predictions indicate that the rate-sensitive dislocation hardening model, previously developed and validated on mechanical testing and microstructural data collected over strain rates of 0.001 /s to 4500 /s, applies to much higher strain rates without adjusting the parameters. The agreement suggests that thermally activated glide and deformation twinning are still controlling mechanisms of plastic deformation.

The variations in distortions along the length are a signature of differences in microstructural evolution. The calculated textures at different points along the cylinder are compared with experimental measurements made by EBSD. Specifically five different points along the cylinder were examined located at: 0.1 µm, 2 mm, 8 mm, 14 mm, and 44 mm from the foot of the sample. Figure 11 presents side-by-side the calculated and measured basal and prismatic pole figures using the same multiples of random distribution (MRD) scale. The comparison indicates that the model achieves good agreement with the measurements in both the main components and their variation along the length of the cylindrical sample. The vertical twinning fiber predicted on $\{10\bar{1}0\}$ simulation pole figures appears not as distributed as in the experimental pole figures. Also, the weakening from the tail towards the foot of the strong $\{0001\}$ peak along the TT direction seems to be over predicted. Texture differences between the first portion of the cylinder (from 0 to 14 mm) and the end at 44 mm, can easily be attributed to variances in twinning activity. EBSD was used to detect deformation twinning, including the type activated and its volume fraction, at these same points along the cylinder. The scans were taken around the
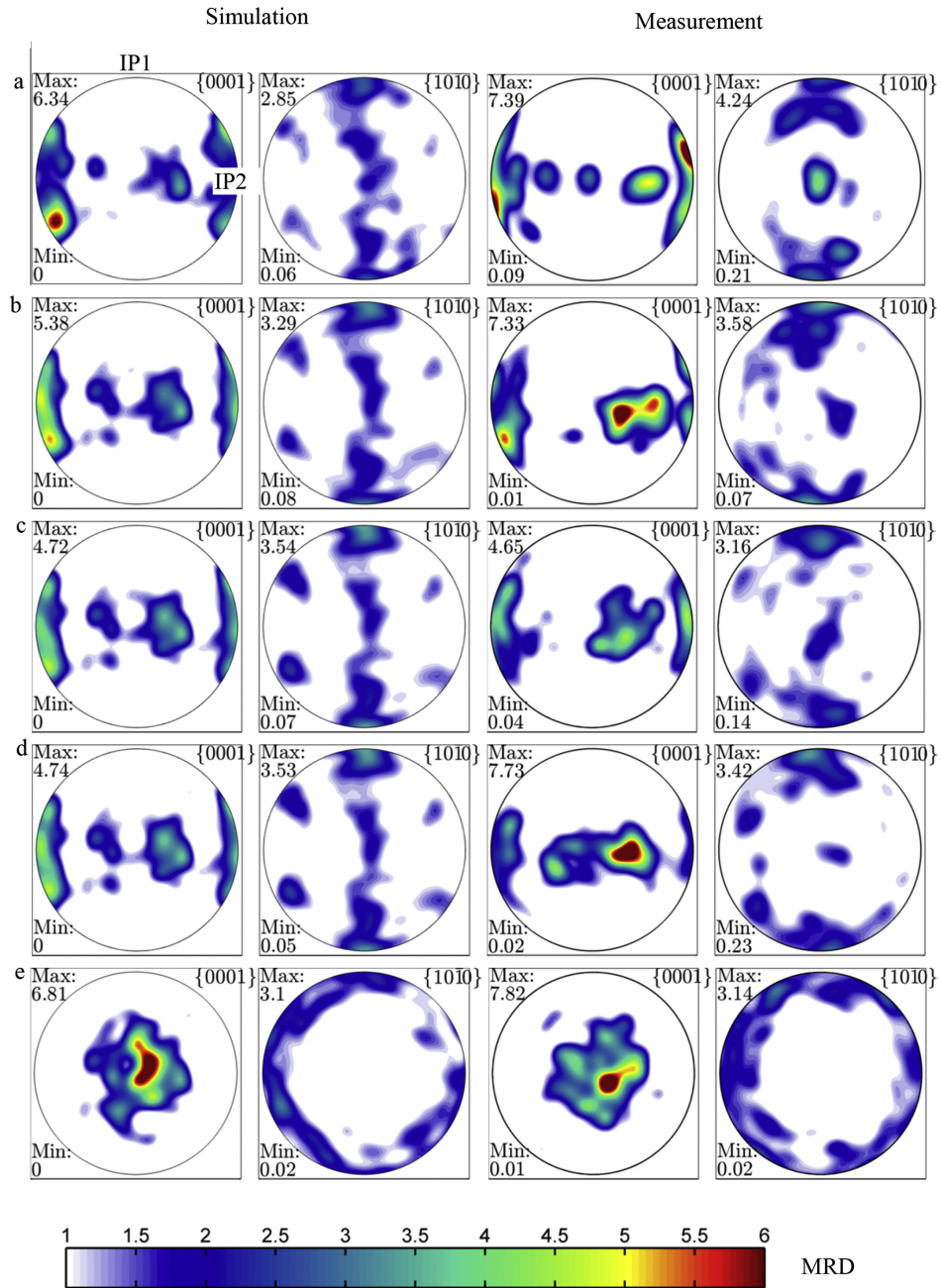
Fig. 11. Texture evolution in the cylinder after the impact: (a) 0.1 μm, (b) 2 mm, (c) 8 mm, (d) 14 mm, and (e) 44 mm from the foot. Texture is measured by EBSD.

centerline of the cylinder. Figure 12 presents the maps, where reoriented twin domains that are several tens of nm in thickness are visible. These measurements show that amount of twinning varies substantially along the cylinder. At the foot, twinning is profuse and consists predominantly of tensile $\{10\bar{1}2\}$ twinning and less than 5% of the compression $\{11\bar{2}2\}$ twin. The

twin fraction appears to not vary much from 0.1 µm to 14 mm from the foot. Farther away the twin fraction decreases. Figure 13 indicates a good agreement between the model predictions and measurement of twin volume fraction.
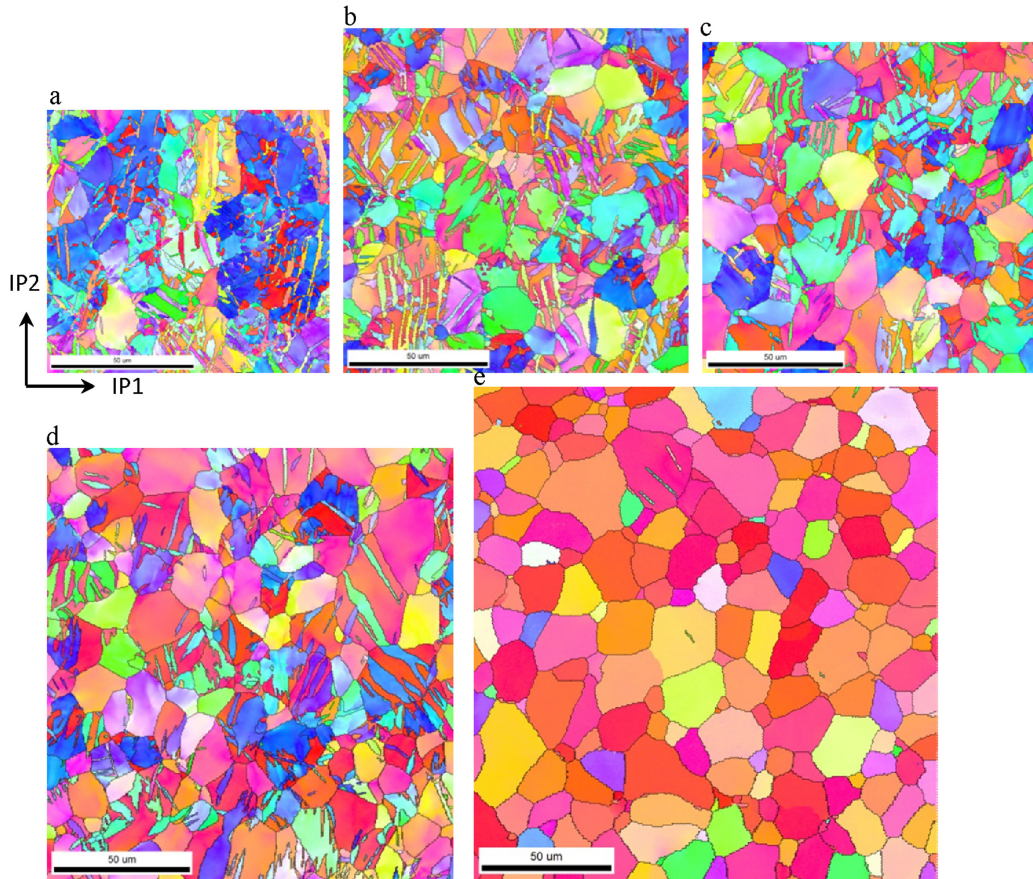
Fig. 12. EBSD maps showing microstructure in the cylinder after the impact at: (a) 0.1 µm, (b) 2 mm, (c) 8 mm, (d) 14 mm, and (e) 44 mm distance from the foot.
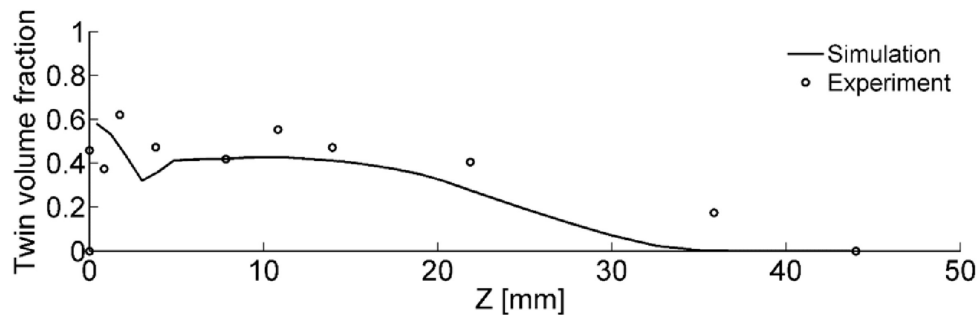
Fig. 13. Comparison of measured and predicted twin volume fraction in the cylinder after the impact as a function of distance from the foot. The twin volume fraction was determined by counting % of twin boundaries, which is regarded as an upper bound estimate.

6 Conclusions

In this work, we have presented a finite element based multi-scale constitutive model for the high-rate deformation of polycrystals that deform by multiple slip and twinning systems. The model enables treatment of strain-rate sensitivities of a material response to be a consequence of dislocation motion on active crystallographic slip systems. This is a significant achievement because the prior approaches to single crystal visco-plasticity intrinsically include some rate sensitivity through the power-law flow rule. Here, the rate sensitivities enter from choices of the exponent n, which is typically selected to be well below 100 and this does not adequately represent the strain-rate sensitive plastic deformation behavior of a material. We develop a methodology that relaxes the rate sensitivities that are introduced by the power-law exponent and still retain use of the visco-plastic power-law formulation. This method enables us to indirectly increase values of n, achieving the desired effect of embedding the rate sensitivity into the evolution of resistance to slip and slip-slip and slip-twin interactions. We have developed a UMAT, which integrates this new methodology for treating the strain-rate sensitivity and also allows for imposing the strain-rate boundary conditions over a polycrystal in VPSC. The latter, along with other implemented improvements, overcomes the limitation of prior FE-VPSC approaches that were capable of handling solely stress-imposed boundary conditions and were less numerically stable. Through these two chief advancements, the scale transitions from crystal plasticity to polycrystalline plasticity and from polycrystalline plasticity to the FE UMAT are effectively treated enabling simulations of dynamic tests. With the model, the shape changes, texture evolution, and twin fractions are calculated for Zr in a Taylor impact cylinder test and all aspects achieve very good agreement with measurements. Another significant outcome was the fact that the thermally activated hardening law for Zr apply to much higher strain-rates than the

quasi-static ones under which it was characterized. It suggests that dislocation motion at the high strain-rates generated by the Taylor impact test (10^4 /s - 10^5 /s) is still dominated by thermal activation.

More generally, the modeling of microstructure-property relationships in mechanical tests can be significantly improved by allowing only the strain-rate dependencies of material behavior due to the physics of dislocation motion to enter into the formulation. Particularly, when the test generates spatially and temporally varying mechanical fields varying widely in strain-rate, it is also desirable that the FE formulation and UMAT are sufficiently flexible to replicate the actual boundary conditions.

Acknowledgements

Appendix

We present a summary of the main equations for the evolution of slip and twin resistances. The slip resistances per slip system evolve using:

$$\tau_c^s = \tau_0^\alpha + \tau_{0,HP}^\alpha + \tau_{for}^s + \tau_{deb}^\alpha. \tag{A1}$$

The initial slip resistances per slip mode are:

$$\tau_0^\alpha = A^\alpha \left(1 + B^\alpha \log\left(\frac{\dot{\varepsilon}}{\dot{\varepsilon}_{ref}}\right)\right) \exp\left(-\frac{T}{C^\alpha}\right) \left(1 + E^\alpha lognormal(\sigma^\alpha, v^\alpha)\right), \tag{A2}$$

where A^α, B^α, and C^α are constants and T and $\dot{\varepsilon}$ are the current temperature and strain rate, respectively. The constant E^α and lognormal terms, σ^α and ν^α, are used to capture the saturation of the resistances at high temperatures seen experimentally. The grain size barrier term is:

$$\tau_{HP}^s = \mu^\alpha(T)HP^\alpha\sqrt{\frac{b^\alpha}{d_g}}, \tag{A3}$$

where b^α is the magnitude of the Burgers vector, d_g is the initial grain size, $\mu^\alpha(T) = 40.06 - 0.022T$ is the effective shear modulus taken to be the same for all shear directions and HP^α is the Hall-Petch parameter. The evolution of the forest and the debris terms are governed by the evolution of the forest $\rho_{for}^s(\dot{\varepsilon},T)$ and debris $\rho_{deb}(\dot{\varepsilon},T)$ dislocation densities:

$$\tau_{for}^s(\dot{\varepsilon},T) = b^\alpha\mu^\alpha(T)\sqrt{\chi^{ss}\,\rho_{for}^{s\prime}(\dot{\varepsilon},T)}, \tag{A4}$$

$$\tau_{deb}^\alpha(\dot{\varepsilon},T) = k_{deb}\mu^\alpha(T)b^\alpha\sqrt{\rho_{deb}(\dot{\varepsilon},T)}\log\left(\frac{1}{b^\alpha\sqrt{\rho_{deb}(\dot{\varepsilon},T)}}\right). \tag{A5}$$

The evolution of the stored forest density is governed by competition between the rate of storage/generation and the rate of dynamic recovery/removal:

$$\frac{\partial\rho_{for}^s}{\partial\gamma^s} = \frac{\partial\rho_{gen,for}^s}{\partial\gamma^s} - \frac{\partial\rho_{rem,for}^s}{\partial\gamma^s} = k_1^s\sqrt{\rho_{for}^s} - k_2^s(\dot{\varepsilon},T)\rho_{for}^s. \tag{A6}$$

The rate of debris development is coupled to the rate of recovery of all active dislocations through:

$$d\rho_{deb} = q^\alpha b^\alpha\sqrt{\rho_{deb}}\frac{\partial\rho_{rem,for}^s}{\partial\gamma^s}|d\gamma^s|. \tag{A7}$$

k_1^s is a rate-insensitive coefficient for dislocation storage by statistical trapping of mobile dislocations and k_2^s is a rate-sensitive coefficient that accounts for dynamic recovery by thermally activated mechanisms calculated using:

$$\frac{k_2^S}{k_1^S} = \frac{1}{\sqrt{(\chi^{-1})^{ss'} \frac{\tau_{sat}^{s'}}{b^{\alpha'} \mu^{\alpha'}}}}, \quad \tau_{sat}^S = \frac{D^\alpha (b^\alpha)^3 g^\alpha \mu^\alpha}{D^\alpha (b^\alpha)^3 - kT \log\left(\frac{\dot{\varepsilon}}{\dot{\varepsilon}_0}\right)}. \tag{A8}$$

Here, k, $\dot{\varepsilon}^0$, g^α, $\chi^{ss'}$, and D^α are the Boltzmann constant, a reference strain rate taken to be 10^9 /s, an effective activation enthalpy, anisotropic dislocation interaction coefficient, and a drag stress, respectively.

The evolution of twin resistances follows:

$$\tau_c^\beta = \tau_0^\beta + \tau_{0,HP}^t + \tau_{slip}^\beta. \tag{A9}$$

Here, the twin activation stress accounts for a temperature-independent friction term τ_0^β, a Hall-Petch-like term $\tau_{0,HP}^t$, and a latent hardening term that couples slip and twin systems.

$$\tau_0^\beta = \tau_{prop}^\beta + \left(\tau_{crit}^\beta - \tau_{prop}^\beta\right) \exp\left(-\frac{\Sigma \rho_{for}^s}{n^\alpha \rho_{sat}^s}\right) \tag{A10}$$

where τ_{crit}^β and τ_{prop}^β are the nucleation and propagation stresses, whose contribution to twin activation is leveraged by the probability term $\frac{\Sigma \rho_{for}^s}{n^\alpha \rho_{sat}^s}$. The Hall-Petch-like term and the latent hardening term are:

$$\tau_{0,HP}^t = \frac{HP^\beta}{\sqrt{d_g}}, \tag{A11}$$

$$\tau_{slip}^\beta = \Sigma_s C^{\alpha\beta} b^\beta \mu^\alpha(T) b^\alpha \rho_{for}^s, \tag{A12}$$

where μ^β is the elastic shear modulus on the twin system, b^β is the Burgers vector of a given twin system, and $C^{\beta\alpha}$ is the latent hardening matrix in function of strain rate.

References

2013. ABAQUS Version 6.11-2, Dassault Systèmes, Providence, RI, USA.

Abdolvand, H., Majkut, M., Oddershede, J., Wright, J.P., Daymond, M.R., 2015. Study of 3-D stress development in parent and twin pairs of a hexagonal close-packed polycrystal: Part I – in-situ three-dimensional synchrotron X-ray diffraction measurement. Acta Materialia 93, 246-255.

Akhtar, A., 1973a. Basal slip in zirconium. Acta Metallurgica 21, 1-11.

Akhtar, A., 1973b. Compression of zirconium single crystals parallel to the c-axis. Journal of Nuclear Materials 47, 79-86.

Akhtar, A., 1975a. Prismatic slip in zirconium single crystals at elevated temperatures. MTA 6, 1217-1222.

Akhtar, A., 1975b. Schmid's law and prismatic slip of zirconium. Scripta Metallurgica 9, 859-861.

Akhtar, A., Teghtsoonian, A., 1971. Plastic deformation of zirconium single crystals. Acta Metallurgica 19, 655-663.

Al-Harbi, H.F., Knezevic, M., Kalidindi, S.R., 2010. Spectral approaches for the fast computation of yield surfaces and first-order plastic property closures for polycrystalline materials with cubic-triclinic textures. CMC: Computers, Materials, & Continua 15, 153-172.

Ardeljan, M., Beyerlein, I.J., Knezevic, M., 2014. A dislocation density based crystal plasticity finite element model: Application to a two-phase polycrystalline HCP/BCC composites. Journal of the Mechanics and Physics of Solids 66, 16-31.

Ardeljan, M., Knezevic, M., Nizolek, T., Beyerlein, I.J., Mara, N.A., Pollock, T.M., 2015a. A study of microstructure-driven strain localizations in two-phase polycrystalline HCP/BCC composites using a multi-scale model. International Journal of Plasticity 74, 35-57.

Ardeljan, M., McCabe, R.J., Beyerlein, I.J., Knezevic, M., 2015b. Explicit incorporation of deformation twins into crystal plasticity finite element models. Computer Methods in Applied Mechanics and Engineering 295, 396-413.

Armijo, L., 1966. Minimization of functions having Lipschitz continuous first partial derivatives. Pacific Journal of mathematics 16, 1-3.

Asaro, R.J., 1979. Geometrical effects in the inhomogeneous deformation of ductile single crystals. Acta Metallurgica 27, 445-453.

Asaro, R.J., Needleman, A., 1985. Texture development and strain hardening in rate dependent polycrystals. Acta Metallurgica et Materialia 33, 923-953.

Asaro, R.J., Rice, J.R., 1977. Strain localization in ductile single crystals. Journal of the Mechanics and Physics of Solids 25, 309-338.

Bhattacharyya, A., Knezevic, M., Abouaf, M., 2015. Characterization of Crystallographic Texture and Intra-Grain Morphology in Cross-Rolled Tantalum. Metallurgical and Materials Transactions A 46, 1085-1096.

Bieler, T.R., Wang, L., Beaudoin, A.J., Kenesei, P., Lienert, U., 2014. In situ characterization of twin nucleation in pure Ti using 3D-XRD. Metallurgical and Materials Transactions A 45, 109-122.

Bingert, J., Mason, T., Kaschner, G., Gray III, G., Maudlin, P., 2002. Deformation twinning in polycrystalline Zr: Insights from electron backscattered diffraction characterization. Metallurgical and Materials Transactions A 33, 955-963.

Capolungo, L., Beyerlein, I.J., Kaschner, G.C., Tomé, C.N., 2009. On the interaction between slip dislocations and twins in HCP Zr. Materials Science and Engineering: A 513-514, 42-51.

Carpenter, J.S., Nizolek, T., McCabe, R.J., Knezevic, M., Zheng, S.J., Eftink, B.P., Scott, J.E., Vogel, S.C., Pollock, T.M., Mara, N.A., Beyerlein, I.J., 2015. Bulk texture evolution of nanolamellar Zr–Nb composites processed via accumulative roll bonding. Acta Materialia 92, 97-108.

Cerreta, E.K., Bingert, J.F., Gray Iii, G.T., Trujillo, C.P., Lopez, M.F., Bronkhorst, C.A., Hansen, B.L., 2013. Microstructural examination of quasi-static and dynamic shear in high-purity iron. International Journal of Plasticity 40, 23-38.

Eshelby, J.D., 1957. The determination of the elastic field of an ellipsoidal inclusion, and related problems. Proc R. Soc. Lond. A 241, 376-396.

Fast, T., Knezevic, M., Kalidindi, S.R., 2008. Application of microstructure sensitive design to structural components produced from hexagonal polycrystalline metals. Computational Materials Science 43, 374-383.

Fromm, B.S., Adams, B.L., Ahmadi, S., Knezevic, M., 2009. Grain size and orientation distributions: Application to yielding of α-titanium. Acta Materialia 57, 2339-2348.

Hawkyard, J., 1969. A theory for the mushrooming of flat-ended projectiles impinging on a flat rigid anvil, using energy considerations. International Journal of Mechanical Sciences 11, 313-333.

Hill, 1966. Generalized constitutive relations for incremental deformation of metal crystals by multislip. J. Mech. Phys.Solids 14, 95-102.

Hill, R., Rice, J.R., 1972. Constitutive analysis of elastic-plastic crystals at arbitrary strain. Journal of the Mechanics and Physics of Solids 20, 401-413.

Hosford, W.F., Caddell, R.M., 2011. Metal forming: mechanics and metallurgy. Cambridge University Press.

Hughes, T.J.R., Winget, J., 1980. Finite rotation effects in numerical integration of rate constitutive equations arising in large-deformation analysis. International Journal for Numerical Methods in Engineering 15, 1862-1867.

Hutchinson, J.W., 1976. Bounds and self-consistent estimates for creep of polycrystalline materials. Proceedings of the Royal Society of London. Series A, Mathematical and Physical Sciences, 101-126.

Jahedi, M., Ardeljan, M., Beyerlein, I.J., Paydar, M.H., Knezevic, M., 2015a. Enhancement of orientation gradients during simple shear deformation by application of simple compression. Journal of Applied Physics 117, 214309.

Jahedi, M., Knezevic, M., Paydar, M., 2015b. High-Pressure Double Torsion as a Severe Plastic Deformation Process: Experimental Procedure and Finite Element Modeling. J. of Materi Eng and Perform 24, 1471-1482.

Jahedi, M., Paydar, M.H., Knezevic, M., 2015c. Enhanced microstructural homogeneity in metal-matrix composites developed under high-pressure-double-torsion. Materials Characterization 104, 92-100.

Jahedi, M., Paydar, M.H., Zheng, S., Beyerlein, I.J., Knezevic, M., 2014. Texture evolution and enhanced grain refinement under high-pressure-double-torsion. Materials Science and Engineering: A 611, 29-36.

Kalidindi, S.R., Bronkhorst, C.A., Anand, L., 1992. Crystallographic texture evolution in bulk deformation processing of FCC metals. Journal of the Mechanics and Physics of Solids 40, 537-569.

Kalidindi, S.R., Duvvuru, H.K., Knezevic, M., 2006. Spectral calibration of crystal plasticity models. Acta Materialia 54, 1795-1804.

Kaschner, G., Gray III, G., 2000. The influence of crystallographic texture and interstitial impurities on the mechanical behavior of zirconium. Metallurgical and Materials Transactions A 31, 1997-2003.

Knezevic, M., Al-Harbi, H.F., Kalidindi, S.R., 2009. Crystal plasticity simulations using discrete Fourier transforms. Acta Materialia 57, 1777-1784.

Knezevic, M., Beyerlein, I.J., Brown, D.W., Sisneros, T.A., Tomé, C.N., 2013a. A polycrystal plasticity model for predicting mechanical response and texture evolution during strain-path changes: Application to beryllium. International Journal of Plasticity 49, 185-198.

Knezevic, M., Beyerlein, I.J., Lovato, M.L., Tomé, C.N., Richards, A.W., McCabe, R.J., 2014a. A strain-rate and temperature dependent constitutive model for BCC metals incorporating non-

Schmid effects: Application to tantalum–tungsten alloys. International Journal of Plasticity 62, 93-104.

Knezevic, M., Beyerlein, I.J., Nizolek, T., Mara, N.A., Pollock, T.M., 2013b. Anomalous Basal Slip Activity in Zirconium under High-strain Deformation. Materials Research Letters 1, 133-140.

Knezevic, M., Carpenter, J.S., Lovato, M.L., McCabe, R.J., 2014b. Deformation behavior of the cobalt-based superalloy Haynes 25: Experimental characterization and crystal plasticity modeling. Acta Materialia 63, 162-168.

Knezevic, M., Crapps, J., Beyerlein, I.J., Coughlin, D.R., Clarke, K.D., McCabe, R.J., 2016. Anisotropic modeling of structural components using embedded crystal plasticity constructive laws within finite elements. International Journal of Mechanical Sciences 105, 227-238.

Knezevic, M., Drach, B., Ardeljan, M., Beyerlein, I.J., 2014c. Three dimensional predictions of grain scale plasticity and grain boundaries using crystal plasticity finite element models. Computer Methods in Applied Mechanics and Engineering 277, 239-259.

Knezevic, M., Jahedi, M., Korkolis, Y.P., Beyerlein, I.J., 2014d. Material-based design of the extrusion of bimetallic tubes. Computational Materials Science 95, 63-73.

Knezevic, M., Kalidindi, S.R., 2007. Fast computation of first-order elastic-plastic closures for polycrystalline cubic-orthorhombic microstructures. Computational Materials Science 39, 643-648.

Knezevic, M., Kalidindi, S.R., Fullwood, D., 2008a. Computationally efficient database and spectral interpolation for fully plastic Taylor-type crystal plasticity calculations of face-centered cubic polycrystals. International Journal of Plasticity 24, 1264-1276.

Knezevic, M., Kalidindi, S.R., Mishra, R.K., 2008b. Delineation of first-order closures for plastic properties requiring explicit consideration of strain hardening and crystallographic texture evolution. International Journal of Plasticity 24, 327-342.

Knezevic, M., Landry, N.W., 2015. Procedures for reducing large datasets of crystal orientations using generalized spherical harmonics. Mechanics of Materials 88, 73-86.

Knezevic, M., Lebensohn, R.A., Cazacu, O., Revil-Baudard, B., Proust, G., Vogel, S.C., Nixon, M.E., 2013c. Modeling bending of α-titanium with embedded polycrystal plasticity in implicit finite elements. Materials Science and Engineering: A 564, 116-126.

Knezevic, M., Levinson, A., Harris, R., Mishra, R.K., Doherty, R.D., Kalidindi, S.R., 2010. Deformation twinning in AZ31: Influence on strain hardening and texture evolution. Acta Materialia 58, 6230-6242.

Knezevic, M., McCabe, R.J., Lebensohn, R.A., Tomé, C.N., Liu, C., Lovato, M.L., Mihaila, B., 2013d. Integration of self-consistent polycrystal plasticity with dislocation density based

hardening laws within an implicit finite element framework: Application to low-symmetry metals. Journal of the Mechanics and Physics of Solids 61, 2034-2046.

Knezevic, M., McCabe, R.J., Tomé, C.N., Lebensohn, R.A., Chen, S.R., Cady, C.M., Gray Iii, G.T., Mihaila, B., 2013e. Modeling mechanical response and texture evolution of α-uranium as a function of strain rate and temperature using polycrystal plasticity. International Journal of Plasticity 43, 70-84.

Knezevic, M., Nizolek, T., Ardeljan, M., Beyerlein, I.J., Mara, N.A., Pollock, T.M., 2014e. Texture evolution in two-phase Zr/Nb lamellar composites during accumulative roll bonding. International Journal of Plasticity 57, 16-28.

Knezevic, M., Savage, D.J., 2014. A high-performance computational framework for fast crystal plasticity simulations. Computational Materials Science 83, 101-106.

Knezevic, M., Zecevic, M., Beyerlein, I.J., Bhattacharyya, A., McCabe, R.J., 2015a. Predicting Texture Evolution in Ta and Ta-10W Alloys Using Polycrystal Plasticity. JOM 67, 2670-2674.

Knezevic, M., Zecevic, M., Beyerlein, I.J., Bingert, J.F., McCabe, R.J., 2015b. Strain rate and temperature effects on the selection of primary and secondary slip and twinning systems in HCP Zr. Acta Materialia 88, 55-73.

Kocks, U.F., Mecking, H., 2003. Physics and phenomenology of strain hardening: the FCC case. Progress in Materials Science 48, 171-273.

Kok, S., Beaudoin, A.J., Tortorelli, D.A., 2002. A polycrystal plasticity model based on the mechanical threshold. International Journal of Plasticity 18, 715-741.

Landry, N., Knezevic, M., 2015. Delineation of First-Order Elastic Property Closures for Hexagonal Metals Using Fast Fourier Transforms. Materials 8, 6326-6345.

Lebensohn, R.A., Tomé, C.N., 1993. A self-consistent anisotropic approach for the simulation of plastic deformation and texture development of polycrystals: Application to zirconium alloys. Acta Metallurgica et Materialia 41, 2611-2624.

Lebensohn, R.A., Tomé, C.N., Castaneda, P.P., 2007. Self-consistent modelling of the mechanical behaviour of viscoplastic polycrystals incorporating intragranular field fluctuations. Philosophical Magazine 87, 4287-4322.

Lebensohn, R.A., Zecevic, M., Knezevic, M., McCabe, R.J., 2016. Average intragranular misorientation trends in polycrystalline materials predicted by a viscoplastic self-consistent approach. Acta Materialia 104, 228-236.

Lee, E., Tupper, S., 1954. Analysis of plastic deformation in a steel cylinder striking a rigid target. J. appl. Mech 21, 63-70.

Lemaignan, C., Motta, A.T., 2006. Zirconium Alloys in Nuclear Applications, Materials Science and Technology. Wiley-VCH Verlag GmbH & Co. KGaA.

Lentz, M., Klaus, M., Beyerlein, I.J., Zecevic, M., Reimers, W., Knezevic, M., 2015a. In situ X-ray diffraction and crystal plasticity modeling of the deformation behavior of extruded Mg–Li–(Al) alloys: An uncommon tension–compression asymmetry. Acta Materialia 86, 254-268.

Lentz, M., Klaus, M., Wagner, M., Fahrenson, C., Beyerlein, I.J., Zecevic, M., Reimers, W., Knezevic, M., 2015b. Effect of age hardening on the deformation behavior of an Mg–Y–Nd alloy: In-situ X-ray diffraction and crystal plasticity modeling. Materials Science and Engineering: A 628, 396-409.

Li, S.F., Lind, J., Hefferan, C.M., Pokharel, R., Lienert, U., Rollett, A.D., Suter, R.M., 2012. Three-dimensional plastic response in polycrystalline copper via near-field high-energy X-ray diffraction microscopy. Journal of Applied Crystallography 45, 1098-1108.

Lind, J., Li, S.F., Pokharel, R., Lienert, U., Rollett, A.D., Suter, R.M., 2014. Tensile twin nucleation events coupled to neighboring slip observed in three dimensions. Acta Materialia 76, 213-220.

Masson, R., Bornert, M., Suquet, P., Zaoui, A., 2000. An affine formulation for the prediction of the effective properties of nonlinear composites and polycrystals. Journal of the Mechanics and Physics of Solids 48, 1203-1227.

Maudlin, P., Bingert, J., House, J., Chen, S., 1999a. On the modeling of the Taylor cylinder impact test for orthotropic textured materials: experiments and simulations. International Journal of Plasticity 15, 139-166.

Maudlin, P., Gray, G., Cady, C., Kaschner, G., 1999b. High–rate material modelling and validation using the Taylor cylinder impact test. Philosophical Transactions of the Royal Society of London A: Mathematical, Physical and Engineering Sciences 357, 1707-1729.

Mecking, H., Kocks, U.F., 1981. Kinetics of flow and strain-hardening. Acta Metallurgica et Materialia 29, 1865-1875.

Mercier, S., Molinari, A., 2009. Homogenization of elastic–viscoplastic heterogeneous materials: Self-consistent and Mori-Tanaka schemes. International Journal of Plasticity 25, 1024-1048.

Meyers, M.A., Chawla, K.K., 1998. Mechanical Behavior of Materials. Prentice Hall, Upper Saddle River, New Jersey.

Mihaila, B., Knezevic, M., Cardenas, A., 2014. Three orders of magnitude improved efficiency with high - performance spectral crystal plasticity on GPU platforms. International Journal for Numerical Methods in Engineering 97, 785-798.

Nielsen, R., 2000. Zirconium and Zirconium Compounds, Ullmann's Encyclopedia of Industrial Chemistry. Wiley-VCH Verlag GmbH & Co. KGaA.

Obara, T., Yoshinga, H., Morozumi, S., 1973. {112-2}<-1-123> Slip system in magnesium. Acta Metallurgica 21, 845-853.

Peirce, D., Asaro, R., Needleman, A., 1982a. An analysis of nonuniform and localized deformation in ductile single crystals. Acta metallurgica 30, 1087-1119.

Peirce, D., Asaro, R.J., Needleman, A., 1982b. An analysis of nonuniform and localized deformation in ductile single crystals. Acta Metallurgica 30, 1087-1119.

Revil-Baudard, B., Cazacu, O., Flater, P., Kleiser, G., 2015. Plastic deformation of high-purity α-titanium: Model development and validation using the Taylor cylinder impact test. Mechanics of Materials 80, Part B, 264-275.

Sachs, G., 1929. Zur ableitung einer fliessbedingung, Mitteilungen der deutschen Materialprüfungsanstalten. Springer, pp. 94-97.

Savage, D.J., Knezevic, M., 2015. Computer implementations of iterative and non-iterative crystal plasticity solvers on high performance graphics hardware. Computational Mechanics 56, 677–690.

Segurado, J., Lebensohn, R.A., Llorca, J., Tomé, C.N., 2012. Multiscale modeling of plasticity based on embedding the viscoplastic self-consistent formulation in implicit finite elements. International Journal of Plasticity 28, 124-140.

Shaffer, J.B., Knezevic, M., Kalidindi, S.R., 2010. Building texture evolution networks for deformation processing of polycrystalline fcc metals using spectral approaches: Applications to process design for targeted performance. International Journal of Plasticity 26, 1183-1194.

Smith, D.H., Bicknell, J., Jorgensen, L., Patterson, B.M., Cordes, N.L., Tsukrov, I., Knezevic, M., 2016. Microstructure and mechanical behavior of direct metal laser sintered Inconel alloy 718. Materials Characterization 113, 1-9.

Taylor, G.I., 1938. Plastic strain in metals. Journal of the Institute of Metals 62, 307-324.

Taylor, G.I., 1948. The use of flat-ended projectiles for determining dynamic yield stress. I. Theoretical considerations, Proceedings of the Royal Society of London A: Mathematical, Physical and Engineering Sciences. The Royal Society, pp. 289-299.

Ungár, T., Castelnau, O., Ribárik, G., Drakopoulos, M., Béchade, J.L., Chauveau, T., Snigirev, A., Snigireva, I., Schroer, C., Bacroix, B., 2007. Grain to grain slip activity in plastically deformed Zr determined by X-ray micro-diffraction line profile analysis. Acta Materialia 55, 1117-1127.

Ungár, T., Holden, T.M., Jóni, B., Clausen, B., Balogh, L., Csiszár, G., Brown, D.W., 2015. Dislocation structure in different texture components determined by neutron diffraction line profile analysis in a highly textured Zircaloy-2 rolled plate. Journal of Applied Crystallography 48, 409-417.

Wu, X., Proust, G., Knezevic, M., Kalidindi, S.R., 2007. Elastic-plastic property closures for hexagonal close-packed polycrystalline metals using first-order bounding theories. Acta Materialia 55, 2729-2737.

Zecevic, M., Knezevic, M., Beyerlein, I.J., McCabe, R.J., 2016a. Origin of texture development in orthorhombic uranium. Materials Science and Engineering: A 665, 108-124.

Zecevic, M., Knezevic, M., Beyerlein, I.J., McCabe, R.J., 2016b. Texture formation in orthorhombic alpha-uranium under simple compression and rolling to high strains. Journal of Nuclear Materials 473, 143-156.

Zecevic, M., Knezevic, M., Beyerlein, I.J., Tomé, C.N., 2015a. An elasto-plastic self-consistent model with hardening based on dislocation density, twinning and de-twinning: Application to strain path changes in HCP metals. Materials Science and Engineering: A 638, 262-274.

Zecevic, M., McCabe, R.J., Knezevic, M., 2015b. A new implementation of the spectral crystal plasticity framework in implicit finite elements. Mechanics of Materials 84, 114-126.

Zecevic, M., McCabe, R.J., Knezevic, M., 2015c. Spectral database solutions to elasto-viscoplasticity within finite elements: Application to a cobalt-based FCC superalloy. International Journal of Plasticity 70, 151-165.

Zecevic, M., Roemer, T., Knezevic, M., Korkolis, Y., Kinsey, B., 2016c. Residual Ductility and Microstructural Evolution in Continuous-Bending-under-Tension of AA-6022-T4. Materials 9, 130.

Chapter 2: A new visco-plastic self-consistent formulation implicit in dislocation-based hardening within implicit finite elements: Application to high strain rate and impact deformation of tantalum

This chapter was published as: "A new visco-plastic self-consistent formulation implicit in dislocation-based hardening within implicit finite elements: Application to high strain rate and impact deformation of tantalum", Miroslav Zecevic and Marko Knezevic, Computer Methods in Applied Mechanics and Engineering 341 (2018): 888-916. My contribution to this chapter was:

- development and implementation of implicit integration of slip resistances within the rate insensitive visco-plastic self-consistent model coupled with implicit finite elements

- implementation of the remeshing procedure and the algorithm for interpolation of the model state variables

- calibration of the hardening parameters for Ta

- finite element modeling of Taylor impact of Ta cylinder and comparison of predictions with experimental measurements

- writing the first draft of the paper.

A new visco-plastic self-consistent formulation implicit in dislocation-based hardening within implicit finite elements: Application to high strain rate and impact deformation of tantalum

Miroslav Zecevic[a] and Marko Knezevic[a]

[a] Department of Mechanical Engineering, University of New Hampshire, Durham, NH 03824, USA

Abstract

Modeling deformation processes of materials under high strain rate and impact conditions in which the strain rates vary spatiotemporally over several orders of magnitude is challenging, especially in terms of constitutive description. Visco-plastic power-law flow rule, commonly used within crystal plasticity constitutive models, usually introduces superfluous strain rate effects, entering numerically via the slip activation criterion, which result in artificially high flow stress predictions under high strain rate deformation conditions. This paper presents a novel, implicit finite element implementation of a visco-plastic self-consistent polycrystal model that is implicit in dislocation-based hardening with removed strain rate sensitivity introduced by the power-law flow rule. In the model, the strain rate dependence of the flow stress is defined solely by the rate sensitivity of Peierls stress and the evolution of dislocation density within the hardening law, enabling the prediction of high strain rate and impact deformation. As a result, the predicted flow stress is accurate in its magnitude. The physically based strain rate and temperature sensitive model also features, in addition to Schmid, the non-Schmid activation contribution for slip, which is necessary for understanding and modeling the plastic deformation of body-centered cubic metals. The model is calibrated to simulate the strain rate- and temperature-sensitive monotonic deformation of tantalum and is subsequently applied to a Taylor impact test of the same material. Since the impact simulation required remeshing and interpolation of state variables, the spherical linear interpolation algorithm in the space of

quaternions is implemented to facilitate the interpolation of texture. Predictions of the simulation were found to compare favorably with experimental measurements of post-test geometrical changes and texture evolution. The implementation and insights from these predictions are presented and discussed in the paper.

1   Introduction

Body-centered-cubic (BCC) refractory metals often operate under extreme mechanical and thermal conditions in applications such as anti-armor systems, missile bodies, space vehicle components (including vanes and nozzles that guide propulsion in rocket motors), aircraft structural components (including aircraft engines and engine parts), particle accelerators, electronic heat sinks, and heat treating and glass-melting furnaces [1-4]. Tantalum (Ta) belongs to the group of the refractory metals, which are known to exhibit strong temperature and strain rate dependent mechanical behavior [5-8].

Crystal plasticity constitutive theories have been developed and utilized over the past several decades to physically describe the behavior of metals by accounting for the details of their microstructure and the crystallography of the prevalent grain-scale deformation mechanisms [9-13]. Such theories facilitate a deeper understanding of the deformation behavior of polycrystalline metals and allow more accurate simulations of metal fabrication processes, when compared to the commonly used phenomenological plasticity models [14-18]. The predictions of the mechanical response and concomitant microstructure evolution of metallic materials under high strain rate and impact are critically important for the evaluation of metallic components in service and during their fabrication on a computer rather than the shop floor. The present paper is concerned with the development of more accurate descriptions of the deformation behavior of materials under high strain rate and high temperature, as well as the integration of such descriptions into the finite element (FE) framework to facilitate predictions of microstructure and deformed geometries. The stress needed to activate crystallographic slip depends on strain-rate and temperature and evolves with strain as dislocations interact and become stored in the crystal. Therefore, the deformation response under high strain rate and temperature conditions can be

61

better understood and predicted with knowledge of crystallography of the deformation mechanisms and their contribution to microstructure evolution.

Taylor impact testing is used for determining dynamic yield stresses of polycrystalline metals [19]. The same test was useful in validating various constitutive laws for high strain rate deformation of metals because the metal undergoes a wide range of strain rates and strain levels during the test [20-22]. The test involves propelling a cylindrical specimen at a rigid target. The shape changes, and the microstructure can be characterized. As a result of the cylinder's highly heterogeneous deformation, the underlying microstructure can substantially vary throughout the cylinder.

Several classical plasticity models have been developed to describe the temperature and strain rate dependent behaviors of various metals, including BCC. In the Johnson-Cook model, the von Mises flow stress is expressed as a function of strain rate and temperature [23]. Later, Zerilli and Armstrong proposed a different strain rate and temperature sensitive analytical expression for flow stress, motivated by dislocation mechanics, and they applied the model specifically to simulate Ta behavior [24, 25]. However, both formulations are largely empirical. Models known as the internal state variables (ISV) models, with parameters therein as a function of the strain-rate and temperature, have also been used in large deformation of metals [26]. However, accuracy of ISV models depends on the expense of a laborious tabulation of model parameters from experiments. More advanced models accounting for thermal activation of dislocations in a largely phenomenological manner, known as the Steinberg-Guinan [27] and Preston-Tonks-Wallace [28] models, have reproduced the behavior of Ta at a broad range of temperatures and strain rates. However, these models rely on fitting to macroscopic data while not explicitly considering the deformation physics at the level of crystallographic slip systems.

The mechanical threshold stress (MTS) model, originally proposed by Follansbee and Kocks [29], was used for modeling dynamic deformation of Ta [6, 30]. The main drawback of the above-described models is that they only capture the rate and temperature sensitive behavior of flow stress. The shape of the yield surface remains constant throughout the deformation process regardless of the microstructural changes happening within the material (e.g. texture evolution, twinning), which can greatly affect the anisotropy of the response. Continuum anisotropic yield surfaces, which evolve during deformation, specifically developed to account for plastic anisotropy and tension-compression asymmetry incorporated into a FE framework, represent an attractive alternative mainly due to their computational efficiency and accuracy [31, 32]. These models have been successfully applied to predict the deformation and geometric changes of the Taylor impact specimens. However, evolution of the yield surface is captured for only one strain path while the deformation within the Taylor cylinder is very heterogeneous. Therefore, the evolution of the yield surface will be inappropriate for large number of points because their strain history is different from the one to which the yield surface was fitted. Alternatively, the models for the evolution of flow stress can be implemented into crystal plasticity models. The MTS model has been implemented in crystal plasticity models to operate at the slip system level in [7, 33], where the MTS is the slip resistance at 0 °K and the flow rule is an exponential function. While predictive, the model has a large number of fitting parameters. Physics-based constitutive model relying on the Orowan's equation and transition state theory with a Taylor type full-constraint homogenization has been applied to simulate constitutive behavior and microstructural evolution of Ta in [34]. Good agreement with the experiments was achieved.

The strain-rate and temperature sensitivity of metals can be well described by models that are based on thermally activated glide kinetics within crystal plasticity [35]. The activation stress

for dislocation glide usually relies solely on the Schmid law. In this law, slip is activated when the stress tensor projected onto the glide plane in its glide direction reaches a value of slip resistance [36]. However, the glide in BCC metals, such as Ta, is known to violate the Schmid law. The behavior manifests in tension-compression asymmetry and plastic anisotropy [37-42]. The behavior is referred to as non-Schmid and has been attributed to the motion of the non-planar core of screw dislocations and the role that non-glide stresses play in the movement of the dislocation through the lattice [43-48]. Specifically, in addition to the Schmid tensor, there are other stress components resolved in the remaining two shear directions and the three normal components [49]. A visco-plastic self-consistent (VPSC) polycrystal model for BCC metals that includes the local non-Schmid effects has recently been developed in [50, 51] and will be used in the present work.

It is desirable for rate dependence in the macroscale response to arise solely due to the rate dependence of dislocation motion on individual slip systems at the slip system level [10, 52]. However, difficulty can arise from power-law, rate-sensitive, hardening law crystal visco-plasticity models [53]. The visco-plastic rate-dependent flow theory is used to uniquely determine the set of independent slip systems accommodating the imposed plastic strain [54]. The flow rule in this theory involves a power-law relation whose exponent n represents the inverse of material rate sensitivity [11, 55]. Hence, the flow rule introduces undesirable rate sensitivity, which can have a marked effect on macroscale response, making it unrealistic.

The objective of this study is to develop a multi-level model that links dislocation-crystal-polycrystal-component-scale within an FE framework for simulating the rate- and temperature-sensitive deformation response of metals (where the rate sensitivity is coming solely from slip resistance) and thermally activated glide. The new formulation uses the visco-plastic flow rule at

a single crystal level, with removed rate sensitivity coming from the visco-plastic power-law relation. The hardening law used is dislocation density-based [56] relying on both Schmid and non-Schmid activation stresses for dislocation glide [50]. Self-consistent method is used for homogenization and the overall procedure is formulated as implicit in hardening. Therefore, the proposed polycrystal plasticity model is a modification of the widely used VPSC model [57]. The comprehensive formulation is calibrated to simulate high strain rate- and temperature-sensitive deformation of Ta and subsequently applied to simulate a Taylor impact test of the same material. The predictions in terms of geometry and evolution of texture are compared with experiments. The implementation and results are presented and discussed in this paper.

2   Modeling framework

This section presents details of the multi-level modeling framework aimed at simulating the microstructure-property relationships in a BCC polycrystal during high strain rate and impact deformation conditions. At the macro scale, the implicit FE solver is used for solving initial boundary value problem. Local constitutive response at FE integration points is solved by self-consistent homogenization of visco-plastic polycrystal (VPSC model) [57], which integrates a dislocation density-based hardening law [58, 59]. In the proposed model, the slip resistances are evolved implicitly while all the other state variables (crystal orientations, grain shape, temperature, etc) are evolved explicitly. In addition, the macroscopic constitutive equation is also integrated implicitly.

The Taylor impact test of Ta cylinder was previously modeled in [30, 34, 60]. First, Bingert et al. employed a multisurface algorithm [61] to describe the yield surface of Ta obtained by Taylor-Bishop-Hill polycrystal calculations. The yield surface was only allowed to expand with the evolution of yield stress described by the MTS model [6], while the shape of the yield surface

remained constant during deformation. Consequently, the texture evolution and heterogeneous hardening during deformation had no influence on the shape of the yield surface. Despite these simplifications model predicts the post-test geometry well. Subsequently, Plunkett et al. used a more sophisticated model capable of predicting effects of texture evolution and twinning on the shape of the yield surface to simulate Taylor impact tests of zirconium and tantalum cylinders [60]. In the case of zirconium cylinder, the evolution of the yield surface was predicted using the VPSC model. Next, the predicted evolution of the yield surface was fitted with the macroscopic yield criterion (CPB06). As noted before, the main drawback of this approach is that the yield surface evolution is recorded for only one specific strain history. It is clear that during Taylor impact simulation strain histories of different points are quite heterogeneous. Consequently, the predicted yield surface will deviate from the actual yield surface for points that experience strain history different from the one used during the fitting procedure. In addition, both of the modeling approaches are incapable of predicting microstructural evolution. On the other hand, Kothari and Anand proposed a sophisticated polycrystal plasticity model for simulating deformation of Ta and successfully predicted the mechanical response and microstructural evolution as a function of strain rate and temperature, including the Taylor impact tests at two different strain rates and temperatures [34]. Single crystal response was modeled using the equation of Orowan, which relates the slip system shear rates with a density of mobile dislocations and an average value of dislocation velocity [62]. The average dislocation velocity was defined in terms of the resolved shear stress, critical resolved shear stress, and temperature using the transition-state theory [63]. A homogenized response at every integration point was obtained by the full-constraint Taylor type homogenization.

In summary, the models developed by Bingert et al. and Plunkett et al. rely on fitting the yield surfaces predicted by polycrystal plasticity models. On the other hand, the model developed by Kothari and Anand as well as the model presented in this work directly use the polycrystal plasticity constitutive law at each integration point of the finite element model facilitating more accurate predictions at a higher computational cost. As mentioned above, the work of Kothari and Anand utilized the physics-based Orowan's equation as the single crystal flow rule, while the work presented here relies on the power-law flow rule. While the former work utilized a simple empirical hardening law, the work presented here relies on a rate and temperature sensitive dislocation density-based hardening law. Moreover, the self-consistent homogenization method utilized in the present model is more advanced than the full constraint Taylor approach. In summary, we show that the widely used visco-plastic flow rule when appropriately modified, in combination with a physics-based dislocation density hardening law, can successfully predict a complex strain rate and temperature dependent response of Ta.

We begin by describing the kinematics, the single crystalline constitutive response and the hardening law (sections 2.1, 2.2 and 2.3). Subsequently, we describe the homogenization procedure and finite element implementation (sections 2.4 and 2.5). In our notation, tensors will be denoted by bold letters, while scalars and tensor components will be italic and not bold. The dyadic and contracted product between two tensors will be denoted by $\otimes$ and $\cdot$, respectively.

2.1 Kinematics

In what follows we briefly describe the kinematics of a purely plastic crystal plasticity model [57, 64]. Polycrystal is assumed to consist of a set of grains undergoing plastic deformation, meaning that the elasticity of the individual grains is neglected. As a result, the

effective behavior of a plastic polycrystal is evaluated first. Next, the purely plastic effective medium is coupled with elasticity in an average manner [65, 66], as discussed later.

Deformation gradient of grain r is given by:

$$\mathbf{F}^{(r)} = \frac{\partial \mathbf{x}}{\partial \mathbf{X}}, \tag{1}$$

where $\mathbf{x}$ and $\mathbf{X}$ are coordinates of a material point in the current and initial configurations. Velocity gradient of grain r, in the current configuration, is defined as:

$$\mathbf{L}^{(r)} = \frac{\partial \mathbf{v}}{\partial \mathbf{x}}, \tag{2}$$

where $\mathbf{v}$ is the velocity in the current configuration. Velocity gradient can be decomposed into symmetric, $\mathbf{D}^{(r)}$, and anti-symmetric, $\mathbf{W}^{(r)}$, parts. The relation between the velocity gradient and the deformation gradient is given by:

$$\dot{\mathbf{F}}^{(r)} = \mathbf{L}^{(r)}\mathbf{F}^{(r)}. \tag{3}$$

Polar decomposition allows us to decompose the total deformation gradient into pure rotation, $\mathbf{R}^{(r)}$, and plastic distortion, $\mathbf{F}_p^{(r)}$:

$$\mathbf{F}^{(r)} = \mathbf{R}^{(r)}\mathbf{F}_p^{(r)}. \tag{4}$$

The plastic distortion is assumed to shear the lattice without rotation or stretch. Next the rotation tensor rotates the lattice into final configuration. In the elasto-plastic formulation the total deformation gradient is decomposed into elastic and plastic deformation gradients. Since the elasticity is neglected the elastic deformation gradient is replaced with pure rotation. By solving Eq. (3) for velocity gradient and substituting Eq. (4) we obtain:

$$\mathbf{L}^{(r)} = \dot{\mathbf{F}}^{(r)}\mathbf{F}^{(r)-1} = \dot{\mathbf{R}}^{(r)}\mathbf{R}^{(r)-1} + \mathbf{R}^{(r)}\dot{\mathbf{F}}_p^{(r)}\mathbf{F}_p^{(r)-1}\mathbf{R}^{(r)-1}. \tag{5}$$

Term $\dot{\mathbf{R}}^{(r)}\mathbf{R}^{(r)^{-1}}$ is the lattice spin, $\mathbf{W}^{*,(r)}$, in the current configuration associated with the pure rotation. Term $\dot{\mathbf{F}}_p^{(r)}\mathbf{F}_p^{(r)^{-1}}$ is the plastic velocity gradient in the configuration before rotation, which can be expressed as superposition of slip system shear rates:

$$\mathbf{L}_p^{i,(r)} = \sum_s \dot{\gamma}^{s,(r)}\mathbf{b}^{s,i,(r)} \otimes \mathbf{n}^{s,i,(r)}, \tag{6}$$

where $\mathbf{b}^{s,i,(r)}$ and $\mathbf{n}^{s,i,(r)}$ are Burgers vector and slip plane normal in the configuration before rotation. Substituting Eq. (6) into Eq. (5) and noting that Burgers vector and slip plane normal in current configuration are given by $\mathbf{b}^{s,(r)} = \mathbf{R}^{(r)}\mathbf{b}^{s,i,(r)}$ and $\mathbf{n}^{s,(r)} = \mathbf{R}^{(r)}\mathbf{n}^{s,i,(r)}$, allows us to write the velocity gradient in current configuration as:

$$\mathbf{L}^{(r)} = \mathbf{W}^{*,(r)} + \sum_s \dot{\gamma}^{s,(r)}\mathbf{b}^{s,(r)} \otimes \mathbf{n}^{s,(r)}. \tag{7}$$

From here the symmetric part of the velocity gradient and the lattice spin are:

$$\mathbf{D}^{(r)} = \sum_s \dot{\gamma}^{s,(r)}\mathbf{m}^{s,(r)}, \tag{8}$$

$$\mathbf{W}^{*,(r)} = \mathbf{W}^{(r)} - \sum_s \dot{\gamma}^{s,(r)}\boldsymbol{\alpha}^{s,(r)}, \tag{9}$$

where $\mathbf{m}^{s,(r)}$ and $\boldsymbol{\alpha}^{s,(r)}$ are symmetric and anti-symmetric parts of Schmid tensor for slip system s calculated as $\frac{1}{2}(\mathbf{b}^{s,(r)} \otimes \mathbf{n}^{s,(r)} + \mathbf{n}^{s,(r)} \otimes \mathbf{b}^{s,(r)})$ and $\frac{1}{2}(\mathbf{b}^{s,(r)} \otimes \mathbf{n}^{s,(r)} - \mathbf{n}^{s,(r)} \otimes \mathbf{b}^{s,(r)})$. The lattice spin is used for incremental updating of crystallographic orientations, while the total deformation gradient within the grain is used for calculation of grain shape. In VPSC, the tensor $\mathbf{D}$ which is based on the finite kinematic structure, is replaced with a strain rate tensor, $\dot{\boldsymbol{\varepsilon}}_{vp}$, which is based on the infinitesimal kinematic structure, as will be discussed later. In the next section the relation between the instantaneous rate of deformation and stress is derived.

2.2 Single crystal constitutive relation

The functional relationship between the slip system shear rate, stress and the microstructural state represents the constitutive equation [67], which are either phenomenological or physically based. The former constitutive models relate the shear rate on slip system s with the resolved shear stress, τ^s, and the critical resolved shear stress of system s, τ_c^s. The first such constitutive model was the rate independent slip criterion. According to this model, once the resolved shear stress reaches the critical resolved shear stress, the slip system becomes active and the shear rate on that system can take any value:

$$\dot{\gamma}^s = 0 \text{ if } |\tau^s| < \tau_c^s, \tag{10}$$

$$\dot{\gamma}^s \neq 0 \text{ if } |\tau^s| > \tau_c^s. \tag{11}$$

The main drawback of the rate independent slip criterion is the difficulty and non-uniqueness involved in determination of active slip systems. The visco-plastic regularization of the rate independent slip criterion was introduced to alleviate those problems [11, 68]:

$$\dot{\gamma}^s = \dot{\gamma}_0 \left(\frac{\tau^s}{\tau_c^s}\right)^n, \tag{12}$$

where n is the inverse of rate sensitivity and $\dot{\gamma}_0$ is the reference shear rate. The visco-plastic regularization resolves the non-uniqueness issue and provides continuous functional relationship between shear rates and stress. However, it also introduces a dependence of the magnitude of shear rate on the magnitude of stress defined by the rate exponent n.

Physics-based constitutive models use the Orowan equation to relate the shear rate on slip system s with the dislocation density of mobile dislocations on slip systems s, ρ_m^s [62]:

$$\dot{\gamma}^s = \rho_m^s b^s v^s, \tag{13}$$

where b^s is the magnitude of Burgers vector and v^s is the average velocity of mobile dislocations. The dislocation density of mobile dislocations can be related to the statistically stored dislocation density through the temperature dependent scaling law [69]. The average velocity of mobile dislocations can be expressed as a complex function of resolved shear stress, critical resolved shear stress and temperature [34, 67, 69].

In the present model, we adopt the visco-plastic constitutive relation at the single crystal level. The visco-plastic regularization provides sufficiently accurate selection of slip system activity and continues functional relationship between stress and strain rate, which results in stable convergence properties of the overall procedure. In addition, the visco-plastic formulation with dislocation density-based hardening law has been previously successfully used for modeling of high rate deformation [56, 70, 71]. As will be seen in the next section, in the modified visco-plastic flow rule, the rate sensitivity is defined solely through the rate dependence of slip resistance, while the rate exponent n only determines the accuracy of slip system selection. Therefore, the slip system selection is not influenced by the material rate sensitivity. The Orowan equation approach [34] couples the slip system selection and rate sensitivity and, as a result, the increase in the rate sensitivity causes damping in the relation between shear rate and resolved shear stress, which is similar to reducing the rate exponent n in Eq. (12). Since the rate sensitivity increases with temperature at higher rates, the damping effect increases as well. As a result, it is possible to have shifts in active slip systems with increase of temperature, which cannot happen in simulations using the modified power-law flow rule, where the slip system selection and rate sensitivity are separated. In the modified visco-plastic flow rule, the slip system activation is determined solely by a constant rate exponent, while the slip resistances scale with strain rate and temperature and, in turn, determine the rate sensitivity. Physically, at elevated temperature, the

71

Peierls barrier decreases equally for all slip systems and the activity of slip systems is not expected to change from that at lower temperature, unless different slip modes activate. Finally, it is important to describe advances in the visco-plastic flow rule formulation since a large number of model developments relying on it can take the advantage of any new advances. In the next section, consequences of the adopted visco-plastic flow rule on the rate sensitivity and the necessary modifications to the flow rule are discussed. Subsequently, the functional relationship between the resolved shear stress and the applied stress is derived for the case of BCC Ta.

2.2.1 Accurate representation of strain rate sensitivity with visco-plastic power-law flow rule

Follansbee and Kocks define two rate effects within polycrystalline materials [29]. The first rate effect is the rate sensitivity of stress at constant structure (dislocation density). For FCC materials this rate effect is fairly small [29]. On the other hand, in BCC materials very high rate sensitivity at constant structure and low temperatures is observed and attributed to rate dependence of Peierls barrier [6, 72]. At elevated temperatures the rate sensitivity of BCC materials diminishes. The second rate effect is the rate dependence of structure evolution. Essentially, the rate of dislocation accumulation depends on the rate at which deformation happens [29, 56]. Both of these rate effects influence the macroscopic stress only through the resistance to slip. The rate sensitivity of the material at constant structure, m, is thus defined as:

$$m = \frac{\partial \ln|\sigma|}{\partial \ln|\dot{\varepsilon}|} = \sum_r \sum_s \frac{\partial \ln|\sigma|}{\partial \tau_c^{s,(r)}} \frac{\partial \tau_c^{s,(r)}}{\partial \ln|\dot{\varepsilon}|} \left(\rho^{(r)} = \text{const} \right), \tag{14}$$

where $\rho^{(r)}$ is total dislocation density within the grain r. Therefore, it is physical and thus desirable to describe the rate sensitivity of the material solely through the rate dependence of slip resistance and its evolution.

72

The adopted visco-plastic flow rule with the rate sensitive slip resistance displays a serious issue. The visco-plastic constitutive relation at the grain level (Eq. (12)) introduces an additional, artificial and unphysical rate sensitivity of the stress at constant structure. This rate sensitivity is an undesirable consequence of the adopted power-law flow rule used for the slip system selection. Consequently, the expression for the rate sensitivity of the material at constant structure contains an additional term arising due to the power-law flow rule:

$$m = \frac{\partial \ln|\boldsymbol{\sigma}|}{\partial \ln|\dot{\boldsymbol{\varepsilon}}|} = \underbrace{\frac{\partial \ln|\boldsymbol{\sigma}|}{\partial \ln|\dot{\boldsymbol{\varepsilon}}|} \left(\tau_c^{s,(r)} = \text{const} \right)}_{1/n} + \sum_r \sum_s \frac{\partial \ln|\boldsymbol{\sigma}|}{\partial \tau_c^{s,(r)}} \frac{\partial \tau_c^{s,(r)}}{\partial \ln|\dot{\boldsymbol{\varepsilon}}|} \left(\rho^{(r)} = \text{const} \right). \qquad (15)$$

Next, we consider two methods for removal of the artificially introduced rate sensitivity caused by the power-law flow rule [33, 73]: increase of rate exponent n and rate insensitive approach.
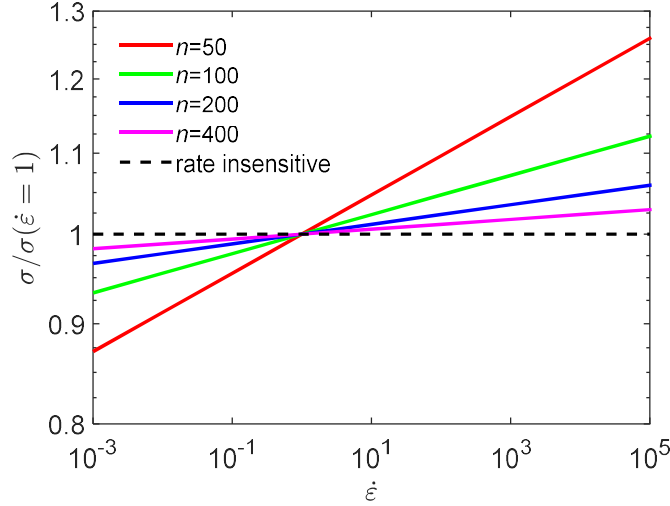
Fig. 1 Effect of the power-law exponent n on the mechanical response in simple compression as a function of imposed strain rate.

The rate sensitivity arising due to the adopted power-law relation at slip system level is inversely proportional to the rate exponent n. Therefore, increase of rate exponent n results in decrease of rate sensitivity and the limiting case when n goes to infinity ($n \to \infty$) results in a rate-insensitive response. However, with the increase of rate exponent n the visco-plastic

equation becomes very stiff and difficult to solve. Numerical considerations limit the rate exponent to values $n \leq 100$ [11, 55, 74]. Consequently, the rate sensitivity due to the power-law flow rule cannot be completely removed using this method. Considering that strain rates during the Taylor impact vary over several orders of magnitude the retained rate sensitivity when $n = 100$ is unacceptable. Fig. 1 shows the rate dependence of stress over a wide range of strain rates for different values of rate exponent. The magnitude of stress is normalized by the stress magnitude at reference strain rate of $1.0 \ s^{-1}$. Figure 1 indicates that the rate exponent in the range $n \leq 400$ results in artificial rate sensitivity affecting the stress. The effect is enhanced with the magnitude of applied strain rate.

In the second method, the reference shear rate, $\dot{\gamma}_0$, is set to the norm of the applied macroscopic strain rate, $\dot{\varepsilon} = \left| \dot{\boldsymbol{\varepsilon}}_{vp} \right| = \left| \langle \dot{\boldsymbol{\varepsilon}}_{vp}^{(r)} \rangle \right|$, where $\langle \ \ \rangle$ denotes volume average over all grains. By moving the reference shear rate to the left side of the expression for strain rate we get:

$$\dot{\boldsymbol{\varepsilon}}_{vp}^{(r)} / \left| \langle \dot{\boldsymbol{\varepsilon}}_{vp}^{(r)} \rangle \right| = \sum_s \left(\frac{\tau^{s,(r)}}{\tau_c^{s,(r)}} \right)^n \mathbf{m}^{s,(r)}. \tag{16}$$

The grain strain rate is thus normalized with the macroscopic strain rate magnitude. The magnitude of the grain stress is then affected only by the ratio of the grain strain rate magnitude and the macroscopic strain rate magnitude. Since the deviation of grain strain rates from the macroscopic strain rate is not large in BCC polycrystals, this effect on grain stress is fairly small. Consequently the effect of the grain strain rate magnitude on the grain stress is minimized and the direction of grain strain rate determines both the magnitude and the direction of the grain stress. Macroscopically, the rate sensitivity of stress due to the power-law flow rule is completely removed and magnitude of the applied strain rate has absolutely no effect on the macroscopic stress magnitude or direction. The rate insensitive approach has been used in numerous studies to

effectively remove the artificial rate sensitivity of macroscopic stress due to the power-law flow rule [33, 56, 75-80]. In the present study we adopt the rate insensitive approach for removal of unphysical rate sensitivity arising due to the power-law flow rule.

The expression for the rate sensitivity of the polycrystal with the rate insensitive visco-plastic flow rule is given by Eq. (14). Let us consider the effect of the integration procedure for the slip resistances on the material rate sensitivity in the context of implicit finite elements. In a large number of implicit finite element crystal plasticity codes the slip resistances and other state variables are held constant while the stress state is calculated implicitly [65, 67, 81-83]. Next the state variables are updated explicitly. Consequently, the expression for the slip resistance at the current time increment is defined solely in terms of the quantities from the previous time increment. As a result of the adopted integration procedure, the slip resistance at the current increment is independent on the currently applied visco-plastic strain rate. Consequently, the derivatives of slip resistance with the strain rate vanish, $\frac{\partial \tau_c^{s,(r)}}{\partial \ln|\dot{\varepsilon}|} = 0$, and the material behaves as completely rate insensitive regardless of the functional relation between the slip resistance and strain rate. The explicit integration of hardening variables would be suitable if used within an explicit finite element formulation. In implicit finite elements, the expression for slip resistance should be a function of the currently applied strain rate. While an improved explicit method, in which the slip resistances are first updated using the current strain rate and strain increment and subsequently used for the calculation of stress, would suffice, we adopt an implicit method for the evolution of slip resistances. The implicit integration of the slip resistances results in the most accurate solution. Shears at each slip system are integrated using an implicit Euler backward method, while the slip resistances are integrated as function of the shear using an implicit Crank–Nicolson method [84]. The slip resistance at the current increment is thus defined based on the

quantities from the current increment. Any change of the currently applied strain rate will result in the change of the slip resistance and thus the stress. Therefore, the rate sensitivity of stress at constant structure is solely defined through the rate dependence of the slip resistance which is the desired behavior. Also, note that the rate sensitivity of the stress due to rate sensitive structure evolution will be captured as well: $\sum_r \sum_s \sum_{s'} \frac{\partial \ln|\boldsymbol{\sigma}|}{\partial \tau_c^{s,(r)}} \frac{\partial \tau_c^{s,(r)}}{\partial \rho^{s',(r)}} \frac{\partial \rho^{s',(r)}}{\partial 1 \ |\dot{\boldsymbol{\varepsilon}}|}$.

In summary, in the adopted rate insensitive power-law flow rule with implicit integration of slip resistances, the rate sensitivity is defined by the functional relationship between slip resistance and strain rate. The rate exponent, n, does not affect the rate sensitivity and only determines the accuracy of the slip system selection.

2.2.2   Non-Schmid activation

Slip resistance, $\tau_c^{s,(r)}$, in Eq. (12) physically represents the resistance to motion of dislocation on slip system s while the stress projection in Eq. (12), $\tau^{s,(r)} = \mathbf{m}^{s,(r)} \cdot \boldsymbol{\sigma}'^{(r)}$, represents the shear stress in the dislocation glide plane and in the direction of slip. According to the Schmid law, the system becomes active when resolved shear stress reaches or exceeds the resistance of the dislocation motion [36]. However, the glide in BCC metals is known to violate the Schmid law. The non-Schmid effects on the dislocation motion are introduced by adding the contribution of the non-Schmid stress projections to the Schmid resolved shear stress [45, 49, 50, 85]:

$$\tau^{s,(r)} = \mathbf{m}^{s,(r)} \cdot \boldsymbol{\sigma}'^{(r)} + \mathbf{m}_{nS}^{s,(r)} \cdot \boldsymbol{\sigma}'^{(r)} = \mathbf{m}_{tot}^{s,(r)} \cdot \boldsymbol{\sigma}'^{(r)}, \tag{17}$$

where $\mathbf{m}_{tot}^{s,(r)} = \mathbf{m}^{s,(r)} + \mathbf{m}_{nS}^{s,(r)}$ and $\mathbf{m}_{nS}^{s,(r)}$ represents a non-Schmid tensor given as weighted sum of the following dyads:

$$\mathbf{m}_{nS}^{s,(r)} = c_1(\mathbf{t}^s \otimes \mathbf{b}^s) + c_2(\mathbf{t}^s \otimes \mathbf{n}^s) + c_3(\mathbf{n}^s \otimes \mathbf{n}^s) + c_4(\mathbf{t}^s \otimes \mathbf{t}^s) - (c_3 + c_4)(\mathbf{b}^s \otimes \mathbf{b}^s), \quad (18)$$

where $\mathbf{t}^s$ is unit vector in the glide plane perpendicular to the slip direction, $\mathbf{t}^s = \mathbf{n}^s \times \mathbf{b}^s$ and c_i are non-Schmid coefficients. The coefficients, c_i, for Ta at room temperature reported in [45] are used: $c_1 = -0.15, c_2 = 0.13, c_3 = -0.07, c_4 = 0.04$.

The non-Schmid effects are a complicated function of strain, strain rate and temperature [45, 86-88]. However, in the present study, we assume that the non-Schmid effects do not vary with strain rate due to lack of reliable experimental data in literature. An expression for non-Schmid tensor as a function of temperature and strain is given by [86, 88]:

$$\mathbf{m}_{nS}^{s,(r)}(T, \varepsilon_{eq}) = \exp\left(-\frac{\varepsilon_{eq}}{\varepsilon_0}\right)\left\{c_1(\mathbf{t}^s \otimes \mathbf{b}^s) + \left(1 - \frac{T-300}{T_c-300}\right)^{\frac{\text{sgn}(T_c-T)+1}{2}}[c_2(\mathbf{t}^s \otimes \mathbf{n}^s) + \right.$$

$$c_3(\mathbf{n}^s \otimes \mathbf{n}^s) + c_4(\mathbf{t}^s \otimes \mathbf{t}^s) - (c_3 + c_4)(\mathbf{b}^s \otimes \mathbf{b}^s)]\bigg\}, \qquad (19)$$

where ε_0 is a fitting constant and T_c is a temperature at which non-Schmid effects vanish. For simplicity, the same Eq. (19) is assumed to hold for both $\{1\bar{1}0\}\langle111\rangle$ and $\{11\bar{2}\}\langle111\rangle$ slip modes, although much more is known (by MD work) for the 110 systems. Temperature and strain dependence of non-Schmid effects given by Eq. (19) is an approximation based on the modeling efforts of other authors. We have conducted a detailed study of the effects of the fitting parameters in Eq. (19) on results. It was observed that strong presence of non-Schmid effects leads to unreasonable texture predictions at higher strains indicating that their effect likely quickly diminishes with strain which is in agreement with [86]. With straining of a crystal, dislocations accumulate and dislocation-dislocation interactions diminish the effect of non-Schmid stresses [86]. The constant ε_0 determining the rate at which non-Schmid effects decay with strain was thus set to 0.07. The temperature at which non-Schmid effects vanish, T_c, was approximated as 700 K for Ta [88]. The decay of non-Schmid effects with temperature was

approximated as linear. The chosen values for the fitting parameters in Eq. (19) are quite conservative, limiting the influence of the non-Schmid effects only to small strains where the non-Schmid effects are experimentally observed and measured.

2.3 Dislocation density-based hardening law

Hardening law defines the slip resistance and its evolution as a function of strain rate, temperature and accumulated shear. Phenomenological hardening laws are still predominantly used in crystal plasticity models [67, 89-91]. However, in the past decades several dislocation density-based hardening laws have been developed and successfully used for constitutive modeling of materials at different strain rates and temperatures. We adopt dislocation density-based hardening law developed by Beyerlein and Tome [56], which was previously used numerous times for modeling of constitutive behavior at high rates and temperatures. In what follows, the quantities from the start of the time increment will be explicitly denoted with superscript t, while all the other variables will be understood to be at the end of the time increment. The slip resistance of slip mode α is defined as [56]:

$$\tau_c^\alpha = \tau_0^\alpha + \tau_{for}^\alpha(\rho_{for}^\alpha) + \tau_{deb}^\alpha(\rho_{deb}). \tag{20}$$

where τ_0^α is an initial value of slip resistance, τ_{for}^α is a contribution to the slip resistance due to accumulation of forest dislocations, ρ_{for}^α, and τ_{deb}^α is a contribution to the slip resistance due to accumulation of debris dislocations, ρ_{deb}. The initial slip resistance, τ_0^α, represents resistance to intrinsic barriers (such as the Peierls stress), and it is dependent on strain rate and temperature [70-72, 92]. We use the following empirical function to model the dependence (no summation over repeated indices):

$$\tau_0^\alpha = G^\alpha + A^\alpha \exp\left(-\frac{T^t}{B^\alpha}\right)\left(\frac{\dot{\varepsilon}}{\dot{\varepsilon}_{ref}}\right)^{C^\alpha}, \tag{21}$$

where A^α, B^α, C^α, and G^α are constants, $\dot{\varepsilon} = \sqrt{2/3}|\dot{\boldsymbol{\varepsilon}}_{vp}|$ is macroscopic equivalent plastic strain rate, and T^t is temperature. $\dot{\varepsilon}_{ref} = 1\ s^{-1}$ is a reference strain rate, which normalizes the applied strain rate and makes the quantity raised to power dimensionless. As the temperature increases and the strain rate decreases, τ_0^α conveniently approaches the value of G^α for high temperature deformation under quasi-static conditions. Exponential decay of initial slip resistance with temperature is often reported in literature [50, 56, 70]. The power law dependence of initial slip resistance with strain rate provides the best fit to the initial yield stresses. The initial slip resistance does not evolve with strain.

The force required to move a dislocation increases with the increase of the dislocation density within the grain because the dislocations which intersect the slip plane of gliding dislocation act as barriers for the dislocation motion. The forest and debris contributions to slip resistance, dependent on forest (ρ_{for}^α) and debris (ρ_{deb}) dislocation densities, are given by (no summation over repeated indices):

$$\tau_{for}^\alpha = b^\alpha \mu \sqrt{\sum_{\alpha'} \chi^{\alpha\alpha'} \rho_{for}^{\alpha'}}, \tag{22}$$

$$\tau_{deb}^\alpha = -k_{deb}\mu b^\alpha \sqrt{\rho_{deb}} \log\left(b^\alpha \sqrt{\rho_{deb}}\right), \tag{23}$$

where b^α is the Burgers vector of mode α (which is $2.8579 \times 10^{-1}\ m$), $\chi^{\alpha\alpha}$ is the interaction between mode α and α', and k_{deb} is a material-independent constant determined to be 0.086, which ensures that the extended law Eq. (23) converges to the conventional law (i.e. Eq. (22))

when ρ_{deb} is sufficiently small. The interaction matrix is 0.9, if $\alpha = \alpha'$ and 0, if $\alpha \neq \alpha'$. Shear modulus, μ, is assumed to be a function of temperature [72]:

$$\mu(T^t) = \mu_0 - \frac{D}{\exp\left(\frac{T_0}{T^t}\right)-1}, \tag{24}$$

with $\mu_0 = 65250\ MPa$, $D = 380\ MPa$, and $T_0 = 40K$. Resistance to the short range obstacles (forest dislocations) was observed to be rate sensitive [29, 72]. However, considering that this dependence is fairly weak, it was neglected [56].

During deformation, the dislocation generation mechanisms increase the density of the forest dislocations while the temperature and rate sensitive dislocation removal mechanisms reduce it. As a result, the forest dislocation density quickly increases with strain and saturates at higher strains. A fraction of the removed dislocations become debris dislocations. The forest and debris dislocation densities are evolved with shear using the implicit Crank–Nicolson method [84] (no summation over repeated indices):

$$\rho_{for}^\alpha = \rho_{for}^{\alpha,t} + \frac{1}{2}\left[\frac{\partial \rho_{for}^\alpha}{\partial \gamma^\alpha}\left(\rho_{for}^{\alpha,t}\right) + \frac{\partial \rho_{for}^\alpha}{\partial \gamma^\alpha}\left(\rho_{for}^\alpha\right)\right]\Sigma_{s(\alpha)}|\dot{\gamma}^s|\Delta t, \tag{25}$$

$$\rho_{deb} = \rho_{deb}^t + \sqrt{\rho_{deb}}\,\Sigma_\alpha\left\{q^\alpha b^\alpha \frac{1}{2}\left[\frac{\partial \rho_{rem,for}^\alpha}{\partial \gamma^\alpha}\left(\rho_{for}^{\alpha,t}\right) + \frac{\partial \rho_{rem,for}^\alpha}{\partial \gamma^\alpha}\left(\rho_{for}^\alpha\right)\right]\Sigma_{s(\alpha)}|\dot{\gamma}^s|\Delta t\right\}, \tag{26}$$

where $s(\alpha)$ denotes a set of slip systems within slip mode α. The increments in shears on slip systems are calculated using the implicit Euler backward method. The rate of change of forest dislocations with shear strain on mode α is given by (no summation over repeated indices):

$$\frac{\partial \rho_{for}^\alpha}{\partial \gamma^\alpha} = \frac{\partial \rho_{gen,for}^\alpha}{\partial \gamma^\alpha} - \frac{\partial \rho_{rem,for}^\alpha}{\partial \gamma^\alpha} = k_1^\alpha\sqrt{\rho_{for}^\alpha} - k_2^\alpha(\dot{\varepsilon}, T^t)\rho_{for}^\alpha. \tag{27}$$

The coefficient k_1^α accounts for dislocation storage, while rate and temperature sensitive coefficient k_2^α accounts for the dislocation removal through thermally activated mechanisms and is given by (no summation over repeated indices):

$$k_2^\alpha = \frac{k_1^\alpha}{\sqrt{\sum_{\alpha'}(\chi^{-1})^{\alpha\alpha'}\left(\frac{\tau_{sat}^{\alpha'}}{b^{\alpha'}\mu}\right)^2}} ; \quad \tau_{sat}^{\alpha'} = \frac{D^\alpha(b^\alpha)^3 g^\alpha \mu}{D^\alpha(b^\alpha)^3 - kT^t \log\left(\frac{\dot{\varepsilon}}{\dot{\varepsilon}_0}\right)}, \tag{28}$$

where D^α is drag stress, g^α is the effective activation enthalpy, k is Boltzmann constant, and $\dot{\varepsilon}_0$ is the reference strain rate (taken to be $10^7 s^{-1}$) [56].

At constant structure, the rate and temperature sensitivity is defined by the resistance to intrinsic barriers, τ_0^α. During straining, the accumulation of dislocations reduces the relative contribution of τ_0^α to total slip resistance, τ_c^α. Consequently, the rate and temperature sensitivity will change during straining. Since the evolution of dislocation densities is strain rate and temperature dependent, attempting to capture the complicated strain rate sensitivity of metals such as Ta using the power-law exponent n (or m) would be inappropriate. Therefore, we aim at using the power-law, rate-insensitive visco-plastic flow rule in combination with the rate and temperature sensitive dislocation density-based hardening law, along with the initial slip resistance to describe the strain rate and temperature sensitive deformation of Ta. As a result, dislocation glide while the structure is evolving governs the material behavior. The next section presents homogenization procedure of the visco-plastic polycrystal with the implicit integration of slip resistances.

2.4   Self-consistent homogenization of visco-plastic polycrystal

Homogenization procedure links the response of the constituent grains to the macroscopic response of the polycrystal. Taylor full-constraint, self-consistent and grain cluster

homogenization schemes are most frequently used in the polycrystal plasticity models [67]. In the present model, the self-consistent homogenization method is used. In what follows, the self-consistent homogenization of the visco-plastic polycrystal proposed by Lebensohn and Tome is presented along with the necessary modifications for implicit slip resistance evolution [57]. The non-linear constitutive relation at the grain level is given by the visco-plastic equation with non-Schmid activation:

$$\dot{\boldsymbol{\varepsilon}}_{vp}^{(r)} = \dot{\gamma}_0 \sum_\alpha \left\{ \sum_{s(\alpha)} \left(\frac{\mathbf{m}_{tot}^{s,t,(r)} \cdot \boldsymbol{\sigma}'^{(r)}}{\tau_c^{\alpha,(r)}} \right)^n \mathbf{m}^{s,t,(r)} \right\}. \tag{29}$$

The rate exponent is set to $n = 20$. This value allows accurate selection of slip systems. Increasing the value of n does not change the results predicted by the rate insensitive visco-plastic flow rule in any appreciable way. Note that $\tau_c^{\alpha,(r)}$ is calculated at the end of the time increment, $t + \Delta t$, using the implicit integration rule. The increments in shear are calculated using the Euler backward method while the slip resistance is integrated as a function of the shear using the implicit Crank–Nicolson method [84]. Hence, $\tau_c^{\alpha,(r)}$ is a function of $\left| \dot{\gamma}^{s,(r)} \right|$, where the exact functional relationship is defined by the adopted hardening law. The linearized form of the constitutive relation at the grain level is:

$$\dot{\boldsymbol{\varepsilon}}_{vp}^{(r)} = \mathbf{M}^{(r)} \boldsymbol{\sigma}'^{(r)} + \dot{\boldsymbol{\varepsilon}}_{vp}^{0,(r)}, \tag{30}$$

where $\mathbf{M}^{(r)}$ and $\dot{\boldsymbol{\varepsilon}}_{vp}^{0,(r)}$ are visco-plastic compliance and back extrapolated strain rate [93]. For the affine linearization, the derivation of $\mathbf{M}^{(r)}$ and $\dot{\boldsymbol{\varepsilon}}_{vp}^{0,(r)}$ in the case of implicit hardening is given next.

First, it should be noted that slip resistance, $\tau_c^{\alpha,(r)}$, represents a function of deviatoric stress, defined by the hardening law, through the shear rates, which are functions of deviatoric stress. Next we introduce a function, $\mathbf{f}$, that maps deviatoric stress directly to visco-plastic strain rate:

$$\dot{\boldsymbol{\varepsilon}}_{vp}^{(r)}\left(\boldsymbol{\sigma}'^{(r)}, \tau_c^{\alpha,(r)}(\boldsymbol{\sigma}'^{(r)})\right) = \mathbf{f}(\boldsymbol{\sigma}'^{(r)}). \tag{31}$$

Taylor expansion of strain rate around reference stress value, $\boldsymbol{\sigma}_0'^{,(r)}$, is then given by:

$$\dot{\boldsymbol{\varepsilon}}_{vp}^{lin,(r)}(\boldsymbol{\sigma}'^{(r)}) = \mathbf{f}\left(\boldsymbol{\sigma}_0'^{(r)}\right) + \frac{\partial \mathbf{f}}{\partial \boldsymbol{\sigma}'^{(r)}}\bigg|_{\boldsymbol{\sigma}_0'^{(r)}}\left(\boldsymbol{\sigma}'^{(r)} - \boldsymbol{\sigma}_0'^{(r)}\right). \tag{32}$$

Then the grain compliance and back-extrapolated strain rate are:

$$\mathbf{M}^{(r)} = \frac{\partial \mathbf{f}}{\partial \boldsymbol{\sigma}'^{(r)}}\bigg|_{\boldsymbol{\sigma}_0'^{(r)}}, \tag{33}$$

$$\dot{\boldsymbol{\varepsilon}}_{vp}^{0,(r)} = \mathbf{f}\left(\boldsymbol{\sigma}_0'^{(r)}\right) - \frac{\partial \mathbf{f}}{\partial \boldsymbol{\sigma}'^{(r)}}\bigg|_{\boldsymbol{\sigma}_0'^{(r)}} \boldsymbol{\sigma}_0'^{(r)}. \tag{34}$$

The derivatives of the function, $\mathbf{f}$, w.r.t. deviatoric stress are given by:

$$\mathbf{M}^{(r)} = \frac{\partial \mathbf{f}}{\partial \boldsymbol{\sigma}'^{(r)}} = \underbrace{\frac{\partial \dot{\boldsymbol{\varepsilon}}_{vp}^{(r)}}{\partial \boldsymbol{\sigma}'^{(r)}}}_{\text{Term (1)}} + \underbrace{\frac{\partial \dot{\boldsymbol{\varepsilon}}_{vp}^{(r)}}{\partial \tau_c^{\alpha,(r)}}}_{\text{Term (2)}} \underbrace{\frac{\partial \tau_c^{\alpha,(r)}}{\partial \boldsymbol{\sigma}'^{(r)}}}_{\text{Term (3)}}. \tag{35}$$

The individual terms are provided in appendix A.

The macroscopic response of the homogenized linear polycrystal will also be linear:

$$\dot{\boldsymbol{\varepsilon}}_{vp} = \mathbf{M}\boldsymbol{\sigma}' + \dot{\boldsymbol{\varepsilon}}_{vp}^0, \tag{36}$$

where $\mathbf{M}$ and $\dot{\boldsymbol{\varepsilon}}_{vp}^0$ are macroscopic visco-plastic compliance and back extrapolated strain rate. In the case of self-consistent homogenization, every grain is treated as an ellipsoidal inhomogeneity within the effective medium, which has the properties of macroscopic homogenized polycrystal. The interaction law is given by [57, 94]:

$$\tilde{\dot{\boldsymbol{\varepsilon}}}_{vp}^{(r)} = -\widetilde{\mathbf{M}}\tilde{\boldsymbol{\sigma}}'^{(r)}, \tag{37}$$

where $\tilde{\dot{\boldsymbol{\varepsilon}}}_{vp}^{(r)}$ and $\tilde{\boldsymbol{\sigma}}'^{(r)}$ are strain rate and stress deviations with respect to macroscopic strain rate and stress, and $\widetilde{\mathbf{M}}$ is interaction tensor calculated as:

$$\widetilde{\mathbf{M}} = (\mathbf{I} - \mathbf{S})^{-1}\mathbf{S}\mathbf{M}, \tag{38}$$

where $\mathbf{S}$ is the Eshelby tensor. The macroscopic moduli are calculated as:

$$\mathbf{M} = \langle \mathbf{M}^{(r)}\mathbf{B}^{(r)} \rangle, \tag{39}$$

$$\dot{\boldsymbol{\varepsilon}}_{vp}^{0} = \langle \mathbf{M}^{(r)}\mathbf{b}^{(r)} + \dot{\boldsymbol{\varepsilon}}_{vp}^{0,(r)} \rangle, \tag{40}$$

where $\mathbf{B}^{(r)}$ and $\mathbf{b}^{(r)}$ are stress localization tensors given by [57]:

$$\mathbf{B}^{(r)} = \left(\mathbf{M}^{(r)} + \widetilde{\mathbf{M}}\right)^{-1}\left(\mathbf{M} + \widetilde{\mathbf{M}}\right), \tag{41}$$

$$\mathbf{b}^{(r)} = \left(\mathbf{M}^{(r)} + \widetilde{\mathbf{M}}\right)^{-1}\left(\dot{\boldsymbol{\varepsilon}}_{vp}^{0} - \dot{\boldsymbol{\varepsilon}}_{vp}^{0,(r)}\right). \tag{42}$$

The lattice spin is given by:

$$\mathbf{W}^{*(r)} = \mathbf{W} + \mathbf{\Pi}^{(r)} - \mathbf{W}^{p,(r)}, \tag{43}$$

where $\mathbf{W}$ is the macroscopic spin, $\mathbf{\Pi}^{(r)}$ is the spin associated with the ellipsoidal inclusion and $\mathbf{W}^{p,(r)}$ is the plastic spin calculated as:

$$\mathbf{W}^{p,(r)} = \sum_s \dot{\gamma}^{s,(r)}\boldsymbol{\alpha}^{s,t,(r)}. \tag{44}$$

The equations are solved numerically by adjusting the grain stresses, $\boldsymbol{\sigma}'^{(r)}$, iteratively using a fixed point method [57]. The procedure starts with the initial guess for grain stresses, $\boldsymbol{\sigma}'^{(r),0}$, obtained using a full constraint (Taylor) approximation ($\dot{\boldsymbol{\varepsilon}}_{vp}^{(r),0} = \dot{\boldsymbol{\varepsilon}}_{vp}$). Subsequently, grain compliances, $\mathbf{M}^{(r),0}$, and back-extrapolated strain rates, $\dot{\boldsymbol{\varepsilon}}_{vp}^{0,(r),0}$, can be calculated based on the

initial guess for stress, $\boldsymbol{\sigma}'^{(r),0}$. The last superscript on the right denotes the iteration number within the loop over grain stresses (0 for initial guess). Table 1 summarizes the procedure for the calculation of new guess for grain stresses ($\boldsymbol{\sigma}'^{(r),i+1}$) from the previous guess ($\boldsymbol{\sigma}'^{(r),i}$). The algorithm iteratively corrects the grain stresses until the convergence is reached. The tolerances for the convergence of grain stresses, tol, appearing in Table 1 are set to 0.001.

Table 1. Numerical procedure for the implicit hardening in VPSC – outer iterative loop for solving for stress in grains.

1) Solve the self-consistent equations and calculate macroscopic compliance and back-extrapolated strain rate:

$$\mathbf{M}^i = \langle \mathbf{M}^{(r),i} \mathbf{B}^{(r),i} \rangle$$
$$\dot{\boldsymbol{\varepsilon}}_{vp}^{0,i} = \langle \mathbf{M}^{(r),i} \mathbf{b}^{(r),i} + \dot{\boldsymbol{\varepsilon}}_{vp}^{0,(r),i} \rangle$$

2) Calculate macroscopic stress, $\boldsymbol{\sigma}'^i$, from the applied strain rate:

$$\boldsymbol{\sigma}'^i = \mathbf{M}^{i^{-1}} \left(\dot{\boldsymbol{\varepsilon}}_{vp} - \dot{\boldsymbol{\varepsilon}}_{vp}^{0,i} \right)$$

3) Solve the interaction equation for each grain and obtain a new guess for grain stresses, $\boldsymbol{\sigma}'^{(r),i+1}$:

$$\dot{\boldsymbol{\varepsilon}}_{vp} - \dot{\gamma}_0 \sum_s \left(\frac{\mathbf{m}_{tot}^{s,t,(r)} \cdot \boldsymbol{\sigma}'^{(r),i+1}}{\tau_c^{\alpha,(r),i+1}} \right)^n \mathbf{m}^{s,t,(r)} = -\widetilde{\mathbf{M}}^i \left(\boldsymbol{\sigma}'^i - \boldsymbol{\sigma}'^{(r),i+1} \right)$$

where slip resistance at the end of the time increment is also a function of the stress:
$$\tau_c^{\alpha,(r),i+1} = g\left(\left| \dot{\gamma}^s \left(\boldsymbol{\sigma}'^{(r),i+1}, \tau_c^{\alpha,(r),i+1} \left(\boldsymbol{\sigma}'^{(r),i+1} \right) \right) \right| \right).$$

4) Calculate the grain compliances, $\mathbf{M}^{(r),i+1}$, and back-extrapolated strain rates, $\dot{\boldsymbol{\varepsilon}}_{vp}^{0(r),i+1}$.

5) Test for convergence:

if $\left(\dfrac{\sqrt{\sum_r \sum_k \left(\sigma_k'^{(r),i+1} - \sigma_k'^{(r),i} \right)^2 w^{(r)}}}{|\boldsymbol{\sigma}'^i|} < \text{tol} \right)$ **and** $\left(\dfrac{|\boldsymbol{\sigma}'^i - \langle \boldsymbol{\sigma}'^{(r),i+1} \rangle|}{\frac{1}{2}|\boldsymbol{\sigma}'^i + \langle \boldsymbol{\sigma}'^{(r),i+1} \rangle|} < \text{tol} \right)$ **and**

$\left(\dfrac{|\dot{\boldsymbol{\varepsilon}}_{vp} - \langle \dot{\boldsymbol{\varepsilon}}_{vp}^{(r),i+1} \rangle|}{\frac{1}{2}|\dot{\boldsymbol{\varepsilon}}_{vp} + \langle \dot{\boldsymbol{\varepsilon}}_{vp}^{(r),i+1} \rangle|} < \text{tol} \right)$: **exit**

else: go to 1)

Table 2. Solution procedure for the interaction equation – inner iterative loop for solving for slip resistance in grains.

1) Solve the interaction equation for stress, $^{j+1}\boldsymbol{\sigma}'^{(r),i+1}$, using Newton's method: $$\dot{\boldsymbol{\varepsilon}}_{vp} - \dot{\gamma}_0 \sum_s \left(\frac{\mathbf{m}_{tot}^{s,t,(r)} \cdot {}^{j+1}\boldsymbol{\sigma}'^{(r),i+1}}{{}^{j}\tau_c^{\alpha,(r),i+1}} \right)^n \mathbf{m}^{s,t,(r)} = -\tilde{\mathbf{M}}^i \left(\boldsymbol{\sigma}'^i - {}^{j+1}\boldsymbol{\sigma}'^{(r),i+1} \right)$$
2) Calculate new guess for slip resistance $${}^{j+1}\tau_c^{\alpha,(r),i+1} = g\left(\left| \dot{\gamma}^s\left({}^{j+1}\boldsymbol{\sigma}'^{(r),i+1},\ {}^{j}\tau_c^{\alpha,(r),i+1} \right) \right| \right).$$
3) Test for convergence: $$\mathbf{if}\ \left(\sqrt{ \frac{ \sum_\alpha \left[{}^{j+1}\tau_c^{\alpha,(r),i+1} - {}^{j}\tau_c^{\alpha,(r),i+1} \right]^2 }{ \sum_\alpha \left[\frac{1}{2}{}^{j+1}\tau_c^{\alpha,(r),i+1} + \frac{1}{2}{}^{j}\tau_c^{\alpha,(r),i+1} \right]^2 } } < \text{tol} \right): \mathbf{exit}$$ $$\mathbf{else:\ go\ to}\ 1)$$

From the numerical procedure outlined in Table 1, it follows that for each iteration, i, of the outer loop over the grain stresses, the interaction equation (step 3 in Table 1) has to be solved numerically. In the case of explicit hardening, the interaction equation is simply solved for the grain stress using a Newton's method. On the other hand, in the case of implicit hardening the slip resistance becomes a function of the grain stress through the shear rates and the hardening law. We have found that a two level numerical procedure is the most stable and computationally efficient approach. The slip resistances, $\tau_c^{\alpha,(r)}$, are iteratively adjusted using a fixed point method. During each iteration over slip resistances the interaction equation has to be solved for stress using the Newton's method. The initial guess for the slip resistances is the value from a previous iteration of the outer loop for grain stresses, $^0\tau_c^{\alpha,(r),i}$. Here, the superscript on the left side denotes the iteration within the inner loop over slip resistances, while superscript on the right side denotes the outer iteration loop over grain stresses. Table 2 outlines the procedure for

the calculation of new guess for slip resistance, ${}^{j+1}\tau_c^{\alpha,(r),i+1}$, based on the previous guess, ${}^{j}\tau_c^{\alpha,(r),i+1}$. The tolerance for convergence of slip resistances, tol, in Table 2 is set to 0.0005.

2.5   Finite element implementation of VPSC implicit in hardening

The implementation of VPSC within implicit finite elements code ABAQUS STANDARD termed FE-VPSC follows the approach presented in [82]. At each integration point of the FE model, the stress rate in global frame, $\dot{\boldsymbol{\sigma}}$, is given by [11, 95]:

$$\dot{\boldsymbol{\sigma}} = \langle \dot{\boldsymbol{\sigma}}^{(r)} \rangle = \langle \mathbf{C}^{(r)} \dot{\boldsymbol{\varepsilon}}_{el}^{(r)} \rangle + \langle \mathbf{W}^{*(r)} \boldsymbol{\sigma}^{(r)} - \boldsymbol{\sigma}^{(r)} \mathbf{W}^{*(r)} \rangle, \tag{45}$$

where $\mathbf{C}^{(r)}$ is elastic stiffness of a grain r and $\dot{\boldsymbol{\varepsilon}}_{el}^{(r)}$ is the elastic strain rate within the grain r. The single crystal elastic constants for Ta are taken as $C_{11} = 267\ GPa$, $C_{12} = 161\ GPa$ and $C_{44} = 82.5\ GPa$. After the integration of the constitutive equation and decoupling of elastic and plastic properties [65, 66], we obtain:

$$\boldsymbol{\sigma} = \mathbf{C}^t \Delta \boldsymbol{\varepsilon}_{el} + \boldsymbol{\sigma}^{t,rot}, \tag{46}$$

where $\mathbf{C}^t$ is the self-consistent estimate of elastic stiffness and $\boldsymbol{\sigma}^{t,rot}$ is stress from the beginning of the time increment rotated to the current configuration given by:

$$\boldsymbol{\sigma}^{t,rot} = \langle \Delta \mathbf{R}^{*t,(r)} \boldsymbol{\sigma}^{t,(r)} \Delta \mathbf{R}^{*t,(r)^T} \rangle. \tag{47}$$

The incremental rotation, $\Delta \mathbf{R}^{*t,(r)}$, is calculated as $\Delta \mathbf{R}^{*t,(r)} = \left(\mathbf{I} - \beta \mathbf{W}^{*t,(r)} \Delta t\right)^{-1} \left(\mathbf{I} + (1-\beta)\mathbf{W}^{*t,(r)} \Delta t\right)$, with $\beta = 0.5$ [96]. The elastic increment is given by:

$$\Delta \boldsymbol{\varepsilon}_{el} = \Delta \boldsymbol{\varepsilon} - \dot{\boldsymbol{\varepsilon}}_{vp} \Delta t, \tag{48}$$

where $\Delta \boldsymbol{\varepsilon}$ is the total strain increment and Δt is the time increment. Equation (46) is decomposed into deviatoric and hydrostatic parts, which can be expressed in the vector form as:

$$\mathbf{s} - \mathbf{s}^{t,rot} - \mathbf{C}'^{t}_{5\times6}\big(\Delta\mathbf{e} - \mathbf{P}_{6\times5}\dot{\mathbf{e}}_{vp}\Delta t\big) = \mathbf{0}, \tag{49}$$

$$\sigma_m - \sigma_m^t - \frac{1}{3}\text{tr}\big[\mathbf{C}^t_{6\times6}\big(\Delta\mathbf{e} - \mathbf{P}_{6\times5}\dot{\mathbf{e}}_{vp}\Delta t\big)\big] = 0 \tag{50}$$

where $\mathbf{s}$, $\mathbf{s}^{t,rot}$, $\dot{\mathbf{e}}_{vp}$, and $\Delta\mathbf{e}$ are the vector representation of tensors $\boldsymbol{\sigma}'$, $\boldsymbol{\sigma}'^{t,rot}$, $\dot{\boldsymbol{\varepsilon}}_{vp}$ and $\Delta\boldsymbol{\varepsilon}$ as:

$$\mathbf{s} = \begin{Bmatrix} \sigma'_{11} \\ \sigma'_{22} \\ \sigma'_{12} \\ \sigma'_{13} \\ \sigma'_{23} \end{Bmatrix}, \mathbf{s}^{t,rot} = \begin{Bmatrix} \sigma'^{t,rot}_{11} \\ \sigma'^{t,rot}_{22} \\ \sigma'^{t,rot}_{12} \\ \sigma'^{t,rot}_{13} \\ \sigma'^{t,rot}_{23} \end{Bmatrix}, \dot{\mathbf{e}}_{vp} = \begin{Bmatrix} \dot{\varepsilon}_{vp,11} \\ \dot{\varepsilon}_{vp,22} \\ \dot{\varepsilon}_{vp,12} \\ \dot{\varepsilon}_{vp,13} \\ \dot{\varepsilon}_{vp,23} \end{Bmatrix}, \Delta\mathbf{e} = \begin{Bmatrix} \Delta\varepsilon_{11} \\ \Delta\varepsilon_{22} \\ \Delta\varepsilon_{33} \\ 2\Delta\varepsilon_{12} \\ 2\Delta\varepsilon_{13} \\ 2\Delta\varepsilon_{23} \end{Bmatrix}. \tag{51}$$

$\mathbf{P}_{6\times5}$ is a transformation matrix that transforms the five-dimensional vector $\dot{\mathbf{e}}_{vp}$ into a six-dimensional representation compatible with $\Delta\mathbf{e}$ [97, 98]. The $\mathbf{C}'^{t}_{5\times6}$ matrix representation of elastic stiffness produces a five-dimensional deviatoric stress vector when multiplied with six-dimensional strain increment vector $\Delta\mathbf{e}$. It is a matrix representation of tensor $C'^{t}_{ijkl} = C^t_{ijkl} - \frac{1}{3}C^t_{mnkl}\delta_{mn}\delta_{ij}$ with the third row removed. σ_m and σ_m^t are the hydrostatic portions of the stress tensors $\boldsymbol{\sigma}$ and $\boldsymbol{\sigma}^{t,rot}$, and $\mathbf{C}^t_{6\times6}$ is the matrix representation of the elastic stiffness tensor consistent with the definition of strain increment $\Delta\mathbf{e}$.

For a given strain increment, $\Delta\mathbf{e}$, Eq. (49) can be solved for visco-plastic strain rate, $\dot{\mathbf{e}}_{vp}$, using Newton's method. The residual and its Jacobian are:

$$\mathbf{F}\big(\dot{\mathbf{e}}_{vp}\big) = \mathbf{s}\big(\dot{\mathbf{e}}_{vp}\big) - \mathbf{s}^{t,rot} - \mathbf{C}'^{t}_{5\times6}\big(\Delta\mathbf{e} - \mathbf{P}_{6\times5}\dot{\mathbf{e}}_{vp}\Delta t\big) = \mathbf{0}, \tag{52}$$

$$\frac{\partial\mathbf{F}}{\partial\dot{\mathbf{e}}_{vp}} = \frac{\partial\mathbf{s}}{\partial\dot{\mathbf{e}}_{vp}} + \mathbf{C}'^{t}_{5\times6}\mathbf{P}_{6\times5}\Delta t, \tag{53}$$

where the derivative $\frac{\partial\mathbf{s}}{\partial\dot{\mathbf{e}}_{vp}}$ can be approximated as $\frac{\partial\mathbf{s}}{\partial\dot{\mathbf{e}}_{vp}} \approx \mathbf{M}^{-1}$ [65, 83]. The Newton iterations are facilitated using:

$$\dot{\mathbf{e}}_{vp}^{i+1} = \dot{\mathbf{e}}_{vp}^{i} - \left(\left.\frac{\partial \mathbf{F}}{\partial \dot{\mathbf{e}}_{vp}}\right|_{\dot{\mathbf{e}}_{vp}^{i}}\right)^{-1} \mathbf{F}(\dot{\mathbf{e}}_{vp}^{i}). \tag{54}$$

The iterative procedure over $\dot{\mathbf{e}}_{vp}^{i}$ terminates when the norm of the residual becomes smaller than the tolerance conveniently defined with respect to the current von Mises stress: $\left|\mathbf{F}(\dot{\mathbf{e}}_{vp}^{i})\right| < 0.001\sigma_{vM}$. The deviatoric stress, $\mathbf{s}$, is available once the visco-plastic strain rate has converged and the hydrostatic portion, σ_m, can be calculated from Eq. (50).

In addition to the total stress at the end of the time increment, $\boldsymbol{\sigma}$, the FE solver also requires the Jacobian matrix obtained by differentiating the constitutive equation, i.e. Eq. (46):

$$\left(\frac{\partial \boldsymbol{\sigma}}{\partial \Delta \boldsymbol{\varepsilon}}\right)_{6\times6} = \left[\mathbf{I}_{6\times6} + \mathbf{C}_{6\times6}^{t}\mathbf{P}_{6\times5}\mathbf{M}\left(\frac{\partial \mathbf{s}}{\partial \boldsymbol{\sigma}}\right)_{5\times6}\Delta t\right]^{-1}\mathbf{C}_{6\times6}^{t}, \tag{55}$$

where $\left(\frac{\partial \mathbf{s}}{\partial \boldsymbol{\sigma}}\right)_{5\times6}$ is the derivative of five-dimensional deviatoric stress with respect to the six independent components of stress tensor ordered analogously to the strain increment [82].

After the convergence of Newton's method, the texture is updated for plastic spin and inclusion spin. In addition, the shape of the ellipsoid is updated for the applied plastic deformation. Note that the texture and ellipsoid are already rotated for the macroscopic spin provided by the FE solver at the beginning of the time increment to ensure that they are in the same configuration as the strain increment and other quantities.

As was noted before, in a large number of implicit finite element implementations of crystal plasticity codes the state variables are held constant while the stress is updated implicitly [65, 67, 82, 83]. The state variables are subsequently updated explicitly. Consequently, the magnitude of the current strain increment does not affect the current slip resistances and thus does not influence the current deviatoric stress magnitude, $\frac{\partial |\boldsymbol{\sigma}\prime|}{\partial |\Delta\boldsymbol{\varepsilon}|} = \sum_r \sum_s \frac{\partial |\boldsymbol{\sigma}\prime|}{\partial \tau_c^{s,(r),expl}} \frac{\partial \tau_c^{s,(r),expl}}{\partial |\Delta\boldsymbol{\varepsilon}|} = 0.$

Therefore, the stress magnitude cannot increase regardless of the magnitude or direction of currently applied strain increment since it is bound to a constant yield surface defined by the slip resistances from the beginning of the time increment. There can be no loading and the stress can only move along the constant yield surface (neutral loading) or to the interior of the yield surface (unloading) [99]. On the other hand, the implicit evolution of slip resistances employed here causes the expansion of the yield surface with the increase of the currently applied strain increment and thus an increase in the stress magnitude. It should also be noted that an explicit evolution of the slip resistances before the evaluation of stress would achieve similar results as the implicit integration.

2.6   Conversion of plastic work to heat

During plastic deformation there is conversion of plastic work to heat known as adiabatic heating, which causes an increase in the sample temperature. At low strain rates (below $10^{-3} \ s^{-1}$) the generation of heat is small since any heat is quickly conducted away from the specimen. Therefore, behavior is approximately isothermal. At higher strain rates (above $10 \ s^{-1}$) there is no sufficient time for the generated heat to be conducted away. Therefore almost all plastic work is transferred into heat, and the conditions are adiabatic. For the strain rates between these two limiting values, the conditions are in-between adiabatic and isothermal. In what follows we define the expressions for the calculation of temperature increase due to adiabatic heating during high strain rate compression and impact simulations.

The governing equation for calculating the temperature at the end of the time increment, T, during compression test is given by the explicit Euler forward update [100]:

$$T = T^t + \eta(\dot{\varepsilon})\xi \frac{\dot{W}^p}{\rho C_p}\Delta t, \tag{56}$$

where ξ is the fraction of plastic work converted into heat, ρ is density of Ta (taken for pure Ta as $16640\ kg/m^3$ [30]), and C_p is the specific heat given as a function of temperature for Ta [72]:

$$C_p = A_0 + A_1 T^t + \frac{A_2}{(T^t)^2}, \tag{57}$$

with $A_0 = 145.5\ \frac{J}{kgK}$, $A_1 = 0.009544\ \frac{J}{kgK^2}$, and $A_2 = -68900\ \frac{J}{kg}K$. $\dot{W}^p$ is the plastic work rate calculated as:

$$\dot{W}^p = \boldsymbol{\sigma}' \cdot \dot{\boldsymbol{\varepsilon}}_{vp}. \tag{58}$$

η is the adiabatic correction factor and represents a fraction of the heat retained within the compression specimen for the rates between $10^{-3}\ s^{-1}$ and $10\ s^{-1}$ when the compression test conditions are neither isothermal nor adiabatic [100]. It is calculated as:

$$\eta = \begin{cases} 0, \text{if } \dot{\varepsilon} < 10^{-3}s^{-1} \\ 0.25(\log \dot{\varepsilon} + 3), \text{if } 10s^{-1} < \dot{\varepsilon} < 10^{-3}s^{-1}. \\ 1, \text{if } \dot{\varepsilon} > 10s^{-1} \end{cases} \tag{59}$$

The fraction of plastic work converted into heat, ξ, is usually taken between 0.8 and 0.95. However, ξ varies with the material [101], and for Ta this value was measured to be close to 1.0 [102, 103], which is what we used in all the simulations.

In the impact tests, the strain rates are well above $10\ s^{-1}$, requiring the consideration of the adiabatic conditions (Eq. (56)). In the case of forming processes where strain rates are such that the process cannot be considered neither adiabatic nor isothermal, it is recommended that the heat conduction be considered in coupled temperature-displacement FE analysis.

3 Remeshing and interpolation procedures for state variables including texture

During the FE simulations to large strains, the elements can become severely distorted, requiring remeshing. When the ratio of the longest edge to the shortest edge of the most distorted element reaches a value 7, the remeshing is triggered. The deformed part is imported as geometry into ABAQUS/CAE and completely remeshed using the ABAQUS Mesh module. After remeshing all variables defining the current state of the part require mapping/interpolation. Most of the state variables can be interpolated linearly except for the variables defining grain orientations. The latter will be interpolated using the spherical linear interpolation (Slerp) in the space of quaternions. Additionally, the deformation gradients, because they consist of both rotation and deformation, will be interpolated using a combination of the Slerp method and the linear shape functions method. In what follows, we describe the adopted interpolation procedures for field variables, grain orientations, and deformation gradients.

Fields of strain, stress, temperature, velocity, slip resistance within each grain, and dislocation densities within each grain are interpolated linearly using the finite element shape functions [104]. Shape functions of linear 3D elements can be viewed as a linear interpolation technique that can be easily applied to quantities available at both nodes and integration points. Figure 2 illustrates the interpolation procedure in the Taylor impact simulation for the velocity component v_z, which is parallel to the cylinder axis. For a given integration point or node of the new mesh, the algorithm is:

1. Determine the element of the old mesh to which the point belongs and calculate natural coordinates, (g, h, r), of the point within the element.

2. Interpolate the variable value at the point of new mesh using nodal variables of the old mesh, x^i, and shape functions, $N^i(g, h, r)$,:

$$x = \mathbf{N} \cdot \mathbf{x}. \tag{60}$$
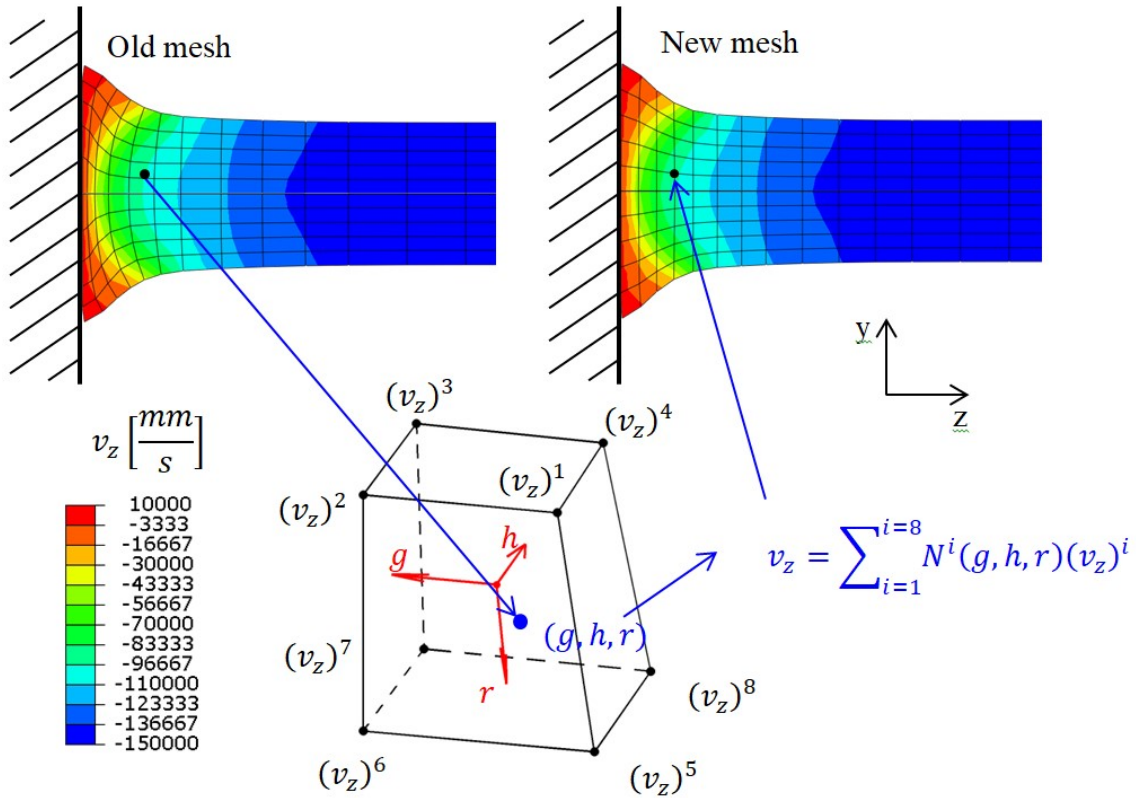
Fig. 2. Schematic showing the interpolation procedure, based on the finite element shape functions, for the calculation of the velocity component v_z at a point of new mesh using the velocity components $(v_z)^i$ at the element vertices from the old mesh. The contour plots verify accuracy of the interpolated field over the new mesh against the original field from the old mesh.

Figure 2 also shows the old (deformed) and new mesh upon remeshing, along with the contours of velocity fields. The similarity between the fields in two meshes demonstrates the accuracy of the interpolation procedure for field variables. Due to interpolation and remeshing the stress equilibrium will be violated at the macro (FEA) and meso (VPSC) level. However, considering the similarity between meshes before and after remeshing the interpolated state is very close to the equilibrium. The equilibrium is enforced in the first increment after remeshing. The difference between equilibrated stress fields before and after remeshing is negligible. Some small discrepancy in the equivalent plastic strain rate fields before and after remeshing is

observed for several nodes close to the center of the foot, which can be expected considering a very high gradient of the equivalent plastic strain rate in that region.

The crystal orientations of grains are interpolated using the spherical linear interpolation (Slerp) algorithm in the quaternion space [105, 106]. Expression for spherical linear interpolation between two quaternions, $\mathbf{q}_1$ and $\mathbf{q}_2$, with parameter u going from 0 to 1 is given by:

$$\text{Slerp}(\mathbf{q}_1, \mathbf{q}_2; u) = \frac{\sin(1-u)\theta}{\sin\theta}\mathbf{q}_1 + \frac{\sin u\theta}{\sin\theta}\mathbf{q}_2 \qquad (61)$$

where $\mathbf{q}_1 \cdot \mathbf{q}_2 = \cos\theta$. Since the orientation of each grain within the polycrystal is interpolated separately, texture of the polycrystal is also indirectly interpolated. Figure 3 shows three textures obtained by interpolating orientation of each grain between its initial orientation and final orientation after compression to a high strain, for three different values of the parameter u. The Slerp method imposes two constraints: (1) textures must be represented by the same number of discrete orientations and (2) pairing between the orientations from the discrete sets must be assumed. Due to these limitations the Slerp method is limited when compared to other probability distribution interpolation techniques [107-112]. However, it is quite convenient for the interpolation between textures of two polycrystals with the same initial texture after similar strain history. Other texture interpolation techniques are not investigated here since they would likely yield similar results considering that the texture does not vary appreciably within one element. In addition, there is an additional complication associated with the texture interpolation methods that are not based on the direct pairing of discrete orientations. Once the texture is interpolated and represented by the discrete set of orientations, the interpolation of grain properties becomes an issue since there is no longer a natural pairing between the grains, which is preserved with the Slerp method.
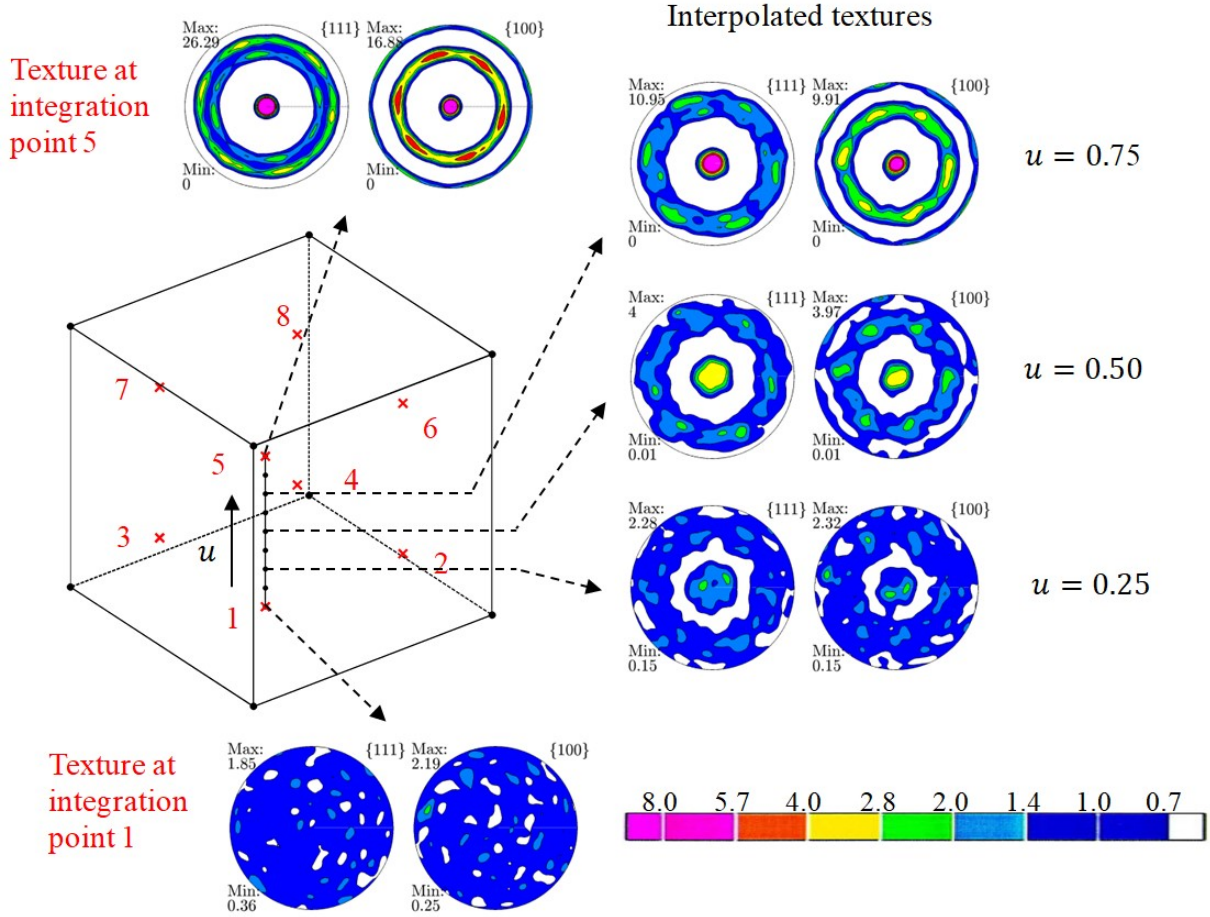
Fig. 3. Texture interpolation between two integration points using the Slerp algorithm. Three interpolated textures weighted between the two textures used in the interpolation are shown.

The average grain shape is defined by the deformation gradient tensor. The interpolation of deformation gradient follows the algorithm given in [105]. The deformation gradient, **F**, is decomposed into a stretching tensor, **U**, and a rotation tensor, **R**, using the polar decomposition:

$$\mathbf{F} = \mathbf{R}\mathbf{U}. \tag{62}$$

Each component of the stretch tensor, **U**, is independently interpolated using shape functions as described above. The rotation tensor, **R**, represents pure rotation and is thus transferred to quaternion form and interpolated using the Slerp algorithm.

4   Material and model calibration for strain rate and temperature sensitive deformation

The hardening parameters for commercially pure Ta were calibrated on a set of stress strain curves reported in [30, 72, 113]. The Ta plate was prepared by melting ingots with the following composition (in weight ppm): C 12, O<50, N<10, H<5, W 60, Nb 250, and Ta balance [113]. The quasi-static and dynamic compression tests were performed at various temperatures on the cylindrical samples machined from the Ta plate. The cylindrical specimens had their axes in the through-thickness (TT) direction. Orientation distribution function (ODF) of the plate was derived from the experimental X-ray pole figures. {111} and {100}, pole figures of the derived ODF, are plotted on Fig. 4. The ODF was then approximated with 200 weighted orientations for simulations (Fig. 4b).
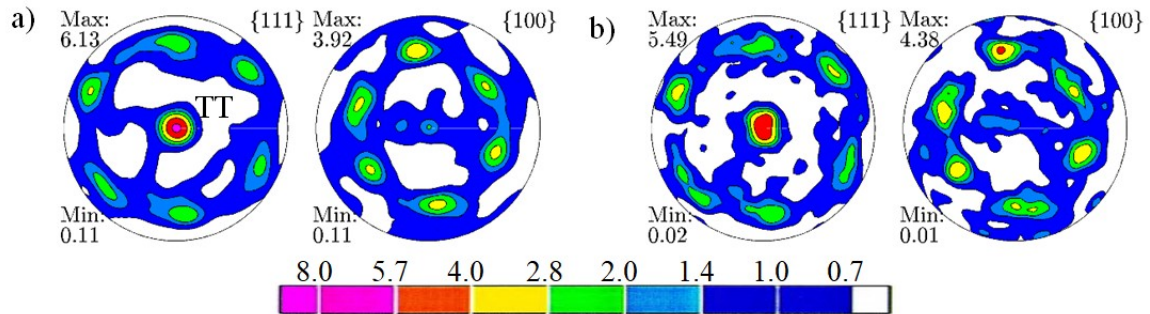
Fig. 4. {111} and {100} equal area projection-type pole figures showing initial texture of the tantalum plate: (a) measured data and (b) representation of the measured data using 200 weighted orientations for simulations. TT direction of the plate is in the center of the pole figures.

In the simulations, we assume grains are initially spherical and deform by $\{1\bar{1}0\}\langle111\rangle$ and $\{11\bar{2}\}\langle111\rangle$ slip modes. The initial slip resistance and hardening parameters of both modes are assumed to be the same. Constants for initial slip resistance are determined first from the initial yield stresses at different temperatures and strain rates (Table 3). Next, the hardening parameters are calibrated and presented in Table 3. The predictions of the model are compared to the experimental stress strain curves in Fig. 5, and good agreement is achieved.

Table 3. Calibrated parameters of the dislocation density-based hardening model for tantalum.

	$\alpha = 1, \{1\bar{1}0\}\langle 111 \rangle$ and $\alpha = 2, \{11\bar{2}\}\langle 111 \rangle$
$k_1^\alpha [m]$	3.75×10^7
g^α	0.005
$D^\alpha [MPa]$	1200
q^α	5
$A^\alpha [MPa]$	233.93
$B^\alpha [K]$	209.03
C^α	0.14
$G^\alpha [MPa]$	71.25

Fig. 5. Comparison between experimental (full line) and predicted (dashed line) compressive true stress-true strain curves for tantalum in the TT direction at various strain rates and temperatures.

5 Verification of VPSC with implicit hardening and application of FE-VPSC to impact

We begin by presenting the results, verifying the implicit hardening model within VPSC, and then present the predictions of the Taylor impact simulation by FE-VPSC.

5.1   Verification of the implicit hardening implementation within VPSC

Predictions of the VPSC model with implicit and explicit hardening are compared for the case of room temperature, quasi-static deformation to a true strain of 0.4. The strain increment was set to 0.001. Figure 6a compares the stress strain curves, while Fig. 6b compares the deformed textures. Good agreement is achieved, which is expected for any sufficiently low strain increment. Figure 7 shows the influence of the strain increment on the results of the implicit hardening VPSC model. The decay in non-Schmid effects with strain is removed so that the differences in hardening behavior can be better observed. Negligible dependence of the stress-strain response on the magnitude of strain increment is observed. This is caused predominantly by the implicit updating of the dislocation densities (Eqs. (25) and (26)).
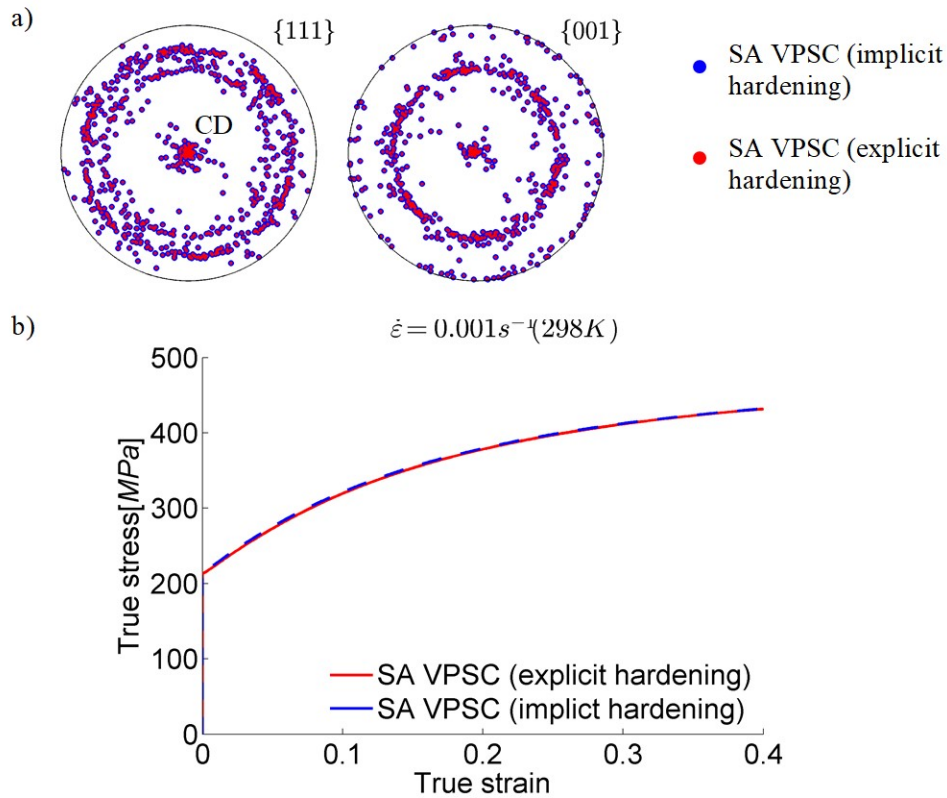
Fig. 6. Comparison of (a) texture evolution and (b) true stress-true strain response, calculated using explicit and implicit implementation of the dislocation density-based hardening law within VPSC for simple compression at room temperature under a strain rate of $\dot{\varepsilon} = 0.001\ s^{-1}$.

$Implicit; \dot{\varepsilon} = 0.001 s^{-1} (298K)$
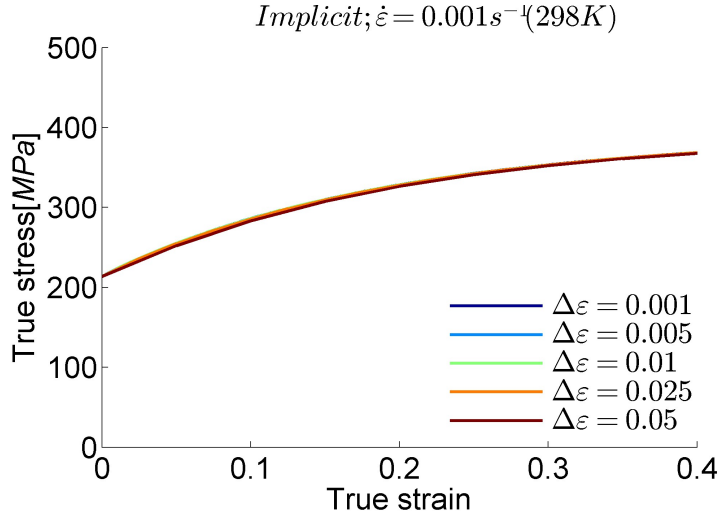
Fig. 7. Effect of the strain increment size used in predicting compressive true stress-true strain response of tantalum at room temperature under a strain rate of $\dot{\varepsilon} = 0.001 \ s^{-1}$ with implicit hardening implementation in VPSC.

5.2   Taylor impact simulations

We use the FE-VPSC model calibrated for Ta to simulate the Taylor impact test of Ta cylinder reported in [20, 30]. Taylor impact specimens were made from the Ta plate with the cylinder axis parallel to one of the in-plane directions. The length of the cylinder was 38.1 mm and the diameter was 7.62 mm, while the impact velocity was 175 m/s. Geometric profiles of the cylinder after testing were reported for three different tests. In addition, texture was measured using X-rays at several axial positions for one of the cylinders after testing.

Simulation setup is given on Fig. 8a. ABAQUS STANDARD dynamic FE code is used. Due to symmetry of the process, only ¼ of the cylinder is modeled and meshed with 384 full integration brick elements (C3D8 – continuum 3D eight nodal). The symmetry boundary conditions are applied to the faces, along which cuts are made. A mesh sensitivity study was performed to exclude any appreciable effect of the mesh and element size on the results. Further refinement of the mesh leaves the results unchanged and only increases the computational time involved. The anvil target is modeled as a discrete rigid surface, and the friction between the

cylinder and anvil is neglected. Consistent with the experiment, the initial velocity of the cylinder was 175 m/s. The initial texture embedded at each integration point plotted in the global frame of the FE model is given on Fig. 8b.
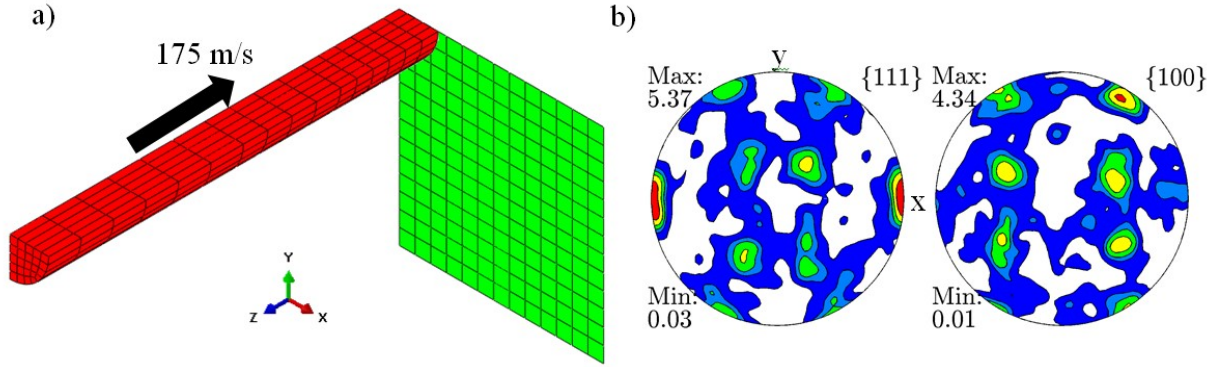
Fig. 8. (a) Finite element model of the Taylor impact test and (b) the initial texture of tantalum plotted in the global frame of the FE model (this texture is the same as the one in Fig. 3b but rotated to the global frame). The texture in (b) is embedded and evolved during deformation at each finite element integration point.

The equivalent plastic strain rate, $\dot{\varepsilon}_{eq}$, fields developing in the cylinder during the simulation are shown in Fig. 9. Since the strain rate changes dramatically over the course of the simulation, it is not possible to facilitate the comparison between the distributions of equivalent plastic strain rate in the plots using the same scale. Hence, the fields were normalized with the maximal value of $\dot{\varepsilon}_{eq}$ present in the cylinder at that time. At the beginning of the impact, the highest $\dot{\varepsilon}_{eq}$ develops at the center of the foot and reaches values above $90000 \ s^{-1}$. As the deformation progresses, the $\dot{\varepsilon}_{eq}$ at the center of the foot decreases, and regions that are away from the foot and cylinder axis start deforming. Finally, at the end of the simulation, the plastic wave propagates toward the tail of the cylinder.

Figure 10 compares the side profile and footprint of the simulated cylinder after the impact with photographs of the cylinder geometry after the test. The plastic deformation is highly heterogeneous, with the highest equivalent plastic strains occurring at the center of the foot and

reaching values above 3.6. On the other hand, the tail of the cylinder is not experiencing any plastic deformation. In addition, the shape of the footprint is ellipsoidal, indicating that the deformation in lateral directions is also non-uniform.

$t = 0\ s$
$\max(\dot{\varepsilon}_{eq}) = 0\ s^{-1}$

$t = 6.76 \times 10^{-5}\ s$
$\max(\dot{\varepsilon}_{eq}) = 14662\ s^{-1}$

$t = 2.24 \times 10^{-5}\ s$
$\max(\dot{\varepsilon}_{eq}) = 65469\ s^{-1}$

$t = 9.00 \times 10^{-5}\ s$
$\max(\dot{\varepsilon}_{eq}) = 1872\ s^{-1}$

$t = 4.52 \times 10^{-5}\ s$
$\max(\dot{\varepsilon}_{eq}) = 41308\ s^{-1}$

$t = 12.60 \times 10^{-5}\ s$
$\max(\dot{\varepsilon}_{eq}) = 0\ s^{-1}$

$\dfrac{\dot{\varepsilon}_{eq}}{\max(\dot{\varepsilon}_{eq})}$ 0.00 0.08 0.17 0.25 0.33 0.42 0.5 0.58 0.67 0.75 0.83 0.92 1.0
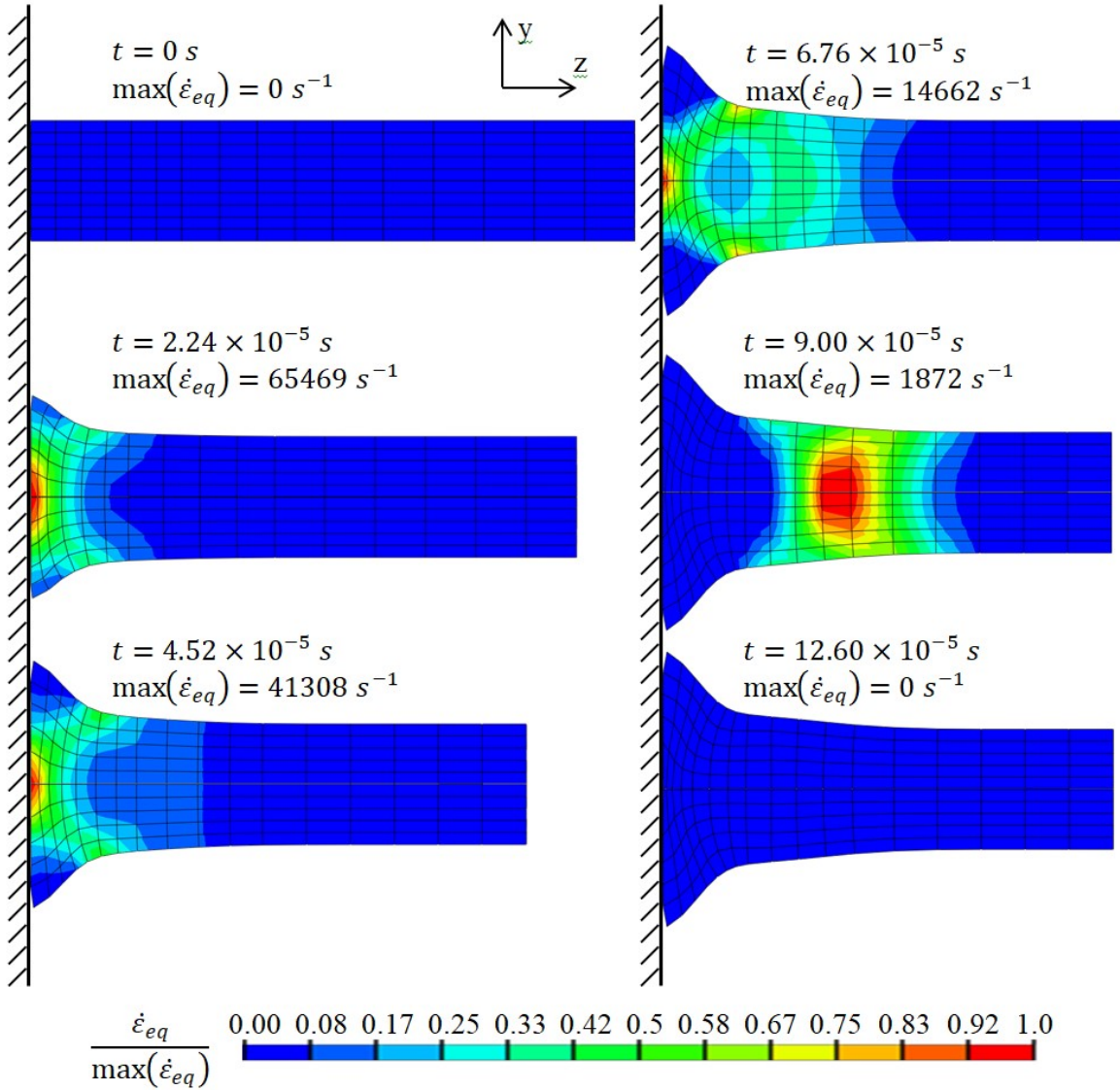
Fig. 9. Evolution of equivalent plastic strain rate field during the impact simulation at instants of time *t*. The strain rates used for the normalization are indicated in the figure for each contour plot.

The deformed major and minor profiles are compared with the experimental measurements on Fig. 11a. Radial strains are calculated based on the profiles as $\varepsilon_r = \ln\dfrac{d}{d_0}$ and plotted as a

function of axial position on Fig. 11b. The difference between major and minor profiles is quantified with the R-value, calculated as $\varepsilon_r^{major}/\varepsilon_r^{minor}$. The results are plotted in Fig. 11c as a function of axial position. The observed difference between major and minor profiles is driven by the initial texture and subsequent texture evolution. The TT is the hard direction, which is along the minor profile of the cylinder. Due to the texture evolution, the anisotropy of the material changes, and at higher strains, the TT direction actually becomes the softest.
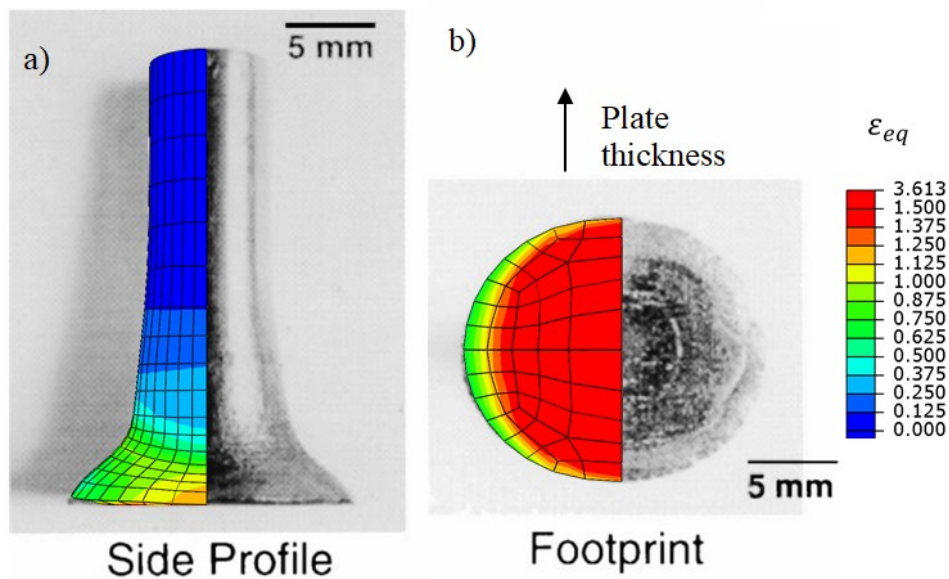
Fig. 10. Comparison of measured and predicted cylinder geometry after the test with the superimposed contours of equivalent plastic strain over the latter.

Figure 12 compares the predicted and measured footprints. The initial footprint is plotted with dashed line as a reference to easier assess the amount of plastic deformation at the foot.

The large heterogeneity of plastic distortions in the axial direction induces a variation of microstructural evolution. The texture variation along the axis of the cylinder is compared with the experimental measurements at four axial locations: 9.2 mm, 6.5 mm, 1.6 mm, and 0.5 mm from the impact surface in Fig. 13. At location furthest away from the foot, the texture resembles the initial one since plastic deformation is negligible. As we move toward the foot we see devel-
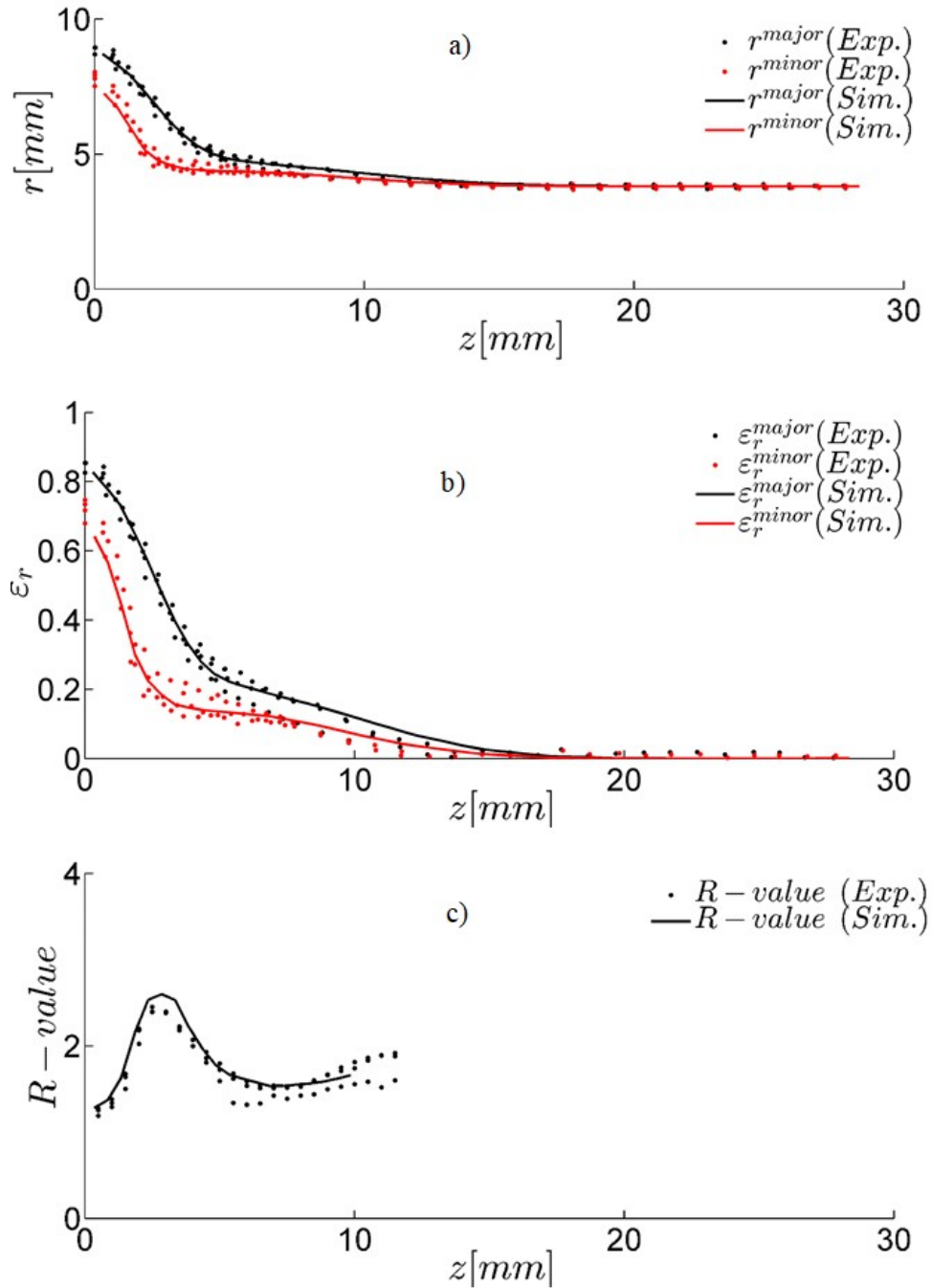
Fig. 11. Predicted by FE-VPSC (solid line) and experimentally measured (dots) post-test geometrical characteristics of the cylinder - (a) radius, (b) radial strains, and (c) *R*-values - plotted as functions of axial distance from the foot, *z*.

opment of BCC compression texture with {111} and {001} parallel to the compression direction

[114, 115]. Agreement of the main texture features between simulation and experiment is good.

However, it is noted that simulated textures close to the foot display very high intensities. This is

likely caused by the fact that in the VPSC model, each grain is represented with only one orientation: uniform within the grain domain, which causes the predicted textures to be consistently stronger than the measured ones [9, 116]. Accounting for intragranular misorientation distributions using a second order moments within VPSC is aimed at relaxing typically predicted texture intensities by VPSC [117, 118].
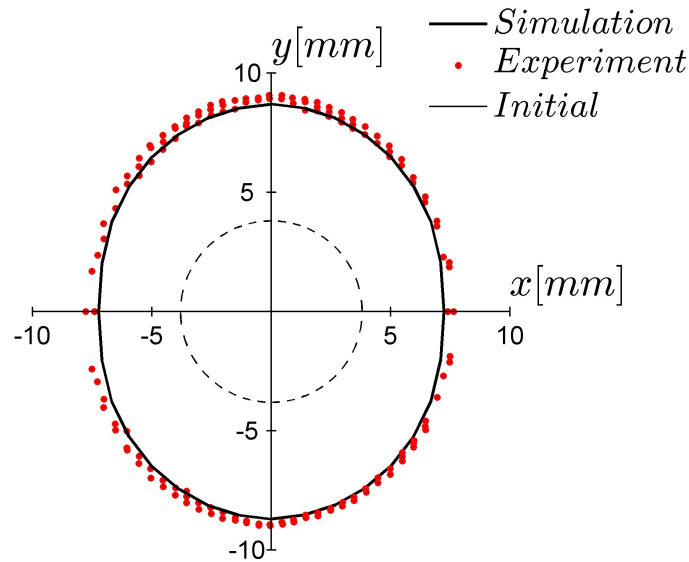
Fig. 12. Comparison of predicted and measured footprint geometry. As a reference, the initial cross-section geometry is plotted using the dashed line.

Very high strain rates and adiabatic heating are two competing mechanisms that influence flow stress, especially at the foot of the cylinder. The very high strain rate causes an increase in the resistance to intrinsic barriers, giving rise to a higher flow stress, while the increase in temperature lowers it. It is found that the temperature effects are stronger than the strain rate effects and the deformation, particularly at the center of the foot, is extremely high. Temperature at this region reaches almost 1000 °C which is still considerably below the melting temperature of Ta (3017 °C). Complex dependence of the flow stress on temperature and strain rate is accounted for using the thermally activated glide. The anisotropic plastic flow of Ta during the impact is primarily governed by the evolution of crystallographic texture, while the non-Schmid
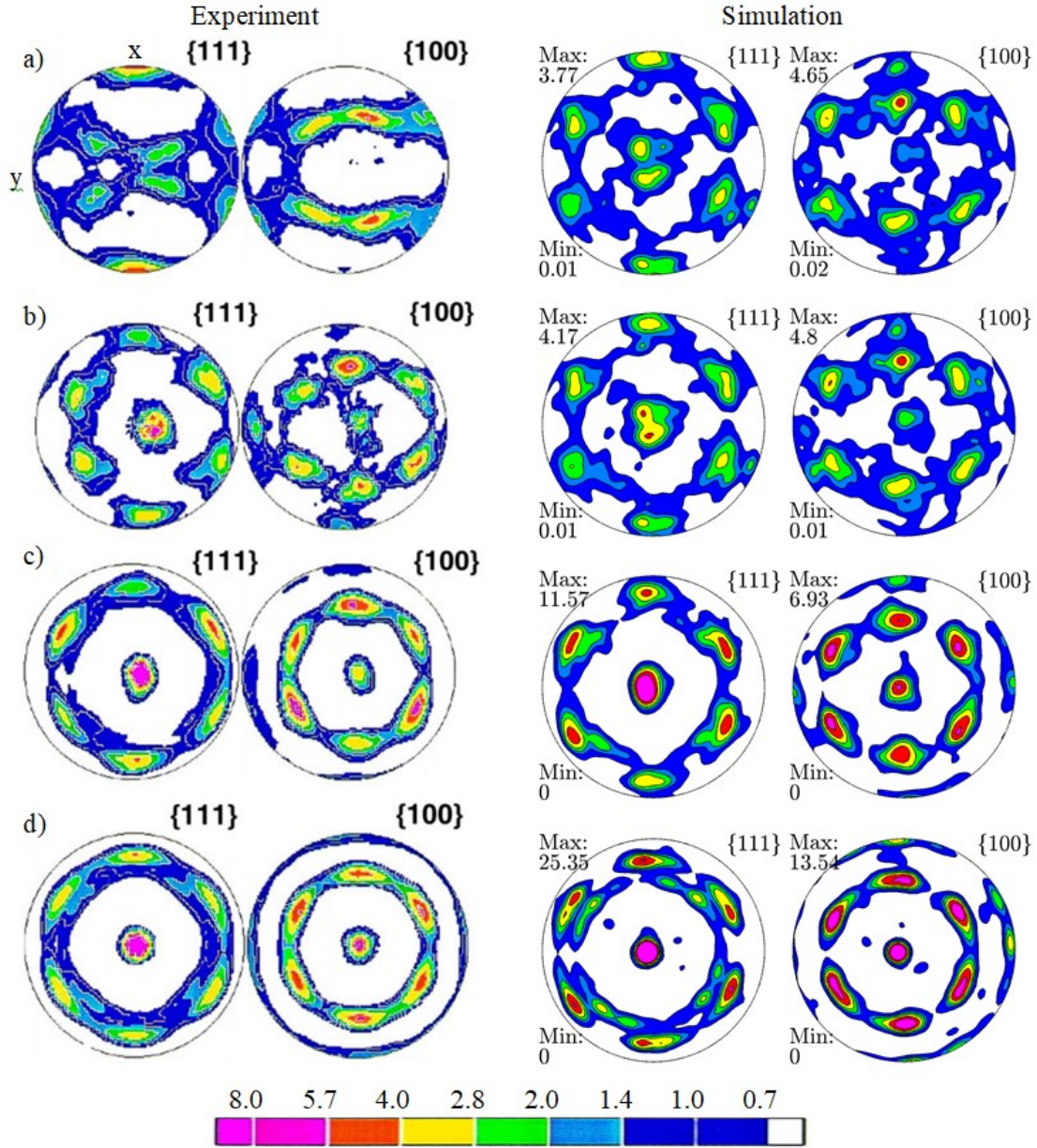
Fig. 13. Comparison of measured (by X-ray diffraction) and predicted texture evolution in the cylinder after the impact at (a) 9.2 mm, (b) 6.5 mm, (c) 1.6 mm, and (d) 0.5 mm away from the foot.

effects do not contribute appreciably mainly due to large plastic strain levels. Since the model developed here is texture-sensitive, evolves texture, and captures the rate and temperature dependence of flow stress, it is able to successfully capture the geometrical changes of the

cylinder in a numerically stable manner. Future work will concentrate on incorporating damage criteria to facilitate coupled plasticity-damage simulations under high strain rate deformation.

6   Conclusions

This work presented an implementation of VPSC with removed rate sensitivity coming from the single crystal power-law flow rule into implicit finite elements (FE-VPSC) to enable the prediction of high strain rate and impact deformation of polycrystals. The implementation permits the description of the complex strain rate sensitivity of a material solely through the thermally activated dislocation density-based hardening law. As a result, magnitudes of flow stress can be accurately calculated during high strain rate deformation. The implementation required the development of an implicit numerical scheme for the hardening law within VPSC to enable the prediction of high strain rate and impact deformation. Moreover, deformation of individual single crystals in the model is activated not only from the resolved shear stress along the direction of slip (Schmid law), but also from shear stresses resolved along directions orthogonal to the slip direction and the three normal stress components (non-Schmid effects). Therefore, the model is capable of predicting the coupled texture and non-Schmid effects on anisotropic flow of BCC polycrystals. The developed model was used for the prediction of deformation behavior of Ta during high strain rate conditions, including the Taylor impact of a cylindrical specimen. Since the impact simulations required remeshing and interpolation of state variables, the spherical linear interpolation algorithm in the space of quaternions is implemented to facilitate the interpolation of texture. Adiabatic heating was also considered by the model. The predicted deformed shape of the cylinder is compared to the corresponding experimental measurements, and good agreement is achieved. Furthermore, the predicted texture evolution at several locations along the cylinder axis is also compared with measurements, and good

106

agreement is achieved. It is found that the anisotropic plastic flow of Ta during impact is primarily governed by the evolution of crystallographic texture, while the non-Schmid effects do not contribute appreciably, mainly due to the large plastic strain levels and temperature increase. The developed FE-VPSC model can be broadly applied to understanding and predicting microstructure-property relationships in high strain rate deformation processes that generate spatially and temporarily heterogeneous mechanical fields.

Appendix A

Below, we present the derivation of individual terms of Eq. (35). The superscript denoting grain number, r, is dropped for simplicity.

Term (1):

$$\frac{\partial \dot{\boldsymbol{\varepsilon}}_{vp}}{\partial \boldsymbol{\sigma}'} = \dot{\gamma}_0 \sum_\alpha \left\{ \sum_{s(\alpha)} n \left(\frac{\mathbf{m}_{tot}^{s,t} \cdot \boldsymbol{\sigma}'}{\tau_c^\alpha} \right)^{n-1} \mathbf{m}^{s,t} \otimes \mathbf{m}_{tot}^{s,t} \right\} \tag{A1}$$

Term (2):

$$\frac{\partial \dot{\boldsymbol{\varepsilon}}_{vp}}{\partial \tau_c^\alpha} = -\sum_{s(\alpha)} n \underbrace{\dot{\gamma}_0 \left(\frac{\mathbf{m}_{tot}^{s,t} \cdot \boldsymbol{\sigma}}{\tau_c^\alpha} \right)^n}_{\dot{\gamma}^s} \frac{1}{\tau_c^\alpha} \mathbf{m}^{s,t} = -\sum_{s(\alpha)} n \dot{\gamma}^s \frac{1}{\tau_c^\alpha} \mathbf{m}^{s,t} \tag{A2}$$

Term (3):

We assume there is a function τ_c^α that maps deviatoric stress directly to slip resistance at the end of the time increment given by the implicit equation:

$$\tau_c^\alpha(\boldsymbol{\sigma}') = g\left(\left| \dot{\gamma}^s\left(\boldsymbol{\sigma}', \tau_c^\alpha(\boldsymbol{\sigma}') \right) \right| \right). \tag{A3}$$

Function g maps the absolute shear rates to slip resistance at the end of the time increment and is defined by the hardening law. In order to obtain derivatives of slip resistance w.r.t. deviatoric stress, we differentiate both sides of the equation:

$$\frac{\partial \tau_c^\alpha}{\partial \boldsymbol{\sigma}\prime} = \frac{\partial g}{\partial |\dot{\gamma}^{s\prime}|}\frac{\partial |\dot{\gamma}^{s\prime}|}{\partial \boldsymbol{\sigma}\prime} + \frac{\partial g}{\partial |\dot{\gamma}^{s\prime}|}\frac{\partial |\dot{\gamma}^{s\prime}|}{\partial \tau_c^{\alpha\prime}}\frac{\partial \tau_c^\alpha}{\partial \boldsymbol{\sigma}\prime} \tag{A4}$$

If we consider slip resistance and shear rates as vectors with length equal to number of slip modes and systems, respectively, we get:

$$\frac{\partial \boldsymbol{\tau}_c}{\partial \boldsymbol{\sigma}\prime} = \frac{\partial \mathbf{g}}{\partial |\dot{\boldsymbol{\gamma}}|}\frac{\partial |\dot{\boldsymbol{\gamma}}|}{\partial \boldsymbol{\sigma}\prime} + \frac{\partial \mathbf{g}}{\partial |\dot{\boldsymbol{\gamma}}|}\frac{\partial |\dot{\boldsymbol{\gamma}}|}{\partial \boldsymbol{\tau}_c}\frac{\partial \boldsymbol{\tau}_c}{\partial \boldsymbol{\sigma}\prime} \tag{A6}$$

where $|\ \ |$ denotes the absolute value. From here we can calculate the derivatives of slip resistance w.r.t. stress as:

$$\frac{\partial \boldsymbol{\tau}_c}{\partial \boldsymbol{\sigma}\prime} = \left[\mathbf{I}_{n_\alpha \times n_\alpha} - \frac{\partial \mathbf{g}}{\partial |\dot{\boldsymbol{\gamma}}|}\frac{\partial |\dot{\boldsymbol{\gamma}}|}{\partial \boldsymbol{\tau}_c}\right]^{-1}\frac{\partial \mathbf{g}}{\partial |\dot{\boldsymbol{\gamma}}|}\frac{\partial |\dot{\boldsymbol{\gamma}}|}{\partial \boldsymbol{\sigma}\prime} \tag{A7}$$

where $\mathbf{I}_{n_\alpha \times n_\alpha}$ is an identity matrix with dimensions defined by the number of slip modes n_α. The derivatives appearing in the above equation are calculated as:

$$\frac{\partial |\dot{\gamma}^s|}{\partial \boldsymbol{\sigma}\prime} = \dot{\gamma}_0 n \left(\frac{|\mathbf{m}_{tot}^{s,t}\cdot\boldsymbol{\sigma}\prime|}{\tau_c^\alpha}\right)^{n-1}\frac{1}{\tau_c^\alpha}\mathbf{m}^{s,t} \tag{A8}$$

$$\frac{\partial |\dot{\gamma}^s|}{\partial \tau_c^\alpha} = \begin{cases} -\dot{\gamma}_0 n \left(\frac{|\mathbf{m}_{tot}^{s,t}\cdot\boldsymbol{\sigma}\prime|}{\tau_c^\alpha}\right)^{n-1}\frac{|\mathbf{m}_{tot}^{s,t}\cdot\boldsymbol{\sigma}\prime|}{\tau_c^{\alpha 2}}; \text{if } s \in \alpha \\ 0; \text{if } s \notin \alpha \end{cases} \tag{A9}$$

The term $\frac{\partial \mathbf{g}}{\partial |\dot{\boldsymbol{\gamma}}|}$ represents the derivative of slip resistance w.r.t. absolute shear rates, and it is defined separately for different hardening laws. We use dislocation-based hardening law, where only forest and debris terms depend on the shear rates through the dislocation densities (Eq. 20). The derivatives of the slip resistance are:

$$\frac{\partial \tau_c^\alpha}{\partial |\dot{\gamma}^s|} = \frac{\partial \tau_{for}^\alpha}{\partial \rho_{for}^{\alpha'}} \frac{\partial \rho_{for}^{\alpha'}}{\partial |\dot{\gamma}^s|} + \frac{\partial \tau_{deb}^\alpha}{\partial \rho_{deb}} \frac{\partial \rho_{deb}}{\partial |\dot{\gamma}^s|} \tag{A10}$$

where the individual terms are (no summation over repeated indices):

$$\frac{\partial \tau_{for}^\alpha}{\partial \rho_{for}^{\alpha'}} = b^\alpha \mu \frac{1}{2} \frac{1}{\sqrt{\sum_{\alpha'} \chi^{\alpha\alpha} \rho_{for}^{\alpha'}}} \chi^{\alpha\alpha'} \tag{A11}$$

$$\frac{\partial \rho_{for}^\alpha}{\partial |\dot{\gamma}^s|} = \left\{ 1 - \frac{1}{2} \left[\frac{1}{2} k_1 \frac{1}{\sqrt{\rho_{for}^\alpha}} - k_2 \right] \sum_{s(\alpha)} |\dot{\gamma}^s| \Delta t \right\}^{-1} \frac{1}{2} \left[\frac{\partial \rho_{for}^\alpha}{\partial \gamma^\alpha} (\rho_{for}^{\alpha,t}) + \frac{\partial \rho_{for}^\alpha}{\partial \gamma^\alpha} (\rho_{fo}^\alpha) \right];$$

with $s \in \alpha$ \hfill (A13)

$$\frac{\partial \tau_{deb}^\alpha}{\partial \rho_{deb}} = -k_{deb} \mu b^\alpha \left[\log \left(b^\alpha \sqrt{\rho_{deb}} \right) + 1 \right] \frac{1}{2} \frac{1}{\sqrt{\rho_{deb}}} \tag{A14}$$

$$\frac{\partial \rho_{deb}}{\partial |\dot{\gamma}^s|} = \left[1 - \frac{1}{2} \frac{\Delta \rho_{deb}}{\rho_{deb}} \right]^{-1} \left\{ \frac{1}{2} \sqrt{\rho_{deb}} q^{\alpha'} b^{\alpha'} k_2 \frac{\partial \rho_{for}^{\alpha'}}{\partial |\dot{\gamma}^s|} \sum_{s(\alpha)} |\dot{\gamma}^s| \Delta t + \sqrt{\rho_{deb}} q^{\alpha'} b^{\alpha'} 0.5 k_2 \left[\rho_{for}^{\alpha',t} + \right. \right.$$

$$\left. \rho_{for}^{\alpha'} \right] \Delta t \Bigg\} ; \text{with } s \in \alpha' \tag{A15}$$

where

$$\Delta \rho_{deb} = \sqrt{\rho_{deb}} \sum_\alpha q^\alpha b^\alpha \frac{1}{2} \left[\frac{\partial \rho_{rem,for}^\alpha}{\partial \gamma^\alpha} (\rho_{for}^{\alpha,t}) + \frac{\partial \rho_{rem,for}^\alpha}{\partial \gamma^\alpha} (\rho_{for}^\alpha) \right] \sum_{s(\alpha)} |\dot{\gamma}^s| \Delta t. \tag{A16}$$

Acknowledgements

References

[1] Fabricated Products High Performance Solutions, H.C. Starck Inc., (2013).

[2] L. Hesla, Seamless cavity performance, International Linear Collider Newsline, (2011).

[3] J. Shields Jr, P. Lipetzky, A. Mueller, Fracture Toughness of 6.4 mm arc-cast molybdenum and molybdenum-TZM plate at room temperature and 300 deg C, in: DE-AC11-98PN38206, 1999.

[4] R.W. Buckman, New applications for tantalum and tantalum alloys, JOM, 52 (2000) 40-41.

[5] J. Christian, Some surprising features of the plastic deformation of body-centered cubic metals and alloys, Metall. Mater. Trans. A, 14 (1983) 1237-1256.

[6] S. Chen, G. Gray, Constitutive behavior of tantalum and tantalum-tungsten alloys, Metall. Mater. Trans. A, 27 (1996) 2994-3006.

[7] C.A. Bronkhorst, G.T. Gray III, F.L. Addessio, V. Livescu, N. Bourne, S. McDonald, P. Withers, Response and representation of ductile damage under varying shock loading conditions in tantalum, J. Appl. Phys., 119 (2016) 085103.

[8] K. Hoge, A. Mukherjee, The temperature and strain rate dependence of the flow stress of tantalum, J. Mater. Sci., 12 (1977) 1666-1672.

[9] U.F. Kocks, C.N. Tomé, H.-R. Wenk, Texture and Anisotropy, Cambridge University Press, Cambridge, UK, 1998.

[10] U.F. Kocks, H. Mecking, Physics and phenomenology of strain hardening: the FCC case, Prog. Mater. Sci., 48 (2003) 171-273.

[11] R.J. Asaro, A. Needleman, Texture development and strain hardening in rate dependent polycrystals, Acta Metall. Mater., 33 (1985) 923-953.

[12] H.F. Al-Harbi, M. Knezevic, S.R. Kalidindi, Spectral approaches for the fast computation of yield surfaces and first-order plastic property closures for polycrystalline materials with cubic-triclinic textures, CMC: Computers, Materials, & Continua, 15 (2010) 153-172.

[13] J.B. Shaffer, M. Knezevic, S.R. Kalidindi, Building texture evolution networks for deformation processing of polycrystalline fcc metals using spectral approaches: Applications to process design for targeted performance, Int. J. Plast., 26 (2010) 1183-1194.

[14] Mathur, K. K., P.R. Dawson, On modelling the development of crystallographic texture in bulk forming processes, Int. J. Plast., 5 (1989) 67-94.

[15] M. Zecevic, I.J. Beyerlein, M. Knezevic, Coupling elasto-plastic self-consistent crystal plasticity and implicit finite elements: Applications to compression, cyclic tension-compression, and bending to large strains, Int. J. Plast., 93 (2017) 187-211.

[16] M. Zecevic, M. Knezevic, Modeling of Sheet Metal Forming Based on Implicit Embedding of the Elasto-Plastic Self-Consistent Formulation in Shell Elements: Application to Cup Drawing of AA6022-T4, JOM, 69 (2017) 922-929.

[17] M. Knezevic, B. Drach, M. Ardeljan, I.J. Beyerlein, Three dimensional predictions of grain scale plasticity and grain boundaries using crystal plasticity finite element models, Computer Methods in Applied Mechanics and Engineering, 277 (2014) 239-259.

[18] M. Ardeljan, R.J. McCabe, I.J. Beyerlein, M. Knezevic, Explicit incorporation of deformation twins into crystal plasticity finite element models, Computer Methods in Applied Mechanics and Engineering, 295 (2015) 396-413.

[19] G.I. Taylor, The use of flat-ended projectiles for determining dynamic yield stress. I. Theoretical considerations, in: Proceedings of the Royal Society of London A: Mathematical, Physical and Engineering Sciences, The Royal Society, 1948, pp. 289-299.

[20] P. Maudlin, G. Gray, C. Cady, G. Kaschner, High–rate material modelling and validation using the Taylor cylinder impact test, Philosophical Transactions of the Royal Society of London A: Mathematical, Physical and Engineering Sciences, 357 (1999) 1707-1729.

[21] E. Lee, S. Tupper, Analysis of plastic deformation in a steel cylinder striking a rigid target, J. appl. Mech, 21 (1954) 63-70.

[22] J. Hawkyard, A theory for the mushrooming of flat-ended projectiles impinging on a flat rigid anvil, using energy considerations, International Journal of Mechanical Sciences, 11 (1969) 313-333.

[23] G.R. Johnson, W.H. Cook, A constitutive model and data for metals subjected to large strains, high strain rates and high temperatures, in: Proceedings of the 7th International Symposium on Ballistics, The Hague, The Netherlands, 1983, pp. 541-547.

[24] F.J. Zerilli, R.W. Armstrong, Description of tantalum deformation behavior by dislocation mechanics based constitutive relations, J. Appl. Phys., 68 (1990) 1580-1591.

[25] F.J. Zerilli, R.W. Armstrong, Dislocation-mechanics-based constitutive relations for material dynamics calculations, J. Appl. Phys., 61 (1987) 1816-1825.

[26] D.J. Bammann, Modeling temperature and strain rate dependent large deformations of metals, Applied Mechanics Reviews, 43 (1990) S312-S319.

[27] D. Steinberg, C. Lund, A constitutive model for strain rates from $10-4$ to 106 s−, J. Appl. Phys., 65 (1989) 1528-1533.

[28] D.L. Preston, D.L. Tonks, D.C. Wallace, Model of plastic deformation for extreme loading conditions, J. Appl. Phys., 93 (2003) 211-220.

[29] P. Follansbee, U. Kocks, A constitutive description of the deformation of copper based on the use of the mechanical threshold stress as an internal state variable, Acta Metall., 36 (1988) 81-93.

[30] P. Maudlin, J. Bingert, J. House, S. Chen, On the modeling of the Taylor cylinder impact test for orthotropic textured materials: experiments and simulations, Int. J. Plast., 15 (1999) 139-166.

[31] B. Revil-Baudard, O. Cazacu, P. Flater, G. Kleiser, Plastic deformation of high-purity α-titanium: Model development and validation using the Taylor cylinder impact test, Mechanics of Materials, 80, Part B (2015) 264-275.

[32] B. Plunkett, O. Cazacu, R.A. Lebensohn, F. Barlat, Elastic-viscoplastic anisotropic modeling of textured metals and validation using the Taylor cylinder impact test, Int. J. Plast., 23 (2007) 1001-1021.

[33] S. Kok, A.J. Beaudoin, D.A. Tortorelli, A polycrystal plasticity model based on the mechanical threshold, Int. J. Plast., 18 (2002) 715-741.

[34] M. Kothari, L. Anand, Elasto-viscoplastic constitutive equations for polycrystalline metals: application to tantalum, Journal of the Mechanics and Physics of Solids, 46 (1998) 51-83.

[35] W. Kocks, Thermodynamics and kinetics of slip, Progr. Mater. Sci., 19 (1975) 291.

[36] E. Schmid, W. Boas, Plasticity of crystals with special reference to metals, English translation F.A. Hughes, London 1950.

[37] M.a.-S. Duesbery, V. Vitek, Plastic anisotropy in bcc transition metals, Acta. Mater., 46 (1998) 1481-1492.

[38] B. Peeters, S.R. Kalidindi, C. Teodosiu, P.V. Houtte, E. Aernoudt, A theoretical investigation of the influence of dislocation sheets on evolution of yield surfaces in single-phase BCC polycrystals, J. Mech. Phys. Solids, 50 (2002) 783-807.

[39] L. Stainier, A.M. Cuitiño, M. Ortiz, A micromechanical model of hardening, rate sensitivity and thermal softening in BCC single crystals, J. Mech. Phys. Solids, 50 (2002) 1511-1545.

[40] G. Taylor, Thermally-activated deformation of BCC metals and alloys, Prog. Mater. Sci., 36 (1992) 29-61.

[41] Z.Q. Wang, I.J. Beyerlein, An atomistically-informed dislocation dynamics model for the plastic anisotropy and tension–compression asymmetry of BCC metals, Int. J. Plast., 27 (2011) 1471-1484.

[42] C. Alleman, S. Ghosh, D. Luscher, C.A. Bronkhorst, Evaluating the effects of loading parameters on single-crystal slip in tantalum using molecular mechanics, Philosophical Magazine, 94 (2014) 92-116.

[43] J. Chang, W. Cai, V.V. Bulatov, S. Yip, Dislocation motion in BCC metals by molecular dynamics, Mater. Sci. Eng. A, 309 (2001) 160-163.

[44] P. Gordon, T. Neeraj, Y. Li, J. Li, Screw dislocation mobility in BCC metals: the role of the compact core on double-kink nucleation, Modelling and Simulation in Materials Science and Engineering, 18 (2010) 085008.

[45] H. Lim, C.R. Weinberger, C.C. Battaile, T.E. Buchheit, Application of generalized non-Schmid yield law to low-temperature plasticity in bcc transition metals, Modelling and Simulation in Materials Science and Engineering, 21 (2013) 045015.

[46] R. Gröger, V. Racherla, J.L. Bassani, V. Vitek, Multiscale modeling of plastic deformation of molybdenum and tungsten: II. Yield criterion for single crystals based on atomistic studies of glide of screw dislocations, Acta. Mater., 56 (2008) 5412-5425.

[47] Q. Qin, J.L. Bassani, Non-Schmid yield behavior in single crystals, J. Mech. Phys. Solids, 40 (1992) 813-833.

[48] V. Vitek, M. Mrovec, R. Gröger, J. Bassani, V. Racherla, L. Yin, Effects of non-glide stresses on the plastic flow of single and polycrystals of molybdenum, Mater. Sci. Eng. A, 387 (2004) 138-142.

[49] M. Dao, R.J. Asaro, Non-Schmid effects and localized plastic flow in intermetallic alloys, Mater. Sci. Eng. A, 170 (1993) 143-160.

[50] M. Knezevic, I.J. Beyerlein, M.L. Lovato, C.N. Tomé, A.W. Richards, R.J. McCabe, A strain-rate and temperature dependent constitutive model for BCC metals incorporating non-Schmid effects: Application to tantalum–tungsten alloys, Int. J. Plast., 62 (2014) 93-104.

[51] M. Knezevic, M. Zecevic, I.J. Beyerlein, A. Bhattacharyya, R.J. McCabe, Predicting Texture Evolution in Ta and Ta-10W Alloys Using Polycrystal Plasticity, JOM, 67 (2015) 2670-2674.

[52] H. Mecking, U.F. Kocks, Kinetics of flow and strain-hardening., Acta Metall. Mater., 29 (1981) 1865-1875.

[53] M. Knezevic, M. Zecevic, I.J. Beyerlein, R.A. Lebensohn, A numerical procedure enabling accurate descriptions of strain rate-sensitive flow of polycrystals within crystal visco-plasticity theory, Computer Methods in Applied Mechanics and Engineering, 308 (2016) 468-482.

[54] G.I. Taylor, Plastic strain in metals, Journal of the Institute of Metals, 62 (1938) 307-324.

[55] J.W. Hutchinson, Bounds and self-consistent estimates for creep of polycrystalline materials, Proceedings of the Royal Society of London. Series A, Mathematical and Physical Sciences, 348 (1976) 101-126.

[56] I.J. Beyerlein, C.N. Tomé, A dislocation-based constitutive law for pure Zr including temperature effects, Int. J. Plast., 24 (2008) 867-895.

[57] R.A. Lebensohn, C.N. Tomé, A self-consistent anisotropic approach for the simulation of plastic deformation and texture development of polycrystals: Application to zirconium alloys, Acta Metall. Mater., 41 (1993) 2611-2624.

[58] M. Knezevic, J. Crapps, I.J. Beyerlein, D.R. Coughlin, K.D. Clarke, R.J. McCabe, Anisotropic modeling of structural components using embedded crystal plasticity constructive laws within finite elements, International Journal of Mechanical Sciences, 105 (2016) 227-238.

[59] M. Zecevic, M. Knezevic, I.J. Beyerlein, R.J. McCabe, Texture formation in orthorhombic alpha-uranium under simple compression and rolling to high strains, Journal of Nuclear Materials, 473 (2016) 143-156.

[60] B. Plunkett, O. Cazacu, R. Lebensohn, F. Barlat, Elastic-viscoplastic anisotropic modeling of textured metals and validation using the Taylor cylinder impact test, International Journal of Plasticity, 23 (2007) 1001-1021.

[61] P. Maudlin, S. Schiferl, Computational anisotropic plasticity for high-rate forming applications, Computer methods in applied mechanics and engineering, 131 (1996) 1-30.

[62] E. Orowan, Problems of plastic gliding, Proceedings of the Physical Society, 52 (1940) 8.

[63] A.S. Krausz, H. Eyring, Deformation kinetics, Wiley, 1975.

[64] L.R.A. Tomé C.N., Manual for Code Viscoplastic Self-consistent (version 7c). (2011).

[65] J. Segurado, R.A. Lebensohn, J. Llorca, C.N. Tomé, Multiscale modeling of plasticity based on embedding the viscoplastic self-consistent formulation in implicit finite elements, Int. J. Plast., 28 (2012) 124-140.

[66] S. Mercier, A. Molinari, Homogenization of elastic–viscoplastic heterogeneous materials: Self-consistent and Mori-Tanaka schemes, Int. J. Plast., 25 (2009) 1024-1048.

[67] F. Roters, P. Eisenlohr, L. Hantcherli, D.D. Tjahjanto, T.R. Bieler, D. Raabe, Overview of constitutive laws, kinematics, homogenization and multiscale methods in crystal plasticity finite-element modeling: Theory, experiments, applications, Acta. Mater., 58 (2010) 1152-1211.

[68] J.W. Hutchinson, Bounds and self-consistent estimates for creep of polycrystalline materials, Proceedings of the Royal Society of London. Series A, Mathematical and Physical Sciences, (1976) 101-126.

[69] A. Ma, F. Roters, A constitutive model for fcc single crystals based on dislocation densities and its application to uniaxial compression of aluminium single crystals, Acta materialia, 52 (2004) 3603-3612.

[70] M. Knezevic, M. Zecevic, I.J. Beyerlein, J.F. Bingert, R.J. McCabe, Strain rate and temperature effects on the selection of primary and secondary slip and twinning systems in HCP Zr, Acta. Mater., 88 (2015) 55-73.

[71] M. Ardeljan, I.J. Beyerlein, B.A. McWilliams, M. Knezevic, Strain rate and temperature sensitive multi-level crystal plasticity model for large plastic deformation behavior: Application to AZ31 magnesium alloy, Int. J. Plast., 83 (2016) 90-109.

[72] S. Chen, G. Gray III, S. Bingert, Mechanical properties and constitutive relations for tantalum and tantalum alloys under high-rate deformation, in, Los Alamos National Lab., NM (United States), 1996.

[73] M. Knezevic, H.F. Al-Harbi, S.R. Kalidindi, Crystal plasticity simulations using discrete Fourier transforms, Acta. Mater., 57 (2009) 1777-1784.

[74] S.R. Kalidindi, C.A. Bronkhorst, L. Anand, Crystallographic texture evolution in bulk deformation processing of FCC metals, J. Mech. Phys. Solids, 40 (1992) 537-569.

[75] M. Knezevic, L. Capolungo, C.N. Tomé, R.A. Lebensohn, D.J. Alexander, B. Mihaila, R.J. McCabe, Anisotropic stress-strain response and microstructure evolution of textured α-uranium, Acta. Mater., 60 (2012) 702-715.

[76] M. Knezevic, R.J. McCabe, C.N. Tomé, R.A. Lebensohn, S.R. Chen, C.M. Cady, G.T. Gray Iii, B. Mihaila, Modeling mechanical response and texture evolution of α-uranium as a function of strain rate and temperature using polycrystal plasticity, Int. J. Plast., 43 (2013) 70-84.

[77] M. Knezevic, I.J. Beyerlein, D.W. Brown, T.A. Sisneros, C.N. Tomé, A polycrystal plasticity model for predicting mechanical response and texture evolution during strain-path changes: Application to beryllium, Int. J. Plast., 49 (2013) 185-198.

[78] R. McCabe, L. Capolungo, P. Marshall, C. Cady, C. Tomé, Deformation of wrought uranium: experiments and modeling, Acta Materialia, 58 (2010) 5447-5459.

[79] L. Capolungo, I. Beyerlein, G. Kaschner, C. Tomé, On the interaction between slip dislocations and twins in HCP Zr, Materials Science and Engineering: A, 513 (2009) 42-51.

[80] G. Zhou, Z. Li, D. Li, Y. Peng, H.S. Zurob, P. Wu, A polycrystal plasticity based discontinuous dynamic recrystallization simulation method and its application to copper, International Journal of Plasticity, 91 (2017) 48-76.

[81] R.A. Lebensohn, C.N. Tomé, A self-consistent viscoplastic model: prediction of rolling textures of anisotropic polycrystals, Mater. Sci. Eng. A, 175 (1994) 71-82.

[82] M. Zecevic, I.J. Beyerlein, R.J. McCabe, B.A. McWilliams, M. Knezevic, Transitioning rate sensitivities across multiple length scales: microstructure-property relationships in the Taylor cylinder impact test on zirconium, International Journal of Plasticity, 84 (2016) 138-159.

[83] M. Knezevic, R.J. McCabe, R.A. Lebensohn, C.N. Tomé, C. Liu, M.L. Lovato, B. Mihaila, Integration of self-consistent polycrystal plasticity with dislocation density based hardening laws within an implicit finite element framework: Application to low-symmetry metals, J. Mech. Phys. Solids, 61 (2013) 2034-2046.

[84] J. Crank, P. Nicolson, A practical method for numerical evaluation of solutions of partial differential equations of the heat-conduction type, in: Mathematical Proceedings of the Cambridge Philosophical Society, Cambridge University Press, 1947, pp. 50-67.

[85] D.J. Savage, I.J. Beyerlein, M. Knezevic, Coupled texture and non-Schmid effects on yield surfaces of body-centered cubic polycrystals predicted by a crystal plasticity finite element approach, International Journal of Solids and Structures, 109 (2017) 22-32.

[86] A. Patra, T. Zhu, D.L. McDowell, Constitutive equations for modeling non-Schmid effects in single crystal bcc-Fe at low and ambient temperatures, Int. J. Plast., 59 (2014) 1-14.

[87] H. Lim, L. Hale, J. Zimmerman, C. Battaile, C. Weinberger, A multi-scale model of dislocation plasticity in α-Fe: incorporating temperature, strain rate and non-schmid effects, International Journal of Plasticity, 73 (2015) 100-118.

[88] R. Gröger, V. Vitek, Multiscale modeling of plastic deformation of molybdenum and tungsten. III. Effects of temperature and plastic strain rate, Acta Materialia, 56 (2008) 5426-5439.

[89] R. Becker, Analysis of texture evolution in channel die compression—I. Effects of grain interaction, Acta metallurgica et materialia, 39 (1991) 1211-1230.

[90] E. Voce, The Relationship between Stress and Strain for homogeneous deformation, Journal of the Institute of Metals, 74 (1948) 537-562.

[91] U.F. Kocks, Laws for work-hardening and low-temperature creep., Journal of Engineering Materials and Technology, Transactions of the ASME, 98 Ser H (1976) 76-85.

[92] M. Knezevic, J.S. Carpenter, M.L. Lovato, R.J. McCabe, Deformation behavior of the cobalt-based superalloy Haynes 25: Experimental characterization and crystal plasticity modeling, Acta. Mater., 63 (2014) 162-168.

[93] R. Masson, M. Bornert, P. Suquet, A. Zaoui, An affine formulation for the prediction of the effective properties of nonlinear composites and polycrystals, J. Mech. Phys. Solids, 48 (2000) 1203-1227.

[94] R.A. Lebensohn, C.N. Tomé, P.P. Castaneda, Self-consistent modelling of the mechanical behaviour of viscoplastic polycrystals incorporating intragranular field fluctuations, Philosophical Magazine, 87 (2007) 4287-4322.

[95] R.J. Asaro, J.R. Rice, Strain localization in ductile single crystals, Journal of the Mechanics and Physics of Solids, 25 (1977) 309-338.

[96] T.J.R. Hughes, J. Winget, Finite rotation effects in numerical integration of rate constitutive equations arising in large-deformation analysis, International Journal for Numerical Methods in Engineering, 15 (1980) 1862-1867.

[97] M. Zecevic, R.J. McCabe, M. Knezevic, Spectral database solutions to elasto-viscoplasticity within finite elements: application to a cobalt-based FCC superalloy, International Journal of Plasticity, 70 (2015) 151-165.

[98] M. Zecevic, R.J. McCabe, M. Knezevic, A new implementation of the spectral crystal plasticity framework in implicit finite elements, Mechanics of Materials, 84 (2015) 114-126.

[99] J.C. Simo, Numerical analysis and simulation of plasticity, Handbook of numerical analysis, 6 (1998) 183-499.

[100] R. Goetz, S. Semiatin, The adiabatic correction factor for deformation heating during the uniaxial compression test, JMEP, 10 (2001) 710-717.

[101] P. Knysh, Y.P. Korkolis, Determination of the fraction of plastic work converted into heat in metals, Mechanics of materials, 86 (2015) 71-80.

[102] R. Kapoor, S. Nemat-Nasser, Determination of temperature rise during high strain rate deformation, Mechanics of Materials, 27 (1998) 1-12.

[103] D. Rittel, A. Bhattacharyya, B. Poon, J. Zhao, G. Ravichandran, Thermomechanical characterization of pure polycrystalline tantalum, Materials Science and Engineering: A, 447 (2007) 65-70.

[104] K.-J. Bathe, Finite element procedures, Englewood Cliffs, N.J.: Prentice Hall, 1996.

[105] A. Prakash, W. Nöhring, R. Lebensohn, H. Höppel, E. Bitzek, A multiscale simulation framework of the accumulative roll bonding process accounting for texture evolution, Materials Science and Engineering: A, 631 (2015) 104-119.

[106] K. Shoemake, Animating rotation with quaternion curves, in: ACM SIGGRAPH computer graphics, ACM, 1985, pp. 245-254.

[107] M. Knezevic, N.W. Landry, Procedures for reducing large datasets of crystal orientations using generalized spherical harmonics, Mechanics of Materials, 88 (2015) 73-86.

[108] B.E. Hollister, A. Pang, Interpolation of non-Gaussian probability distributions for ensemble visualization, in: Proc. IEEE Vis. Posters, 2013.

[109] N. Bonneel, M. Van De Panne, S. Paris, W. Heidrich, Displacement interpolation using Lagrangian mass transport, in: ACM Transactions on Graphics (TOG), ACM, 2011, pp. 158.

[110] F.H. Bursal, On interpolating between probability distributions, Applied Mathematics and Computation, 77 (1996) 213-244.

[111] V. Sundararaghavan, N. Zabaras, Linear analysis of texture–property relationships using process-based representations of Rodrigues space, Acta materialia, 55 (2007) 1573-1587.

[112] M. Miller, T. Turner, A methodology for measuring and modeling crystallographic texture gradients in processed alloys, International Journal of Plasticity, 17 (2001) 783-805.

[113] S.R. Chen, G.T. Gray III, Constitutive behavior of tungsten and tantalum: experiments and modeling, in: Proceedings of the 2nd international conference on tungsten and refractory metals, metal powders industries federation, Princeton, New Jersey, 1995, pp. 489-498.

[114] I. Dillamore, W. Roberts, Preferred orientation in wrought and annealed metals, Metallurgical Reviews, 10 (1965) 271-380.

[115] I. Dillamore, H. Katoh, K. Haslam, The nucleation of recrystallisation and the development of textures in heavily compressed iron-carbon alloys, Texture, Stress, and Microstructure, 1 (1974) 151-156.

[116] R.A. Lebensohn, N-site modeling of a 3D viscoplastic polycrystal using Fast Fourier Transform, Acta Materialia, 49 (2001) 2723-2737.

[117] M. Zecevic, W. Pantleon, R.A. Lebensohn, R.J. McCabe, M. Knezevic, Predicting intragranular misorientation distributions in polycrystalline metals using the viscoplastic self-consistent formulation, Acta. Mater., 140 (2017) 398-410.

[118] R.A. Lebensohn, M. Zecevic, M. Knezevic, R.J. McCabe, Average intragranular misorientation trends in polycrystalline materials predicted by a viscoplastic self-consistent approach, Acta. Mater., 104 (2016) 228-236.

Chapter 3: Predicting intragranular misorientation distributions in polycrystalline metals using the viscoplastic self-consistent formulation

This chapter was published as: "Predicting intragranular misorientation distributions in polycrystalline metals using the viscoplastic self-consistent formulation", Zecevic Miroslav, Wolfgang Pantleon, Ricardo A. Lebensohn, Rodney J. McCabe, and Marko Knezevic, Acta Materialia 140 (2017): 398-410. My contribution to this chapter was:

- development and implementation of two methods for calculation of intragranular misorientation distributions (Taylor expansion approximation and discrete approximation) from the intragranular rotation rate distributions within the visco-plastic self-consistent model

- simulation of tension and plane-strain compression of fcc polycrystal using the proposed VPSC model and the full-field VPFFT model

- processing of the simulation and experimental results and their comparison

- writing the first draft of the paper.

Predicting intragranular misorientation distributions in polycrystalline metals using the viscoplastic self-consistent formulation

Miroslav Zecevic[1,2], Wolfgang Pantleon[3], Ricardo A. Lebensohn[2], Rodney J. McCabe[2], and Marko Knezevic[1]

1 Department of Mechanical Engineering, University of New Hampshire, Durham, NH 03824 USA
2 Materials Science and Technology Division, Los Alamos National Laboratory, Los Alamos, NM 87544
3 Department of Mechanical Engineering, Technical University of Denmark, Produktionstorvet 425, 2800 Kgs. Lyngby, Denmark

Abstract

In a recent paper, we reported the methodology to calculate intragranular fluctuations in the instantaneous lattice rotation rates in polycrystalline materials within the mean-field viscoplastic self-consistent (VPSC) model. This paper is concerned with the time integration and subsequent use of these fluctuations to predict orientation-dependent misorientation distributions developing inside each grain representing the polycrystalline aggregate. To this end, we propose and assess two approaches to update the intragranular misorientation distribution within the VPSC framework. To illustrate both approaches, we calculate intragranular misorientations in face-centered cubic polycrystals deformed in tension and plane-strain compression. These predictions are tested by comparison with corresponding experiments for polycrystalline copper and aluminum, respectively, and with full-field calculations. It is observed that at sufficiently high strains some grains develop large misorientations that may lead to grain fragmentation and/or act as driving forces for recrystallization. The proposed VPSC-based prediction of intragranular misorientations enables modeling of grain fragmentation, as well as a more accurate modeling of texture using a computationally efficient mean-field approach, as opposed to computationally more expensive full-field approaches.

1   Introduction

During forming operations, polycrystalline metals are subjected to shape changes and plastic deformation that result in highly heterogeneous micromechanical fields (stress and strain fields) in the material [1]. It is well known that dislocation glide accommodates most of the imposed plastic deformation at the level of single grains. Crystallographic slip is potentially associated with local lattice rotations, which in turn induce anisotropy in the mechanical response by texture evolution and microstructure formation. Additionally, intra- and intergranular heterogeneities develop in the material, playing an important role in determining the deformation and hardening behavior, as well as the subsequent grain fragmentation and recrystallization of the deformed microstructure.

Intragranular orientation spreads have been related to the formation of transition bands, which are favorable places for recrystallization nucleation [2, 3]. In addition, recrystallization nuclei forming near grain boundaries may have quite different crystallographic orientation compared to the average grain orientation due to large orientation variations developed across the grains [3, 4]. Therefore, accurate predictions of intragranular orientation distributions are crucial to model recrystallization processes. Furthermore, such misorientation predictions can improve the modelling of deformation textures and provide a physical basis for grain fragmentation.

Plastic deformation of polycrystalline metals is usually modeled using either full-field or mean-field approaches. Full-field models, for example, can be based on the crystal plasticity finite element (CPFE) method [5-9] or on the spectral fast Fourier transform (FFT)-based approach of Moulinec and Suquet [10], extended to polycrystals by Lebensohn [11]. These models are able to predict local micromechanical fields, including intragranular orientation

gradients, resulting from grain-to-grain interactions, at the expense of a relatively high computational cost. Among mean-field models, self-consistent schemes, originally conceived for linear problems [12] and later extended to non-linear material's behavior [13-16], are widely used for simulating plastic deformation of polycrystalline materials considering grain interaction in an average sense. These non-linear homogenization-based models are computationally efficient, but most of them use information on first moments of the intragranular fields only, for the definition of a material with linearized behavior on which the self-consistency is actually imposed. In the last two decades, improved homogenization techniques have been developed that also take into account second moments of the micromechanical fields to define an optimized linearization [17, 18]. However, until very recently this available information on second moments of the intragranular fields had not been used in calculations of intragranular misorientation spreads.

There have been numerous phenomenological attempts to predict the development of intragranular orientation spreads without the use of computationally expensive full-field approaches. Berveiller et al. [19] divided grains into homogeneous regions where plastic deformation occurred by single or multiple slip. They showed that these regions developed quite different orientations upon plastic deformation, indicating the formation of an orientation spread. Bolmaro et al. [20] represented each grain within the viscoplastic self-consistent (VPSC) model by two fragments to which random neighbors were assigned. Co-rotation of grain fragments and their respective neighbors was assumed, resulting in the development of local misorientation between fragments. This model was later used to initialize the local states to drive a recrystallization model [21]. The idea of co-rotation in VPSC was further extended by [22], representing each grain by six fragments, each one co-rotating with its own neighbor. In a similar

approach developed by Toth et al. [23], a Taylor-type polycrystal model was used, in which each grain was divided into two regions, one at the center of the grain and another close to grain boundaries. In the latter, rotation was impeded by "friction" with the surrounding medium. Due to the difference in rotation between the two regions, lattice curvature was predicted and in turn used in a fragmentation model. Raabe [24] estimated the intragranular misorientation by assuming one part of the grain was next to a hard grain and thus deformed according to the Taylor model, while another part had a soft neighbor and consequently deformed according to the Sachs model. In [2] rotation rate fields were analyzed to determine the divergent and convergent orientations under different applied strains. A similar idea was developed by Raabe et al. [25] where the divergence of the rotation rate field was used to determine which orientations would be prone to develop strong orientation differences. Lee and Duggan [26] used an intragranular deformation banding model within the Taylor framework to simulate rolling textures of copper. A similar model was later used by Leffers [27] for simulating microstructure development in rolled aluminum. Butler and McDowell [28] introduced additional plastic rotations within the Taylor model to account for accumulation of geometrically necessary dislocations related to grain subdivision. In recent work Guo and Seefeldt [29] have used VPSC to model formation of reorientation bands and resulting grain fragmentation, caused by slip bands in neighboring grains. Slip rate within slip band for slip system s was assumed to be proportional to mean slip rate value within grain and the coefficient of proportionality was assumed to be a fitting parameter. A majority of the described approaches have been introduced to improve texture predictions and to allow incorporation of the effect of grain fragmentation. Detailed analysis of the orientation spreads for a large number of grains and comparison with experimental measurements were generally missing in the aforementioned approaches.

123

In this work, the widely-used VPSC model [15] is extended to calculate intragranular misorientation spreads. The VPSC model is able to provide intragranular second moments of stress and strain rate fields [30, 31]. In turn, this information can be used to calculate second moments of the rotation rates within individual grains [32]. In this paper, the latter information is further utilized to calculate corresponding intragranular misorientation spreads. In doing so, we formulate two algorithms to predict accumulation of intragranular misorientations based on time integration of first and second moments of the rotation rate fields. The two approaches are applied to uniaxial tension of copper and plane-strain compression of aluminum. The predictions are compared with experimental measurements and also with predictions using the full-field viscoplastic FFT-based (VPFFT) model. Considering the approximations involved in the formulation of the proposed mean-field model, reasonable agreement with experiments and the VPFFT model predictions is demonstrated for both approaches.

2 Modeling framework

In what follows we provide a short summary of the VPSC model, including the expressions to calculate second moments of the micromechanical fields in the grains. In our notation, tensors are denoted by bold letters while scalars and tensor components are indicated in italics and not bold. The contracted product and the tensor product between two tensors are denoted by ":" and "$\otimes$", respectively. The constitutive relationship between the viscoplastic strain rate, $\dot{\boldsymbol{\varepsilon}}$, and the deviatoric stress, $\boldsymbol{\sigma}$, at material point $\mathbf{x}$ is given by the rate-sensitivity equation:

$$\dot{\boldsymbol{\varepsilon}}(\mathbf{x}) = \sum_s \dot{\gamma}^s(\mathbf{x})\mathbf{m}^s(\mathbf{x}) = \dot{\gamma}_0 \sum_s \left(\frac{\boldsymbol{\sigma}(\mathbf{x}):\mathbf{m}^s(\mathbf{x})}{\tau_c^s(\mathbf{x})}\right)^n \text{sign}\big(\boldsymbol{\sigma}(\mathbf{x}):\mathbf{m}^s(\mathbf{x})\big)\,\mathbf{m}^s(\mathbf{x}). \tag{1}$$

The constitutive parameters τ_c^s, $\dot{\gamma}_0$, and n are the critical resolved shear stress of slip system s, a reference shear rate, and the inverse of the rate sensitivity; $\dot{\gamma}^s$ is the shear rate and $\mathbf{m}^s$ is the symmetric part of the Schmid tensor, given by:

$$\mathbf{m}^s(\mathbf{x}) = \frac{1}{2}\left(\mathbf{b}^s(\mathbf{x}) \otimes \mathbf{n}^s(\mathbf{x}) + \mathbf{n}^s(\mathbf{x}) \otimes \mathbf{b}^s(\mathbf{x})\right), \tag{2}$$

with $\mathbf{n}^s$ and $\mathbf{b}^s$ denoting, respectively, the slip plane normal and the Burgers vector of slip system s.

The plastic *spin*, $\dot{\boldsymbol{\omega}}^p$, at material point $\mathbf{x}$ is given by:

$$\dot{\boldsymbol{\omega}}^p(\mathbf{x}) = \sum_s \dot{\gamma}^s(\mathbf{x})\boldsymbol{\alpha}^s(\mathbf{x}), \tag{3}$$

where $\boldsymbol{\alpha}^s(\mathbf{x}) = \frac{1}{2}\left(\mathbf{b}^s(\mathbf{x}) \otimes \mathbf{n}^s(\mathbf{x}) - \mathbf{n}^s(\mathbf{x}) \otimes \mathbf{b}^s(\mathbf{x})\right)$ is the antisymmetric part of the Schmid tensor of slip system s. By performing linearization of the nonlinear constitutive relationships, we obtain the following expressions:

$$\dot{\boldsymbol{\varepsilon}}(\mathbf{x}) = \mathbf{M}^{(r)} : \boldsymbol{\sigma}(\mathbf{x}) + \dot{\boldsymbol{\varepsilon}}^{0(r)}, \tag{4}$$

$$\dot{\gamma}^s(\mathbf{x}) = \eta^{s(r)}\tau^s(\mathbf{x}) + \dot{g}^{0s(r)}, \tag{5}$$

where $\tau^s(\mathbf{x}) = \mathbf{m}^s(\mathbf{x}):\boldsymbol{\sigma}(\mathbf{x})$ is the resolved shear stress on slip system s. $\mathbf{M}^{(r)}$ and $\dot{\boldsymbol{\varepsilon}}^{0(r)}$ are the linearized compliance and the back-extrapolated strain rate for grain r, respectively, while $\eta^{s(r)}$ and $\dot{g}^{0s(r)}$ are the linearized compliance and the back-extrapolated shear rate of slip system s in grain r, respectively. These moduli depend on the adopted linearization procedure. In what follows, we assume an affine linearization [33].

In order to obtain the macroscopic response of the linear polycrystal, we perform a self-consistent homogenization, which implies a similar linear constitutive relation for the effective medium:

$$\dot{\mathbf{E}} = \bar{\mathbf{M}} : \boldsymbol{\Sigma} + \dot{\mathbf{E}}^0, \tag{6}$$

$\dot{\mathbf{E}}$ and $\boldsymbol{\Sigma}$ are the macroscopic strain rate and stress and $\bar{\mathbf{M}}$ and $\dot{\mathbf{E}}^0$ are the macroscopic compliance and back-extrapolated strain rate, respectively. Within the self-consistent scheme every grain r is treated as an ellipsoidal inhomogeneity embedded in the effective medium. This problem is solved using the equivalent inclusion approach [34] and the following interaction equation can be derived [15]:

$$\tilde{\boldsymbol{\varepsilon}}^{(r)} = -\tilde{\mathbf{M}} : \tilde{\boldsymbol{\sigma}}^{(r)}, \tag{7}$$

where $\tilde{\boldsymbol{\varepsilon}}$ and $\tilde{\boldsymbol{\sigma}}$ are the deviations of strain rate and stress in grain r from the macroscopic values. The interaction tensor $\tilde{\mathbf{M}} = (\mathbf{I} - \mathbf{S})^{-1} : \mathbf{S} : \bar{\mathbf{M}}$ is a function of the classical (symmetric) Eshelby tensor, $\mathbf{S}$, and the unknown macroscopic compliance can be derived from the self-consistent equations:

$$\bar{\mathbf{M}} = \langle \mathbf{M}^{(r)} \mathbf{B}^{(r)} \rangle, \tag{8}$$

$$\dot{\mathbf{E}}^0 = \langle \mathbf{M}^{(r)} \mathbf{b}^{(r)} + \dot{\boldsymbol{\varepsilon}}^{0(r)} \rangle, \tag{9}$$

where $\mathbf{B}^{(r)}$ and $\mathbf{b}^{(r)}$ are the stress localization tensors, which are functions of the microscopic and macroscopic moduli. The self-consistent equations are, therefore, implicit in $\bar{\mathbf{M}}$ and $\dot{\mathbf{E}}^0$ and need to be solved iteratively using a fixed-point method based on Eqs. (8-9). The reorientation rate of the ellipsoid is given by:

$$\tilde{\boldsymbol{\omega}}^{(r)} = \boldsymbol{\Pi} : \mathbf{S}^{-1} : \tilde{\boldsymbol{\varepsilon}}^{(r)}, \tag{10}$$

where $\boldsymbol{\Pi}$ is the antisymmetric Eshelby tensor. Assuming that the applied macroscopic rigid body rotation rate is equal to zero (as is the case for all of the performed simulations in this work) the total rate of lattice rotation at the material point can be written as:

$$\dot{\boldsymbol{\omega}}^{(r)}(\mathbf{x}) = \tilde{\dot{\boldsymbol{\omega}}}^{(r)} - \dot{\boldsymbol{\omega}}^p(\mathbf{x}). \tag{11}$$

Once the self-consistent scheme converges, second moments of stress within each grain r can be calculated as [30]:

$$\langle \boldsymbol{\sigma} \otimes \boldsymbol{\sigma} \rangle^{(r)} = \frac{2}{c^{(r)}} \frac{\partial \tilde{U}_T}{\partial \mathbf{M}^{(r)}}, \tag{12}$$

where $c^{(r)}$ is the grain volume fraction and $\tilde{U}_T$ represents the effective potential given by:

$$\tilde{U}_T = \frac{1}{2} \bar{\mathbf{M}} :: (\boldsymbol{\Sigma} \otimes \boldsymbol{\Sigma}) + \dot{\mathbf{E}}^0 : \boldsymbol{\Sigma} + \frac{1}{2} \bar{G}. \tag{13}$$

The additional term $\bar{G}$ is the energy under zero applied stress. The second moment of the lattice rotation-rate within grain r can be calculated as [32]:

$$\langle \dot{\boldsymbol{\omega}} \otimes \dot{\boldsymbol{\omega}} \rangle^{(r)} = \langle \dot{\boldsymbol{\omega}}^p \otimes \dot{\boldsymbol{\omega}}^p \rangle^{(r)} + \tilde{\dot{\boldsymbol{\omega}}}^{(r)} \otimes \tilde{\dot{\boldsymbol{\omega}}}^{(r)} - \tilde{\dot{\boldsymbol{\omega}}}^{(r)} \otimes \langle \dot{\boldsymbol{\omega}}^p \rangle^{(r)} - \langle \dot{\boldsymbol{\omega}}^p \rangle^{(r)} \otimes \tilde{\dot{\boldsymbol{\omega}}}^{(r)}. \tag{14}$$

Eq. (5) implies linearity between the plastic spin and stress. As a result, an expression for the second moment of plastic spin, $\langle \dot{\boldsymbol{\omega}}^p \otimes \dot{\boldsymbol{\omega}}^p \rangle^{(r)}$ can be obtained as a function of the first and second moments of stress [32]:

$$\langle \dot{\boldsymbol{\omega}}^p \otimes \dot{\boldsymbol{\omega}}^p \rangle^{(r)} = \left\{ \sum_{k,k'} \left(\eta^{k(r)} \eta^{k'(r)} \right) \left(\boldsymbol{\alpha}^{k(r)} \otimes \boldsymbol{\alpha}^{k'(r)} \right) \otimes \left(\mathbf{m}^{k(r)} \otimes \mathbf{m}^{k'(r)} \right) \right\} :: \langle \boldsymbol{\sigma} \otimes \boldsymbol{\sigma} \rangle^{(r)}$$

$$+ \left\{ \sum_{k,k'} \left(\boldsymbol{\alpha}^{k(r)} \otimes \boldsymbol{\alpha}^{k'(r)} \right) \otimes \left[\left(\eta^{k(r)} \dot{g}^{0k'(r)} \right) \mathbf{m}^{k(r)} + \left(\eta^{k'(r)} \dot{g}^{0k(r)} \right) \mathbf{m}^{k'(r)} \right] \right\} : \langle \boldsymbol{\sigma} \rangle^{(r)}$$

$$+ \sum_{k,k'} \left(\boldsymbol{\alpha}^{k(r)} \otimes \boldsymbol{\alpha}^{k'(r)} \right) \left(\dot{g}^{0k(r)} \dot{g}^{0k'(r)} \right). \tag{15}$$

Since $\langle \dot{\boldsymbol{\omega}}^p \rangle^{(r)} = \dot{\boldsymbol{\omega}}^{p(r)}$ is calculated based on the mean value of stress, the remaining terms in Eq. (14) can be readily evaluated. The covariance [35] of lattice rotation rate fluctuations is given by:

$$\langle \delta\dot{\boldsymbol{\omega}} \otimes \delta\dot{\boldsymbol{\omega}} \rangle^{(r)} = \langle \dot{\boldsymbol{\omega}} \otimes \dot{\boldsymbol{\omega}} \rangle^{(r)} - \langle \dot{\boldsymbol{\omega}} \rangle^{(r)} \otimes \langle \dot{\boldsymbol{\omega}} \rangle^{(r)} = \langle \dot{\boldsymbol{\omega}}^p \otimes \dot{\boldsymbol{\omega}}^p \rangle^{(r)} - \langle \dot{\boldsymbol{\omega}}^p \rangle^{(r)} \otimes \langle \dot{\boldsymbol{\omega}}^p \rangle^{(r)}, \tag{16}$$

where $\delta\dot{\boldsymbol{\omega}}(\mathbf{x}) = \dot{\boldsymbol{\omega}}^{(r)}(\mathbf{x}) - \langle\dot{\boldsymbol{\omega}}^{(r)}\rangle$ represents the fluctuation of the lattice rotation rate. Consequently, the fluctuation of the rotation rate within a grain is determined by the fluctuation of plastic spin since the reorientation rate of the ellipsoid does not vary within the grain.

Finally, we turn our attention to the problem of incrementally updating the orientation field within grain r using the available expressions for the moments of the rotation rate field. We assume that the orientation field within grain r at the beginning of the current time increment, t, is known. In order to obtain the expression for the first and second moments of the orientation field at the end of the time increment, $t + \Delta t$, two approaches are considered: (1) a *Taylor expansion approximation* of misorientations and (2) a *discrete approximation* of misorientations. The two approaches will be compared with each other, with experiments and full-field simulation results.

2.1   Taylor expansion approximation of misorientations

In what follows, we use (unit) quaternion representation of crystal orientations and rotations. Quaternions are represented in matrix form [36], so that matrix algebra and notation can be used in the derivations. The matrix representation of quaternions is recalled in Appendix A. The orientation update at a material point $\mathbf{x}$ is given by:

$$\mathbf{q}^{t+\Delta t}(\mathbf{x}) = \mathbf{q}^t_{inc}(\mathbf{x})\mathbf{q}^t(\mathbf{x}), \tag{17a}$$

$$q_{ij}^{t+\Delta t}(\mathbf{x}) = (q^t_{inc})_{ik}(\mathbf{x})q^t_{kj}(\mathbf{x}) \quad \text{(in index notation, with indices going from 1 to 4)}, \tag{17b}$$

where $\mathbf{q}^t_{inc}(\mathbf{x})$ represents the active incremental rotation (expressed in sample frame) at time t and $\mathbf{q}^t(\mathbf{x})$ and $\mathbf{q}^{t+\Delta t}(\mathbf{x})$ represent the active rotations (also expressed in sample frame) that rotate the sample frame into alignment with the crystal frame at times t and $t + \Delta t$, respectively. Next, we express the crystal orientation at each material point $\mathbf{x}$ composing the mean rotation of

grain r to which the material point belongs and the local misorientation with respect to this average:

$$\mathbf{q}^{t+\Delta t}(\mathbf{x}) = \delta\mathbf{q}^{t+\Delta t}(\mathbf{x})\overline{\mathbf{q}}^{t+\Delta t(r)}, \tag{18}$$

where the bar over a quaternion denotes the mean rotation of the grain and the δ in front of a quaternion denotes the misorientation with respect to that mean. By assuming analogous relations for $\mathbf{q}^t_{inc}(\mathbf{x})$ and $\mathbf{q}^t(\mathbf{x})$ we get:

$$\delta\mathbf{q}^{t+\Delta t}(\mathbf{x})\overline{\mathbf{q}}^{t+\Delta t(r)} = \left(\delta\mathbf{q}^t_{inc}(\mathbf{x})\overline{\mathbf{q}}^{t(r)}_{inc}\right)\left(\delta\mathbf{q}^t(\mathbf{x})\overline{\mathbf{q}}^{t(r)}\right). \tag{19}$$

Assuming that $\overline{\mathbf{q}}^{t+\Delta t(r)} \approx \overline{\mathbf{q}}^{t(r)}_{inc}\overline{\mathbf{q}}^{t(r)}$ and right multiplying both sides of Eq. (19) by $\overline{\mathbf{q}}^{t+\Delta t(r)^{-1}}$ leads to:

$$\delta\mathbf{q}^{t+\Delta t}(\mathbf{x}) = \delta\mathbf{q}^t_{inc}(\mathbf{x})\delta\mathbf{q}^{t,rot}(\mathbf{x}), \tag{20}$$

where $\delta\mathbf{q}^{t,rot}(\mathbf{x}) = \overline{\mathbf{q}}^{t(r)}_{inc}\delta\mathbf{q}^t(\mathbf{x})\overline{\mathbf{q}}^{t(r)^{-1}}_{inc}$ is the rotated misorientation at time t. The misorientation at time t, $\delta\mathbf{q}^t(\mathbf{x})$, represents a physical quantity: the rotation from the mean orientation to the orientation at material point $\mathbf{x}$. The operation $\overline{\mathbf{q}}^{t(r)}_{inc}(...)\overline{\mathbf{q}}^{t(r)^{-1}}_{inc}$ rotates the quantity in parenthesis by $\overline{\mathbf{q}}^{t(r)}_{inc}$. Hence, the rotated misorientation, $\delta\mathbf{q}^{t,rot}(\mathbf{x})$, represents the misorientation at time t, $\delta\mathbf{q}^t(\mathbf{x})$, rotated in space by the mean increment in rotation, $\overline{\mathbf{q}}^{t(r)}_{inc}$. The misorientation angle with respect to the mean orientation of the grain associated to the quaternion $\delta\mathbf{q}^t(\mathbf{x})$ will not change during this rotation to $\delta\mathbf{q}^{t,rot}(\mathbf{x})$. However, the misorientation axis associated to the rotated quaternion $\delta\mathbf{q}^{t,rot}(\mathbf{x})$ is physically rotated in space by the mean increment in rotation when compared to misorientation axis of $\delta\mathbf{q}^t(\mathbf{x})$.

To simplify the notation, in what follows we shall not explicitly write the spatial dependence of the quaternions with the material point $\mathbf{x}$. According to Eq. (20), $\delta\mathbf{q}^{t+\Delta t}$ is a function of two independent variables, $\delta\mathbf{q}_{inc}^t$ and $\delta\mathbf{q}^{t,rot}$, whose distributions, defined by their first and second moments, can be calculated. Explicit expressions for first and second moments of a function in terms of first and second moments of the corresponding variables are available only for linear functions of those variables. Therefore, we perform a first-order Taylor expansion of $\delta\mathbf{q}^{t+\Delta t}$ with respect to the variables $\delta\mathbf{q}_{inc}^t$ and $\delta\mathbf{q}^{t,rot}$ so that we can derive explicit expressions for first and second moments of $\delta\mathbf{q}^{t+\Delta t}$. The natural choice of the reference points for this Taylor expansion are the mean values of variables $\delta\mathbf{q}_{inc}^t$ and $\delta\mathbf{q}^{t,rot}$, which leads to the following linearized expression [37]:

$$\delta\mathbf{q}^{t+\Delta t} \approx \langle\delta\mathbf{q}_{inc}^t\rangle^{(r)}\langle\delta\mathbf{q}^{t,rot}\rangle^{(r)} + \frac{\partial\delta\mathbf{q}^{t+\Delta t}}{\partial\delta\mathbf{q}_{inc}^t}\bigg|_{\langle\delta\mathbf{q}_{inc}^t\rangle^{(r)},\langle\delta\mathbf{q}^{t,rot}\rangle^{(r)}} : \left(\delta\mathbf{q}_{inc}^t - \langle\delta\mathbf{q}_{inc}^t\rangle^{(r)}\right)$$

$$+ \frac{\partial\delta\mathbf{q}^{t+\Delta t}}{\partial\delta\mathbf{q}^{t,rot}}\bigg|_{\langle\delta\mathbf{q}_{inc}^t\rangle^{(r)},\langle\delta\mathbf{q}^{t,rot}\rangle^{(r)}} : \left(\delta\mathbf{q}^{t,rot} - \langle\delta\mathbf{q}^{t,rot}\rangle^{(r)}\right). \tag{21}$$

The volume average of misorientations defined with respect to the mean orientation amounts to the identity rotation [38]: $\langle\delta\mathbf{q}_{inc}^t\rangle^{(r)} = \langle\delta\mathbf{q}^{t,rot}\rangle^{(r)} = \mathbf{I}$, where $\mathbf{I}$ represents the identity matrix (Kronecker delta) in 4-D. The derivatives evaluated around the mean misorientation lead to (in index notation, with indices from 1 to 4):

$$\frac{\partial\delta q_{ij}^{t+\Delta t}}{\partial(\delta q_{inc}^t)_{kl}}\bigg|_{\langle\delta q_{inc}^t\rangle^{(r)},\langle\delta q^{t,rot}\rangle^{(r)}} = I_{ik}I_{ml}\langle\delta q_{mj}^{t,rot}\rangle = I_{ik}I_{jl}, \tag{22}$$

$$\frac{\partial\delta q_{ij}^{t+\Delta t}}{\partial\delta q_{kl}^{t,rot}}\bigg|_{\langle\delta q_{inc}^t\rangle^{(r)},\langle\delta q^{t,rot}\rangle^{(r)}} = \langle(\delta q_{inc}^t)_{im}\rangle I_{mk}I_{jl} = I_{ik}I_{jl}. \tag{23}$$

Substitution into Eq. (21) leads to:

$$\delta \mathbf{q}^{t+\Delta t} \approx \delta \mathbf{q}_{inc}^{t} + \delta \mathbf{q}^{t,rot} - \mathbf{I}. \tag{24}$$

Therefore, the linearized expression based on first-order Taylor expansion of Eq. (20) is a simple summation of unit quaternions. Starting with Eq. (20) and assuming that the misorientations with respect to the mean are infinitesimal rotations, the same expression (Eq. (24)) can be derived.

Since only three independent parameters are required to fully describe an arbitrary rotation and the vector parts of misorientation quaternions can be used for quantification of orientation spreads [38], we re-write the above equation (replacing " $\approx$ " by " $=$ ") in terms of the vector parts of the misorientation quaternions (see Appendix A):

$$\delta \mathbf{r}^{t+\Delta t} = \delta \mathbf{r}_{inc}^{t} + \delta \mathbf{r}^{t,rot}. \tag{25}$$

The identity quaternion present in Eq. (24) vanishes since the vector part of identity quaternion is zero. Finally, the expressions for the first and second moments of the vector parts of misorientation quaternion are given as:

$$\langle \delta \mathbf{r}^{t+\Delta t} \rangle^{(r)} = \langle \delta \mathbf{r}_{inc}^{t} \rangle^{(r)} + \langle \delta \mathbf{r}^{t,rot} \rangle^{(r)} = \mathbf{0} \tag{26}$$

$$\langle \delta \mathbf{r}^{t+\Delta t} \otimes \delta \mathbf{r}^{t+\Delta t} \rangle^{(r)} = \langle \delta \mathbf{r}_{inc}^{t} \otimes \delta \mathbf{r}_{inc}^{t} \rangle^{(r)} + \langle \delta \mathbf{r}^{t,rot} \otimes \delta \mathbf{r}_{inc}^{t} \rangle^{(r)} + \langle \delta \mathbf{r}_{inc}^{t} \otimes \delta \mathbf{r}^{t,rot} \rangle^{(r)} +$$

$$+ \langle \delta \mathbf{r}^{t,rot} \otimes \delta \mathbf{r}^{t,rot} \rangle^{(r)}. \tag{27}$$

The first moments of the vector parts of misorientation quaternions vanish because of our choice for the mean orientation value, which implies that the second moment is already centered. Consequently, the second moment of the vector parts of misorientation quaternions is a suitable quantity for characterization of the orientation spread [38].

As it was noted before, the quaternion $\delta \mathbf{q}^{t,rot}$ is obtained by rotation of the quaternion $\delta \mathbf{q}^t$ in space by the mean increment in rotation $\bar{\mathbf{q}}_{inc}^{t(r)}$. Since we are now dealing with 3-dimensional Cartesian vectors, this rotation can be written compactly as:

$$\delta \mathbf{r}^{t,rot} = \bar{\mathbf{R}}_{inc}^{t,(r)} \delta \mathbf{r}^t \tag{28}$$

where $\bar{\mathbf{R}}_{inc}^t$ stands for the rotation matrix representation of the mean incremental rotation $\bar{\mathbf{q}}_{inc}^{t(r)}$. Then, the second moments appearing in expression (27) are given by:

$$\langle \delta \mathbf{r}^{t,rot} \otimes \delta \mathbf{r}^{t,rot} \rangle^{(r)} = \bar{\mathbf{R}}_{inc}^{t,(r)} \langle \delta \mathbf{r}^t \otimes \delta \mathbf{r}^t \rangle^{(r)} \bar{\mathbf{R}}_{inc}^{t,(r)T} \tag{29}$$

$$\langle \delta \mathbf{r}^{t,rot} \otimes \delta \mathbf{r}_{inc}^t \rangle^{(r)} = \bar{\mathbf{R}}_{inc}^{t,(r)} \langle \delta \mathbf{r}^t \otimes \delta \mathbf{r}_{inc}^t \rangle^{(r)} \tag{30}$$

In Eq. (27), the rotated second moment of misorientation at time t, $\langle \delta \mathbf{r}^{t,rot} \otimes \delta \mathbf{r}^{t,rot} \rangle^{(r)}$, is calculated by rotating the available second moments of misorientation at time t by the mean increment in rotation, while the second moment of misorientation increments, $\langle \delta \mathbf{r}_{inc}^t \otimes \delta \mathbf{r}_{inc}^t \rangle^{(r)}$, can be calculated based on the first and second moments of the spin, $\langle \dot{\boldsymbol{\omega}} \rangle^{(r)}$ and $\langle \dot{\boldsymbol{\omega}} \otimes \dot{\boldsymbol{\omega}} \rangle^{(r)}$ (see Appendix B). It is important to note that these second moments are already centered and thus are equivalent to covariance matrices [38].

The term $\langle \delta \mathbf{r}^{t,rot} \otimes \delta \mathbf{r}_{inc}^t \rangle^{(r)}$ represents the cross-covariance between misorientations and misorientation increments at time t, and it is unknown at this point. We propose an approximation of cross-covariance term $\langle \delta \mathbf{r}^{t,rot} \otimes \delta \mathbf{r}_{inc}^t \rangle^{(r)}$ based on full-field VPFFT simulations for a face-centered cubic (FCC) polycrystal under tension assuming $\{111\}\langle 1\bar{1}0\rangle$ slip, a viscoplastic exponent of $n=10$, and no strain hardening. Thirty different Voronoi polycrystals of 400 grains initialized with exactly the same 400 random orientations, deformed in tension to a strain of 24%, were simulated for this purpose.

The following calculations are performed at three different strain levels (2%, 13% and 24% tensile strain) for each grain within each realization of the Voronoi polycrystal. We begin by calculating the eigenvectors $\mathbf{v}^{i,t,rot}$ and $\mathbf{v}_{inc}^{i,t}$ and eigenvalues $\lambda^{i,t,rot}$ and $\lambda_{inc}^{i,t}$ of $\langle \delta\mathbf{r}^{t,rot} \otimes \delta\mathbf{r}^{t,rot} \rangle^{(r)}$ and $\langle \delta\mathbf{r}_{inc}^{t} \otimes \delta\mathbf{r}_{inc}^{t} \rangle^{(r)}$, respectively. In both cases, the eigenvalues essentially represent variances (i.e. the squares of the standard deviations, SD_i) along corresponding eigenvectors, which, due to the symmetry of the above matrices, form an orthonormal basis of principal axes. The eigenvector corresponding to the largest eigenvalue represents the direction of greatest variation, while the eigenvector corresponding to smallest eigenvalue represents the direction of least variation. The eigenvalues are ordered in descending order and the corresponding eigenvectors are stacked as columns into matrices that transform (note these are not active rotation tensors but coordinate transformation matrices) from principal axes to sample axes: $\mathbf{Q}^{t,rot} = [\mathbf{v}^{1,t,rot}, \mathbf{v}^{2,t,rot}, \mathbf{v}^{3,t,rot}]$ and $\mathbf{Q}_{inc}^{t} = [\mathbf{v}_{inc}^{1,t}, \mathbf{v}_{inc}^{2,t}, \mathbf{v}_{inc}^{3,t}]$. The cross-covariance term $\langle \delta\mathbf{r}^{t,rot} \otimes \delta\mathbf{r}_{inc}^{t} \rangle$ can now be written as:

$$\langle \delta\mathbf{r}^{t,rot} \otimes \delta\mathbf{r}_{inc}^{t} \rangle^{(r)} = \mathbf{Q}^{t,rot} \langle \delta\mathbf{r}^{p,t,rot} \otimes \delta\mathbf{r}_{inc}^{p,t} \rangle^{(r)} (\mathbf{Q}_{inc}^{t})^{T}, \tag{31}$$

where $\delta\mathbf{r}^{p,t,rot}$ and $\delta\mathbf{r}_{inc}^{p,t}$ represent the misorientation and the increment in misorientation, respectively, expressed in the corresponding principal axes associated with their respective covariance matrices.

The cross-correlation matrix can then be expressed as:

$$\langle \delta r_i^{p,t,rot} (\delta r_{inc}^{p,t})_j \rangle^{(r)} = \rho_{ij}^{(r)} \sqrt{\lambda^{i,t,rot}} \sqrt{\lambda_{inc}^{j,t}} \text{ (no sumation over } i \text{ or } j). \tag{32}$$

The cross-correlation coefficient $\rho_{ij}^{(r)}$ represents the strength of linear dependence between variables. The maximal value of $\rho_{ij}^{(r)}$ is 1 and indicates perfect correlation while the minimal

value of -1 represents a prefect anti-correlation. Uncorrelated variables will have a correlation coefficient of 0.

The cross-correlation matrices $\rho_{ij}^{(r)}$ for a grain r of specific orientation were averaged over the thirty different realizations of the Voronoi polycrystals. These matrices turned out to be strongly diagonal after averaging, with fairly similar diagonal values for the entire set of grains. This implies that a strong positive cross-covariance exists between misorientations and increments of misorientation along the corresponding principal directions of largest variation. Analogously, there is also a strong positive cross-covariance between misorientations and increments of misorientation along the corresponding principal directions of medium variation and least variation.
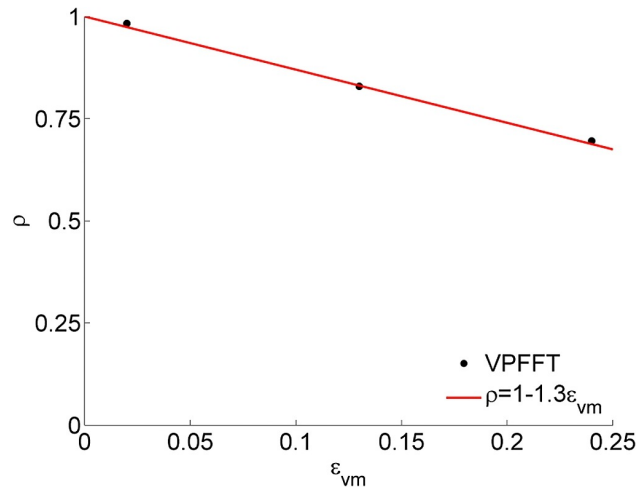
Fig. 1. Correlation parameter ρ derived from VPFFT simulation of 30 realizations of Voronoi polycrystals with 400 grains as an average over all grains at three different strain levels fitted with linear function.

We simplify our analysis even further by averaging cross-correlation matrices over all grains of all orientations and diagonal elements to define the cross-correlation at each strain level by a single value ρ. A linear dependence of ρ on the von Mises strain was observed at low strains in the VPFFT simulations and approximated as:

$$\rho \approx \rho_0 - \rho_1 \varepsilon_{VM} \tag{33}$$

where $\rho_0 = 1$ represents the cross-correlation coefficient at the beginning of deformation and $\rho_1 = 1.3$ represents the strength of the cross-correlation decay with strain (Figure 1).

In the full-field simulations outlined above, a strong correlation between $\delta \mathbf{r}^{t,rot}$ and $\delta \mathbf{r}^t_{inc}$ is evident. Neglecting the cross-covariance term in the mean-field model would hence result in poor correspondence between the VPFFT and VPSC simulations. With the approximation of the cross-correlation coefficient, $\rho(\varepsilon_{VM})$, we can easily calculate the cross-covariance $\langle \delta \mathbf{r}^{t,rot} \otimes \delta \mathbf{r}^t_{inc} \rangle^{(r)}$ at any given strain level within the VPSC model.

2.2 Discrete approximation of misorientations

For this approximation, we start from the equation for the local orientation update (Eq. 17). As we noted before, orientation, $\mathbf{q}^t(\mathbf{x})$, and rotation increment, $\mathbf{q}^t_{inc}(\mathbf{x})$, at time t vary within the grain. Thus, there are certain distributions associated with the orientations and rotation increments at time t within each grain. Consequently, there is a distribution associated with the updated orientations, $\mathbf{q}^{t+\Delta t}(\mathbf{x})$, as well. If we assume each one of these distributions is represented by a discrete set, we obtain a discretized form of Eq. (17):

$$\mathbf{q}^{t+\Delta t, i} = \mathbf{q}^{t,i}_{inc} \mathbf{q}^{t,i} \; ; \; i = 1, n \; \text{(no summation over } i\text{).} \tag{34}$$

The discrete set of n orientations, $\mathbf{q}^{t,i}$, representing the distribution of orientations within the grain at time t is assumed to be known. 27 discrete values within a set are used to describe any distribution assuming that the orientation distribution can be described as multivariate normal distribution (see Appendix C). The discrete set of 27 rotation increments, $\mathbf{q}^{t,i}_{inc}$, representing the distribution of rotation increments within the grain at time t can be calculated based on the first and second moments of rotation rates, $\langle \dot{\boldsymbol{\omega}} \rangle^{(r)}$ and $\langle \dot{\boldsymbol{\omega}} \otimes \dot{\boldsymbol{\omega}} \rangle^{(r)}$, given by Eq. (11) and (14) in the

following way. First, we assume that the distribution associated with the rotation rates, $\dot{\boldsymbol{\omega}}$, is also a multivariate normal distribution. Next, using the first and second moments of rotation rates, we construct a discrete set of values, $\dot{\boldsymbol{\omega}}^{t,i}$, which represents the associated distribution (details are given in Appendix C). Finally, a discrete set of rotation increments is calculated as:

$$\mathbf{q}_{inc}^{t,i} = \begin{Bmatrix} \cos\left(\frac{|\dot{\boldsymbol{\omega}}^{t,i}|\Delta t}{2}\right) \\ \sin\left(\frac{|\dot{\boldsymbol{\omega}}^{t,i}|\Delta t}{2}\right)\frac{\dot{\boldsymbol{\omega}}^{t,i}}{|\dot{\boldsymbol{\omega}}^{t,i}|} \end{Bmatrix}. \tag{35}$$

Once both sets $\mathbf{q}^{t,i}$ and $\mathbf{q}_{inc}^{t,i}$ are known, the cross-correlation between the rotation increments and orientations needs to be determined. Specifically, we must determine which increment of rotation, $\mathbf{q}_{inc}^{t,i}$, from the set representing the distribution of rotation increments, corresponds to which orientation, $\mathbf{q}^{t,i}$, from the orientation set. Only then we can calculate the discrete set of n updated orientations, $\mathbf{q}^{t+\Delta t,i}$, using Eq. (34). Note that we needed to approximate a similar type of cross-correlation in the previous approach. In what follows, a specific pairing between the elements of two sets $\mathbf{q}^{t,i}$ and $\mathbf{q}_{inc}^{t,i}$ will be proposed.

The number of possible pairings between two sets $\mathbf{q}^{t,i}$ and $\mathbf{q}_{inc}^{t,i}$ with n elements is $n!$. Each one of these pairings corresponds to a different cross-correlation between the increments in rotation and the orientations. If we approximate the cross-correlation based on the results of the VPFFT simulations (as we did for the Taylor expansion approximation) then we have to find the pairing that would result in the resolved cross-correlation. This becomes a difficult task when we consider the number of possible pairings for $n=27$.

In order to choose a paring between sets $\mathbf{q}^{t,i}$ and $\mathbf{q}_{inc}^{t,i}$ we make the following assumption: if the orientation of a point within the grain reorients in a certain way during the current increment,

then that same point will reorient in a similar manner in the next increment. This implies that a strong positive cross-correlation exists between increments in rotation from two subsequent time steps ($\mathbf{q}_{inc}^{t,i}$ and $\mathbf{q}_{inc}^{t-\Delta t,i}$). Therefore, we adopt such pairing between discrete increments in rotation from current, $\mathbf{q}_{inc}^{t,i}$, and previous increment, $\mathbf{q}_{inc}^{t-\Delta t,i}$, that results in the strongest possible positive cross-correlation. Finding such a pairing is not difficult, since these two sets are quite similar considering that they correspond to two subsequent increments. Consequently, we have also defined the pairing between $\mathbf{q}_{inc}^{t,i}$ and $\mathbf{q}^{t,i}$, since the pairing between $\mathbf{q}_{inc}^{t-\Delta t,i}$ and $\mathbf{q}^{t,i}$ is available from the previous increment. Therefore, the achieved correlation between the rotation increments, $\mathbf{q}_{inc}^{t,i}$, and orientations, $\mathbf{q}^{t,i}$, is a consequence of the assumed correlation between rotation increments from two subsequent steps $\mathbf{q}_{inc}^{t,i}$ and $\mathbf{q}_{inc}^{t-\Delta t,i}$.

Once the updated set of orientations $\mathbf{q}^{t+\Delta t,i}$ is obtained, the mean orientation, misorientations with respect to the mean orientation, and their second moments can be easily calculated [38]. In the discrete approach the updating of orientations is done in the proper way (Eq. (34)), while in the Taylor expansion approach we used a first order Taylor approximation (Eq. (21)). Certain errors will come from the fact that all of the distributions are represented with only a finite number of points (27 in our simulations). However, the biggest issue of the discrete approach is related to the fact that the cross-correlation of rotation increments between two subsequent time steps is always assumed as the strongest possible. Consequently, we should expect to obtain large orientation spreads along largest principal direction.

In both approaches the intragranular stress distributions drive the development of intragranular misorientation. On the other hand, in the previous attempts for prediction of intragranular misorientation implemented within VPSC, different reorientations of grains from

co-rotation with their respective neighbors was considered as driving force for the misorientation evolution, interpreting the developing intergranular misorientation distribution between grains of same initial orientation simply as intragrain misorientation distribution of grains with this initial orientation [20, 22]. As the reorientation is completely determined by the grains neighborhood defined usually in a random manner, the predicted misorientation distributions were practically independent of the particular grain orientation and completely unrelated to existing intragranular distributions of micromechanical fields.

3   Results and discussion

In what follows, we exercise the two developed models on two FCC materials and compare the results to experiments and simulation results obtained by the full-field VPFFT model [11, 39]. In all the simulations, it is assumed that the grains deform by $\{111\}\langle 1\bar{1}0\rangle$ slip with a viscoplastic power-law exponent of $n=10$ without any strain hardening. For every grain, the mean orientation and second order moment of misorientation distribution are calculated as described above. The Taylor expansion approximation provides these quantities as an output. The dominant axis of rotation is defined as the principal direction of misorientation covariance matrix corresponding to the largest standard deviation [38, 40]. As a measure of the magnitude of the misorientation spread, we use the equivalent isotropic spread calculated as the geometrical mean of the three standard deviations $SD = \sqrt[3]{SD1 \times SD2 \times SD3}$ [41]. The specific case studies considered are uniaxial tension of Cu and plane-strain compression of Al.

3.1   Tension of polycrystalline copper

We simulate tension of polycrystalline Cu to a strain of 11% with the VPSC model accounting for intragranular misorientation evolution using the Taylor expansion approximation
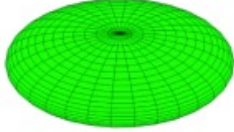
and the discrete approximation of misorientations, on the one hand; and with VPFFT, on the other hand. The initial texture of the recrystallized Cu sample is represented by 400 grains (Figure 2). These grains are assumed to be initially spherical for the VPSC simulations and to be arranged in a Voronoi tessalation microstructural cell in case of the VPFFT model. Predictions of the intragranular misorientation distributions are compared with experimental results published in [39].
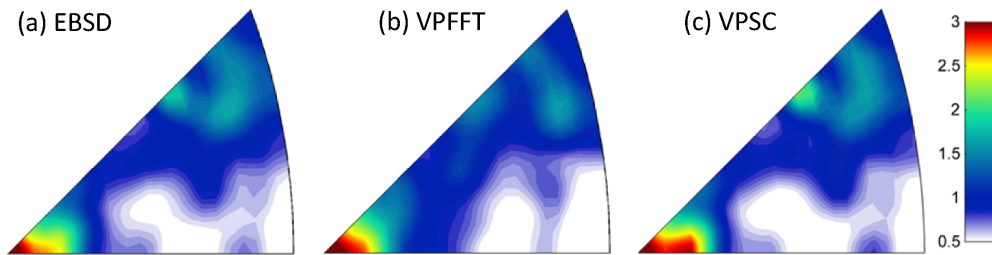
Fig. 2. Inverse pole figures for the crystallographic direction along the tensile axis illustrating the measured initial texture (a) and the initial textures used in VPFFT (b) and VPSC (c) simulations.

For the experimental results obtained by EBSD, only grains with more than 350 indexed scan points (corresponding to an apparent area larger than 1400 μm^2) are considered, to facilitate comparisons. Small grains in two-dimensional EBSD scans could correspond to sections close to the center of mass of small grains within the sample or they could represent sections far away from the center of mass of larger grains. In the former case, the obtained misorientation distribution might not be representative, since the deformation within small grains might be influenced greatly by its larger neighbors [39]. In the latter case, the misorientation distribution is not representative since we have sampled only small and localized number of points within a large grain. In addition, the evolution in small parts of a large grain is also affected by the neighbors.

Table 1. Shapes of the misorientation distribution classified according to the ratios between standard deviations along principal directions. This classification is a variation of the one proposed by [41].

	$\dfrac{SD1}{SD2} \leq 1.5$	$\dfrac{SD1}{SD2} > 1.5$
$\dfrac{SD2}{SD3} \leq 1.5$	Sphere	Prolate
$\dfrac{SD2}{SD3} > 1.5$	Oblate	

The shapes of the misorientation distributions are classified into three categories (see Table 1) according to the ratios of the standard deviations along principal directions. This classification is a variation of the one proposed by [41] with the classes "ellipsoid" and "prolate" merged into a single "prolate" category. Figure 3 compares the dependence between shapes of misorientation distributions and orientation for all of the considered cases. Whereas EBSD and VPFFT results show variations of the shape for similar orientations, VPSC subdivides the triangle into certain regions preferring a singular type. This is expected since in VPSC there is no neighborhood effect and behavior of every grain is defined solely by its orientation. Table 2 indicates that fractions of different distribution shapes are similar between all cases. In the EBSD and VPFFT results, spherical shapes develop in regions close to [111] and [001], while in VPSC spherical shapes concentrate only around [111]. Prolate shapes seem to be spread out over the entire IPF in the EBSD and VPFFT results. VPSC predicts relatively similar trends but with special regions, where no prolates are found. Oblate shapes also seem to be distributed evenly for the EBSD and

VPFFT results, while VPSC predictions of oblates are concentrated around [111], [001] and [114] to [112].
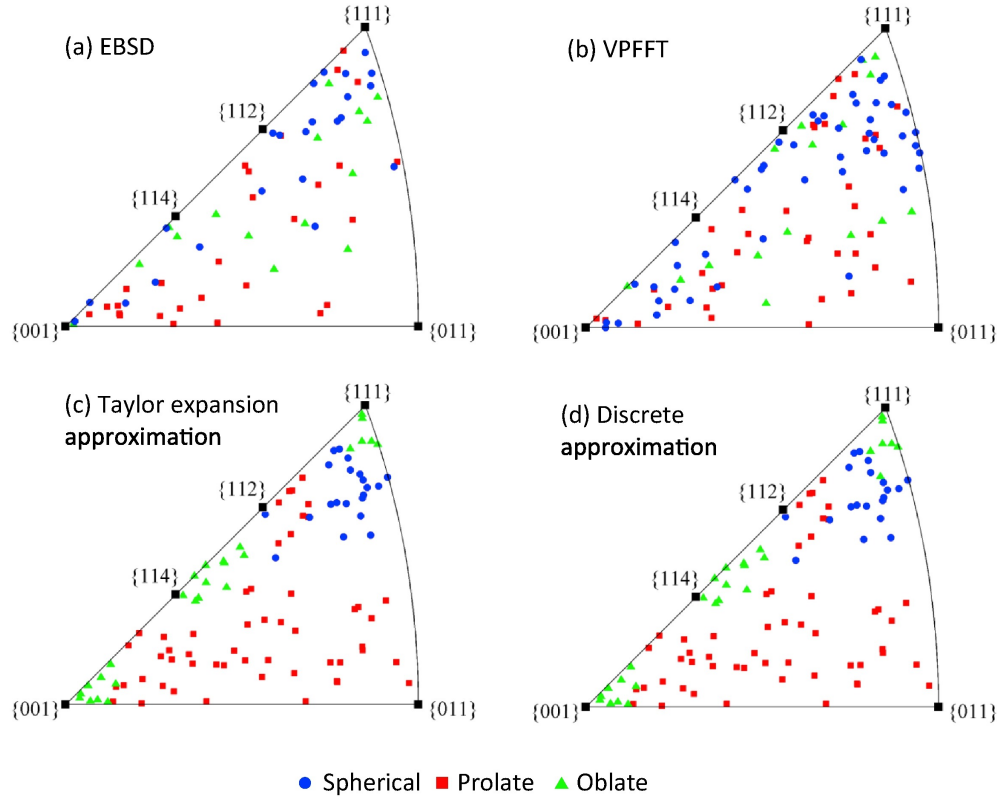
Fig 3. Shapes of misorientation spreads at 11% tensile strain categorized according to Table 1 plotted as inverse pole figures for (a) EBSD data, (b) full-field VPFFT results, (c) Taylor expansion approximation and (d) discrete approximation approaches. For better visualization, plots of simulation results are for 100 grains randomly picked from the simulated polycrystals. For the both VPSC simulations the same 100 grains are used.

Figure 4 compares the direction of the dominant rotation axes of grains with oblate and prolate misorientation distribution shapes plotted in the sample frame. The dominant rotation axes predominantly lie in a plane perpendicular to the tension direction in the simulation results. On the other hand, the experimental results show a considerably weaker trend of the dominant rotation axes to align perpendicular to the tension direction, with much more scatter.

Table 2. Fractions of different distribution shapes after 11% tensile deformation of copper obtained from experimental data, VPFFT simulation, Taylor expansion approximation and discrete approximation approach.

	EBSD	VPFFT	Taylor expansion approx.	Discrete approx.
Prolate	42%	40%	50%	50%
Oblate	23%	17%	24%	24%
Sphere	35%	43%	26%	26%

The evolution of misorientation spread is determined by the plastic spin distribution which is in turn caused by the stress distribution within the grain. We can examine the sensitivity of the plastic spin components to fluctuations in stress by calculating the derivatives of plastic spin with respect to stress [42]:

$$\frac{\partial \dot{\omega}^p}{\partial \sigma} = \sum_s \frac{\partial \dot{\gamma}^s}{\partial \tau^s} \alpha^s \otimes m^s. \tag{36}$$

These calculations are performed using the VPSC model. The stress tensor and the symmetric Schmid tensor are represented as five dimensional vectors of the form [43]: $\sigma = \sqrt{2} \left(\frac{(\sigma_{33}-\sigma_{11})+(\sigma_{33}-\sigma_{22})}{2\sqrt{3}}, \frac{\sigma_{22}-\sigma_{11}}{2}, \sigma_{23}, \sigma_{13}, \sigma_{12} \right)$. The derivative of i-th component of plastic spin with respect to stress vector, $\frac{\partial \dot{\omega}_i^p}{\partial \sigma}$, represents a gradient vector in stress space, which defines the rate of change of i-th plastic spin component with respect to changes in stress. By examining the gradient vectors of each plastic spin component within the grains we find that the length of the gradient vector of the plastic spin component along the tension direction is considerably smaller than the lengths of the other two gradient vectors. Therefore, the plastic spin component in the tension direction is less sensitive to the fluctuations in stress than the other two components. Consequently, for isotropic fluctuations in stress, the fluctuations in plastic spin

will have only a small component in the tension direction which in turn causes the dominant

rotation axes to lie in the plane perpendicular to the tension direction. In addition, an anisotropic

shape of the stress distribution also affects the plastic spin distribution. However, the fact that the

dominant rotation axes are perpendicular to the tension direction in the simulations is

predominantly caused by the insensitivity of plastic spin component in the tension direction to

fluctuations in stress.
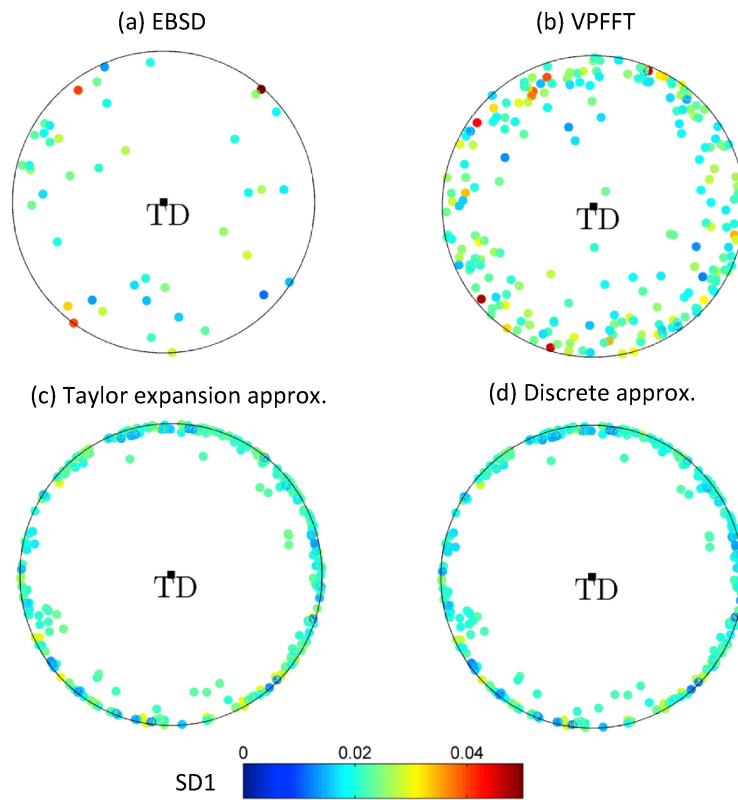
Fig. 4. Dominant rotation axes for oblate and prolate shapes plotted in the sample frame and color-coded according to magnitude of standard deviation along this direction for (a) EBSD data, (b) VPFFT results, (c) Taylor expansion approximation and (d) discrete approximation approach at 11% tensile strain. Tension direction (TD) is in the center of pole figures.

Figure 5 shows the predicted and experimental probability density functions (pdf) of the

standard deviations along the principal directions and the equivalent isotropic spreads. The pdfs

for the first two standard deviations match quite well for all considered cases. Both, VPFFT and

experimental pdfs of the smallest standard deviation display a single characteristic peak around 0.01. On the other hand, the VPSC pdfs of the smallest standard deviation develop an additional peak close to 0 indicating that the spread is almost two-dimensional within a certain number of grains. The occasionally small magnitude of the third standard deviation significantly reduces the magnitude of the corresponding equivalent isotropic spread and therefore the VPSC predictions for the pdfs of the equivalent isotropic spread also develop two peaks while corresponding pdfs from the VPFFT simulations and the experiment develop only one. In addition, we have also performed simulations up to a strain of 25% and compared the misorientation distribution shapes with experimental results published in [41] (Table 3). Prolate shapes dominate the region near [011] and other regions away from [001] or [111] both in the simulations and experimental results. According to Dillamore and Katoh (Dillamore and Katoh, 1974), grains with tensile axis on the line connecting [114] and [011] show divergent re-orientations and large orientation spreads within them are expected to develop along a particular axis. Due to such a strong orientation spread developing around a preferred axis, grains from divergent regions should develop prolate shapes of misorientation distribution which is in agreement with both simulation results and experiment (see the region near [110] and the remaining region away from [011] and [111] in Table 3). The regions near [001] and [111] are convergent and hence should develop lower orientation spreads [2]. While the experimental results reveal a rather high fraction of prolates above 50% even for these regions, the predictions of the simulations are significantly lower. In particular, a quite low fraction of prolates is expected from the simulations for the [111] region.

In summary, we observe a reasonable agreement between the simulations and the experimental results, with some peculiar differences between VPFFT and VPSC, but no

significant difference between the two developed VPSC models for updating of misorientation spreads at lower strain levels in FCC metals.
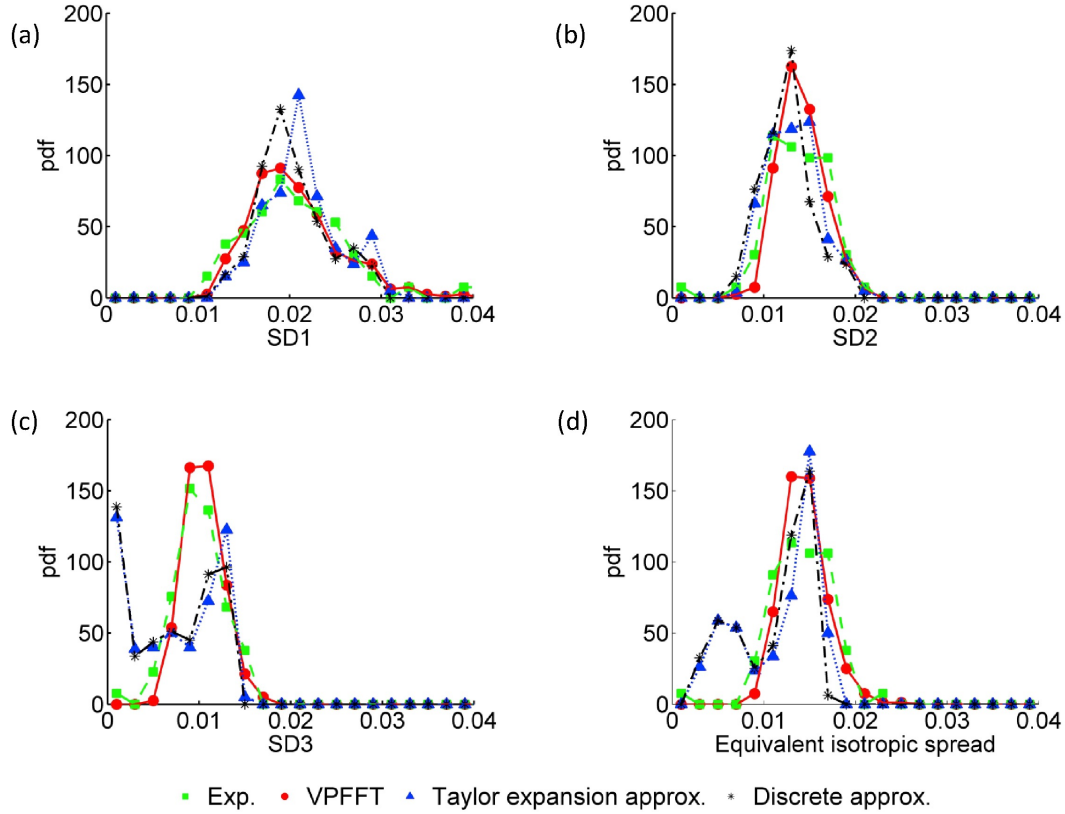
Fig. 5. Probability density functions of the standard deviations along the principal axis of the misorientation distribution (a) SD1, (b) SD2, (c) SD3 and (d) equivalent isotropic spread for experimental results and simulation predictions for copper after 11% tensile strain.

Table 3. Fractions of prolate shapes for different texture components after 25% tensile deformation of copper obtained from experimental data[41], VPFFT simulation, Taylor expansion approximation and discrete approximation approach.

Fraction of prolates	Exp.	VPFFT	Taylor expansion approx.	Discrete approx.
[001] 10°	56%	19%	41%	39%
[011] 20°	86%	76%	91%	91%
[111] 15°	55%	19%	13%	14%
Remaining	68%	64%	80%	79%

3.2   Plane-strain compression of polycrystalline aluminum

In addition to uniaxial deformation, we also simulate plane-strain compression of fcc polycrystal to 38% reduction and compare the predictions to results obtained after cold-rolling of aluminum [44]. The initial texture was represented by 400 randomly oriented grains of equal volume fraction.
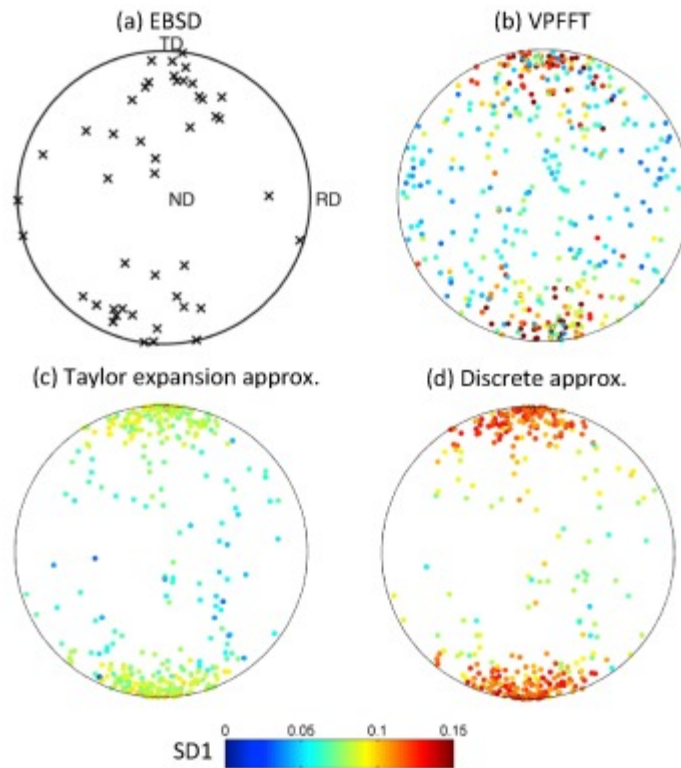
Fig. 6. Dominant rotation axes plotted in the sample frame and color-coded according to magnitude of standard deviation along this direction for (a) EBSD data [44], (b) VPFFT results, (c) Taylor expansion approximation and (d) discrete approximation approach for aluminium after 38% plane strain compression or rolling reduction.

The orientations of the dominant rotation axes are shown in Fig. 6. The dominant rotation axes are predominantly aligned with the transverse direction in both, simulations and experiment. Clustering of the dominant rotation axes around the transverse direction is considerably stronger in the VPSC predictions. Similar trends were observed for hot rolled aluminum at lower reductions [42].

Figure 7 shows the probability density functions of the equivalent isotropic spreads which all show only a single peak and no second peak at lower equivalent isotropic spreads is observed. It is seen that the simulations overpredict the magnitudes of the equivalent isotropic spread. The discrete approximation approach displays the largest values for the equivalent isotropic spread, since in this model a strong correlation between subsequent misorientation increments is enforced. This corroborates the statement that the main difference between the two approaches lies in the approximation of the cross-correlation term. The simulated equivalent orientation spreads are in all cases too large in comparison to the experimental results. This discrepancy can be attributed to a number of reasons. At higher strains, certain grains in the VPFFT simulation will develop a quite large misorientation spread along the dominant rotation axis. Closer inspection reveals that the sign-carrying misorientation distribution along this direction is actually bimodal, which indicates that grain has fragmented into two parts [45, 46]. By not considering the fragmented grains separately we have indirectly increased the values of equivalent isotropic spread. Similarly, in a VPSC simulation some grains develop very large spreads in a certain direction indicating that they should be fragmented and considered separately. In addition, the threshold angle used for identification of individual grains in the orientation maps was 8° which also affects the evaluation of the experimental results. During deformation, deformation-induced boundaries are forming within the grains causing their subdivision [47]. Some of these boundaries will have misorientation angles greater than 8°. Therefore, fragments of initially one grain will be treated as separate grains in the experimental results, when entirely separated by such a deformation-induced boundary with an angle above 8°. This procedure of treating fragments individually as seperate grains reduces, in general, the magnitude of the misorientation spread within the grains.
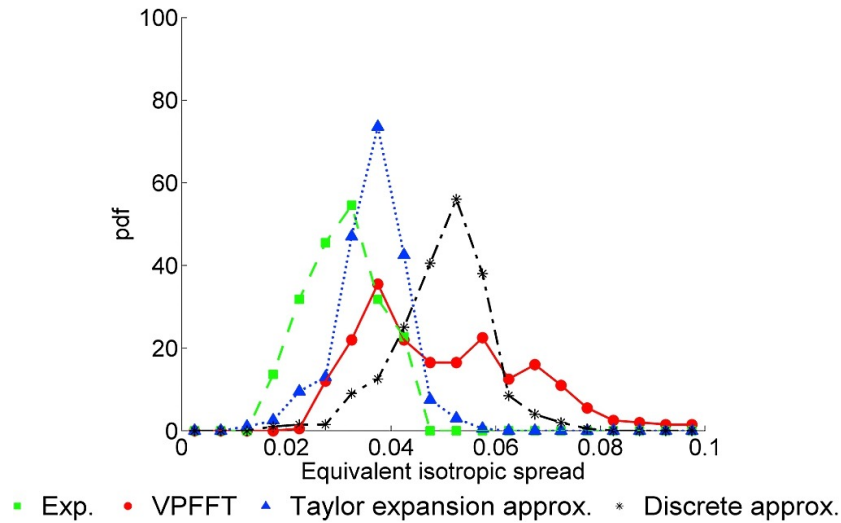
Fig 7. Probability density functions of equivalent isotropic spread for experimental results and simulation predictions for aluminum after 38% plane strain compression or rolling reduction.

The predicted intragranular misorientation spreads obtained here show the need for further development of the VPSC model to include grain fragmentation towards more accurate mean-field simulations of deformation and recrystallization texture evolution. As noted above, the grains with largest standard deviations in VPFFT results develop bimodal sign-carrying misorientation distributions along the dominant rotation axis. Analogously, we could assume that the grains with the largest standard deviations in the VPSC model go through a similar type of fragmentation. The parent grain would be divided into two children grains whose mean orientations and misorientation spreads would be defined based on the mean orientation and the anisotropic misorientation spread of the parent, for instance by replacing the parent grain by two children having a misorientation between their mean orientations along the dominant misorientation axis. The misorientation spreads could also be used for identifying grains that have a tendency to develop transition bands which is a prerequisite for modeling of recrystallization dominated by nucleation at transition bands. Even in cases where the nucleation occurs at existing grain boundaries, the information about the misorientation spreads could improve recrystallization texture predictions.

148

4 Conclusions

In this work, we have extended existing algorithms to obtain second moments of the micromechanical fields already implemented in VPSC to include the calculation of intragranular misorientations. Two approaches were presented for updating the intragranular misorientation distributions. It was found that the Taylor expansion approach was simpler, required less calculations and realized more freedom in the approximation of the cross-correlation term between misorientations and rotation-rates than the discrete approximation. The predictive characteristics of the proposed models were evaluated on the deformation of two FCC polycrystalline materials (Cu deformed in tension and Al deformed in plane-strain compression/rolling), and compared with corresponding experiments and appropriate full-field VPFFT simulation results. Acceptable predictions of orientation spreads were achieved using VPSC, with tremendous computational advantages over full-field models (by approximately three orders of magnitude). It was observed that at higher strains, some of the grains develop quite large misorientation spreads suggesting fragmentation into individual parts. Development of models for grain fragmentation and recrystallization taking advantage of the proposed algorithms, and extensions for metals other than FCC such as hexagonal metals will be pursued in future efforts.

Appendix A

Unit quaternion representation of rotations

Rotations can be represented as unit quaternions in the following form:

$$\mathbf{q} = \left\{ \begin{array}{c} \cos\frac{\theta}{2} \\ n_i \sin\frac{\theta}{2} \end{array} \right\} = \left\{ \begin{array}{c} \cos\frac{\theta}{2} \\ r_i \end{array} \right\} = \left\{ \begin{array}{c} a \\ b \\ c \\ d \end{array} \right\} \tag{1}$$

where n_i and θ represent rotation axis and angle, respectively. The vector part of the unit

quaternion r_i is defined as $r_i = n_i \sin\frac{\theta}{2}$. There are several different matrix representations of unit

quaternions, we have adopted the following [36]:

$$\mathbf{q} = \begin{bmatrix} a & c & b & d \\ -c & a & d & -b \\ -b & -d & a & c \\ -d & b & -c & a \end{bmatrix} \tag{2}$$

Consequently, we can deal with matrices and matrix algebra instead of quaternion algebra.

Product of two unit quaternions can then be expressed as simple matrix multiplication:

$$q_{ij} = q_{ik}^A q_{kj}^B \tag{3}$$

The matrix representation of unit quaternions was used only in derivations of certain equations.

The actual implementation of final equations was not done in matrix form due to computational

inefficiency of this formulation.

Appendix B

Incremental rotations

Incremental rotations and their first and second moments can be directly calculated from

first and second moments of spin. First we define incremental rotation at material point using

small angle approximation:

$$\mathbf{q}_{inc}(\mathbf{x}) = \left\{ \begin{array}{c} \cos\frac{\Delta\theta(\mathbf{x})}{2} \\ \sin\frac{\Delta\theta(\mathbf{x})}{2}\,\mathbf{n}(\mathbf{x}) \end{array} \right\} \approx \left\{ \begin{array}{c} 1 - \frac{1}{8}\Delta\theta^2(\mathbf{x}) \\ \frac{1}{2}\Delta\theta(\mathbf{x})\,\mathbf{n}(\mathbf{x}) \end{array} \right\} \tag{4}$$

First moment of incremental rotation is:

$$\langle \mathbf{q}_{inc} \rangle = \left\{ \begin{array}{c} 1 - \frac{1}{8} \langle \Delta \theta^2 \rangle \\ \frac{1}{2} \langle \Delta \theta \mathbf{n} \rangle \end{array} \right\} \tag{5}$$

The mean incremental rotation can then be calculated as: $\overline{\mathbf{q}}_{inc} = \langle \mathbf{q}_{inc} \rangle / |\langle \mathbf{q}_{inc} \rangle|$. The dyadic product of incremental rotations can be written as:

$$\mathbf{q}_{inc}(\mathbf{x}) \otimes \mathbf{q}_{inc}(\mathbf{x}) = \begin{bmatrix} 1 - \frac{1}{4} \Delta \theta^2 (\mathbf{x}) & \frac{1}{2} \Delta \theta (\mathbf{x}) \, \mathbf{n}^T(\mathbf{x}) \\ -symmetric - & \frac{1}{4} \Delta \theta^2 (\mathbf{x}) \mathbf{n}(\mathbf{x}) \otimes \mathbf{n}(\mathbf{x}) \end{bmatrix} + O(\Delta \theta^3 (\mathbf{x})) \tag{6}$$

The second moment is then simply:

$$\langle \mathbf{q}_{inc} \otimes \mathbf{q}_{inc} \rangle = \begin{bmatrix} 1 - \frac{1}{4} \langle \Delta \theta^2 \rangle & \frac{1}{2} \langle \Delta \theta \mathbf{n}^T \rangle \\ -symmetric - & \frac{1}{4} \langle \Delta \theta^2 \mathbf{n} \otimes \mathbf{n} \rangle \end{bmatrix} \tag{7}$$

After substitution of spin into the above expression we get:

$$\langle \mathbf{q}_{inc} \rangle = \left\{ \begin{array}{c} 1 - \frac{1}{8} \mathbf{I} : \langle \dot{\boldsymbol{\omega}} \otimes \dot{\boldsymbol{\omega}} \rangle \Delta t^2 \\ \frac{1}{2} \langle \dot{\boldsymbol{\omega}} \rangle \Delta t \end{array} \right\} \tag{8}$$

$$\langle \mathbf{q}_{inc} \otimes \mathbf{q}_{inc} \rangle = \begin{bmatrix} 1 - \frac{1}{4} \mathbf{I} : \langle \dot{\boldsymbol{\omega}} \otimes \dot{\boldsymbol{\omega}} \rangle \Delta t^2 & \frac{1}{2} \langle \dot{\boldsymbol{\omega}} \rangle^T \Delta t \\ -symmetric - & \frac{1}{4} \langle \dot{\boldsymbol{\omega}} \otimes \dot{\boldsymbol{\omega}} \rangle \Delta t^2 \end{bmatrix} \tag{9}$$

The second moment of misorientation $\langle \delta \mathbf{q}_{inc} \otimes \delta \mathbf{q}_{inc} \rangle$ can be calculated using the first and second moments of total increments in rotation.

Appendix C

Discrete representation of multivariate distribution

The spin distribution is defined by first, $\langle\dot{\boldsymbol{\omega}}\rangle$, and second, $\langle\dot{\boldsymbol{\omega}}\otimes\dot{\boldsymbol{\omega}}\rangle$, moments from which covariance matrix can be calculated as $\langle\dot{\boldsymbol{\omega}}\otimes\dot{\boldsymbol{\omega}}\rangle - \langle\dot{\boldsymbol{\omega}}\rangle\otimes\langle\dot{\boldsymbol{\omega}}\rangle$. We shall assume that the distribution associated with the spin field within the phase r is multivariate normal distribution.

First, the principal values and directions of covariance matrix are calculated. The multivariate normal distribution implies that distributions associated with the principal directions are univariate normal. Next each one of these univariate distributions is approximated by certain number, m, of discrete values with equal probability [48]. In all of the simulations we have used three (m=3) points along each principal direction, one as a mean and the other two were symmetric for + and - angle.

Next the approximation of multivariate distribution is constructed from discrete univariate distributions as follows. In the principal frame of covariance matrix there is no correlation between different components of spin vector:

$$\langle\dot{\omega}_i^p\dot{\omega}_j^p\rangle - \langle\dot{\omega}_i^p\rangle\otimes\langle\dot{\omega}_j^p\rangle = 0, \text{for } i \neq j \tag{11}$$

where superscript p denotes a variable expressed in the principal frame. In the case of multivariate normal distribution this implies independence of the spin components. The discrete approximation of the multivariate normal distribution is then defined by combining the discrete values of the univariate distributions associated with each spin component in principal frame, giving in total $n = m^3$ discrete vectors (27 in our simulations). Finally, we transfer the spin vectors to the global frame and obtain a discrete representation of the spin distribution given by a set of n discrete values $\dot{\boldsymbol{\omega}}^i$.

References

[1] W.F. Hosford, The Mechanics of Crystals and Textured Polycrystals, Oxford University Press, USA1993.

[2] I. Dillamore, H. Katoh, Mechanisms of recrystallization in cubic metals with particular reference to their orientation-dependence., Metal Science 8(3) (1974) 73-83.

[3] F. Humphreys, M. Hatherly, Recrystallization and related annealing phenomena, 2004, Elsevier, 2004.

[4] R.J. McCabe, A.W. Richards, D.R. Coughlin, K.D. Clarke, I.J. Beyerlein, M. Knezevic, Microstructure effects on the recrystallization of low-symmetry alpha-uranium, Journal of Nuclear Materials 465 (2015) 189-195.

[5] S.R. Kalidindi, C.A. Bronkhorst, L. Anand, Crystallographic Texture Evolution in Bulk Deformation Processing of Fcc Metals, Journal of the Mechanics and Physics of Solids 40(3) (1992) 537-569.

[6] M. Knezevic, B. Drach, M. Ardeljan, I.J. Beyerlein, Three dimensional predictions of grain scale plasticity and grain boundaries using crystal plasticity finite element models, Computer Methods in Applied Mechanics and Engineering 277(0) (2014) 239-259.

[7] M. Zecevic, R.J. McCabe, M. Knezevic, A new implementation of the spectral crystal plasticity framework in implicit finite elements, Mechanics of Materials 84(0) (2015) 114-126.

[8] M. Ardeljan, I.J. Beyerlein, M. Knezevic, A dislocation density based crystal plasticity finite element model: Application to a two-phase polycrystalline HCP/BCC composites, Journal of the Mechanics and Physics of Solids 66(0) (2014) 16-31.

[9] M. Zecevic, R.J. McCabe, M. Knezevic, Spectral database solutions to elasto-viscoplasticity within finite elements: Application to a cobalt-based FCC superalloy, Int. J. Plast. 70(0) (2015) 151-165.

[10] H. Moulinec, P. Suquet, A numerical method for computing the overall response of nonlinear composites with complex microstructure, Computer methods in applied mechanics and engineering 157(1) (1998) 69-94.

[11] R.A. Lebensohn, N-site modeling of a 3D viscoplastic polycrystal using Fast Fourier Transform, Acta Materialia 49(14) (2001) 2723-2737.

[12] R. Hill, Continuum micro-mechanics of elastoplastic polycrystals, Journal of the Mechanics and Physics of Solids 13(2) (1965) 89-101.

[13] J.W. Hutchinson, Proceedings of the Royal Society of London A319 (1970) 247.

[14] A. Molinari, G.R. Canova, S. Ahzi, Self consistent approach of the large deformation polycrystal viscoplasticity, Acta Metallurgica et Materialia 35(12) (1987) 2983-2994.

[15] R.A. Lebensohn, C.N. Tomé, A self-consistent anisotropic approach for the simulation of plastic deformation and texture development of polycrystals: Application to zirconium alloys, Acta Metallurgica et Materialia 41(9) (1993) 2611-2624.

[16] S. Nemat-Nasser, M. Hori, Micromechanics: overall properties of heterogeneous materials, Elsevier2013.

[17] P. Ponte Castañeda, Second-order homogenization estimates for nonlinear composites incorporating field fluctuations: I—theory, Journal of the Mechanics and Physics of Solids 50(4) (2002) 737-757.

[18] Y. Liu, P.P. Castañeda, Second-order theory for the effective behavior and field fluctuations in viscoplastic polycrystals, Journal of the Mechanics and Physics of Solids 52(2) (2004) 467-495.

[19] M. Berveiller, H. Bouaouine, N. Fakri, P. Lipinski, Texture Transition, Micro Shear Bands and Heterogeneous Plastic Strain in FCC and BCC Metals in Rolling, Texture, Stress, and Microstructure 8 (1988) 351-379.

[20] R.E. Bolmaro, A. Fourty, A. Roatta, M.A. Bertinetti, P.A. Turner, J.W. Signorelli, A new approach to crystal spin calculation during deformation texture development, Scripta Materialia 43(6) (2000) 553-559.

[21] R.E. Bolmaro, A. Roatta, A.L. Fourty, J.W. Signorelli, Recrystallization textures in fcc materials: A simulation based on micromechanical modeling data, Scripta Materialia 53(2) (2005) 147-152.

[22] C. Tomé, C. Necker, R. Lebensohn, Mechanical anisotropy and grain interaction in recrystallized aluminum, Metallurgical and Materials Transactions A 33(8) (2002) 2635-2648.

[23] L.S. Toth, Y. Estrin, R. Lapovok, C.F. Gu, A model of grain fragmentation based on lattice curvature, Acta Materialia 58(5) (2010) 1782-1794.

[24] D. Raabe, Simulation of texture evolution during rolling deformation of an intermetallic Fe-28Al-5Cr polycrystal, Materials Letters 19(1-2) (1994) 75-78.

[25] D. Raabe, Z. Zhao, S.-J. Park, F. Roters, Theory of orientation gradients in plastically strained crystals, Acta Materialia 50(2) (2002) 421-440.

[26] C.S. Lee, B.J. Duggan, Deformation banding and copper-type rolling textures, Acta Metall. Mater. 41(9) (1993) 2691-2699.

[27] T. Leffers, A model for rolling deformation with grain subdivision. Part I: The initial stage, International Journal of Plasticity 17(4) (2001) 469-489.

[28] G.C. Butler, D.L. McDowell, Polycrystal constraint and grain subdivision, International Journal of Plasticity 14(8) (1998) 703-717.

[29] X. Guo, M. Seefeldt, Modeling grain fragmentation and deformation textures for titanium using a combined approach of the viscoplastic self-consistent model and a shear fluctuation model, Journal of Materials Science 52(13) (2017) 8132-8148.

[30] R.A. Lebensohn, Y. Liu, P.P. Castaneda, On the accuracy of the self-consistent approximation for polycrystals: comparison with full-field numerical simulations, Acta Materialia 52(18) (2004) 5347-5361.

[31] R.A. Lebensohn, C.N. Tome, P.P. Castaneda, Self-consistent modelling of the mechanical behaviour of viscoplastic polycrystals incorporating intragranular field fluctuations, Philosophical Magazine 87(28) (2007) 4287-4322.

[32] R.A. Lebensohn, M. Zecevic, M. Knezevic, R.J. McCabe, Average intragranular misorientation trends in polycrystalline materials predicted by a viscoplastic self-consistent approach, Acta Materialia 104 (2016) 228-236.

[33] R. Masson, M. Bornert, P. Suquet, A. Zaoui, An affine formulation for the prediction of the effective properties of nonlinear composites and polycrystals, Journal of the Mechanics and Physics of Solids 48(6) (2000) 1203-1227.

[34] J.D. Eshelby, The determination of the elastic field of an ellipsoidal inclusion, and related problems, Proc R. Soc. Lond. A 241 (1957) 376-396.

[35] A. Papoulis, Probability, Random Variables and Stochastic Processes. Series in Electrical Engineering: Communications and Signal Processing, McGraw-Hill, Inc., New York, 1991.

[36] R.W. Farebrother, J. Gross, S.O. Troschke, Matrix representation of quaternions, Linear Algebra Appl 362 (2003) 251-255.

[37] A.H.S. Ang, W.H. Tang, Probability Concepts in Engineering Planning and Design, Basic Principles, Wiley1975.

[38] W. Pantleon, Retrieving orientation correlations in deformation structures from orientation maps, Materials Science and Technology 21(12) (2005) 1392-1396.

[39] R.A. Lebensohn, R. Brenner, O. Castelnau, A.D. Rollett, Orientation image-based micromechanical modelling of subgrain texture evolution in polycrystalline copper, Acta Materialia 56(15) (2008) 3914-3926.

[40] F. Bachmann, R. Hielscher, P.E. Jupp, W. Pantleon, H. Schaeben, E. Wegert, Inferential statistics of electron backscatter diffraction data from within individual crystalline grains, Journal of Applied Crystallography 43(6) (2010) 1338-1355.

[41] S. Krog-Pedersen, J.R. Bowen, W. Pantleon, Quantitative characterization of the orientation spread within individual grains in copper after tensile deformation, International Journal of Materials Research 100(3) (2009) 433-438.

[42] R. Quey, J.H. Driver, P.R. Dawson, Intra-grain orientation distributions in hot-deformed aluminium: Orientation dependence and relation to deformation mechanisms, Journal of the Mechanics and Physics of Solids 84 (2015) 506-527.

[43] P. Lequeu, P. Gilormini, F. Montheillet, B. Bacroix, J.J. Jonas, Yield Surfaces for Textured Polycrystals .1. Crystallographic Approach, Acta Metallurgica 35(2) (1987) 439-451.

[44] W. Pantleon, W. He, T.P. Johansson, C. Gundlach, Orientation inhomogeneities within individual grains in cold-rolled aluminium resolved by electron backscatter diffraction, Mater. Sci. Eng. A-Struct. Mater. Prop. Microstruct. Process. 483-84 (2008) 668-671.

[45] T.E. Buchheit, J.D. Carroll, B.G. Clark, B.L. Boyce, Evaluating Deformation-Induced Grain Orientation Change in a Polycrystal During In Situ Tensile Deformation using EBSD, Microsc Microanal 21(4) (2015) 969-984.

[46] R. Quey, P.R. Dawson, J.H. Driver, Grain orientation fragmentation in hot-deformed aluminium: Experiment and simulation, Journal of the Mechanics and Physics of Solids 60(3) (2012) 509-524.

[47] D.A. Hughes, N. Hansen, High angle boundaries formed by grain subdivision mechanisms, Acta. Mater. 45(9) (1997) 3871-3886.

[48] A.C. Miller, T.R. Rice, Discrete Approximations of Probability-Distributions, Manage Sci 29(3) (1983) 352-362.

Chapter 4: Modeling of intragranular misorientation and grain fragmentation in polycrystalline materials using the viscoplastic self-consistent formulation

This chapter was published as: "Modeling of intragranular misorientation and grain fragmentation in polycrystalline materials using the viscoplastic self-consistent formulation", Zecevic Miroslav, Ricardo A. Lebensohn, Rodney J. McCabe, and Marko Knezevic, International Journal of Plasticity (2018). My contribution to this chapter was:

- development and implementation of the approach for calculation of the effects of the intragranular misorientation distributions on the intragranular stress and rotation rate distributions within VPSC

- development and implementation of the grain fragmentation model based in the orientation space

- simulation of the plane-plane strain compression of Al specimen using the proposed VPSC model and the full-field VPFFT model

- processing of the model and experimental results and their comparison

- development of the method for identification of transition bands based on the shapes of the intragranular misorientation distributions

- writing the first draft of the paper.

Modeling of intragranular misorientation and grain fragmentation in polycrystalline materials using the viscoplastic self-consistent formulation

Miroslav Zecevic[a], Ricardo A. Lebensohn[b], Rodney J. McCabe[b], and Marko Knezevic[a],

a Department of Mechanical Engineering, University of New Hampshire, Durham, NH 03824, USA
b Materials Science and Technology Division, Los Alamos National Laboratory, Los Alamos, NM 87544, USA

Abstract

The recently established methodology to use known algorithmic expressions of the second moments of the stress field in the grains of a polycrystalline aggregate for calculating average fluctuations of lattice rotation rates and the associated average intragranular misorientation distributions using the mean-field viscoplastic self-consistent (VPSC) formulation is extended to solve the coupled problem of considering the effect of intragranular misorientations on stress and rotation rate fluctuations. In turn, these coupled expressions are used to formulate and implement a grain fragmentation (GF) model in VPSC. Case studies, including tension and plane-strain compression of face-centered cubic polycrystals are used to illustrate the capabilities of the new model. GF-VPSC predictions of intragranular misorientation distributions and texture evolution are compared with experiments and full-field numerical simulations, showing good agreement. In particular, the inclusion of misorientation spreads reduced the intensity of the deformed texture and thus improved the texture predictions. Moreover, considering that intragranular misorientations act as driving forces for recrystallization, the new GF-VPSC formulation is shown to enable modeling of microstructure evolution during deformation and recrystallization, in a computationally efficient manner.

Keywords: A Microstructures; B Crystal plasticity; B Viscoplastic material; C Numerical algorithms; GF-VPSC.

1   Introduction

Mean-field polycrystal plasticity models provide a balance between computational efficiency and accuracy. One of such models is the widely-used viscoplastic self-consistent (VPSC) formulation (Lebensohn and Tomé, 1993). In VPSC, each single crystal grain is represented as an ellipsoidal inclusion within a matrix that has the averaged properties of all grains. The state of each inclusion/grain is described by the average values of the micromechanical (stress and strain rate), and microstructural (slip resistance and orientation) fields inside the grain, which evolve during deformation. Consequently, the effect of intragranular misorientation developing in the grains as deformation accumulates is not accounted for (Winther et al., 2017).

Accurate predictions of the intragranular misorientation distributions at high strains are important for simulation of deformation textures and necessary for modeling of recrystallization. Mean-field models tend to predict sharper deformation textures than experimental measurements and those predicted by full-field models, because the orientation distribution of each grain is described only by one mean orientation (Knezevic et al., 2012; Lebensohn, 2001). Therefore, incorporation and consideration of intragranular misorientation spreads in mean-field models can improve texture predictions, reducing peak intensities in orientation space. Moreover, modeling of recrystallization of deformed polycrystals also requires accurate predictions of intragranular misorientations. Misorientation distributions can be used as indicators of whether a given grain has developed deformation and transition bands, and the trends of the crystal orientations developing within those bands can be identified as well. Transition bands are regions of high orientation gradients between deformation bands and, therefore, are favorable places for nucleation of recrystallization (Dillamore and Katoh, 1974; Humphreys and Hatherly, 2004).

Recrystallization nuclei are observed to develop from the subgrains already present in the transition band (Humphreys and Hatherly, 2004; Ridha and Hutchinson, 1982). Hence, prediction of transition bands and the crystallographic orientations present in them is crucial for the prediction of recrystallization textures.

In the last decade, the VPSC formulation was extended to calculate intragranular second moments of stress, which statistically describe the stress fields inside the grains, beyond their average values (Lebensohn et al., 2004; Lebensohn et al., 2007). These second moments can be used to obtain a better linear approximation of the grain's non-linear constitutive behavior (Castañeda, 2002; Doghri et al., 2011; Liu and Castañeda, 2004). In our recent work, we have utilized these second moments of stress to obtain average fluctuations of the lattice rotation rate field in each grain (Lebensohn et al., 2016). Moreover, a time integration procedure of the latter for updating the average intragranular misorientations was developed in (Zecevic et al., 2017), and used for the prediction of intragranular misorientation spreads at moderate strains.

In order to accurately predict the intragranular misorientation spreads at higher strains, the current model must be improved to include grain fragmentation and the mutual influence of intragranular misorientations, and stress and rotation rate fluctuations. The intragranular orientation distribution may become quite large at higher strains (Jahedi et al., 2015; Jahedi et al., 2017; Liu et al., 1998) and thus it cannot be represented accurately with only one mean value and one second moment (Ardeljan et al., 2015; Buchheit et al., 2015; Kanjarla et al., 2010; Quey et al., 2012). Therefore, a grain fragmentation criterion becomes necessary at those high strains. Several ad-hoc grain fragmentation models have been developed within mean-field frameworks, and were capable of predicting the reduction in grain size and the increase in high-angle boundaries with strain (Beyerlein et al., 2003; Butler and McDowell, 1998; Jahedi et al., 2014;

Kumar and Mahesh, 2013; Lee and Duggan, 1993; Ostapovets et al., 2012; Tomé et al., 2002; Toth et al., 2010). However, none of these approaches utilize the micromechanically consistent intragranular stress fluctuations as the driving force for the fragmentation. It is important to note that VPSC provides only a statistical description (i.e. average) of fluctuations within the grains. Hence, the actual spatial distribution of the fluctuations within the grains remains unknown. Consequently, the approach cannot *directly* predict the increase in high-angle boundaries, reduction of grain size and formation of intragranular orientation gradients. However, additional assumptions describing the spatial correlation of the intragranular misorientation spread can be introduced. Moreover, cumulative misorientation within grains causes additional fluctuations of stress and lattice rotation rates, and these become significant as the magnitude of misorientation spread increases. These corrections need to be accounted for, since they are essential for predicting the development of intragranular fluctuations at higher strains.

In this paper, the standard VPSC model is extended to calculate intragranular misorientation distributions at high strains. First, the second moments of intragranular stresses calculated with VPSC (Lebensohn et al., 2004; Lebensohn et al., 2007) are extended to include the influence of the intragranular misorientations. Next, the second moments of lattice rotation rate calculated based on the second moment of stress (Lebensohn et al., 2016), are also extended to include the influence of the intragranular misorientation. The second moments of lattice rotation rate are then accounted for in the calculation of intragranular misorientation spreads (Zecevic et al., 2017). These improvements allow more accurate predictions of intragranular misorientations developing at high strains. Finally, a grain fragmentation (GF) model is formulated in orientation space. This GF-VPSC model is applied to simulate tension and plane-strain compression (PSC) of face-centered cubic (fcc) polycrystals. The predicted intragranular misorientation distributions

161

and texture evolution are compared with experimental data taken from (Quey et al., 2010) for rolled Al, and full-field calculations obtained using the viscoplastic Fast Fourier Transform-based (VPFFT) micromechanical model (Lebensohn, 2001; Lebensohn et al., 2008). Additionally, the GF-VPSC model is shown to enable modeling of evolution of microstructural features necessary for subsequent recrystallization modeling in a computationally efficient manner.

2 Modeling framework

This section summarizes the standard VPSC formulation (Lebensohn and Tomé, 1993) and then describes the algorithms to calculate intragranular stress and lattice rotation rate fluctuations, and intragranular misorientation distributions (Lebensohn et al., 2004; Lebensohn et al., 2016; Zecevic et al., 2017). These developments are combined in the new grain fragmentation model implemented in VPSC, which is termed GF-VPSC.

In the adopted notation, the inner products between two vectors or tensors are denoted by "." (summation over one contracted index), ":" (summation over two contracted indices) and "::" (summation over four contracted indices). The outer product of two tensors is denoted by "⊗".

2.1 Standard VPSC formulation

The viscoplastic strain rate, $\dot{\boldsymbol{\varepsilon}}(\mathbf{x})$, at single crystal material point $\mathbf{x}$ deforming by dislocation glide is given by:

$$\dot{\boldsymbol{\varepsilon}}(\mathbf{x}) = \sum_s \dot{\gamma}^s(\mathbf{x})\mathbf{m}^s(\mathbf{x}), \tag{1}$$

where $\mathbf{m}^s(\mathbf{x}) = \frac{1}{2}\big(\mathbf{b}^s(\mathbf{x}) \otimes \mathbf{n}^s(\mathbf{x}) + \mathbf{n}^s(\mathbf{x}) \otimes \mathbf{b}^s(\mathbf{x})\big)$ is the symmetric part of the Schmid tensor and $\mathbf{b}^s$ and $\mathbf{n}^s$ are the Burgers vector and slip plane normal of slip system s. $\dot{\gamma}^s(\mathbf{x})$ is the shear rate on slip system s at material point $\mathbf{x}$ given by:

162

$$\dot{\gamma}^s(\mathbf{x}) = \dot{\gamma}_0 \left(\frac{|\tau^s(\mathbf{x})|}{\tau_c^s(\mathbf{x})} \right)^n \mathrm{sign}\big(\tau^s(\mathbf{x})\big), \tag{2}$$

where $\tau^s(\mathbf{x}) = \mathbf{m}^s(\mathbf{x}){:}\boldsymbol{\sigma}(\mathbf{x})$ is the resolved shear stress on slip system s, $\dot{\gamma}_0$ is the reference shear rate, n is the inverse of rate sensitivity, and τ_c^s is the critical resolved shear stress. Substituting Eq. (2) in Eq. (1) gives the non-linear relation (i.e. the *rate-sensitive* constitutive equation) between strain rate and stress:

$$\dot{\boldsymbol{\varepsilon}}(\mathbf{x}) = \dot{\gamma}_0 \sum_s \left(\frac{|\boldsymbol{\sigma}(\mathbf{x}){:}\mathbf{m}^s(\mathbf{x})|}{\tau_c^s(\mathbf{x})} \right)^n \mathrm{sign}\big(\boldsymbol{\sigma}(\mathbf{x}){:}\mathbf{m}^s(\mathbf{x})\big)\, \mathbf{m}^s(\mathbf{x}). \tag{3}$$

The non-linear relationship at the slip system level (Eq. 2) can be linearized as:

$$\dot{\gamma}^s(\mathbf{x}) = \eta^{s(r)}\tau^s(\mathbf{x}) + \dot{g}^{0s(r)}, \tag{4}$$

where $\eta^{s(r)}$ and $\dot{g}^{0s(r)}$ are the linearized compliance and the back-extrapolated shear rate of slip system s in grain r. Consequently, the linearized behavior at the grain level is given by:

$$\dot{\boldsymbol{\varepsilon}}(\mathbf{x}) = \mathbf{M}^{(r)} : \boldsymbol{\sigma}(\mathbf{x}) + \dot{\boldsymbol{\varepsilon}}^{0(r)}, \tag{5}$$

where $\mathbf{M}^{(r)}$ and $\dot{\boldsymbol{\varepsilon}}^{0(r)}$ are the linearized compliance and the back-extrapolated strain rate for grain r. The grain moduli are defined by the linearization procedure. In this work, we adopt the affine linearization (Masson et al., 2000).

Since the grain behavior is now approximated by a linear relation, self-consistent homogenization can be performed, resulting in an analogous linear relation at the macroscopic level:

$$\dot{\mathbf{E}} = \overline{\mathbf{M}} : \boldsymbol{\Sigma} + \dot{\mathbf{E}}^0, \tag{6}$$

where $\dot{\mathbf{E}}$ and $\boldsymbol{\Sigma}$ are the macroscopic strain rate and stress; $\overline{\mathbf{M}}$ and $\dot{\mathbf{E}}^0$ are the macroscopic compliance and back-extrapolated strain rate. In the self-consistent scheme, each single crystal

grain is assumed to be an ellipsoidal inhomogeneity embedded in an infinite matrix, to which the boundary conditions are applied and whose macroscopic properties need to be determined from weighted averages over the grain's moduli. Consequently, the spatial arrangement of the grains in the polycrystal has no effect on the predictions of the model. The solution for the strain rate and stress in the inhomogeneity representing each grain orientation is obtained by means of the equivalent Eshelby's inclusion approach (Eshelby, 1957).

The interaction equation, relating the deviations in strain rate, $\tilde{\dot{\varepsilon}}^{(r)}$, and in stress, $\tilde{\sigma}^{(r)}$, in the inhomogeneity with respect to the macroscopic values is (Lebensohn and Tomé, 1993):

$$\tilde{\dot{\varepsilon}}^{(r)} = -\widetilde{\mathbf{M}} : \tilde{\sigma}^{(r)}, \tag{7}$$

where the interaction tensor, $\widetilde{\mathbf{M}}$, is calculated as:

$$\widetilde{\mathbf{M}} = (\mathbf{I} - \mathbf{S})^{-1} : \mathbf{S} : \overline{\mathbf{M}}, \tag{8}$$

where $\mathbf{S}$ is the symmetric Eshelby tensor. The macroscopic properties are calculated via the self-consistent equations:

$$\overline{\mathbf{M}} = \langle \mathbf{M}^{(r)} : \mathbf{B}^{(r)} \rangle, \tag{9}$$

$$\dot{\mathbf{E}}^0 = \langle \mathbf{M}^{(r)} : \mathbf{b}^{(r)} + \dot{\varepsilon}^{0(r)} \rangle, \tag{10}$$

where $\mathbf{B}^{(r)}$ and $\mathbf{b}^{(r)}$ are stress localization tensors relating the macroscopic stress and stress in grain r, given by:

$$\mathbf{B}^{(r)} = \left(\mathbf{M}^{(r)} + \widetilde{\mathbf{M}} \right)^{-1} : \left(\overline{\mathbf{M}} + \widetilde{\mathbf{M}} \right), \tag{11}$$

$$\mathbf{b}^{(r)} = \left(\mathbf{M}^{(r)} + \widetilde{\mathbf{M}} \right)^{-1} : \left(\dot{\mathbf{E}}^0 - \dot{\varepsilon}^{0(r)} \right). \tag{12}$$

and where $\langle \; \rangle$ denotes volume average. The self-consistent equations are implicit in macroscopic moduli, $\overline{\mathbf{M}}$ and $\dot{\mathbf{E}}^0$, and are thus solved numerically using a fix-point method.

In the absence of an applied macroscopic rigid-body rotation, the total lattice rotation rate at a material point $\mathbf{x}$ belonging to grain r is given by:

$$\dot{\boldsymbol{\omega}}^{(r)}(\mathbf{x}) = \widetilde{\boldsymbol{\omega}}^{(r)} - \dot{\boldsymbol{\omega}}^p(\mathbf{x}), \tag{13}$$

where $\widetilde{\boldsymbol{\omega}}^{(r)} = \boldsymbol{\Pi} : \mathbf{S}^{-1} : \widetilde{\boldsymbol{\varepsilon}}^{(r)}$ is the rigid-body rotation rate of the ellipsoidal inclusion and $\boldsymbol{\Pi}$ is the anti-symmetric Eshelby tensor. $\dot{\boldsymbol{\omega}}^p(\mathbf{x})$ is the lattice rotation rate at material point $\mathbf{x}$ of grain r calculated as:

$$\dot{\boldsymbol{\omega}}^p(\mathbf{x}) = \sum_s \dot{\gamma}^s(\mathbf{x})\boldsymbol{\alpha}^s(\mathbf{x}), \tag{14}$$

where $\boldsymbol{\alpha}^s(\mathbf{x}) = \frac{1}{2}\big(\mathbf{b}^s(\mathbf{x}) \otimes \mathbf{n}^s(\mathbf{x}) - \mathbf{n}^s(\mathbf{x}) \otimes \mathbf{b}^s(\mathbf{x})\big)$ is the antisymmetric part of the Schmid tensor of slip system s.

2.2   Stress fluctuations

After convergence of the self-consistent scheme at time t, the mean values of micromechanical fields in the grains and the effective properties of the polycrystal are known, and the average fluctuations (second moment of the distribution) of the stress field within each grain can be determined, as well (Lebensohn et al., 2007). Since the grain volume average of intragranular fluctuations of any field variable is zero, the fluctuations do not affect the mean values in any way. In what follows, we represent the symmetric deviatoric second-rank tensors as five-dimensional vectors (Lebensohn and Tomé, 1993; Lequeu et al., 1987) and antisymmetric second-rank tensors as three-dimensional dual vectors.

Let us first assume a homogeneous orientation within each grain r, given by the active rotation quaternion at time t, $\overline{\mathbf{q}}^{t(r)}$, which brings the sample frame into alignment with the crystal frame. Spatial variations of mean grain properties from grain to grain cause fluctuations in stress, $\delta\boldsymbol{\sigma}^{t(\overline{q})}(\mathbf{x})$, within each grain (Bobeth and Diener, 1986):

$$\boldsymbol{\sigma}^t(\mathbf{x}) = \boldsymbol{\sigma}^{t(r)} + \delta\boldsymbol{\sigma}^{t(\overline{q})}(\mathbf{x}). \tag{15}$$

The second moment of stress within each grain can be calculated as (Lebensohn et al., 2004):

$$\langle\boldsymbol{\sigma}^t \otimes \boldsymbol{\sigma}^t\rangle^{(r)} = \boldsymbol{\sigma}^{t(r)} \otimes \boldsymbol{\sigma}^{t(r)} + \langle\delta\boldsymbol{\sigma}^{t(\overline{q})} \otimes \delta\boldsymbol{\sigma}^{t(\overline{q})}\rangle^{(r)} = \frac{2}{c^{t(r)}}\frac{\partial \widetilde{U}_T^t}{\partial \mathbf{M}^{t(r)}}, \tag{16}$$

where $\widetilde{U}_T^t$ is the effective stress potential given by:

$$\widetilde{U}_T^t = \frac{1}{2}\overline{\mathbf{M}}^t : (\boldsymbol{\Sigma}^t \otimes \boldsymbol{\Sigma}^t) + \dot{\mathbf{E}}^{0t} \cdot \boldsymbol{\Sigma}^t + \frac{1}{2}\overline{G}^t. \tag{17}$$

$\overline{G}^t$ is the energy under zero applied stress. This second moment of stress statistically describes the average stress fluctuations within the grain in the absence of the intragranular misorientation. Since the effective properties in Eq. 17 are calculated by the self-consistent procedure, the spatial arrangement of grains in the polycrystal has no influence on the effective stress potential and the stress fluctuations.

We now introduce a misorientation quaternion field, $\delta\mathbf{q}^t(\mathbf{x})$, inside of each grain at time t, which is defined with respect to the mean orientation quaternion of the corresponding grain, $\overline{\mathbf{q}}^{t(r)}$ (Pantleon, 2005). The crystal orientation, $\mathbf{q}^t(\mathbf{x})$, at each material point is then obtained composing the mean orientation of the grain containing the point and the misorientation at that point:

$$\mathbf{q}^t(\mathbf{x}) = \delta\mathbf{q}^t(\mathbf{x})\overline{\mathbf{q}}^{t(r)}. \tag{18}$$

Since three independent variables are enough to fully define a misorientation (or an orientation), we describe the misorientation field with the vector part, $\delta \mathbf{r}^t(\mathbf{x})$, of the misorientation quaternion, $\delta \mathbf{q}^t(\mathbf{x})$ (Pantleon, 2005). The volume average of the vector part of the quaternion misorientation field within each grain vanishes, $\langle \delta \mathbf{r}^t \rangle^{(r)} = \mathbf{0}$, meaning that the misorientation field does not alter the mean grain orientation, $\overline{\mathbf{q}}^{t(r)}$ (Pantleon, 2005). Consequently, the misorientation field will not affect the mean grain properties and thus it will not influence the existing stress fluctuation $\delta \boldsymbol{\sigma}^{t(\overline{q})}(\mathbf{x})$ in any way. However, since the stress is a function of orientation and thus misorientation (Eq. 3), the misorientation field will cause additional fluctuations of the stress field, $\delta \boldsymbol{\sigma}^{t(\delta r)}(\mathbf{x})$, at each material point, $\mathbf{x}$, which should be superimposed to the existing stress fluctuations:

$$\boldsymbol{\sigma}^t(\mathbf{x}) = \boldsymbol{\sigma}^{t(r)} + \delta \boldsymbol{\sigma}^{t(\overline{q})}(\mathbf{x}) + \delta \boldsymbol{\sigma}^{t(\delta r)}(\mathbf{x}). \tag{19}$$

As was noted before, the fluctuations within the grains will be described by the corresponding second moments. Calculation of the second moment of a nonlinear function requires knowledge of the higher order moments of the corresponding independent variables, which are not available in our approach. In order to work only with second moments, we perform linearization of each function that depends on variables that vary within the grain (Ang and Tang, 1975). To this end, we approximate the fluctuation of stress due to misorientation variation within the grain, $\delta \boldsymbol{\sigma}^{t(\delta r)}$, with a linear relation between stress fluctuation and the misorientation vector by performing a first order Taylor expansion of the nonlinear Eq. (3) around the mean grain values:

$$\delta \boldsymbol{\sigma}^{t(\delta r)}(\mathbf{x}) = \left. \frac{\partial \boldsymbol{\sigma}}{\partial \delta \mathbf{r}} \right|^t_{\boldsymbol{\sigma}^{(r)}, \overline{\mathbf{q}}^{(r)}} \delta \mathbf{r}^t(\mathbf{x}), \tag{20}$$

where $\left.\frac{\partial\boldsymbol{\sigma}}{\partial\delta\mathbf{r}}\right|_{\boldsymbol{\sigma}^{(r)},\overline{\mathbf{q}}^{(r)}}^{t}$ represents rate of change of stress with misorientation, with the strain rate held

constant at the mean grain value, and is given in Appendix A. The fluctuations of stress due to

misorientation are hence assumed to be linearly proportional to the misorientation vectors, where

the linear map is defined by the derivative of stress with respect to misorientation vector. Eq.

(19) implies that there are two fundamental sources of stress fluctuations within each grain: the

spatial variation of grain properties within the polycrystal, and the intragranular misorientation

field.

Upon consideration of the intragranular misorientations, the second moment of stress in

grain r (i.e. Eq. 16) becomes:

$$\langle\boldsymbol{\sigma}^t \otimes \boldsymbol{\sigma}^t\rangle^{(r)} = \boldsymbol{\sigma}^{t(r)} \otimes \boldsymbol{\sigma}^{t(r)} + \langle\delta\boldsymbol{\sigma}^{t(\overline{q})} \otimes \delta\boldsymbol{\sigma}^{t(\overline{q})}\rangle^{(r)} + \langle\delta\boldsymbol{\sigma}^{t(\delta r)} \otimes \delta\boldsymbol{\sigma}^{t(\delta r)}\rangle^{(r)} +$$

$$+\langle\delta\boldsymbol{\sigma}^{t(\overline{q})} \otimes \delta\boldsymbol{\sigma}^{t(\delta r)}\rangle^{(r)} + \langle\delta\boldsymbol{\sigma}^{t(\delta r)} \otimes \delta\boldsymbol{\sigma}^{t(\overline{q})}\rangle^{(r)}. \tag{21}$$

The term $\langle\delta\boldsymbol{\sigma}^{t(\delta r)} \otimes \delta\boldsymbol{\sigma}^{t(\delta r)}\rangle^{(r)}$ represents the second moment of stress fluctuations caused

solely by the misorientation field within the grain, and is given by:

$$\langle\delta\boldsymbol{\sigma}^{t(\delta r)} \otimes \delta\boldsymbol{\sigma}^{t(\delta r)}\rangle^{(r)} = \left.\frac{\partial\boldsymbol{\sigma}}{\partial\delta\mathbf{r}}\right|_{\boldsymbol{\sigma}^{(r)},\overline{\mathbf{q}}^{(r)}}^{t} \langle\delta\mathbf{r}^t \otimes \delta\mathbf{r}^t\rangle^{(r)} \left(\left.\frac{\partial\boldsymbol{\sigma}}{\partial\delta\mathbf{r}}\right|_{\boldsymbol{\sigma}^{(r)},\overline{\mathbf{q}}^{(r)}}^{t}\right)^T. \tag{22}$$

where $\langle\delta\mathbf{r}^t \otimes \delta\mathbf{r}^t\rangle^{(r)}$ represents the second moment of the vector part of the misorientation

quaternions in grain r. The last two terms of Eq. (21) are transposed relative to each other and

represent the cross-covariance between two stress fluctuations caused by different sources, and

are calculated as:

$$\langle\delta\boldsymbol{\sigma}^{t(\overline{q})} \otimes \delta\boldsymbol{\sigma}^{t(\delta r)}\rangle^{(r)} = \langle\delta\boldsymbol{\sigma}^{t(\overline{q})} \otimes \delta\mathbf{r}^t\rangle^{(r)} \left(\left.\frac{\partial\boldsymbol{\sigma}}{\partial\delta\mathbf{r}}\right|_{\boldsymbol{\sigma}^{(r)},\overline{\mathbf{q}}^{(r)}}^{t}\right)^T, \tag{23}$$

where $\langle \delta\boldsymbol{\sigma}^{t(\bar{q})} \otimes \delta\mathbf{r}^t \rangle^{(r)}$ represents the cross-covariance between the stress fluctuation caused by variation of the mean grain properties in the polycrystal, and the misorientation. The approach for calculation of cross-covariance $\langle \delta\boldsymbol{\sigma}^{t(\bar{q})} \otimes \delta\mathbf{r}^t \rangle^{(r)}$ will be given at the end of this section.

2.3   Lattice rotation rate fluctuations

Once the stress fluctuations have been defined and characterized with second moments, the lattice rotation rate (or *lattice spin*) fluctuations at time t can be calculated as follows. Eq. (13) and (14) define lattice rotation rate as a nonlinear function of stress and orientation. In order to derive the second moment of the lattice spin as a function of the first and second moments of stress and misorientation, we approximate the fluctuation of the lattice spin within grain r with a first order Taylor expansion around the mean grain value with respect to stress and the vector part of the misorientation quaternion:

$$\dot{\boldsymbol{\omega}}^t(\mathbf{x}) = \dot{\boldsymbol{\omega}}^{t(r)} + \left.\frac{\partial\dot{\boldsymbol{\omega}}}{\partial\boldsymbol{\sigma}}\right|^t_{\boldsymbol{\sigma}^{(r)},\bar{\mathbf{q}}^{(r)}} \delta\boldsymbol{\sigma}^t(\mathbf{x}) + \left.\frac{\partial\dot{\boldsymbol{\omega}}}{\partial\delta\mathbf{r}}\right|^t_{\boldsymbol{\sigma}^{(r)},\bar{\mathbf{q}}^{(r)}} \delta\mathbf{r}^t(\mathbf{x}), \tag{24}$$

where $\left.\frac{\partial\dot{\boldsymbol{\omega}}}{\partial\boldsymbol{\sigma}}\right|^t_{\boldsymbol{\sigma}^{(r)},\bar{\mathbf{q}}^{(r)}}$ and $\left.\frac{\partial\dot{\boldsymbol{\omega}}}{\partial\delta\mathbf{r}}\right|^t_{\boldsymbol{\sigma}^{(r)},\bar{\mathbf{q}}^{(r)}}$ are derivatives of the lattice spin with respect to stress and the vector part of the misorientation quaternion given in Appendix A. Eq. (24) can be rewritten as:

$$\dot{\boldsymbol{\omega}}^t(\mathbf{x}) = \dot{\boldsymbol{\omega}}^{t(r)} + \delta\dot{\boldsymbol{\omega}}^{t(\delta\sigma)}(\mathbf{x}) + \delta\dot{\boldsymbol{\omega}}^{t(\delta r)}(\mathbf{x}), \tag{25}$$

where $\delta\dot{\boldsymbol{\omega}}^{t(\delta\sigma)}(\mathbf{x}) = \left.\frac{\partial\dot{\boldsymbol{\omega}}}{\partial\boldsymbol{\sigma}}\right|^t_{\boldsymbol{\sigma}^{(r)},\bar{\mathbf{q}}^{(r)}} \delta\boldsymbol{\sigma}^t(\mathbf{x})$ is the lattice spin fluctuation caused by the stress fluctuation (Lebensohn et al., 2016) and $\delta\dot{\boldsymbol{\omega}}^{t(\delta r)}(\mathbf{x}) = \left.\frac{\partial\dot{\boldsymbol{\omega}}}{\partial\delta\mathbf{r}}\right|^t_{\boldsymbol{\sigma}^{(r)},\bar{\mathbf{q}}^{(r)}} \delta\mathbf{r}^t(\mathbf{x})$ is the lattice spin fluctuation caused by the misorientation fluctuation. Note that the stress fluctuation, $\delta\boldsymbol{\sigma}^t(\mathbf{x})$, contains the effect of the misorientation fluctuation and thus the term $\delta\dot{\boldsymbol{\omega}}^{t(\delta\sigma)}(\mathbf{x})$ also includes the effects of the misorientation fluctuation through the stress.

The second moment of lattice spin is calculated as:

$$\langle \dot{\boldsymbol{\omega}}^t \otimes \dot{\boldsymbol{\omega}}^t \rangle^{(r)} = \dot{\boldsymbol{\omega}}^{t(r)} \otimes \dot{\boldsymbol{\omega}}^{t(r)} + \langle \delta\dot{\boldsymbol{\omega}}^{t(\delta\sigma)} \otimes \delta\dot{\boldsymbol{\omega}}^{t(\delta\sigma)} \rangle^{(r)} + \langle \delta\dot{\boldsymbol{\omega}}^{t(\delta r)} \otimes \delta\dot{\boldsymbol{\omega}}^{t(\delta r)} \rangle^{(r)} +$$

$$+ \langle \delta\dot{\boldsymbol{\omega}}^{t(\delta\sigma)} \otimes \delta\dot{\boldsymbol{\omega}}^{t(\delta r)} \rangle^{(r)} + \langle \delta\dot{\boldsymbol{\omega}}^{t(\delta r)} \otimes \delta\dot{\boldsymbol{\omega}}^{t(\delta\sigma)} \rangle^{(r)}. \tag{26}$$

Expressions for terms on the right hand side are:

$$\langle \delta\dot{\boldsymbol{\omega}}^{t(\delta\sigma)} \otimes \delta\dot{\boldsymbol{\omega}}^{t(\delta\sigma)} \rangle^{(r)} = \left.\frac{\partial \dot{\boldsymbol{\omega}}}{\partial \boldsymbol{\sigma}}\right|^t_{\boldsymbol{\sigma}^{(r)}, \overline{\mathbf{q}}^{(r)}} \langle \delta\boldsymbol{\sigma}^t \otimes \delta\boldsymbol{\sigma}^t \rangle^{(r)} \left(\left.\frac{\partial \dot{\boldsymbol{\omega}}}{\partial \boldsymbol{\sigma}}\right|^t_{\boldsymbol{\sigma}^{(r)}, \overline{\mathbf{q}}^{(r)}} \right)^T \tag{27}$$

$$\langle \delta\dot{\boldsymbol{\omega}}^{t(\delta r)} \otimes \delta\dot{\boldsymbol{\omega}}^{t(\delta r)} \rangle^{(r)} = \left.\frac{\partial \dot{\boldsymbol{\omega}}}{\partial \delta\mathbf{r}}\right|^t_{\boldsymbol{\sigma}^{(r)}, \overline{\mathbf{q}}^{(r)}} \langle \delta\mathbf{r}^t \otimes \delta\mathbf{r}^t \rangle^{(r)} \left(\left.\frac{\partial \dot{\boldsymbol{\omega}}}{\partial \delta\mathbf{r}}\right|^t_{\boldsymbol{\sigma}^{(r)}, \overline{\mathbf{q}}^{(r)}} \right)^T \tag{28}$$

$$\langle \delta\dot{\boldsymbol{\omega}}^{t(\delta\sigma)} \otimes \delta\dot{\boldsymbol{\omega}}^{t(\delta r)} \rangle^{(r)} = \left.\frac{\partial \dot{\boldsymbol{\omega}}}{\partial \boldsymbol{\sigma}}\right|^t_{\boldsymbol{\sigma}^{(r)}, \overline{\mathbf{q}}^{(r)}} \langle \delta\boldsymbol{\sigma}^t \otimes \delta\mathbf{r}^t \rangle^{(r)} \left(\left.\frac{\partial \dot{\boldsymbol{\omega}}}{\partial \delta\mathbf{r}}\right|^t_{\boldsymbol{\sigma}^{(r)}, \overline{\mathbf{q}}^{(r)}} \right)^T, \tag{29}$$

where the cross-covariance $\langle \delta\boldsymbol{\sigma}^t \otimes \delta\mathbf{r}^t \rangle^{(r)}$ is given by:

$$\langle \delta\boldsymbol{\sigma}^t \otimes \delta\mathbf{r}^t \rangle^{(r)} = \langle \delta\boldsymbol{\sigma}^{t(\overline{q})} \otimes \delta\mathbf{r}^t \rangle^{(r)} + \left.\frac{\partial \boldsymbol{\sigma}}{\partial \delta\mathbf{r}}\right|^t_{\boldsymbol{\sigma}^{(r)}, \overline{\mathbf{q}}^{(r)}} \langle \delta\mathbf{r}^t \otimes \delta\mathbf{r}^t \rangle^{(r)}. \tag{30}$$

2.4 Misorientation fluctuations

Next, an algorithm for integration of lattice spin fluctuations and updating of second moments of misorientation vectors from time t to time $t + \Delta t$ is described (Zecevic et al., 2017). The updated orientation at material point $\mathbf{x}$ and time, $t + \Delta t$, is given by:

$$\mathbf{q}^{t+\Delta t}(\mathbf{x}) = \mathbf{q}^t_{inc}(\mathbf{x}) \mathbf{q}^t(\mathbf{x}), \tag{31}$$

where $\mathbf{q}^t_{inc}(\mathbf{x})$ represents the increment in rotation at material point $\mathbf{x}$ and time t and $\mathbf{q}^t(\mathbf{x})$ and $\mathbf{q}^{t+\Delta t}(\mathbf{x})$ are the active rotations rotating the sample frame to local crystal frame at t and $t + \Delta t$. The orientations $\mathbf{q}^t(\mathbf{x})$ and $\mathbf{q}^{t+\Delta t}(\mathbf{x})$ can be written as composition of the corresponding mean

grain orientations, $\overline{\mathbf{q}}^{t(r)}$ and $\overline{\mathbf{q}}^{t+\Delta t(r)}$, and the local misorientations at those material points with respect to the corresponding mean orientation of the corresponding grain, $\delta\mathbf{q}^{t+\Delta t}(\mathbf{x})$ and $\delta\mathbf{q}^t(\mathbf{x})$:

$$\mathbf{q}^t(\mathbf{x}) = \delta\mathbf{q}^t(\mathbf{x})\overline{\mathbf{q}}^{t(r)}, \tag{32A}$$

$$\mathbf{q}^{t+\Delta t}(\mathbf{x}) = \delta\mathbf{q}^{t+\Delta t}(\mathbf{x})\overline{\mathbf{q}}^{t+\Delta t(r)}. \tag{32B}$$
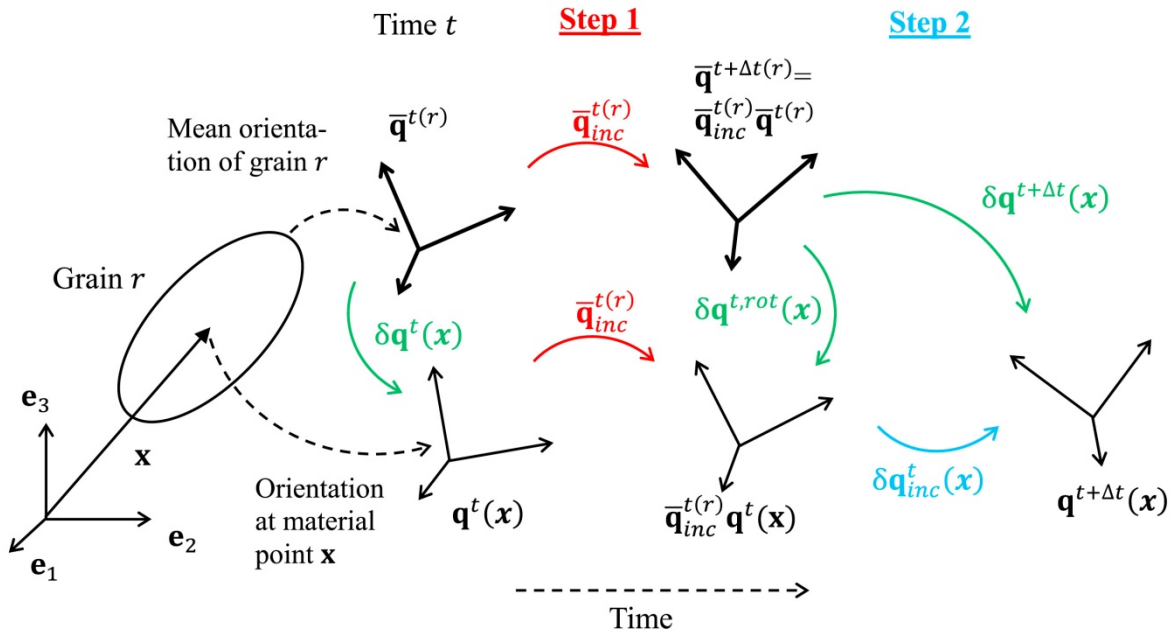
In addition, the increment in rotation can also be decomposed into the mean increment in rotation, $\overline{\mathbf{q}}^{t(r)}_{inc}$, and the increment in misorientation defined with respect to that mean increment in rotation, $\delta\mathbf{q}^t_{inc}(\mathbf{x})$:

$$\mathbf{q}^t_{inc}(\mathbf{x}) = \delta\mathbf{q}^t_{inc}(\mathbf{x})\overline{\mathbf{q}}^{t(r)}_{inc}. \tag{33}$$

By substituting Eq. 33 into Eq. 31 we obtain: $\mathbf{q}^{t+\Delta t}(\mathbf{x}) = \delta\mathbf{q}^t_{inc}(\mathbf{x})\overline{\mathbf{q}}^{t(r)}_{inc}\mathbf{q}^t(\mathbf{x})$. Consequently, the orientation update can be decomposed into two separate steps illustrated on Fig. 1 (Zecevic et al., 2017): 1) Update for the mean increment in rotation, $\overline{\mathbf{q}}^{t(r)}_{inc}$, which is constant within the grain, 2) Update for the increment in misorientation, $\delta\mathbf{q}^t_{inc}(\mathbf{x})$. Figure 1 shows the evolution of mean grain orientation, $\overline{\mathbf{q}}^{t(r)}$, and misorientation at time t, $\delta\mathbf{q}^t(\mathbf{x})$, during the two step update of the orientation. In the first step, the mean increment in rotation is applied to the orientation of every material point within the grain. Consequently, the mean orientation of the grain becomes: $\overline{\mathbf{q}}^{t(r)}_{inc}\overline{\mathbf{q}}^{t(r)}$. Since the same increment in rotation, $\overline{\mathbf{q}}^{t(r)}_{inc}$, is applied to the orientation of every material point of the grain, $\mathbf{q}^t(\mathbf{x})$, and to the mean orientation of the grain, the misorientations between the orientations at material points and the mean orientation physically rotate in the sample frame for $\overline{\mathbf{q}}^{t(r)}_{inc}$: $\delta\mathbf{q}^{t,rot}(\mathbf{x}) = \overline{\mathbf{q}}^{t(r)}_{inc}\delta\mathbf{q}^t(\mathbf{x})\overline{\mathbf{q}}^{t(r)-1}_{inc}$.

In the second step, the increments in misorientation, $\delta\mathbf{q}^t_{inc}(\mathbf{x})$, are applied to the orientation of every material point. It is assumed that the increments in the misorientation do not affect the

mean orientation of the grain since their mean value corresponds to the identity rotation quaternion. Therefore, the mean orientation after the second step remains the same: $\overline{\mathbf{q}}^{t+\Delta t(r)} \approx \overline{\mathbf{q}}_{inc}^{t(r)}\overline{\mathbf{q}}^{t(r)}$. Since the mean orientation remains the same, and since the orientation at each material point is updated for the $\delta\mathbf{q}_{inc}^{t}(\mathbf{x})$, the misorientation between the mean orientation and orientation at material point becomes $\delta\mathbf{q}^{t+\Delta t}(\mathbf{x}) = \delta\mathbf{q}_{inc}^{t}(\mathbf{x})\delta\mathbf{q}^{t,rot}(\mathbf{x})$ (Zecevic et al., 2017). Note that in the first step, the mean increment in the misorientation is applied resulting in the evolution of the mean grain orientation while the misorientations only physically rotate in the sample frame. In contrast, in the second step the increments in misorientation are applied and the mean orientation of the grain remains unaltered while the misorientations evolve to their final values.

Fig. 1 Evolution of: (1) the mean grain orientation, (2) the orientation at a material point $\mathbf{x}$ and (3) the misorientation at the material point $\mathbf{x}$ during orientation update from time t to time $t + \Delta t$. The increment in rotation is decomposed into two rotations: the mean increment in rotation, $\overline{\mathbf{q}}_{inc}^{t(r)}$, and the increment in misorientation, $\delta\mathbf{q}_{inc}^{t}(\mathbf{x})$, which are applied sequentially in two steps.

172

By performing a first order Taylor expansion of the expression for the misorientation update, $\delta\mathbf{q}^{t+\Delta t}(\mathbf{x}) = \delta\mathbf{q}_{inc}^{t}(\mathbf{x})\delta\mathbf{q}^{t,rot}(\mathbf{x})$, around the mean grain values with respect to $\delta\mathbf{q}_{inc}^{t}(\mathbf{x})$ and $\delta\mathbf{q}^{t,rot}(\mathbf{x})$, the linearized expression for orientation update is obtained (Zecevic et al., 2017):

$$\delta\mathbf{q}^{t+\Delta t}(\mathbf{x}) \approx \delta\mathbf{q}_{inc}^{t}(\mathbf{x}) + \delta\mathbf{q}^{t,rot}(\mathbf{x}) - \mathbf{I}^{q}, \tag{34}$$

where $\mathbf{I}^{q}$ is the identity rotation quaternion. Eq. (34) can be rewritten in terms of the vector parts of the misorientation quaternions:

$$\delta\mathbf{r}^{t+\Delta t}(\mathbf{x}) = \delta\mathbf{r}^{t,rot}(\mathbf{x}) + \delta\mathbf{r}_{inc}^{t}(\mathbf{x}). \tag{35}$$

The vector part of the rotated misorientation quaternion at time t can be written as $\delta\mathbf{r}^{t,rot}(\mathbf{x}) = \overline{\mathbf{R}}_{inc}^{t(r)}\delta\mathbf{r}^{t}(\mathbf{x})$, where $\overline{\mathbf{R}}_{inc}^{t(r)}$ is the mean increment in rotation written in the rotation matrix representation. The vector part of the incremental rotation quaternion is approximated as:

$$\delta\mathbf{r}_{inc}^{t}(\mathbf{x}) \approx \frac{\delta\dot{\boldsymbol{\omega}}^{t}(\mathbf{x})}{|\delta\dot{\boldsymbol{\omega}}^{t}(\mathbf{x})|}\sin\left(\frac{|\delta\dot{\boldsymbol{\omega}}^{t}(\mathbf{x})|\Delta t}{2}\right). \tag{36}$$

By assuming a small angle approximation, $\sin\theta \approx \theta$, the above equation can be simplified to:

$$\delta\mathbf{r}_{inc}^{t}(\mathbf{x}) \approx \delta\dot{\boldsymbol{\omega}}^{t}(\mathbf{x})\frac{\Delta t}{2}. \tag{37}$$

The second moment of the vector part of the misorientation quaternion at time $t + \Delta t$ is given by:

$$\langle\delta\mathbf{r}^{t+\Delta t} \otimes \delta\mathbf{r}^{t+\Delta t}\rangle^{(r)} = \langle\delta\mathbf{r}_{inc}^{t} \otimes \delta\mathbf{r}_{inc}^{t}\rangle^{(r)} + \langle\delta\mathbf{r}^{t,rot} \otimes \delta\mathbf{r}_{inc}^{t}\rangle^{(r)} + \langle\mathbf{r}_{inc}^{t} \otimes \delta\mathbf{r}^{t,rot}\rangle^{(r)}$$

$$+\langle\delta\mathbf{r}^{t,rot} \otimes \delta\mathbf{r}^{t,rot}\rangle^{(r)}, \tag{38}$$

where the individual terms on the right hand side are:

$$\langle\delta\mathbf{r}_{inc}^{t} \otimes \delta\mathbf{r}_{inc}^{t}\rangle^{(r)} = \frac{\Delta t^{2}}{4}\langle\delta\dot{\boldsymbol{\omega}}^{t} \otimes \delta\dot{\boldsymbol{\omega}}^{t}\rangle^{(r)} \tag{39}$$

$$\langle \delta \mathbf{r}^{t,rot} \otimes \delta \mathbf{r}^{t,rot} \rangle^{(r)} = \overline{\mathbf{R}}_{inc}^{t(r)} \langle \delta \mathbf{r}^t \otimes \delta \mathbf{r}^t \rangle^{(r)} \overline{\mathbf{R}}_{inc}^{t(r)^T} \tag{40}$$

$$\langle \delta \mathbf{r}^{t,rot} \otimes \delta \mathbf{r}_{inc}^t \rangle^{(r)} = \overline{\mathbf{R}}_{inc}^{t(r)} \langle \delta \mathbf{r}^t \otimes \delta \boldsymbol{\sigma}^t \rangle^{(r)} \left(\frac{\partial \dot{\boldsymbol{\omega}}}{\partial \boldsymbol{\sigma}} \bigg|_{\boldsymbol{\sigma}^{(r)}, \overline{\mathbf{q}}^{(r)}}^t \right)^T \frac{\Delta t}{2} +$$

$$\overline{\mathbf{R}}_{inc}^{t,(r)} \langle \delta \mathbf{r}^t \otimes \delta \mathbf{r}^t \rangle^{(r)} \left(\frac{\partial \dot{\boldsymbol{\omega}}}{\partial \delta \mathbf{r}} \bigg|_{\boldsymbol{\sigma}^{(r)}, \overline{\mathbf{q}}^{(r)}}^t \right)^T \frac{\Delta t}{2}. \tag{41}$$

2.5 Approximation of the cross-covariance $\langle \delta \boldsymbol{\sigma}^{t(\bar{q})} \otimes \delta \boldsymbol{r}^t \rangle^{(r)}$

Term $\langle \delta \boldsymbol{\sigma}^{t(\bar{q})} \otimes \delta \boldsymbol{r}^t \rangle^{(r)}$ represents the cross-covariance between two fundamental sources of fluctuations: stress fluctuations caused by the spatial variation of the mean crystal properties from grain to grain, $\delta \boldsymbol{\sigma}^{t(\bar{q})}$, and the intragranular misorientation fluctuations, $\delta \mathbf{r}^t$. Consequently, the cross-covariance terms appearing in the expressions for second moments of stress, lattice spin and misorientation vectors can be written in terms of $\langle \delta \boldsymbol{\sigma}^{t(\bar{q})} \otimes \delta \boldsymbol{r}^t \rangle^{(r)}$ (Eqs. (23), (29), (30) and (41)). Hence, the cross-covariance $\langle \delta \boldsymbol{\sigma}^{t(\bar{q})} \otimes \delta \boldsymbol{r}^t \rangle^{(r)}$ is the only unknown term in the algorithm outlined above. Let us assume the cross-covariance $\langle \delta \boldsymbol{\sigma}^{t-\Delta t(\bar{q})} \otimes \delta \boldsymbol{r}^{t-\Delta t} \rangle^{(r)}$ at time $t - \Delta t$ is known. We propose an algorithm for calculation of the cross-covariance $\langle \delta \boldsymbol{\sigma}^{t(\bar{q})} \otimes \delta \boldsymbol{r}^t \rangle^{(r)}$ at time t based on an incremental update of the cross-covariance at time $t - \Delta t$.

First, let us assume a linear relation between stress fluctuations at times $t - \Delta t$ and t:

$$\delta \boldsymbol{\sigma}^{t(\bar{q})}(\mathbf{x}) = \mathbf{Z}^{(r)} \delta \boldsymbol{\sigma}^{t-\Delta t(\bar{q})}(\mathbf{x}), \tag{42}$$

where matrix $\mathbf{Z}^{(r)}$ defines the relation between stress fluctuations from two subsequent time increments in grain r. Calculation of matrix $\mathbf{Z}^{(r)}$ is given in Appendix B. By using Eq. (24), (36) and (35), the misorientation at time t can be written as a linear function of $\delta \boldsymbol{\sigma}^{t-\Delta t(\bar{q})}$ and $\delta \boldsymbol{r}^{t-\Delta t}$:

$$\delta \mathbf{r}^t(\mathbf{x}) = \mathbf{Y}^{(\delta r)(r)} \delta \mathbf{r}^{t-\Delta t}(\mathbf{x}) + \mathbf{Y}^{(\delta \sigma)(r)} \delta \boldsymbol{\sigma}^{t-\Delta t(\bar{q})}(\mathbf{x}), \tag{43}$$

where matrices $\mathbf{Y}^{(\delta r)(r)}$ and $\mathbf{Y}^{(\delta\sigma)(r)}$ are given by:

$$\mathbf{Y}^{(\delta r)(r)} = \frac{\Delta t}{2} \frac{\partial\dot{\boldsymbol{\omega}}}{\partial\boldsymbol{\sigma}}\bigg|_{\boldsymbol{\sigma}^{(r)},\overline{\mathbf{q}}^{(r)}}^{t-\Delta t} \frac{\partial\boldsymbol{\sigma}}{\partial\delta\mathbf{r}}\bigg|_{\boldsymbol{\sigma}^{(r)},\overline{\mathbf{q}}^{(r)}}^{t-\Delta t} + \frac{\Delta t}{2} \frac{\partial\dot{\boldsymbol{\omega}}}{\partial\delta\mathbf{r}}\bigg|_{\boldsymbol{\sigma}^{(r)},\overline{\mathbf{q}}^{(r)}}^{t-\Delta t} + \mathbf{R}_{inc}^{t-\Delta t(r)}, \tag{44}$$

$$\mathbf{Y}^{(\delta\sigma)(r)} = \frac{\Delta t}{2} \frac{\partial\dot{\boldsymbol{\omega}}}{\partial\boldsymbol{\sigma}}\bigg|_{\boldsymbol{\sigma}^{(r)},\overline{\mathbf{q}}^{(r)}}^{t-\Delta t}. \tag{45}$$

Eq. (43) illustrates the previous observation that an intragranular fluctuation of any variable stems from the two fundamental sources: intragranular fluctuations of stress due to variation of mean grain properties within the polycrystal, $\delta\boldsymbol{\sigma}^{t-\Delta t(\overline{q})}(\mathbf{x})$, and intragranular fluctuations of misorientation, $\delta\mathbf{r}^{t-\Delta t}(\mathbf{x})$. Substituting Eq. (42) and (43) into cross-covariance $\langle\delta\boldsymbol{\sigma}^{t(\overline{q})} \otimes \delta\mathbf{r}^t\rangle^{(r)}$ yields:

$$\langle\delta\boldsymbol{\sigma}^{t(\overline{q})} \otimes \delta\mathbf{r}^t\rangle^{(r)} = \mathbf{Z}^{(r)}\langle\delta\boldsymbol{\sigma}^{t-\Delta t(\overline{q})} \otimes \delta\mathbf{r}^{t-\Delta t}\rangle^{(r)}\mathbf{Y}^{(\delta r)(r)^T} +$$

$$\mathbf{Z}^{(r)}\langle\delta\boldsymbol{\sigma}^{t-\Delta t(\overline{q})} \otimes \delta\boldsymbol{\sigma}^{t-\Delta t(\overline{q})}\rangle^{(r)}\mathbf{Y}^{(\delta\sigma)(r)^T}. \tag{46}$$

Eq. (46) defines the cross-covariance $\langle\delta\boldsymbol{\sigma}^{t(\overline{q})} \otimes \delta\mathbf{r}^t\rangle^{(r)}$ as a function of cross-covariance from time $t - \Delta t$.

2.6   Grain fragmentation model

Let us consider one grain with a given mean orientation, $\overline{\mathbf{q}}^{(r)}$, and associated second moment of misorientation vectors, $\langle\delta\mathbf{r} \otimes \delta\mathbf{r}\rangle^{(r)}$. During deformation, the misorientation spread will generally increase and, at a certain strain, it may become so large that it cannot be represented accurately with only one mean value and one second moment. In addition, the spread may become so large that it is no longer reasonable to assume that the behavior of the grain is defined solely by the mean orientation of the grain. Furthermore, the Taylor expansion with respect to the misorientation vectors around the mean grain orientation, holds only for reasonably

small misorientation vectors. Therefore, a grain fragmentation model becomes necessary when considering deformation to higher strains.
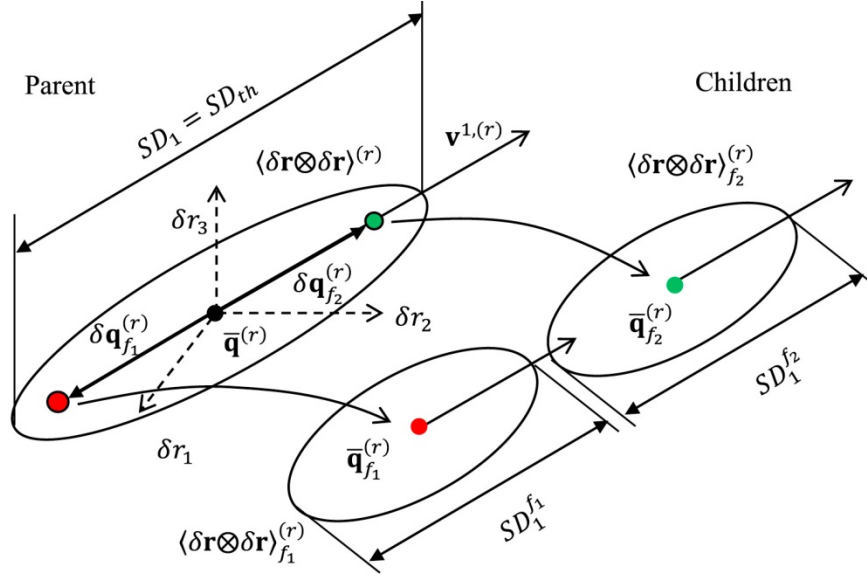
Fig. 2. Fragmentation of the parent grain into two child grains when the standard deviation, SD_1, along the direction of largest variation, $\mathbf{v}^1$, reaches the threshold value, SD_{th}. The orientations of the child grains, $\overline{\mathbf{q}}_{f_1}^{(r)}$ and $\overline{\mathbf{q}}_{f_2}^{(r)}$, are defined based on the parents mean orientation, $\overline{\mathbf{q}}^{(r)}$, and misorientation distribution, $\langle \delta \mathbf{r} \otimes \delta \mathbf{r} \rangle^{(r)}$ (Appendix C). Mean orientations of the children grains are misoriented with respect to the mean orientation of the parent around the axis aligned with the vector $\mathbf{v}^1$. The misorientation distributions are represented by iso-density ellipsoids.

In order to quantify the magnitude of the misorientation spread, we calculate the principal values, λ^i, and directions, $\mathbf{v}^i$, of the misorientation distribution, $\langle \delta \mathbf{r} \otimes \delta \mathbf{r} \rangle^{(r)}$, and sort them in descending order (Pantleon, 2005). The matrix $\langle \delta \mathbf{r} \otimes \delta \mathbf{r} \rangle^{(r)}$ is a covariance matrix and thus has to be positive-semidefinite by definition, implying that the eigenvalues are non-negative: $\lambda^i \geq 0$. The maximum principal value, λ^1, represents the variance along the corresponding principal direction of largest variation, $\mathbf{v}^1$. The standard deviations along principal directions are defined as $SD_i = \sqrt{\lambda^i}$. For the purposes of the fragmentation model, the misorientation distribution is assumed to be multivariate normal.

Misorientation vectors along the direction $\mathbf{v}^1$ are the largest in the misorientation distribution and thus the Taylor expansion of stress and spin (Eq. 20 and 24) might not be sufficiently accurate for these misorientation vectors. In addition, the additive accumulation of misorientation vectors (Eq. 35) holds only for relatively small misorientations. Therefore, when the largest standard deviation, SD_1, reaches a critical value, SD_{th}, further evolution of the intragranular distributions becomes inaccurate. One solution to this problem is division of the grain into two child grains once SD_1 reaches critical value (Fig. 2). The mean orientations of the children grains, $\bar{\mathbf{q}}_{f_1}^{(r)}$ and $\bar{\mathbf{q}}_{f_2}^{(r)}$, are calculated by misorienting the mean orientation of the parent grain, $\bar{\mathbf{q}}^{(r)}$, around the direction of largest variation, $\mathbf{v}^1$, for an angle calculated based on the SD_1 (see Appendix C). The misorientation distributions of children grains are calculated by dividing the parent's misorientation distribution along the direction of largest variation, $\mathbf{v}^1$ (see Appendix C). From all the possible divisions of the parent's misorientation distribution, division along the direction of largest variation gives the fragmented distributions with the smallest maximal standard deviations, $SD_1^{f_1}$ and $SD_1^{f_2}$. Consequently, the Taylor expansion around the mean orientation and the additive accumulation of misorientation vectors hold again for the children grains. The misorientation distributions of the parent grain and children grains are illustrated by iso-density ellipsoids in Fig. 2. Points on the surface of the iso-density ellipsoid have the same probability density. For illustration purposes, the semi axes of iso-density ellipsoids are chosen to correspond to the standard deviations, SD_i. Since the slip resistance is assumed constant within the grain, the children grains inherit the parent's slip resistance. The mean stress and strain rate within the children are also assumed same as parent's and they only serve as initial guesses for the next time increment when they will be calculated by means of the self-consistent procedure.

The threshold value for SD_1 is suitably chosen so that the angle between the mean orientations of the children grains is 15° at the moment of fragmentation. On one hand, higher threshold value for SD_1 might result in reduced accuracy, while on the other hand lower threshold value for SD_1 would give more accurate result but would also cause more excessive fragmentation and very large number of fragments at higher strains. The chosen value is a compromise that yields accurate results and manageable number of grains even at higher strains.

3   Results and discussion

The GF-VPSC model for prediction of intragranular misorientation spreads is applied to tension of an fcc polycrystal at room temperature, and PSC of an fcc polycrystal at elevated temperature. The predictions are compared to VPFFT full-field (Lebensohn, 2001; Lebensohn et al., 2008) simulation results for the case of tension, and to both VPFFT and experimental results (Quey et al., 2010 for rolled Al) in the case of PSC. In addition, coupling of deformation and recrystallization modeling is discussed at the end of this section.

3.1   *Uniaxial tension of an fcc polycrystal*

Uniaxial tension of a polycrystal consisting of 400 spherical, randomly oriented grains is simulated to 40% strain using the GF-VPSC model and compared with full-field VPFFT predictions. The initial microstructure for full-field VPFFT simulation was created by assigning the 400 random orientations used in GF-VPSC simulations to 400 approximately equiaxed and equal-volume grains within a periodic Voronoi unit cell. The grains are assumed to deform by $\{111\}\langle 1\bar{1}0\rangle$ slip with a power-law exponent in Eq. (2) of $n = 10$, and no strain hardening. In addition, the same deformation is simulated with the VPSC model used in (Zecevic et al., 2017). The grain fragmentation scheme described in section 2.6 was implemented in this earlier model as well, in order to facilitate the comparison. The VPSC model reported in (Zecevic et al., 2017)

calculates intragranular misorientation distributions based on the second moments of lattice rotation rates (Lebensohn et al., 2016) in a similar manner to the GF-VPSC model, but does not include the effects of the misorientation distributions on the stress and lattice spin fluctuations. Consequently, the difference between the results of the two grain fragmentation predictions shows the importance of considering the effects of the misorientation on the fluctuations of stress and lattice spin.

The magnitude of the orientation spread for each grain within the polycrystal can be quantified with one scalar parameter: equivalent isotropic spread. Consequently, a discrete set of grain equivalent isotropic spreads can be created for a polycrystal and a probability density (pdf) function of the equivalent isotropic spreads can be defined. Figure 3 shows the pdfs of the equivalent isotropic spreads calculated over the polycrystal for GF-VPSC, GF-VPSC without misorientation effects on fluctuations, and VPFFT. The equivalent isotropic spread, SD, is calculated as the geometric mean of the standard deviations, SD_i, along the principal directions of the intragranular misorientation spread: $SD = \sqrt[3]{SD_1 \times SD_2 \times SD_3}$ (Krog-Pedersen et al., 2009). The standard deviations, SD_i, can be used for construction of iso-density ellipsoids around the mean grain value of misorientation vectors, $\langle \delta \mathbf{r} \rangle^{(r)} = \mathbf{0}$. Misorientation vectors pointing to the surface of the iso-density ellipsoid are exactly one standard deviation away from the grain's mean of the misorientation vectors, and their probability density is the same. Equivalent isotropic spread represents a radius of a sphere which has the same volume as the defined iso-density ellipsoid and thus represents standard deviation of the isotropic spread defined based on the anisotropic misorientation distribution. A majority of grains in the VPFFT model develop equivalent isotropic spreads around 0.045 with relatively high dispersion. On the other hand, both GF-VPSC models predict strong concentration of equivalent isotropic spreads around 0.04

and weaker concentration around 0.02. The presence of an additional peak in the GF-VPSC pdf predictions is caused by the disc shaped misorientation distributions in the grains with tensile axis close to [001]. Very small magnitude of standard deviation along the direction of smallest variation, SD_3, results in an unreasonably small magnitude of the equivalent isotropic spreads within those grains (Zecevic et al., 2017). Main cause for development of such misorientation distributions is the insensitivity of spin component along the tension direction to the fluctuations in stress, as will be detailed below. Considering the discrepancy between the GF-VPSC and VPFFT, we conclude that the Taylor expansion of spin with respect to stress becomes inaccurate for orientations with the tensile direction (TD) close to [001].
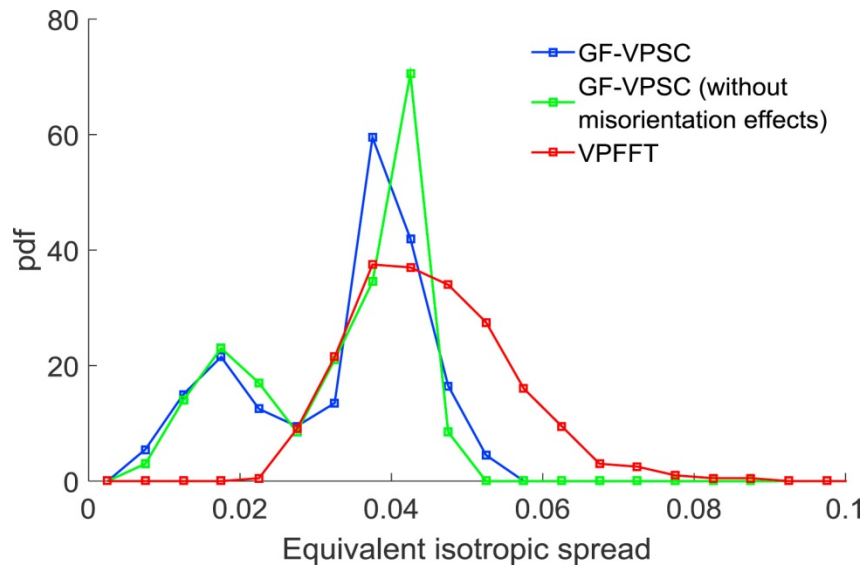
Fig. 3. Probability density functions (pdf) of equivalent isotropic spreads calculated using GF-VPSC, GF-VPSC without misorientation effects, and VPFFT, for an fcc polycrystal deformed in tension to 40% strain.

The direction of the misorientation distribution of each grain in the polycrystal can be quantified with one vector pointing in the direction of the largest variation, i.e. the dominant rotation axis. Figure 4 compares the equal-area projections of dominant rotation axes between GF-VPSC, GF-VPSC without misorientation effects on fluctuations, and VPFFT, for all of the

grains in the polycrystal. The largest variation of intragranular misorientation spread is about the dominant rotation axis, aligned with the direction of the eigenvector, $\mathbf{v}^1$, corresponding to largest eigenvalue, λ^1, of the second moment of misorientation, $\langle \delta\mathbf{r}^t \otimes \delta\mathbf{r}^t \rangle^{(r)}$ (Bachmann et al., 2010; Pantleon, 2005). Physically, the orientations from the grain's orientation spread which are the most misoriented with respect to the mean grain orientation have the axis of misorientation aligned with the dominant rotation axis. For VPFFT, large portion of dominant rotation axes tends to align perpendicular to the tension direction while the remaining portion is randomly spread out around TD. Similarly, GF-VPSC predicts strong alignment of the dominant rotation axes perpendicular to TD. In addition, GF-VPSC predicts a certain portion of dominant rotation axes relatively close to TD but in a ring about 30 degrees away from the tension direction. On the other hand, the GF-VPSC model without effects of misorientation on fluctuations predicts all the axes to be perpendicular to the tension direction. In addition, the magnitudes of SD along the dominant rotation axes in the GF-VPSC simulations without effects of misorientation are generally smaller than the magnitudes observed in the GF-VPSC and VPFFT simulations. In both GF-VPSC and VPFFT simulations, grains with the dominant rotation axis perpendicular to TD tend to develop higher SD in comparison to the grains with the dominant rotation axis parallel to TD.

Figure 5 shows the orientation dependence of the angle between the dominant rotation axis and TD for GF-VPSC, GF-VPSC without misorientation effects on fluctuations, and VPFFT. For VPFFT, the axes displaying the smallest angles are for orientations close to the stable orientations, [001] and [111]. On the other hand, GF-VPSC predicts the smallest angle only in the region close to [111] but not directly at [111]. The GF-VPSC without misorientation effects on fluctuations predicts an angle close to 90 degrees for all of the grains, as expected based on

Fig. 4. Therefore, the rotation of dominant rotation axes toward TD in GF-VPSC is likely caused by the introduced effects of misorientation on the stress and lattice spin fluctuations. The observed behavior for VPFFT and GF-VPSC is analyzed in detail next.
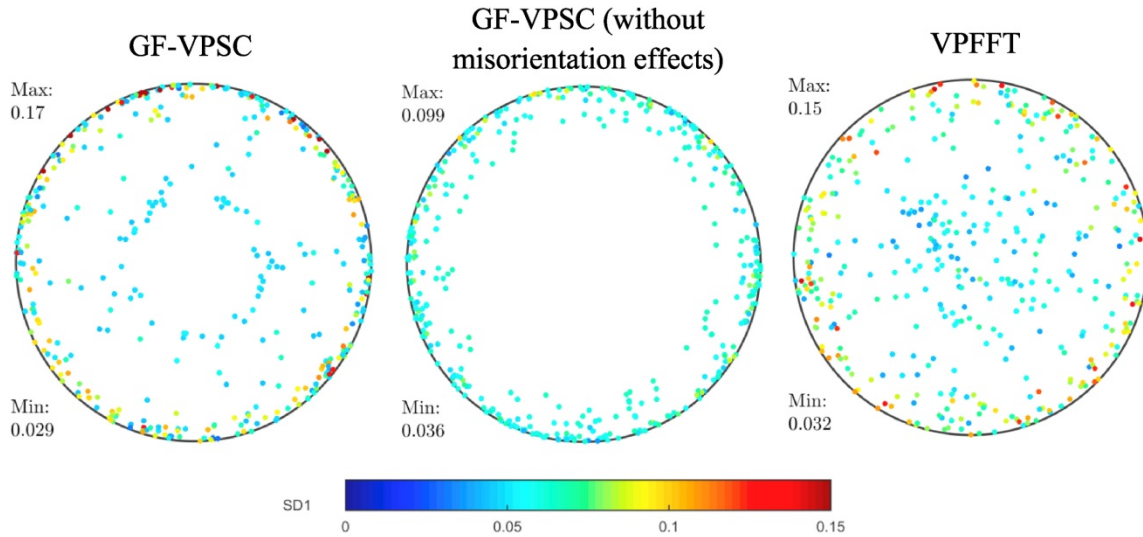

Fig. 4. Comparison of dominant rotation axes calculated using GF-VPSC, GF-VPSC without misorientation effects, and VPFFT, after tension to 40% strain, color-coded according to magnitude of standard deviation along dominant rotation axis.

During the initial stages of tensile loading, grains develop misorientation spreads perpendicular to TD both in GF-VPSC and VPFFT (Zecevic et al., 2017). Lattice spin fluctuations can be decomposed into fluctuations caused by: i) intragranular stress fluctuations, and ii) intragranular misorientation. The fluctuations of lattice spin at lower strains are predominantly driven by the stress fluctuations, since intragranular misorientations are fairly small. The component of lattice spin along TD is less sensitive to stress fluctuations than the other two components lying in the plane perpendicular to the TD, which causes intragranular misorientation spreads to develop perpendicular to TD (Zecevic et al., 2017). This behavior is especially pronounced for orientations with TD within 15 degrees from [001] and 5 degrees from [111] in the GF-VPSC results, for which variations of intragranular misorientation spreads along TD are very small.

At higher strains, the influence of the intragranular misorientation on lattice spin fluctuations becomes dominant due to large misorientation spreads. When a grain with a certain orientation spread reaches either the [001] || TD or [111] || TD stable fibers, the lattice spin fluctuations of the orientations within the spread that are away from the fiber cause reorientation toward the fiber, since the region around the fiber is convergent. On the other hand, lattice spin fluctuations of orientations of the spread that are on the fiber cause very small total reorientations since these intragranular orientations have reached a stable position. Therefore, orientation spreads of these grains tend to assume the shape of the fiber. Similar behavior was observed during PSC of fcc polycrystals (Quey et al., 2015). Consequently, as the grains approach [001] and [111] regions, they start developing misorientation spread with dominant rotation axis parallel to TD because their orientation spread tends to align with the stable fiber. This behavior is observed in VPFFT and is more pronounced around [111] than in the [001] region because orientations tend to converge to [111] faster than to [001] (Lebensohn et al., 2016).

In GF-VPSC, orientations that are initially close to the stable regions [111] and [001] develop very small spreads along TD, as was noted before. The lattice spin fluctuations caused by the intragranular misorientation tend to shrink the spread in the plane perpendicular to TD and thus bring all the orientations of the spread to the fiber. However, regardless of this effect, the dominant rotation axis will remain perpendicular to TD because variations of the intragranular misorientation spread along TD are very small. Only orientations with [111] about 10 degrees away from TD develop sufficiently large components of misorientation spread along TD. Consequently, only these orientations show the dominant rotation axis close to TD as they reorient toward the [111] due to the effect of the plastic spin fluctuations caused by the intragranular misorientation (Fig. 5).
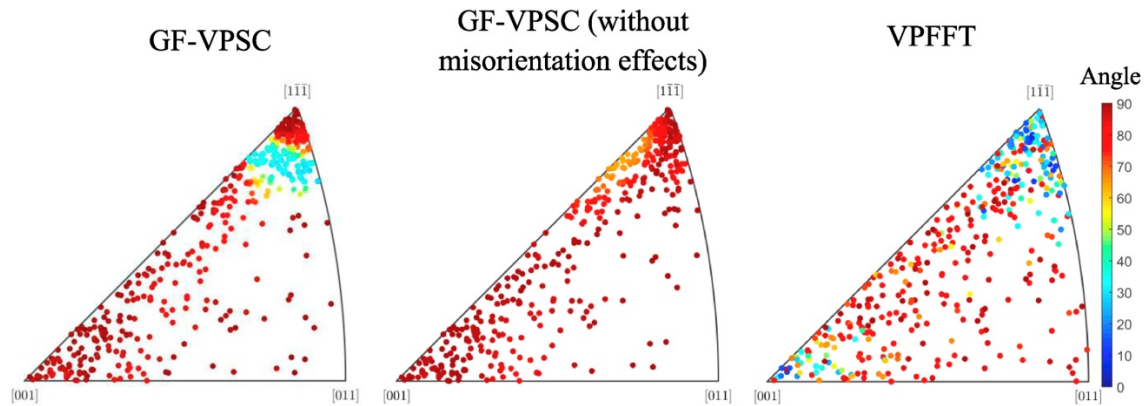
Fig. 5. Inverse pole figures after tension to 40% strain for GF-VPSC, GF-VPSC without misorientation effects, and VPFFT. The poles represent the orientation of TD in the crystal frame of each grain, and their colors represent the angles between the dominant rotation axis and the tensile direction.

### 3.2   PSC of fcc polycrystal at elevated temperature

Quey et al (Quey et al., 2010) performed PSC of recrystallized Al-0.1wt%Mn at 400°C to a final rolling strain of 1.2. The same region of the sample was scanned using EBSD at strain levels of 0.0, 0.42, 0.77 and 1.2. The grains present in the EBSD scan of the initial microstructure were identified in the subsequent scans taken at each strain level. Therefore, the intragranular orientation spread of this subset of grains is available at each strain level. In addition, crystal plasticity finite element (CPFE) modeling of the experiment and analysis of misorientation spreads was performed in (Quey et al., 2012; Quey et al., 2015).

We simulated Quey et al.'s PSC experiment using the GF-VPSC and VPFFT models, using the orientations of 207 grains present in the initial EBSD scan, along with 193 random orientations as the initial texture. The orientations from the initial texture were sorted according to the volume fraction and assigned to the grains within the periodic Voronoi unit cell that was used as the initial microstructure for the VPFFT simulation. The orientation with the largest volume fraction within the initial texture was assigned to the grain with the largest volume fraction within the Voronoi unit cell, etcetera. This method of orientation assignment ensures the

184

smallest difference between the initial texture of the Voronoi unit cell for VPFFT simulations and the initial texture used in GF-VPSC simulations. There was no intragranular misorientation spread within the initial microstructure. At elevated temperature, the slip resistances of non-octahedral slip systems may drastically decrease resulting in their activation (Bacroix and Jonas, 1988). The slip on non-octahedral planes is interpreted as cross-slip from the plane {111}. Perocheu and Driver measured the stress strain response of Al-1wt%Mn single crystals at 400-500 °C and at different strain rates (Perocheau and Driver, 2002). The orientations of single crystals were chosen to favor different slip systems and slip trace analysis revealed activation of non-octahedral slip systems. The ratios of flow stresses between the {111}$\langle 0\bar{1}1 \rangle$, {011}$\langle 0\bar{1}1 \rangle$ and {100}$\langle 0\bar{1}1 \rangle$ slip modes were determined to be: 1.0-0.9-1.4, respectively. Consequently, in both GF-VPSC and VPFFT models we assume same slip systems with the measured ratio of slip resistances. The rate sensitivity of the flow stress was measured to be between 0.07 and 0.11 (Perocheau and Driver, 2002). In both models we assume rate exponent in the rate-sensitive constitutive equation as $n = 10$ and no strain hardening. The same slip modes and slip resistance ratios and similar rate exponent ($n \approx 8$) were used for the CPFE modeling performed in (Quey et al., 2012; Quey et al., 2015). Comparisons of intragranular misorientation distributions were performed for the subset of grains represented in the EBSD scans with at least 500 points at each strain level, resulting in 119 grains. Since the highly deformed grains are more difficult to index during EBSD scanning at higher strains, the highly deformed grains with relatively small area are less likely to be included in the defined subset of grains which thus might be biased toward less deformed grains. However, since the main purpose of this study is comparison of the model predictions with the experiment for the defined subset of grains, this effect can be neglected.

During deformation, certain grains in the divergent regions of the orientation space subdivide into two distinct portions. Due to different slip activity, one portion of the grain reorients toward one stable region while the other portion of the grain reorients towards a different stable region. These highly misoriented portions of the grain are called deformation bands. Thin regions between the deformation bands are called transition bands, and large orientation difference between the deformation bands is accommodated within them (Dillamore and Katoh, 1974; Hansen and Jensen, 1999). Orientation spread of such grain is bi-modal and consists of orientations clustered around two distinct modes which lie in different stable regions of the orientation space (Quey et al., 2012). Since the grain's misorientation spread simply represents the grain's orientation spread defined with respect to the mean orientation, the misorientation distribution is bi-modal as well (Fig 6a). The dominant rotation axis of the bi-modal grain describes the misorientation axis between the two modes of the misorientation distribution. The pdf of the misorientation vector components along the dominant rotation axis is again bi-modal and can be used for identification of the bi-modal grains, Fig. 6b (Quey et al., 2012). The misorientations clustered around different modes of the misorientation distribution correspond to different deformation bands (Fig 6b). On the other hand, the misorientations from the region between the modes of the misorientation distributions correspond to the transition band (Fig 6b). Therefore, by examining the intragranular misorientation spreads, we can identify grains that developed transition bands and the orientations present in transition bands. The calculated fractions of bi-modal grains at each strain level in the experiment and the simulations are compared in Fig. 7. VPFFT over-predicts the number of bi-modal grains, while GF-VPSC under-predicts it. The CPFE simulations performed in (Quey et al., 2012) predicted a similar fraction of bi-modal grains as VPFFT.
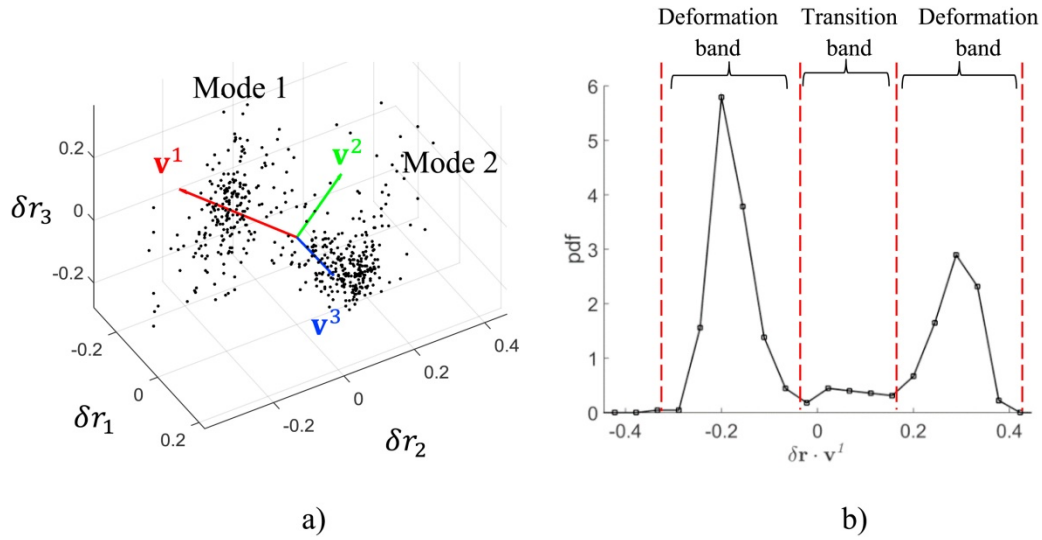
Fig. 6. (a) Scatter plot of misorientation vectors for a bi-modal grain predicted with VPFFT for plane-strain compression, and (b) probability density function of misorientation vector projections along the dominant rotation axis. The principal vectors of misorientation distribution are denoted as $\mathbf{v}^i$.

Grains with bi-modal orientation distributions usually have quite large misorientations between the individual modes, and thus should not be treated as a single grain. As noted above, the dominant rotation axis of the bi-modal grains essentially describes the misorientation axis between the two modes, while the equivalent isotropic spread describes the magnitude of misorientation between the two modes. The misorientation spreads developing around the individual modes have completely different dominant rotation axes and equivalent isotropic spreads. Consequently, the dominant rotation axes and equivalent isotropic spreads of the misorientation distributions are compared only for the grains with unimodal orientation distribution, as was done in (Quey et al., 2015).
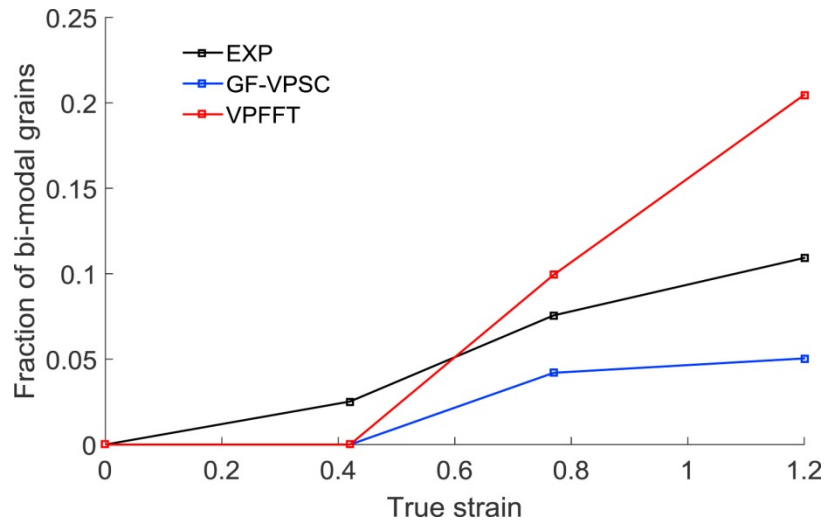
Fig. 7. Comparison between measured (rolled Al) and predicted (GF-VPSC and VPFFT) fractions of bi-modal grains at different strain levels for plane-strain compression.

Figure 8 compares the simulated and experimental pdfs of equivalent isotropic spreads calculated over the entire polycrystal at each strain level. The GF-VPSC tends to over-predict the concentration of equivalent isotropic spreads around certain values, in comparison to the experiment. On the other hand, VPFFT displays too much variation of equivalent isotropic spreads, especially at higher strains, which is consistent with the CPFE simulations performed by (Quey et al., 2015). Initially, the magnitudes of equivalent isotropic spreads increase rapidly with strain in both simulations and experiment. Grains that are initially in divergent regions rapidly develop large misorientation spreads, while grains that are in the stable regions develop misorientation spreads at considerably slower rate. Since initially there is a relatively small number of grains in stable convergent regions, the misorientation spreads develop rapidly for a significant fraction of grains. At higher strains, the equivalent isotropic spreads saturate and do not increase significantly with further deformation, an observation which is especially pronounced in the experimental results (Quey et al., 2010). This is because a majority of grains have reached stable convergent orientations, where the misorientation spreads evolve slowly.
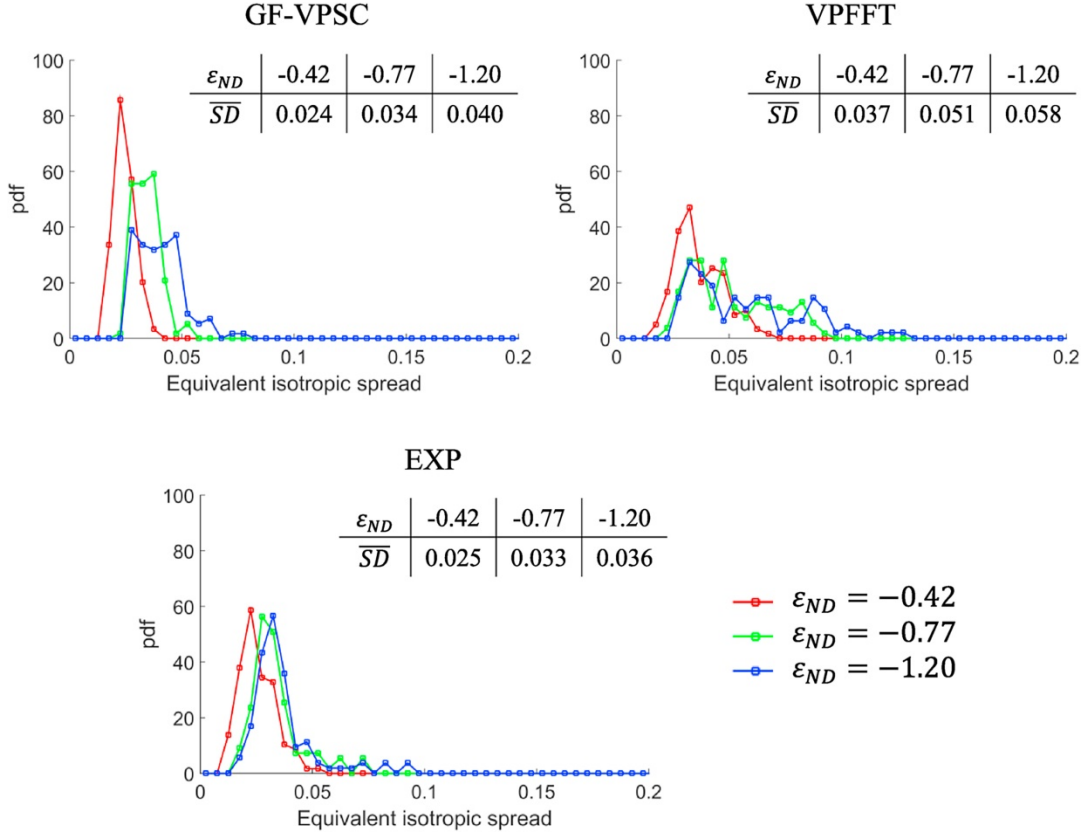
Fig. 8. Experimental (rolled Al) and predicted (GF-VPSC and VPFFT) probability density functions of equivalent isotropic spreads during plane-strain compression at different strain levels. ε_{ND} is the strain in the normal direction while the $\overline{SD} = \frac{1}{n}\sum_r SD^{(r)}$ represents the average value of equivalent isotropic spread over the polycrystal.

Figure 9 shows the directions of dominant rotation axes after applying the rolling symmetry for simulations and experiment, at each strain level. At lower strains, the dominant rotation axes tend to align with TD in both simulations and experiment, in agreement with (Pantleon et al., 2008). This tendency is weaker in VPFFT predictions, compared to experiment and GF-VPSC results. As the strain increases, the dominant rotation axes start rotating toward RD in the experimental results. A similar trend, though noticeably weaker, is predicted with GF-VPSC. On the other hand, VPFFT predicts a significant fraction of the axes aligned with ND and in the TD-ND plane at higher strains, which is not observed in experiment or GF-VPSC. Similar alignment of the dominant rotation axes with ND was also observed in the CPFE simulations (Quey et al.,

189

2015). This behavior was attributed to the alignment of the misorientation spread with the direction of the fiber to which the mean grain orientation belongs (Quey et al., 2015).
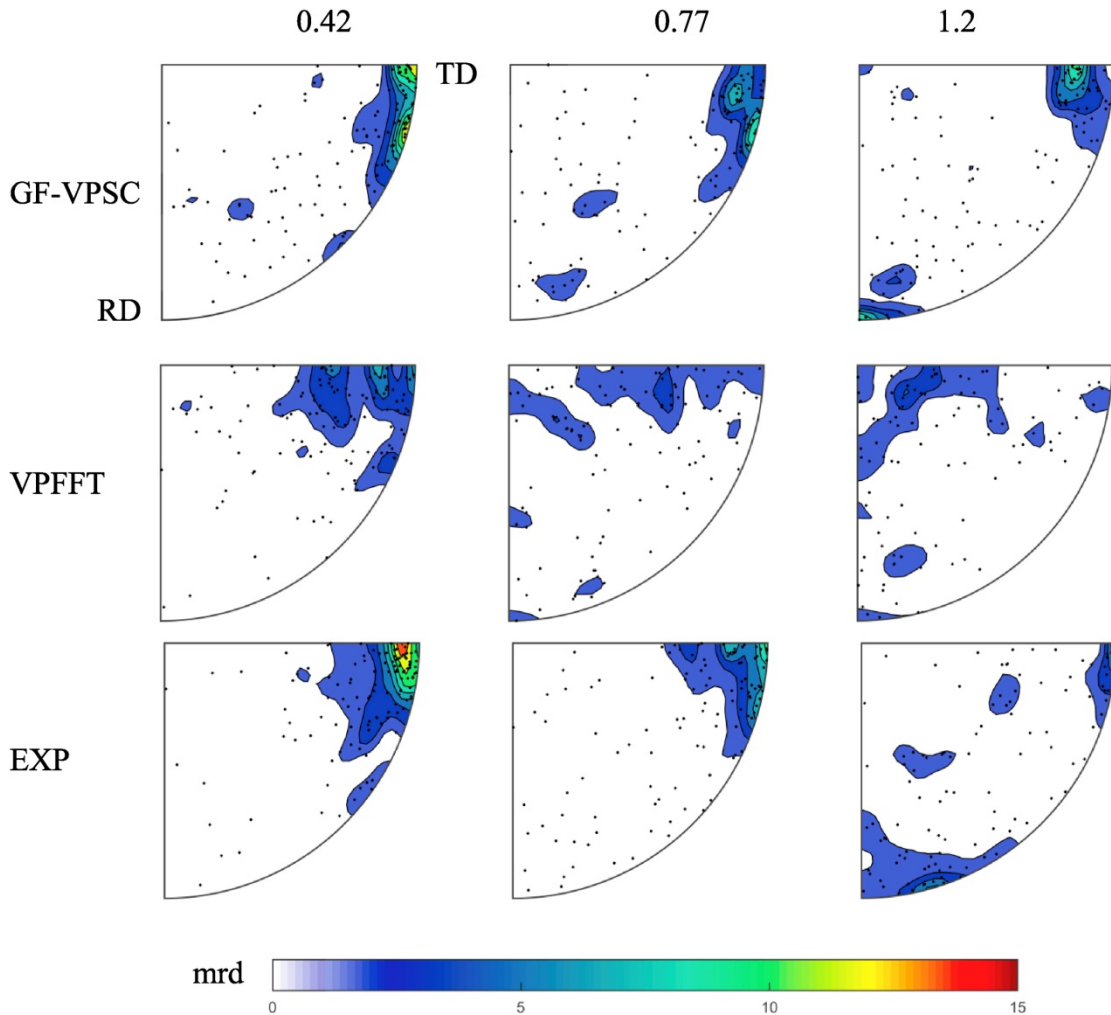
Fig. 9. Dominant rotation axes for experiment (rolled Al) and simulations (GF-VPSC and VPFFT) for plane-strain compression at different strain levels.

Considering the complexities involved in the physics of grain fragmentation, the GF-VPSC predictions are good. Moreover, the model is much more computationally efficient than the full-field models. The GF-VPSC model without the misorientation effects on the stress and lattice spin fluctuations predicts almost zero bi-modal grains, even at 1.2 strain. In addition, the dominant rotation axes remain strongly aligned with the TD throughout the deformation. These

results corroborate our previous assertion, in the sense that field fluctuations caused by the intragranular misorientation become dominant at higher strains.

Both GF-VPSC and VPFFT are three-dimensional (3-D) models, while only two-dimensional (2-D) sections of grains were analyzed in the experiment. Consequently, certain discrepancy between the predictions and measurements is expected (Quey et al., 2015). In addition, the 3-D unit cell used for the VPFFT was generated randomly, solely based on the grain orientations and volume fractions obtained from one 2-D scan of the actual microstructure. Therefore, the generated 3-D unit cell does not correspond to the actual unknown 3-D microstructure of the sample. In the GF-VPSC model, every grain interacts with the effective medium which has the averaged properties of the polycrystal. Consequently, the response of the GF-VPSC model is determined only by the discrete set of grain orientations and volume fractions, while the actual 3-D microstructure corresponding to that set of grains has no influence on the results. In a sense, GF-VPSC gives an averaged response over all possible 3-D microstructures for a defined set of grain orientations and volume fractions (Lebensohn et al., 2004). This statistical representativity can be the explanation for the better agreement of the GF-VPSC model with the experimental results in comparison to the VPFFT. In the absence of the actual 3-D microstructure, averaged response seems to be closer to the experimental measurements than the response of an assumed 3-D microstructure used in VPFFT.

Finally, Fig. 10 compares the textures after deformation in the form of {111} pole figures. The same features are present in both simulations and experiment, but the intensities differ. GF-VPSC predicts a weaker texture than experimentally measured, while VPFFT predicts a peak intensity very close to the experimental value. As a reference, the texture predicted by the VPSC model without the extension for calculation of intragranular misorientation spreads is given in

Fig. 10 as well. The predicted peak intensity is considerably higher than the experimentally measured intensity, as was observed in (Lebensohn, 2001), confirming that the incorporation of intragranular misorientation spreads and grain fragmentation improves texture predictions.
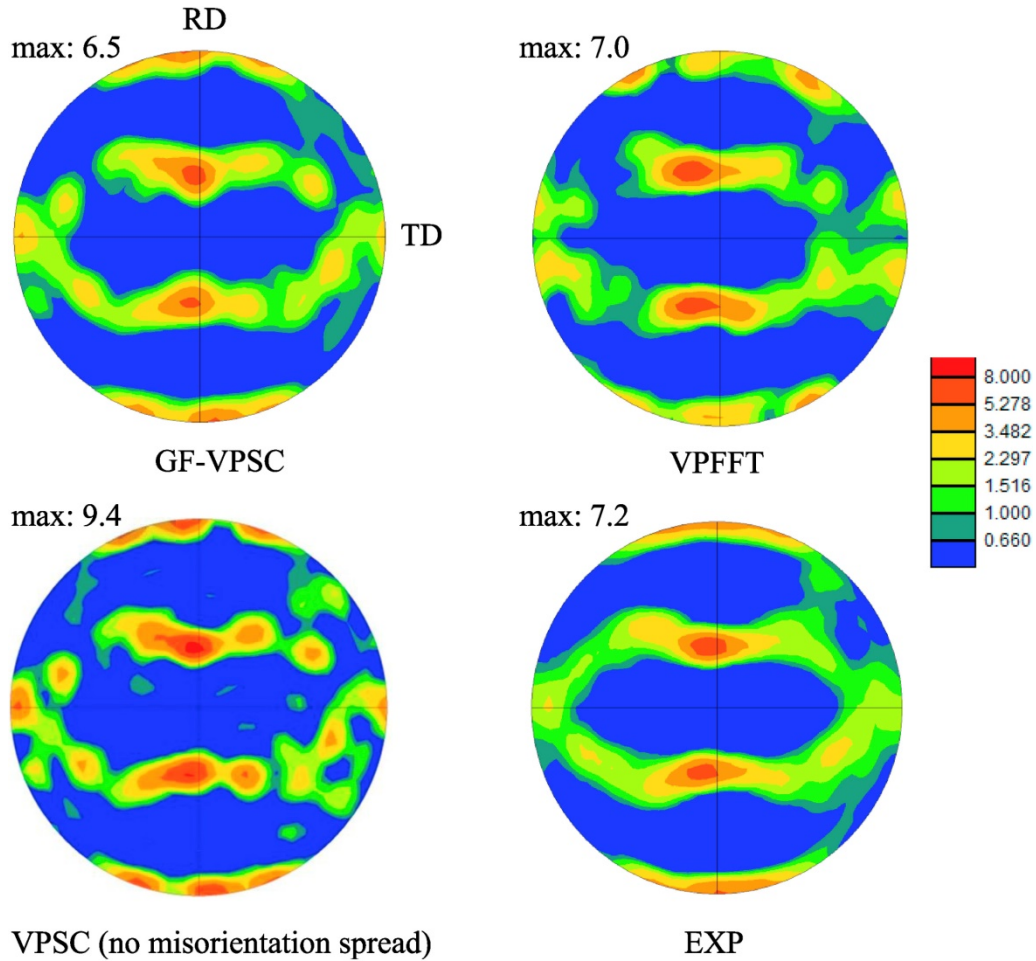
Fig. 10. {111} pole figures measured (rolled Al) and predicted by GF-VPSC, VPFFT, and standard VPSC, for plane-strain compression after 1.2 strain.

## 3.3 *Coupled modeling of deformation and recrystallization*

In closing this section, we show that the new GF-VPSC model is not only able to predict grain fragmentation in a micromechanically-consistent fashion, and validated by comparison with experiments, but it also enables coupled modeling of microstructure evolution during deformation and recrystallization. As already mentioned, intragranular orientation spreads have

been related to the formation of transition bands. These high orientation gradient regions between deformation bands favor recrystallization nuclei, which may have quite different crystallographic orientation compared to the average grain orientation, due to large orientation variations developed in the grains (Humphreys and Hatherly, 2004; Knezevic et al., 2014; McCabe et al., 2015). Therefore, even though the GF-VPSC provides only statistical description of intragranular misorientation distributions, in the special case of bi-modal orientation distributions, it can be assumed that the orientations between the modes of the orientation distribution (transition band orientations) spatially neighbor the orientations from the modes of the orientation distribution (deformation band orientations). Consequently, the orientation gradients for these grains become high.

Let us consider the recrystallization of heavily rolled copper, which results in a strong cube texture. It was found that during rolling of copper, certain grains develop transition bands with the cube orientation present within the center of the transition band (Dillamore and Katoh, 1974; Hjelen et al., 1991; Ridha and Hutchinson, 1982). These cube-oriented nuclei grow and consume the deformed microstructure resulting in cube recrystallization texture. In order to simulate this process, GF-VPSC and VPFFT were used to model PSC of copper to a reduction of 78 %. The initial microstructure consists of 400 randomly oriented spherical grains deforming by $\{111\}\langle0\bar{1}1\rangle$ slip with no strain hardening. The grains that have developed bi-modal orientation distributions, and thus formed transition bands, were flagged at the end of deformation, and a *transition-band ODF* was defined by assembling the orientations present within the transition bands of all bi-modal grains. If nucleation at transition bands is accepted as the likely nucleation mechanism, then the transition-band ODF defines possible orientations of recrystallization nuclei. The transition-band ODFs are plotted on Fig. 11 in the form of {111} pole figures as

predicted by GF-VPSC and VPFFT. A cube texture is predicted in both cases, in accordance with the previous experimental observations and theoretical considerations and interpretations (Dillamore and Katoh, 1974; Ridha and Hutchinson, 1982).
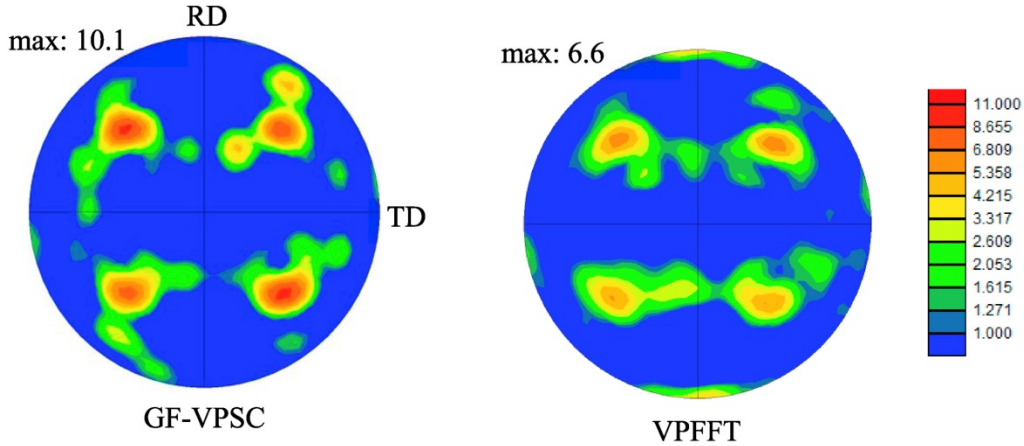
Fig. 11. {111} pole figures corresponding to transition band ODF for plane-strain compression of fcc polycrystal after 78 % reduction predicted by GF-VPSC and VPFFT.

4   Conclusions

In this work, we have developed a formulation and the associated algorithms for the calculation of intragranular misorientation spreads during plastic deformation at high strains. The effect of the misorientation on the stress and lattice spin fluctuations has been included, by assuming linear relations between these fluctuations and misorientation. In addition, a grain fragmentation model, formulated in orientation space, was proposed and implemented in VPSC. The model was applied to tension of an fcc polycrystal and compared to the full-field simulation results obtained by VPFFT. It was observed that the dominant rotation axes tend to rotate toward the tensile direction, for grains that have reached stable [001] and [111] regions. This behavior was attributed to the effect of the lattice spin fluctuations caused by large intragranular misorientation spreads. In addition, PSC of fcc polycrystal at 400°C to a strain of 1.2 was also simulated and compared with corresponding experiments and full-field simulations. It was

194

observed that the dominant rotation axes at higher strains tend to align with RD. The magnitude of the spread evolves rapidly at lower strain and saturates at intermediate and high strains. The inclusion of misorientation spreads reduces the intensity of the deformed texture and thus improves texture prediction. Considering the complexity of the physical problem, satisfactory agreement between the proposed model and full-field simulations and experiment was found. Finally, it was shown that the new GF-VPSC model can be used to predict microstructure evolution during deformation and recrystallization. Further development and applications of this novel modeling capability is on-going work, and will be reported in due time.

Acknowledgments

Appendix A

The derivative of stress with respect to misorientation, $\delta\mathbf{r}$, can be obtained by taking the derivative of the rate-sensitive constitutive equation (Eq. 3), holding the strain rate constant:

$$\frac{\partial \boldsymbol{\sigma}}{\partial \delta \mathbf{r}} = - \left[\sum_s \mathbf{m}^s \otimes \frac{\partial \dot{\gamma}^s}{\partial \boldsymbol{\sigma}} \right]^{-1} \left\{ \sum_s \left[\mathbf{m}^s \otimes \left(\frac{\partial \dot{\gamma}^s}{\partial \mathbf{m}^s} \frac{\partial \mathbf{m}^s}{\partial \delta \mathbf{r}} \right) + \dot{\gamma}^s \frac{\partial \mathbf{m}^s}{\partial \delta \mathbf{r}} \right] \right\}. \tag{A1}$$

The derivatives of lattice reorientation rate (Eq. 13) with respect to stress and misorientation are given by:

$$\frac{\partial \dot{\boldsymbol{\omega}}}{\partial \boldsymbol{\sigma}} = - \frac{\partial \dot{\boldsymbol{\omega}}^p}{\partial \boldsymbol{\sigma}} = - \sum_s \boldsymbol{\alpha}^s \otimes \frac{\partial \dot{\gamma}^s}{\partial \boldsymbol{\sigma}}, \tag{A2}$$

195

$$\frac{\partial \dot{\boldsymbol{\omega}}}{\partial \delta \mathbf{r}} = -\frac{\partial \dot{\boldsymbol{\omega}}^p}{\partial \delta \mathbf{r}} = -\sum_s \left[\boldsymbol{\alpha}^s \otimes \left(\frac{\partial \dot{\gamma}^s}{\partial \mathbf{m}^s} \frac{\partial \mathbf{m}^s}{\partial \delta \mathbf{r}} \right) + \dot{\gamma}^s \frac{\partial \boldsymbol{\alpha}^s}{\partial \delta \mathbf{r}} \right]. \tag{A3}$$

Note that the reorientation rate of ellipsoid is assumed to be constant in the grain. Consequently, derivatives of rotation rate are equal to the negative derivatives of the lattice spin given by Eq. (14).

Next, the expressions for derivatives $\frac{\partial \dot{\gamma}^s}{\partial \boldsymbol{\sigma}}$, $\frac{\partial \dot{\gamma}^s}{\partial \mathbf{m}^s}$, $\frac{\partial \mathbf{m}^s}{\partial \delta \mathbf{r}}$ and $\frac{\partial \boldsymbol{\alpha}^s}{\partial \delta \mathbf{r}}$ appearing in the 3 previous equations are provided. First, the derivatives of the shear rate (Eq. 2) with respect to stress and the symmetric part of Schmid tensor are given by:

$$\frac{\partial \dot{\gamma}^s}{\partial \boldsymbol{\sigma}} = \dot{\gamma}_0 n \left(\frac{|\boldsymbol{\sigma} \cdot \mathbf{m}^s|}{\tau_c^s} \right)^{n-1} \frac{1}{\tau_c^s} \mathbf{m}^s. \tag{A4}$$

$$\frac{\partial \dot{\gamma}^s}{\partial \mathbf{m}^s} = \dot{\gamma}_0 n \left(\frac{|\boldsymbol{\sigma} \cdot \mathbf{m}^s|}{\tau_c^s} \right)^{n-1} \frac{1}{\tau_c^s} \boldsymbol{\sigma}. \tag{A5}$$

The derivative of symmetric Schmid tensors with respect to misorientation vector is given by the chain rule:

$$\frac{\partial m_{ij}^s}{\partial \delta r_m} = \frac{\partial m_{ij}^s}{\partial \delta R_{kl}} \frac{\partial \delta R_{kl}}{\partial \delta r_m}, \tag{A6}$$

where the δR_{kl} is rotation matrix representation of the rotation defined by the misorientation vector, δr_m. The derivative $\frac{\partial m_{ij}^s}{\partial \delta r_m}$ is evaluated at the mean orientation which implies zero misorientation. First, the derivative $\frac{\partial m_{ij}^s}{\partial \delta R_{kl}}$ evaluated at the mean orientation is:

$$\frac{\partial m_{ij}^s}{\partial \delta R_{kl}} = I_{ik} \langle m_{lj}^s \rangle + I_{jk} \langle m_{il}^s \rangle. \tag{A7}$$

In order to obtain the derivative $\frac{\partial \delta R_{ij}}{\partial \delta r_l}$, we write the misorientation matrix, δR_{ij}, as a function of misorientation vector, δr_k (Morawiec, 2004):

$$\delta R_{ij} =$$

$$
\begin{bmatrix}
1 - 2\delta r_2^2 - 2\delta r_3^2 & 2\big(\delta r_1 \delta r_2 - \sqrt{1 - \delta r_i \delta r_i}\,\delta r_3\big) & 2\big(\sqrt{1 - \delta r_i \delta r_i}\,\delta r_2 + \delta r_1 \delta r_3\big) \\
2\big(\delta r_1 \delta r_2 + \sqrt{1 - \delta r_i \delta r_i}\,\delta r_3\big) & 1 - 2\delta r_1^2 - 2\delta r_3^2 & 2\big(\delta r_2 \delta r_3 - \sqrt{1 - \delta r_i \delta r_i}\,\delta r_1\big) \\
2\big(\delta r_1 \delta r_3 - \sqrt{1 - \delta r_i \delta r_i}\,\delta r_2\big) & 2\big(\sqrt{1 - \delta r_i \delta r_i}\,\delta r_1 + \delta r_2 \delta r_3\big) & 1 - 2\delta r_1^2 - 2\delta r_2^2
\end{bmatrix}
\quad \text{(A8)}
$$

The derivatives of the misorientation matrix, δR_{ij}, with respect to misorientation vector, δr_k, evaluated at the mean orientation are:

$$
\frac{\partial \delta R_{ij}}{\partial \delta r_1} =
\begin{bmatrix} 0 & 0 & 0 \\ 0 & 0 & -2 \\ 0 & 2 & 0 \end{bmatrix};\quad
\frac{\partial \delta R_{ij}}{\partial \delta r_2} =
\begin{bmatrix} 0 & 0 & 2 \\ 0 & 0 & 0 \\ -2 & 0 & 0 \end{bmatrix};\quad
\frac{\partial \delta R_{ij}}{\partial \delta r_3} =
\begin{bmatrix} 0 & -2 & 0 \\ 2 & 0 & 0 \\ 0 & 0 & 0 \end{bmatrix}.
\qquad \text{(A9)}
$$

The expressions for derivatives of the antisymmetric Schmid tensor are analogous to those of the symmetric Schmid tensor.

Appendix B

Let us consider two average intragranular stress fluctuation distributions at two subsequent time increments. The linear mapping of the stress fluctuation vectors at time $t - \Delta t$ to the corresponding statistical descriptor at time t, defined by matrix $\mathbf{Z}^{(r)}$, is needed. Let us assume both distributions are normal and perform a Cholesky decomposition of the stress fluctuations at times $t - \Delta t$ and t:

$$\langle \delta\boldsymbol{\sigma}^{t-\Delta t(\bar{q})} \otimes \delta\boldsymbol{\sigma}^{t-\Delta t(\bar{q})} \rangle^{(r)} = \mathbf{L}^{t-\Delta t}(\mathbf{L}^{t-\Delta t})^T \qquad \text{(A10)}$$

$$\langle \delta\boldsymbol{\sigma}^{t(\bar{q})} \otimes \delta\boldsymbol{\sigma}^{t(\bar{q})} \rangle^{(r)} = \mathbf{L}^{t}(\mathbf{L}^{t})^T , \qquad \text{(A11)}$$

where $\mathbf{L}^t$ and $\mathbf{L}^{t-\Delta t}$ are lower triangular matrices. The matrix $\mathbf{L}^t$ maps random five-dimensional vectors with zero mean and unit variance, to random vectors with zero mean and second moment defined by $\langle \delta\boldsymbol{\sigma}^{t(\bar{q})} \otimes \delta\boldsymbol{\sigma}^{t(\bar{q})} \rangle^{(r)}$ (Press, 2007). Analogously, the matrix $\mathbf{L}^{t-\Delta t}$ performs similar

mapping, but to random vectors with zero mean and second moment defined by $\langle \delta\boldsymbol{\sigma}^{t-\Delta t(\bar{q})} \otimes \delta\boldsymbol{\sigma}^{t-\Delta t(\bar{q})} \rangle^{(r)}$. We can write the mapping $\mathbf{L}^t$ as composition of mapping $\mathbf{L}^{t-\Delta t}$ and mapping $\mathbf{Z}^{(r)}$:

$$\mathbf{L}^t = \mathbf{Z}^{(r)}\mathbf{L}^{t-\Delta t}. \tag{A12}$$

From here the matrix $\mathbf{Z}^{(r)}$ can be calculated as:

$$\mathbf{Z}^{(r)} = \mathbf{L}^t(\mathbf{L}^{t-\Delta t})^{-1}. \tag{A13}$$

Further, let us map the stress fluctuations $\delta\boldsymbol{\sigma}^{t-\Delta t(\bar{q})}(\mathbf{x})$ defined by the second moment $\langle \delta\boldsymbol{\sigma}^{t-\Delta t(\bar{q})} \otimes \delta\boldsymbol{\sigma}^{t-\Delta t(\bar{q})} \rangle^{(r)}$ using matrix $\mathbf{Z}^{(r)}$ and show that the resulting distribution has second moment equal to $\langle \delta\boldsymbol{\sigma}^{t(\bar{q})} \otimes \delta\boldsymbol{\sigma}^{t(\bar{q})} \rangle^{(r)}$:

$$\mathbf{Z}^{(r)}\langle \delta\boldsymbol{\sigma}^{t-\Delta t(\bar{q})} \otimes \delta\boldsymbol{\sigma}^{t-\Delta t(\bar{q})} \rangle^{(r)}\left(\mathbf{Z}^{(r)}\right)^T =$$

$$= \mathbf{L}^t \underbrace{(\mathbf{L}^{t-\Delta t})^{-1}\mathbf{L}^{t-\Delta t}}_{\mathbf{I}} \underbrace{(\mathbf{L}^{t-\Delta t})^T((\mathbf{L}^{t-\Delta t})^{-1})^T}_{\mathbf{I}} (\mathbf{L}^t)^T = \langle \delta\boldsymbol{\sigma}^{t(\bar{q})} \otimes \delta\boldsymbol{\sigma}^{t(\bar{q})} \rangle^{(r)} . \tag{A14}$$

$\mathbf{Z}^{(r)}$ represents the mapping of stress fluctuations from time $t - \Delta t$ to t when the cross-correlation between two stress fluctuations is perfect. However, in reality the cross-correlation is most likely very strong but not perfect. In the case of two correlated scalar variables, the proportionality between them is defined by the cross-correlation coefficient, ρ (Papoulis, 1991). We assume analogous relation for the multivariate case: $\mathbf{Z}^{(r)}(\rho) = \rho\mathbf{Z}^{(r)}(\rho = 1)$. The cross-correlation between five-dimensional stress fluctuations from two subsequent time increments is defined by the cross-correlation coefficient matrix but we approximate the strength of cross-correlation with only one scalar number ρ. We assume cross-correlation coefficient, ρ, is a function of strain increment given by:

$$\rho = 1.0 - 2.5 \times \Delta\varepsilon_{vm}. \tag{A15}$$

$\mathbf{Z}^{(r)}(\rho = 1)$ is linear mapping between stress fluctuation distributions when the cross-correlation is perfect (Eq. (A13) of the Appendix).

Appendix C

The three-dimensional parent's misorientation distribution described by the mean value, $\langle \delta \mathbf{r} \rangle^{(r)} = \mathbf{0}$, and the second moment, $\langle \delta \mathbf{r} \otimes \delta \mathbf{r} \rangle^{(r)}$, needs to be divided into two distributions, each described by its own mean value, $\langle \delta \mathbf{r} \rangle_{f_i}^{(r)}$, and second moment, $\langle \delta \mathbf{r} \otimes \delta \mathbf{r} \rangle_{f_i}^{(r)}$. First, we calculate the eigenvectors and eigenvalues of the parent's misorientation distribution and sort them in the descending order: $\mathbf{V} = [\mathbf{v}^1, \mathbf{v}^2, \mathbf{v}^3]$ and $\mathbf{E} = [\lambda^1, \lambda^2, \lambda^3]$. Next, we assume that the misorientation distribution is a multivariate normal distribution which implies that the distributions along the principal directions are normal and independent. Due to the independence of distributions along the different principal directions, the distribution along the direction of largest variation, $\mathbf{v}^1$, can be divided completely separately from the other two principal distributions. The three dimensional distributions of fragments are then created by combining the corresponding divided distributions along the direction of largest variation and the two other principal distributions.

The mean value of the left interval for one dimensional normal distribution is calculated as (Miller and Rice, 1983; Vazquez-Leal et al., 2012):

$$\langle x \rangle^{left} = \frac{1}{F(0) - F(-\infty)} \int_{-\infty}^{0} x f(x) dx = -2\sqrt{\frac{\lambda}{2\pi}}, \tag{A16}$$

where f and F denote probability density function and cumulative distribution function of normal distribution and λ is the variance. The variance of the left interval is calculated as (Miller and Rice, 1983; Vazquez-Leal et al., 2012):

$$\langle \delta x^2 \rangle^{left} = \frac{1}{F(0)-F(-\infty)} \int_{-\infty}^{0} x^2 f(x) dx - (\langle x \rangle^{left})^2 = \lambda \left(1 - \frac{2}{\pi} \right). \tag{A17}$$

The mean value and variance of the right interval are $\langle x \rangle^{right} = -\langle x \rangle^{left}$ and $\langle \delta x^2 \rangle^{right} = \langle \delta x^2 \rangle^{left}$. Using these expressions, the mean misorientations of the fragments with respect to the mean orientation of the parent are given by:

$$\langle \delta \mathbf{r} \rangle_{f_1}^{(r)} = -2 \sqrt{\frac{\lambda^1}{2\pi}} \mathbf{v}^1; \; \langle \delta \mathbf{r} \rangle_{f_2}^{(r)} = 2 \sqrt{\frac{\lambda^1}{2\pi}} \mathbf{v}^1. \tag{A18}$$

The mean orientations of fragments are then given by:

$$\overline{\mathbf{q}}_{f_1}^{(r)} = \langle \delta \mathbf{q} \rangle_{f_1}^{(r)} \overline{\mathbf{q}}^{(r)}; \; \overline{\mathbf{q}}_{f_2}^{(r)} = \langle \delta \mathbf{q} \rangle_{f_2}^{(r)} \overline{\mathbf{q}}^{(r)}, \tag{A19}$$

where misorientations of fragments $\langle \delta \mathbf{q} \rangle_{f_1}^{(r)}$ and $\langle \delta \mathbf{q} \rangle_{f_2}^{(r)}$ are given by:

$$\langle \delta \mathbf{q} \rangle_{f_1}^{(r)} = \left\{ \begin{array}{c} \sqrt{1 - \langle \delta \mathbf{r} \rangle_{f_1}^{(r)} \cdot \langle \delta \mathbf{r} \rangle_{f_1}^{(r)}} \\ \langle \delta \mathbf{r} \rangle_{f_1}^{(r)} \end{array} \right\}; \; \langle \delta \mathbf{q} \rangle_{f_2}^{(r)} = \left\{ \begin{array}{c} \sqrt{1 - \langle \delta \mathbf{r} \rangle_{f_2}^{(r)} \cdot \langle \delta \mathbf{r} \rangle_{f_2}^{(r)}} \\ \langle \delta \mathbf{r} \rangle_{f_2}^{(r)} \end{array} \right\}. \tag{A20}$$

The centered second moments of the fragments in the principal frame of the parent's distribution are:

$$\langle \delta \mathbf{r} \otimes \delta \mathbf{r} \rangle_{f_1}^{(r),p} = \langle \delta \mathbf{r} \otimes \delta \mathbf{r} \rangle_{f_2}^{(r),p} = \begin{bmatrix} \lambda^1 \left(1 - \frac{2}{\pi} \right) & 0 & 0 \\ 0 & \lambda^2 & 0 \\ 0 & 0 & \lambda^3 \end{bmatrix}. \tag{A21}$$

The centered second moments of the fragments in sample frame are then obtained by simple coordinate transformation:

$$\langle \delta \mathbf{r} \otimes \delta \mathbf{r} \rangle_{f_1}^{(r)} = \langle \delta \mathbf{r} \otimes \delta \mathbf{r} \rangle_{f_2}^{(r)} = \mathbf{V} \langle \delta \mathbf{r} \otimes \delta \mathbf{r} \rangle_{f_1}^{(r),p} \mathbf{V}^T. \tag{A22}$$

References

Ang, A.H.S., Tang, W.H., 1975. Probability Concepts in Engineering Planning and Design, Basic Principles. Wiley.

Ardeljan, M., Knezevic, M., Nizolek, T., Beyerlein, I.J., Mara, N.A., Pollock, T.M., 2015. A study of microstructure-driven strain localizations in two-phase polycrystalline HCP/BCC composites using a multi-scale model. Int. J. Plast. 74, 35-57.

Bachmann, F., Hielscher, R., Jupp, P.E., Pantleon, W., Schaeben, H., Wegert, E., 2010. Inferential statistics of electron backscatter diffraction data from within individual crystalline grains. Journal of Applied Crystallography 43, 1338-1355.

Bacroix, B., Jonas, J., 1988. The influence of non-octahedral slip on texture development in fcc metals. Texture, Stress, and Microstructure 8, 267-311.

Beyerlein, I.J., Lebensohn, R.A., Tomé, C.N., 2003. Modeling texture and microstructural evolution in the equal channel angular extrusion process. Materials Science and Engineering: A 345, 122-138.

Bobeth, M., Diener, G., 1986. Field fluctuations in multicomponent mixtures. Journal of the Mechanics and Physics of Solids 34, 1-17.

Buchheit, T.E., Carroll, J.D., Clark, B.G., Boyce, B.L., 2015. Evaluating Deformation-Induced Grain Orientation Change in a Polycrystal During In Situ Tensile Deformation using EBSD. Microsc Microanal 21, 969-984.

Butler, G.C., McDowell, D.L., 1998. Polycrystal constraint and grain subdivision. International Journal of Plasticity 14, 703-717.

Castañeda, P.P., 2002. Second-order homogenization estimates for nonlinear composites incorporating field fluctuations: I—theory. Journal of the Mechanics and Physics of Solids 50, 737-757.

Dillamore, I., Katoh, H., 1974. Mechanisms of recrystallization in cubic metals with particular reference to their orientation-dependence. Metal Science 8, 73-83.

Doghri, I., Brassart, L., Adam, L., Gérard, J.-S., 2011. A second-moment incremental formulation for the mean-field homogenization of elasto-plastic composites. International Journal of Plasticity 27, 352-371.

Eshelby, J.D., 1957. The determination of the elastic field of an ellipsoidal inclusion, and related problems. Proc R. Soc. Lond. A 241, 376-396.

Hansen, N., Jensen, D.J., 1999. Development of microstructure in FCC metals during cold work. Philosophical Transactions of the Royal Society of London A: Mathematical, Physical and Engineering Sciences 357, 1447-1469.

Hjelen, J., Orsund, R., Nes, E., 1991. On the origin of recrystallization textures in aluminium. Acta Metallurgica et Materialia 39, 1377-1404.

Humphreys, F., Hatherly, M., 2004. Recrystallization and related annealing phenomena, 2004. Elsevier.

Jahedi, M., Ardeljan, M., Beyerlein, I.J., Paydar, M.H., Knezevic, M., 2015. Enhancement of orientation gradients during simple shear deformation by application of simple compression. J. Appl. Phys. 117, 214309.

Jahedi, M., Beyerlein, I.J., Paydar, M.H., Zheng, S., Xiong, T., Knezevic, M., 2017. Effects of Pressure and Number of Turns on Microstructural Homogeneity Developed in High-Pressure Double Torsion. Metall. Mater. Trans. A 48, 1249-1263.

Jahedi, M., Paydar, M.H., Zheng, S., Beyerlein, I.J., Knezevic, M., 2014. Texture evolution and enhanced grain refinement under high-pressure-double-torsion. Mater. Sci. Eng. A 611, 29-36.

Kanjarla, A.K., Van Houtte, P., Delannay, L., 2010. Assessment of plastic heterogeneity in grain interaction models using crystal plasticity finite element method. International Journal of Plasticity 26, 1220-1233.

Knezevic, M., Capolungo, L., Tomé, C.N., Lebensohn, R.A., Alexander, D.J., Mihaila, B., McCabe, R.J., 2012. Anisotropic stress-strain response and microstructure evolution of textured α-uranium. Acta Materialia 60, 702-715.

Knezevic, M., Drach, B., Ardeljan, M., Beyerlein, I.J., 2014. Three dimensional predictions of grain scale plasticity and grain boundaries using crystal plasticity finite element models. Computer Methods in Applied Mechanics and Engineering 277, 239-259.

Krog-Pedersen, S., Bowen, J.R., Pantleon, W., 2009. Quantitative characterization of the orientation spread within individual grains in copper after tensile deformation. International Journal of Materials Research 100, 433-438.

Kumar, M.A., Mahesh, S., 2013. Subdivision and microtexture development in fcc grains during plane strain compression. International Journal of Plasticity 44, 95-110.

Lebensohn, R.A., 2001. N-site modeling of a 3D viscoplastic polycrystal using Fast Fourier Transform. Acta Materialia 49, 2723-2737.

Lebensohn, R.A., Brenner, R., Castelnau, O., Rollett, A.D., 2008. Orientation image-based micromechanical modelling of subgrain texture evolution in polycrystalline copper. Acta Materialia 56, 3914-3926.

Lebensohn, R.A., Liu, Y., Castaneda, P.P., 2004. On the accuracy of the self-consistent approximation for polycrystals: comparison with full-field numerical simulations. Acta Materialia 52, 5347-5361.

Lebensohn, R.A., Tomé, C.N., 1993. A self-consistent anisotropic approach for the simulation of plastic deformation and texture development of polycrystals: Application to zirconium alloys. Acta Metallurgica et Materialia 41, 2611-2624.

Lebensohn, R.A., Tomé, C.N., Castaneda, P.P., 2007. Self-consistent modelling of the mechanical behaviour of viscoplastic polycrystals incorporating intragranular field fluctuations. Philosophical Magazine 87, 4287-4322.

Lebensohn, R.A., Zecevic, M., Knezevic, M., McCabe, R.J., 2016. Average intragranular misorientation trends in polycrystalline materials predicted by a viscoplastic self-consistent approach. Acta Materialia 104, 228-236.

Lee, C.S., Duggan, B.J., 1993. Deformation banding and copper-type rolling textures. Acta Metall. Mater. 41, 2691-2699.

Lequeu, P., Gilormini, P., Montheillet, F., Bacroix, B., Jonas, J.J., 1987. Yield Surfaces for Textured Polycrystals .1. Crystallographic Approach. Acta Metallurgica 35, 439-451.

Liu, Q., Jensen, D.J., Hansen, N., 1998. Effect of grain orientation on deformation structure in cold-rolled polycrystalline aluminium. Acta materialia 46, 5819-5838.

Liu, Y., Castañeda, P.P., 2004. Second-order theory for the effective behavior and field fluctuations in viscoplastic polycrystals. Journal of the Mechanics and Physics of Solids 52, 467-495.

Masson, R., Bornert, M., Suquet, P., Zaoui, A., 2000. An affine formulation for the prediction of the effective properties of nonlinear composites and polycrystals. Journal of the Mechanics and Physics of Solids 48, 1203-1227.

McCabe, R.J., Richards, A.W., Coughlin, D.R., Clarke, K.D., Beyerlein, I.J., Knezevic, M., 2015. Microstructure effects on the recrystallization of low-symmetry alpha-uranium. Journal of Nuclear Materials 465, 189-195.

Miller, A.C., Rice, T.R., 1983. Discrete Approximations of Probability-Distributions. Manage Sci 29, 352-362.

Morawiec, A., 2004. Orientations and Rotations. Computations in Crystallographic Textures. Berlin: Springer.

Ostapovets, A., Šedá, P., Jäger, A., Lejček, P., 2012. New misorientation scheme for a visco-plastic self-consistent model: Equal channel angular pressing of magnesium single crystals. International Journal of Plasticity 29, 1-12.

Pantleon, W., 2005. Retrieving orientation correlations in deformation structures from orientation maps. Materials Science and Technology 21, 1392-1396.

Pantleon, W., He, W., Johansson, T.P., Gundlach, C., 2008. Orientation inhomogeneities within individual grains in cold-rolled aluminium resolved by electron backscatter diffraction. Mater. Sci. Eng. A-Struct. Mater. Prop. Microstruct. Process. 483-84, 668-671.

Papoulis, A., 1991. Probability, Random Variables and Stochastic Processes. McGraw-Hill, Inc., New York.

Perocheau, F., Driver, J., 2002. Slip system rheology of Al–1% Mn crystals deformed by hot plane strain compression. International Journal of Plasticity 18, 185-202.

Press, W.H., 2007. Numerical recipes 3rd edition: The art of scientific computing. Cambridge university press.

Quey, R., Dawson, P.R., Driver, J.H., 2012. Grain orientation fragmentation in hot-deformed aluminium: Experiment and simulation. Journal of the Mechanics and Physics of Solids 60, 509-524.

Quey, R., Driver, J.H., Dawson, P.R., 2015. Intra-grain orientation distributions in hot-deformed aluminium: Orientation dependence and relation to deformation mechanisms. Journal of the Mechanics and Physics of Solids 84, 506-527.

Quey, R., Piot, D., Driver, J., 2010. Microtexture tracking in hot-deformed polycrystalline aluminium: Experimental results. Acta Materialia 58, 1629-1642.

Ridha, A., Hutchinson, W., 1982. Recrystallisation mechanisms and the origin of cube texture in copper. Acta metallurgica 30, 1929-1939.

Tomé, C., Necker, C., Lebensohn, R., 2002. Mechanical anisotropy and grain interaction in recrystallized aluminum. Metallurgical and Materials Transactions A 33, 2635-2648.

Toth, L.S., Estrin, Y., Lapovok, R., Gu, C.F., 2010. A model of grain fragmentation based on lattice curvature. Acta Materialia 58, 1782-1794.

Vazquez-Leal, H., Castaneda-Sheissa, R., Filobello-Nino, U., Sarmiento-Reyes, A., Sanchez Orea, J., 2012. High accurate simple approximation of normal distribution integral. Mathematical problems in engineering 2012.

Winther, G., Wright, J.P., Schmidt, S., Oddershede, J., 2017. Grain interaction mechanisms leading to intragranular orientation spread in tensile deformed bulk grains of interstitial-free steel. International Journal of Plasticity 88, 108-125.

Zecevic, M., Pantleon, W., Lebensohn, R.A., McCabe, R.J., Knezevic, M., 2017. Predicting intragranular misorientation distributions in polycrystalline metals using the viscoplastic self-consistent formulation. Acta Materialia 140, 398-410.

Chapter 5: Modelling recrystallization textures driven by intragranular fluctuations implemented in the viscoplastic self-consistent formulation

This chapter was submitted to Acta Materialia as: "Modelling recrystallization textures driven by intragranular fluctuations implemented in the viscoplastic self-consistent formulation", Miroslav Zecevic, Ricardo A. Lebensohn, Rodney J. McCabe, and Marko Knezevic. My contribution to this chapter was:

- development and implementation of the approach for calculation of average orientation gradients within the grains using the viscoplastic self-consistent predictions of intragranular misorientation distributions

- development and implementation of the grain boundary and transition band nucleation rules

- development of the functional relation of the nucleation probability in terms of the time increment and the grain weight

- implementation of the boundary migration model

- simulation of the static recrystallization of fcc material after tension and plane-strain compression and comparison with corresponding experiments

- simulation of the static recrystallization of bcc material after compression and plane-strain compression and comparison with corresponding experiments

- writing the first draft of the paper.

Modelling recrystallization textures driven by intragranular fluctuations implemented in the viscoplastic self-consistent formulation

Miroslav Zecevic[a,b], Ricardo A. Lebensohn[b], Rodney J. McCabe[c], and Marko Knezevic[a]

[a] Department of Mechanical Engineering, University of New Hampshire, Durham, NH 03824, USA
[b] Theoretical Division, Los Alamos National Laboratory, Los Alamos, NM 87544, USA
[c] Materials Science and Technology Division, Los Alamos National Laboratory, Los Alamos, NM 87544, USA

Abstract

This paper presents a recrystallization model driven by intragranular orientation gradients and strain energy fields calculated by means of the viscoplastic self-consistent (VPSC) formulation. The VPSC model is extended for the calculation of the coupling between intragranular stress fluctuations with corresponding second moments of lattice spin and misorientation fields in the grains. Access to these quantities allows modelling of transition bands and nucleation kinetics. In the proposed recrystallization model, grain growth is assumed to be proportional to the difference between the stored energy of each grain and that of the effective medium. Recrystallization textures for several cubic metals are simulated, showing good agreement with corresponding experiments. The model reveals the importance of considering appropriate, microstructurally-based and orientation-dependent recrystallization nucleation mechanisms. The recrystallization texture of heavily rolled copper with a strong cube texture component is found to be a consequence of nucleation at transition bands, which is also the cause of the recrystallization textures in compressed iron and drawn copper wire. In contrast, the recrystallization texture of rolled interstitial-free steel is found to be caused by grain boundary nucleation occurring in the grains with the highest strain energy.

206

1 Introduction

Manufacturing processes of metallic components commonly consist of a sequence of shaping operations with intermediate anneals at appropriate temperatures [1, 2]. During the annealing process, dislocation content, grain size and texture change due to recovery and recrystallization, which in turn affects the mechanical properties of the metallic component, and thus the material response during subsequent shaping operations. Therefore, understanding and predicting the microstructural changes occurring during the recrystallization of metallic material is of great practical importance.

Recrystallization nuclei are experimentally observed at deformation induced inhomogeneities such as grain boundaries, transition bands, shear bands, as well as second phase particles [1]. During grain boundary nucleation, a subgrain that has reached critical radius bulges out into the neighboring grain and becomes a nucleus [3]. The driving force for the growth of the nuclei is the difference in the energy stored during the deformation between two sides of the moving boundary [4]. Hu, and Walter and Koch have first observed formation of nuclei at transition bands [5, 6], which are locations of high orientation gradient and thus stored energy as well [7]. Transition band nucleation has been investigated in detail in [8-11]. Shear band nucleation has also been observed in numerous studies [9, 12-15]. However, the details of the shear band nucleation mechanism are still unknown [1]. Considering the experimental observations of recrystallization, it is clear that the recrystallization process is greatly influenced by the deformed state of the polycrystal. Consequently, an accurate and physics-based recrystallization model should be informed by the measured or predicted deformed state. Since the output of the deformation model serves as an input for the recrystallization model, the complexity and performance of the recrystallization model is determined by the available

information provided by the deformation model. Spatially resolved full-field deformation models [16-20] can be coupled with full-field recrystallization models (e.g. Monte Carlo Potts models [21-25] or cellular autoomata models [26-28]). On the other hand, mean-field deformation models [29-31] can be accompanied by appropriate simpler recrystallization models. This paper formulates a recrystallization model based on the deformed state predicted by the mean-field viscoplastic self-consistent (VPSC) formulation [30].

A number of relatively simple recrystallization models initialized with microstructural quantities predicted by mean-field formulations have been proposed over the past several decades. Bunge and Köhler developed a model for predicting recrystallization textures based on deformation textures [32]. The orientations of the nuclei were chosen randomly and each nucleus was allowed to grow into the deformed matrix based on the misorientation between the nucleus and the matrix. Later, Engler proposed a recrystallization model in which the recrystallized orientation distribution function (ODF) was defined by superimposing the nucleation ODF and the growth ODF [33]. The nucleation ODF was artificially created based on the experimental observations while the growth ODF was derived from the deformation texture. Kestens and Jonas developed a more sophisticated recrystallization model based on deformation texture and applied it to recrystallization of IF steels [34]. The nucleation probability of each orientation was related to its Taylor factor, which was assumed to be a measure representing the strain energy. Additionally, an oriented growth law based on the misorientation angle and misorientation axis between the nucleus and the matrix grains was employed. Hildenbrand et al. coupled the original VPSC model proposed by Molinari et al. [29] with the modified recrystallization model of Kestens and Jonas, and utilized the volume transfer scheme [35, 36] for texture evolution [35, 36]. Along similar lines, Wenk et al developed a deformation-based recrystallization model

coupled with VPSC [30, 37-39]. The nucleation was assumed to occur in the grains with the highest strain energy calculated based on the current values of the critical resolved shear stresses. Since in VPSC each grain is considered to be embedded in a homogenous effective medium, the growth rate was defined by the difference in the strain energy between the grain and the effective medium having the averaged strain energy. Bolmaro et al. further improved the growth model by assuming pairing between the grains and introducing a dependence of the boundary mobility on the misorientation angle [40]. Cram et al. coupled a simple polycrystal plasticity model proposed by Bouaziz and Buessler [41] with the nucleation model of Zurob et al. [42] and a mean-field growth model similar to the one of Wenk et al. [43]. Zurob et al's nucleation criterion, initially developed for static recrystallization, models the formation of the nucleus at grain boundaries through subgrain growth [42]. When the growing subgrain reaches the critical radius, it bulges out into the neighboring grain and becomes a nucleus. A similar nucleation model was previously proposed by Humphreys [44]. In addition, the same type of nucleation model was later adopted by Han et al. within a cellular automata recrystallization approach coupled with crystal plasticity finite elements [45]. Sebald and Gottstein simulated the evolution of recrystallization textures from the deformation textures using different nucleation mechanisms, namely: random nucleation, nucleation at shear bands and nucleation at preexisting nuclei [46]. An oriented growth model was employed with mobility defined based on the misorientation between the nucleus and the deformed grain. The driving force for boundary migration was defined by the difference in strain energy, which was related to the grain's Taylor factor.

Most of the described mean-field recrystallization models are informed only with the average grain orientations predicted by the associated deformation model. However, nucleation of recrystallization is influenced by the intragranular orientation gradients developed during the

deformation process [1]. In this regard, nucleation is often observed at transition bands, which form between portions of the grain deforming by different combinations of slip systems [5, 6, 11]. In the above summarized recrystallization models, the magnitudes of intragranular orientation gradients were either completely neglected or directly related to other grain quantities (e.g. total accumulated shear within the grain or magnitude of the grain's strain rate). The orientation of the nucleus was assumed to be the same as the parent's orientation. This overly simplified treatment of intragranular orientation gradients within the deformation and recrystallization models leads to poor predictions of the recrystallization textures for recrystallization processes driven by intragranular orientation gradients.

In this paper we propose a recrystallization model that utilizes the intragranular misorientation distributions predicted by a recent extension of the VPSC model [47-49]. The model is computationally efficient, despite requiring the calculation of the second-order moments of stress in the grains as deformation accumulates. The intragranular orientation gradients are calculated using the intragranular misorientation distributions, and the grains with transition bands are identified based on the shapes of the intragranular misorientation distributions. Orientations of the nuclei are appropriately chosen from the transition bands. Nucleation at grain boundaries is also considered. The proposed recrystallization model relies on the grain growth model proposed by Wenk et al. [37]. Recrystallization textures of face-centered cubic (fcc) and body-centered cubic (bcc) materials are simulated and reasonable agreement with the experimental measurements is observed. Identification of the grains developing transition bands is found to be critical for the nucleation kinetics ensuring accurate predictions of the recrystallization textures.

2 Model

First, we briefly summarize the standard VPSC model [30, 50] and the recently developed algorithm for calculation of intragranular misorientation distributions [47-48] and grain fragmentation (GF) [49] within the VPSC formulation. This extended VPSC model has been designated as GF-VPSC [49]. Later, we provide a detailed description of the proposed recrystallization model, added to GF-VPSC.

2.1 VPSC model incorporating the calculation of intragranular misorientation distributions

A polycrystal is represented by a discrete set of ellipsoidal grains of a certain volume. The mean crystal orientation of each grain (r) is described by an active rotation quaternion, $\overline{\mathbf{q}}^{(r)}$, which brings the sample frame into alignment with the crystal frame. The crystal orientation varies spatially within the grain and, at a material point $\mathbf{x}$, can be described by the vector part of the misorientation quaternion, $\delta\mathbf{r}(\mathbf{x})$, defined with respect to the mean crystal orientation, $\overline{\mathbf{q}}^{(r)}$. Slip resistance of each slip system (s) is assumed to be spatially constant within each grain (r) and given by the mean grain value, $\tau_c^{s,(r)}$. The constitutive response at grain material point $\mathbf{x}$ is given by the viscoplastic equation:

$$\dot{\boldsymbol{\varepsilon}}(\mathbf{x}) = \dot{\gamma}_0 \sum_s \left(\frac{|\boldsymbol{\sigma}(\mathbf{x}):\mathbf{m}^s(\mathbf{x})|}{\tau_c^{s,(r)}} \right)^n \operatorname{sign}\big(\boldsymbol{\sigma}(\mathbf{x}):\mathbf{m}^s(\mathbf{x})\big)\, \mathbf{m}^s(\mathbf{x}), \tag{1}$$

where $\dot{\gamma}_0$ is the reference shear rate, n is the inverse of rate sensitivity (set to 10 in all the simulations that follow) and $\mathbf{m}^s$ is the symmetric part of the Schmid tensor of slip system (s) in grain (r).

Under boundary conditions applied to a viscoplastic polycrystal, the mean stress and strain rate within each crystal and the homogenized macroscopic properties can be obtained through

self-consistent homogenization [30]. The constitutive response at each material point $\mathbf{x}$ is approximated to be spatially constant within the grains, and described by a first-order Taylor expansion relating the mean values of the strain rate and stress in the grains [51]:

$$\dot{\boldsymbol{\varepsilon}}^{(r)} = \mathbf{M}^{(r)} : \boldsymbol{\sigma}^{(r)} + \dot{\boldsymbol{\varepsilon}}^{0(r)}, \tag{2}$$

where $\mathbf{M}^{(r)}$ and $\dot{\boldsymbol{\varepsilon}}^{0(r)}$ are compliance and back extrapolated strain rate of grain r. Each linearized grain is assumed to be an ellipsoidal inhomogeneity within an infinite matrix with the macroscopic properties, to which the boundary conditions are applied. The stress and strain rate within the inhomogeneity are calculated using the equivalent inclusion approach [52], and the following interaction equation can be derived [30]:

$$\tilde{\dot{\boldsymbol{\varepsilon}}}^{(r)} = -\widetilde{\mathbf{M}} : \tilde{\boldsymbol{\sigma}}^{(r)}, \tag{3}$$

where $\tilde{\dot{\boldsymbol{\varepsilon}}}^{(r)}$ and $\tilde{\boldsymbol{\sigma}}^{(r)}$ are deviations of the average strain rate and stress in the grains from the corresponding macroscopic values, and $\widetilde{\mathbf{M}} = (\mathbf{I} - \mathbf{S})^{-1} : \mathbf{S} : \overline{\mathbf{M}}$ is the interaction tensor, which is a function of the symmetric Eshelby tensor, $\mathbf{S}$, and macroscopic compliance, $\overline{\mathbf{M}}$.

After each deformation step, the lattice rotation rate, velocity gradient and slip resistance rate are multiplied with the time increment, Δt, in order to produce the corresponding increments which are then utilized for explicit updating of the crystal orientation, grain shape and slip resistance, respectively. The slip resistance rate is given by [38]:

$$\dot{\tau}_c^{s,(r)} = \sum_{s'} h^{ss'} \dot{\gamma}^{s',(r)}, \tag{4}$$

where h^{ss} is a micro-hardening matrix. In this study, the values of the micro-hardening matrix are set to $h^{ss'} = 1.0$, resulting in linear isotropic hardening. The initial slip resistance, τ_0^s, is set to unity.

Under the affine linearization (see Eq. 2), VPSC only requires the evaluation of the average stress and strain-rate in the grains, and thus the intragranular spatial variations of orientation have no influence on the results. However, the average fluctuations of intragranular quantities, starting from the second moments of the stress field in the grains, can still be calculated after each deformation step using the algorithms described below. In addition, Castelnau et al. [53] have used the intragranular field fluctuations to improve the hardening model deriving an expression for slip resistance rate in function of both first and second moments of shear rates. Consequently, under this hardening model, the field fluctuations also affect the strain energy within grains and, in turn, should also influence both recrystallization nucleation and growth. Extension of Castelnau et al.'s fluctuation-based hardening model to recrystallization will be the subject of future work.

We consider two sources of intragranular stress fluctuations: variation of mean grain properties within the polycrystal [54-56] and intragranular spatial variation of orientation [49]. The second moment of the intragranular stress fluctuations is given by [50, 55, 57]:

$$\langle \delta \boldsymbol{\sigma}^{(\bar{q})} \otimes \delta \boldsymbol{\sigma}^{(\bar{q})} \rangle^{(r)} = \frac{2}{w^{(r)}} \frac{\partial \widetilde{U}_T}{\partial \mathbf{M}^{(r)}} - \boldsymbol{\sigma}^{(r)} \otimes \boldsymbol{\sigma}^{(r)} \,, \tag{5}$$

where $\delta \boldsymbol{\sigma}^{(\bar{q})}$ is the fluctuation of stress with respect to the average grain stress for a grain with homogenous crystal orientation, $w^{(r)}$ is the grain volume fraction, $\widetilde{U}_T$ is the effective stress potential and $\mathbf{M}^{(r)}$ is the grain compliance. The intragranular stress fluctuations due to the spatial variation of orientation within the grain are assumed to be linearly proportional to the misorientation vectors, where the linear transformation is defined by the derivative of stress with respect to the misorienrentation vector, $\left. \frac{\partial \boldsymbol{\sigma}}{\partial \delta \mathbf{r}} \right|_{\boldsymbol{\sigma}^{(r)}, \overline{\mathbf{q}}^{(r)}}$ (Eq. 1). The second moment of these stress fluctuations is then given by [49]:

$$\langle \delta\boldsymbol{\sigma}^{(\delta r)} \otimes \delta\boldsymbol{\sigma}^{(\delta r)} \rangle^{(r)} = \left.\frac{\partial\boldsymbol{\sigma}}{\partial\delta\mathbf{r}}\right|_{\boldsymbol{\sigma}^{(r)},\overline{\mathbf{q}}^{(r)}} \langle \delta\mathbf{r} \otimes \delta\mathbf{r} \rangle^{(r)} \left(\left.\frac{\partial\boldsymbol{\sigma}}{\partial\delta\mathbf{r}}\right|_{\boldsymbol{\sigma}^{(r)},\overline{\mathbf{q}}^{(r)}}\right)^{T}, \tag{6}$$

where $\delta\boldsymbol{\sigma}^{(\delta r)}$ is the fluctuation of stress with respect to the average grain stress caused by the orientation fluctuation within the grain. The second moment of total intragranular stress fluctuations is obtained by superimposing the two intragranular stress distributions defined by Eqs. (5) and (6):

$$\langle \delta\boldsymbol{\sigma} \otimes \delta\boldsymbol{\sigma} \rangle^{(r)} = \langle \delta\boldsymbol{\sigma}^{(\overline{q})} \otimes \delta\boldsymbol{\sigma}^{(\overline{q})} \rangle^{(r)} + \langle \delta\boldsymbol{\sigma}^{(\delta r)} \otimes \delta\boldsymbol{\sigma}^{(\delta r)} \rangle^{(r)} +$$

$$+\langle \delta\boldsymbol{\sigma}^{(\overline{q})} \otimes \delta\boldsymbol{\sigma}^{(\delta r)} \rangle^{(r)} + \langle \delta\boldsymbol{\sigma}^{(\delta r)} \otimes \delta\boldsymbol{\sigma}^{(\overline{q})} \rangle^{(r)}. \tag{7}$$

The cross-covariance terms ([3]rd and [4]th terms on the right-hand side) define the covariance between the two stress fluctuation distributions.

The intragranular fluctuations of lattice rotation rate are assumed to be linearly proportional to the stress fluctuations and the intragranular misorientation vectors [47-49]. Consequently, an expression for the second moment of intragranular fluctuations of lattice rotation rate can be derived in terms of the second moment of stress fluctuations, $\langle \delta\boldsymbol{\sigma} \otimes \delta\boldsymbol{\sigma} \rangle^{(r)}$, and the second moment of misorientation vectors, $\langle \delta\mathbf{r} \otimes \delta\mathbf{r} \rangle^{(r)}$. Finally, the second moment of misorientation increment is calculated by integrating the intragranular fluctuations of lattice rotation rate and is utilized for updating of the second moment of misorientation vectors for the next time increment. If the intragranular misorientation spread reaches a critical value, the fragmentation model subdivides the grain into two child grains, which then continue to evolve separately. Consequently, certain grains from the initial texture will be represented by multiple fragments during deformation. In the recrystallization model, each such grain will be treated as a single grain whose state is defined by averaging its fragments' states.

2.2   Recrystallization model

During recrystallization new defect-free grains nucleate and grow into the deformed microstructure [1, 58]. The nucleation process is heterogeneous and occurs at locations of high strain energy and high orientation gradient [1, 59]. The growth of a recrystallized grain from a nucleus happens through high-angle boundary migration driven by the difference in strain energy between the two sides of the mobile boundary. Therefore, intragranular orientation gradients and strain energy determine the favorable places for nucleation and govern the subsequent boundary migration process. Consequently, in order to accurately predict recrystallization, intragranular orientation gradients and the strain energy of the microstructure need to be calculated first. Next, the nucleation and growth rules are developed based on these quantities.

2.2.1   Intragranular orientation gradients

In what follows, we consider a grain with orientation spread. The orientation at each material point, $\mathbf{x}$, of the grain is described with respect to the mean orientation of the grain, $\overline{\mathbf{q}}^{(r)}$, by the misorientation vector, $\delta\mathbf{r}(\mathbf{x})$. The spatial variation of the orientation described by $\delta\mathbf{r}(\mathbf{x})$ is unknown. The only available information is the first and second moments of the misorientation vectors within the grain, $\langle\delta\mathbf{r}\rangle^{(r)}$ and $\langle\delta\mathbf{r}\otimes\delta\mathbf{r}\rangle^{(r)}$, calculated with the deformation model. In what follows, we derive an expression for average intragranular orientation gradients as a function of the second moment $\langle\delta\mathbf{r}\otimes\delta\mathbf{r}\rangle^{(r)}$.

Let us consider one reference material point within the grain with an associated orientation described by a misorientation vector $\delta\mathbf{r}^{ref}$. Next, let us assume that a spatially neighboring material point to the reference point has an unknown orientation defined by a misorientation vector $\delta\mathbf{r}$. The misorientation between these two neighboring points can be approximated as:

$\delta\mathbf{r}^{loc} \approx \delta\mathbf{r} - \delta\mathbf{r}^{ref}$. The vector $\delta\mathbf{r}^{loc}$ is a local neighbor misorientation vector that describes the misorientation between the two spatially neighboring points within the grain, unlike the misorientation vectors $\delta\mathbf{r}^{ref}$ and $\delta\mathbf{r}$ which describe the misorientation between the orientation at particular point within the grain and the mean orientation of the grain. Let us assume that the orientation of the spatially neighboring point to the reference point defined by $\delta\mathbf{r}$ can take any value from the grain's orientation spread and let us calculate the first and second moments of $\delta\mathbf{r}^{loc}$:

$$\langle\delta\mathbf{r}^{loc}\rangle^{(r),ref} = \langle\delta\mathbf{r} - \delta\mathbf{r}^{ref}\rangle^{(r),ref} = -\delta\mathbf{r}^{ref}, \tag{8}$$

$$\langle\delta\mathbf{r}^{loc}\otimes\delta\mathbf{r}^{loc}\rangle^{(r),ref} = \langle(\delta\mathbf{r} - \delta\mathbf{r}^{ref})\otimes(\delta\mathbf{r} - \delta\mathbf{r}^{ref})\rangle^{(r),ref} =$$

$$\delta\mathbf{r}^{ref}\otimes\delta\mathbf{r}^{ref} + \langle\delta\mathbf{r}\otimes\delta\mathbf{r}\rangle^{(r)}. \tag{9}$$

The first and second moments of $\delta\mathbf{r}^{loc}$ define a distribution of all the possible local neighbor misorientation vectors in grain r for the orientation described by $\delta\mathbf{r}^{ref}$. The distribution of possible local neighbor misorientations is assumed to be Gaussian with the probability density function (pdf) $f(\delta\mathbf{r}^{loc})$.

Physically, the spatially neighboring points in the grain are more likely to have similar orientations. Consequently, the probability of finding smaller local neighbor misorientations $\delta\mathbf{r}^{loc}$ will be relatively higher in comparison to larger local neighbor misorientations. In order to take this spatial correlation of misorientations into account we introduce a Gaussian spatial correlation pdf, $g(\delta\mathbf{r}^{loc})$, which determines the likelihood of finding particular local neighbor misorientation only based on the spatial correlation criterion. The spatial correlation pdf $g(\delta\mathbf{r}^{loc})$ is assumed to be isotropic with zero mean and covariance matrix, $\mathbf{C} = \alpha\mathbf{I}$, where α is the variance and $\mathbf{I}$ is an identity matrix. Since $g(\delta\mathbf{r}^{loc})$ is isotropic, the misorientation axis has

no effect and only the local misorientation angle determines the probability of finding that particular local neighbor misorientation. Variance α controls the magnitude of local neighbor misorientation angles. For small values of variance α, the probability of finding spatially neighboring points with large misorientation angle is very small. On the other hand, for large values of variance α, the probability of finding two neighboring orientations with large misorientation angle would increase.

The spatial correlation pdf $g(\delta\mathbf{r}^{loc})$ describes the likelihood of finding a local neighbor misorientation $\delta\mathbf{r}^{loc}$ only based on the spatial correlation criterion, without taking into account the available local neighbor misorientations defined by the pdf $f(\delta\mathbf{r}^{loc})$. Consequently, for a given intragranular orientation described by $\delta\mathbf{r}^{ref}$ within the grain r with misorientation spread $\langle\delta\mathbf{r}\otimes\delta\mathbf{r}\rangle^{(r)}$, the spatially correlated likelihood of finding particular local neighbor misorientation $\delta\mathbf{r}^{loc}$ is described by the product of $f(\delta\mathbf{r}^{loc})$ and $g(\delta\mathbf{r}^{loc})$:

$$h(\delta\mathbf{r}^{loc}) = \frac{f(\delta\mathbf{r}^{loc})g(\delta\mathbf{r}^{loc})}{\int f(\delta\mathbf{r}^{loc})g(\delta\mathbf{r}^{loc})d(\delta\mathbf{r})}. \tag{10}$$

The local neighbor pdf $h(\delta\mathbf{r}^{loc})$ is also Gaussian with the first and second moments given by [60]:

$$\langle\delta\mathbf{r}^{loc}\rangle^{(r),ref,cor} = -\left(\langle\delta\mathbf{r}\otimes\delta\mathbf{r}\rangle^{(r)-1} + \frac{1}{\alpha}\mathbf{I}\right)^{-1}\langle\delta\mathbf{r}\otimes\delta\mathbf{r}\rangle^{(r)-1}\delta\mathbf{r}^{ref}, \tag{11}$$

$$\langle\delta\mathbf{r}^{loc}\otimes\delta\mathbf{r}^{loc}\rangle^{(r),ref,cor} = \langle\delta\mathbf{r}^{loc}\rangle^{(r),ref,cor}\otimes\langle\delta\mathbf{r}^{loc}\rangle^{(r),ref,cor} +$$

$$\left(\langle\delta\mathbf{r}\otimes\delta\mathbf{r}\rangle^{(r)-1} + \frac{1}{\alpha}\mathbf{I}\right)^{-1}. \tag{12}$$

For every orientation in the spread we can define such distribution of local neighbor misorientations $\delta\mathbf{r}^{loc}$. Next, we define a distribution of all the local neighbor misorientations for a grain by taking the volume average over $\delta\mathbf{r}^{ref}$ in Eq. 11 and 12:

$$\langle\delta\mathbf{r}^{loc}\rangle^{(r)} = \mathbf{0}, \tag{13}$$

$$\langle\delta\mathbf{r}^{loc}\otimes\delta\mathbf{r}^{loc}\rangle^{(r)} = \left(\langle\delta\mathbf{r}\otimes\delta\mathbf{r}\rangle^{(r)^{-1}} + \frac{1}{\alpha}\mathbf{I}\right)^{-1}\langle\delta\mathbf{r}\otimes\delta\mathbf{r}\rangle^{(r)^{-T}}\left(\langle\delta\mathbf{r}\otimes\delta\mathbf{r}\rangle^{(r)^{-1}} + \frac{1}{\alpha}\mathbf{I}\right)^{-T} +$$

$$\left(\langle\delta\mathbf{r}\otimes\delta\mathbf{r}\rangle^{(r)^{-1}} + \frac{1}{\alpha}\mathbf{I}\right)^{-1}. \tag{14}$$

For $\alpha \to 0$, the second moment is $\langle\delta\mathbf{r}^{loc}\otimes\delta\mathbf{r}^{loc}\rangle^{(r)} \to 0$, and for $\alpha \to \infty$ we have $\langle\delta\mathbf{r}^{loc}\otimes\delta\mathbf{r}^{loc}\rangle^{(r)} \to 2\langle\delta\mathbf{r}\otimes\delta\mathbf{r}\rangle^{(r)}$. Consequently, for any given α, the second moment of local neighbor misorientations is bounded: $0 < \langle\delta\mathbf{r}^{loc}\otimes\delta\mathbf{r}^{loc}\rangle^{(r)} < 2\langle\delta\mathbf{r}\otimes\delta\mathbf{r}\rangle^{(r)}$. The variance α should be determined from the experimental results or full-field simulations. However, for the purposes of the recrystallization model we are only interested in the relative fluctuations of $\langle\delta\mathbf{r}^{loc}\otimes\delta\mathbf{r}^{loc}\rangle^{(r)}$ from grain to grain and not the absolute magnitudes. Consequently, we assume $\alpha \to \infty$, which results in $\langle\delta\mathbf{r}^{loc}\otimes\delta\mathbf{r}^{loc}\rangle^{(r)} = 2\langle\delta\mathbf{r}\otimes\delta\mathbf{r}\rangle^{(r)}$. In this case the distribution of local neighbor misorientations corresponds to the distribution of all possible local neighbor misorientations defined by $f(\delta\mathbf{r}^{loc})$.

For $\alpha \to \infty$, the distribution of local neighbor misorientations defined by $\langle\delta\mathbf{r}^{loc}\rangle^{(r)}$ and $\langle\delta\mathbf{r}^{loc}\otimes\delta\mathbf{r}^{loc}\rangle^{(r)}$ can be viewed as an orientation difference distribution function (ODDF) calculated based on the grain's orientation distribution function (ODF) [61]. The ODDF is calculated by determining the orientation difference between each orientation in the ODF and all the other orientations in the ODF. The ODDF provides statistical information on possible

misorientations between neighboring points within the grain without considering the actual spatial configuration of the orientations within the grain [62].

The length of the local neighbor misorientation vector, $|\delta \mathbf{r}^{loc}|$, defines the local neighbor misorientation angle between spatially neighboring points, $\delta\theta$. Using the small angle approximation, the local neighbor misorientation angle, $\delta\theta$, can be written as:

$$\delta\theta \approx 2|\delta \mathbf{r}^{loc}|. \tag{15}$$

A distribution of magnitudes of three dimensional vectors with a Gaussian isotropic distribution is a Maxwell distribution [63, 64]. Therefore, if we assume that the distribution of local neighbor misorientation vectors, $\delta \mathbf{r}^{loc}$, is multivariate Gaussian and isotropic, the distribution of local neighbor misorientation angles $\delta\theta$ is the Maxwell distribution. In reality, the shape of the distribution of $\delta \mathbf{r}^{loc}$ will be anisotropic resulting in a distribution of local neighbor misorientation angles somewhat different from the Maxwell distribution. We note that Pantleon and Hansen [65] have shown that the measured distributions of misorientation angles of geometrically necessary boundaries closely resemble the Maxwell and Rayleigh distributions [66]. The Rayleigh distribution describes distribution of magnitudes of two dimensional vectors with Gaussian isotropic distribution [64].

The average local neighbor misorientation angle is given by:

$$\langle \delta\theta \rangle^{(r)} \approx 2\langle |\delta \mathbf{r}^{loc}| \rangle^{(r)} = 2\langle \sqrt{\delta \mathbf{r}^{loc} \cdot \delta \mathbf{r}^{loc}} \rangle^{(r)} \approx 2\sqrt{2\mathbf{I} : \langle \delta \mathbf{r} \otimes \delta \mathbf{r} \rangle^{(r)}}. \tag{16}$$

The average local neighbor misorientation angle, $\langle \delta\theta \rangle^{(r)}$, represents an average measure of the misorientation angle between the spatially neighboring points within the grain and it is thus related to the magnitude of the orientation gradient within the grain. If we assume that the distribution of local neighbor misorientation vectors, $\delta \mathbf{r}^{loc}$, is multivariate Gaussian, the

distribution of the local neighbor misorientation angles, $\delta\theta$, follows a Maxwell-like distribution and the variance of the local neighbor misorientation angles, $\langle\delta\theta^2\rangle^{(r)}$, is proportional to the mean value, $\langle\delta\theta\rangle^{(r)}$.

The orientation gradient can be calculated by dividing the local misorientation angle between the two spatially neighboring points, $\delta\theta$, with the distance, δx, between the two points: $\frac{\delta\theta}{\delta x}$. The distance δx depends on the grain size and in the present approach it is assumed to be the same for each grain, for simplicity. Consequently, the average magnitude of the orientation gradient within the grain is directly proportional to the average local neighbor misorientation angle. In the recrystallization model, the average local neighbor misorientation angle is used as a measure of the orientation gradient.

2.2.2 Strain energy

The stored strain energy in the grain is approximated as [37, 67, 68]:

$$E^{(r)} = \rho^{(r)}\mu b^2/2, \tag{17}$$

where $\rho^{(r)}$ is the dislocation density within the grain r, μ is the shear modulus and b is the Burgers vector. Since the increase of slip resistance due to work hardening is proportional to the square root of the accumulated dislocation density, $\sum_s\left(\tau_c^{s,(r)} - \tau_{c,0}^{s,(r)}\right) \sim \sqrt{\rho^{(r)}}$, the strain energy can be written as [37]:

$$E^{(r)} \sim \sum_s\left(\tau_c^{s,(r)} - \tau_{c,0}^{s,(r)}\right)^2. \tag{18}$$

Note that the calculated dislocation density is related only to the accumulated shear strain on slip systems within the grain. The intragranular orientation gradient does not affect the dislocation density within the grain and thus geometrically necessary dislocations (GNDs) are

not accounted for in the present model. The use of misorientation distributions—calculated using the procedure described earlier—for the determination of GNDs, which in turn will affect the hardening and, consequently, the recrystallization behavior through the strain energy (Eq. 18), will be the subject of future work.

2.2.3   Nucleation

Recrystallization nuclei form at heterogeneities in the deformed microstructure. The preferred nucleation sites in single phase alloys are grain boundaries, transition bands and shear bands [1]. High stored energy and orientation gradients at these locations promote subgrain growth during annealing [1, 59]. In addition, the presence of orientation gradients allows formation of high-angle boundaries during subgrain growth. The subgrain that reaches the size advantage becomes the nucleus. Nucleation events, both at grain boundaries and transition bands, are considered next.

2.2.3.1   Grain boundary nucleation

High strain energy and orientation gradient at the grain boundary, caused by activation of additional slip systems necessary to reduce the strain incompatibilities [59], aid the subgrain growth at the grain boundary regions during the recovery, preceding the recrystallization. The subgrain that has gained the size advantage during the recovery subsequently bulges out into the neighboring grain and becomes a nucleus. Presence of the high-angle grain boundary allows the nucleus to further grow into the neighboring grain. In the present model, the strain energy and local neighbor misorientation angle at the grain boundary are assumed to be proportional to the mean grain strain energy, $E^{(r)}$, and mean local neighbor misorientation angle, $\langle \delta\theta \rangle^{(r)}$, respectively. Consequently, it is implied that the variance of the intragranular strain energy and local neighbor misorientation angle distributions is proportional to the corresponding mean

values. This assumption appears correct for the local neighbor misorientation angle, and an approximation for the strain energy. In what follows, the mean grain values will be used for definition of the grain boundary nucleation. Since the recrystallization model is mean-field, the actual spatial configuration of the polycrystal is not considered and each grain boundary is assumed to be a high angle boundary.

A minimum strain energy and orientation gradient are necessary to initiate subgrain formation and growth preceding the nucleation [1]. Consequently, in the model, only the grains that have reached a critical strain energy, E_{th}^{gb}, and critical local neighbor misorientation angle, $\delta\theta_{th}^{gb}$, are allowed to nucleate at the grain boundary. The probability of grain boundary nucleation during time increment Δt^{ref} and for a grain of average weight $w^{avg} = \frac{1}{N}\sum_r w^{(r)}$ can be expressed as [37]:

$$P_{gb}^{(r)}(\Delta t^{ref}, w^{avg}) = \exp\left(-\frac{A_{gb}}{E^{(r)2}}\right), \tag{19}$$

where A_{gb} is a constant determining the likelihood of grain boundary nucleation. The constant A_{gb} is a function of grain boundary energy and temperature and, in the present model, it is assumed to be a fitting parameter [37]. For simplicity, it is assumed that the increase of the local neighbor misorientation angle beyond the threshold value does not appreciably affect the nucleation probability. The scaling of the nucleation probability with the time increment and grain weight will be discussed at the end of this section.

At each time step, for each grain that has sufficiently high strain energy and local neighbor misorientation angle, the nucleation probability is calculated and compared to a random number 0-1. If the nucleation probability is higher than the random number the grain nucleates a new dislocation-free grain with weight $w_{nuc} = 0.0001$. The strain energy of the newly formed grain

222

is set to zero and slip resistance is set to the initial value adopted in the deformation model, before any strain hardening.

As was noted before, a grain boundary nucleus develops from a grain boundary subgrain that has bulged out into a neighboring grain. Therefore, the orientation of the nucleated grain belongs to the set of grain boundary orientations. These orientations are substantially misoriented with respect to the mean grain orientation due to the different slip activity near the grain boundary [69, 70]. Consequently, the orientations close to the grain boundary correspond to the tail of the grain's orientation spread. Fig. 1a shows a discrete representation of grain's misorientation spread with the grain boundary misorientations, which are the potential nuclei misorientations, colored in red. The misorientations, $\delta \mathbf{r}^{gb}$, belonging to the grain boundary region satisfy the following condition: $|\delta \mathbf{r}^{gb}| > c \times SD(\delta \mathbf{r}^{gb}/|\delta \mathbf{r}^{gb}|)$, where c is a constant and $SD(\delta \mathbf{r}^{gb}/|\delta \mathbf{r}^{gb}|)$ is the standard deviation along the misorientation direction, $\delta \mathbf{r}^{gb}/|\delta \mathbf{r}^{gb}|$. The constant c determines the minimal misorientation angle between the mean grain orientation and grain boundary orientation. In conclusion, the orientation of the nucleus originating at the grain boundary is a randomly sampled grain boundary orientation (details are given in Appendix).

2.2.3.2 Transition band nucleation

During deformation, grains may subdivide into deformation bands which are regions that deform by different combinations of slip systems and thus develop large orientation gradients [71]. Transition bands are narrow regions between the deformation bands. The transition bands accommodate the orientation difference between the deformation bands and are thus places of large orientation gradient. The grains with well-developed transition bands have a multi-modal orientation distribution. Therefore, the modes of the orientation distribution correspond to the

mean orientations of the deformation bands, while the orientations between the modes correspond to the transition band orientations. The nucleation during recrystallization is often observed in the transition bands [11, 72]. During the recovery, the growing subgrain in the transition band quickly forms high angle boundary due to presence of high orientation gradient and becomes a nucleus. The orientation of the transition band nucleus thus belongs to the set of transition band orientations.
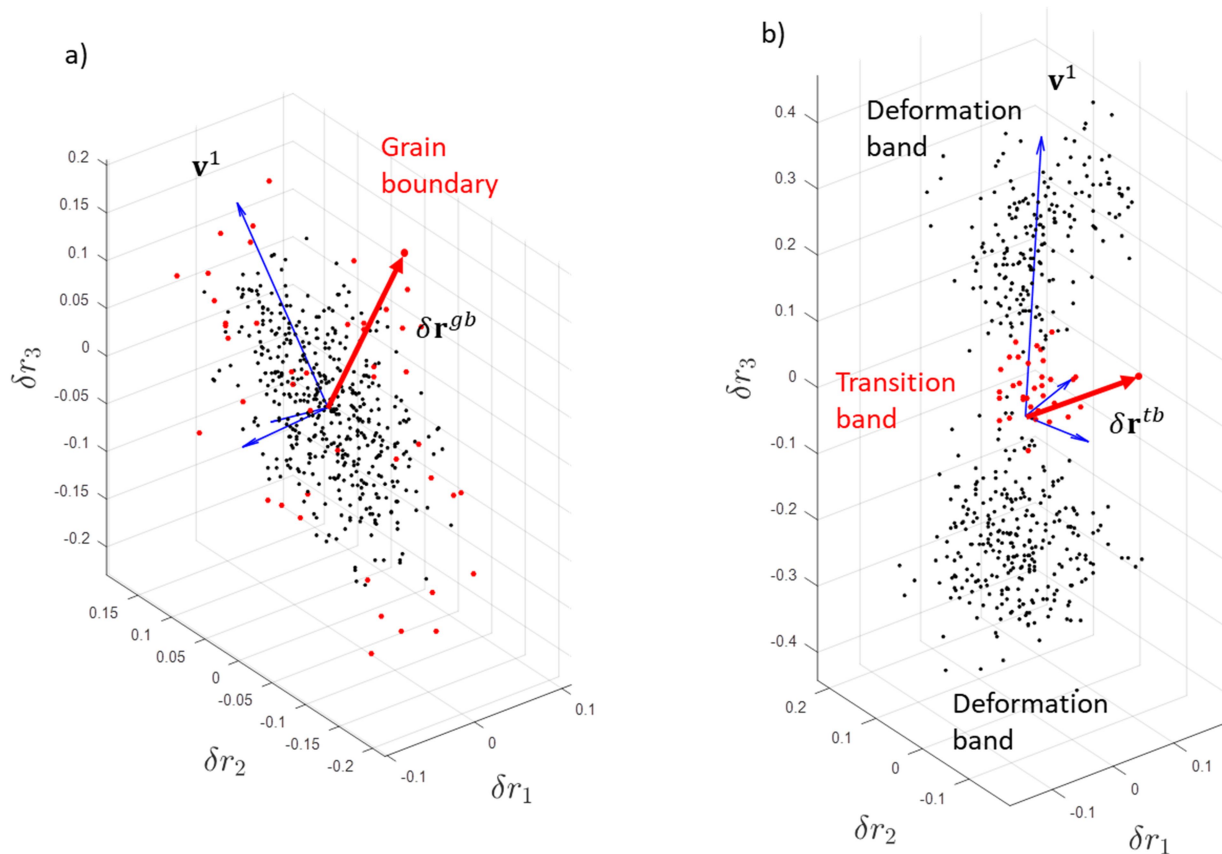
Figure 1 Discrete representation of intragranular misorientation spread showing: a) misorientations corresponding to the points in the vicinity of the grain boundary (potential grain boundary nuclei orientations); b) misorientations corresponding to the transition band region of the bi-modal grain (potential transition band nuclei orientations).

In the present model, the grains that have developed transition bands and the orientations within the transition bands can be identified based on the misorientation distribution [49]. If a grain has developed a bi-modal misorientation distribution it is assumed that the transition band

has formed within the grain and the orientations within the transition band are defined by the region between the modes of the misorientation distribution. Fig. 1b shows discrete representation of the bi-modal misorientation distribution with the identified deformation and transition band misorientations. The projections of the transition band misorientations, $\delta\mathbf{r}^{tb}$, to the direction of dominant rotation axis, $\mathbf{v}^1$, are between the modes of the misorientation distribution. The dominant rotation axis represents the eigenvector corresponding to the largest eigenvalue of second moment $\langle \delta\mathbf{r} \otimes \delta\mathbf{r} \rangle^{(r)}$ [73]. Since the transition band nuclei evolve from the subgrains present at transition bands, the transition band orientations represent a set of possible nuclei orientations.

In the recrystallization model, only the grains with a bi-modal misorientation distribution are considered as possible transition band nucleation sites. In addition, the local orientation gradient and strain energy in the transition bands within those grains have to be larger than the threshold values. We assume that the local orientation gradient and the strain energy in the transition band are proportional to the average grain values, $\langle \delta\theta \rangle^{(r)}$ and $E^{(r)}$. Consequently, only grains with bi-modal misorientation distribution, and local neighbor misorientation angle and strain energy larger than the threshold values, $\delta\theta_{th}^{tb}$ and E_{th}^{tb}, are allowed to nucleate. The transition band nucleation probability is defined analogously to the grain boundary nucleation probability [37]:

$$P_{tb}^{(r)}(\Delta t^{ref}, w^{avg}) = \exp\left(-\frac{A_{tb}}{E^{(r)^2}}\right), \tag{20}$$

where A_{tb} is a constant determining the likelihood of transition band nucleation. Similar to grain boundary nucleation, it is assumed that the increase of average local neighbor misorientation angle above the threshold value does not affect the nucleation probability.

For each grain with a bi-modal misorientation distribution, the probability of nucleation at transition band is calculated and compared to a random number 0-1. If the nucleation probability is larger than the random number, a new grain is nucleated in the same manner as for grain boundary nucleation. The orientation of the nucleus is randomly chosen from the transition band orientations (see Appendix).

2.2.3.3   *Influence of the time increment and grain weight on the nucleation probability*

The nucleation probability scales with the grain boundary area and the transition band area, which are related to the volume of the grain. The shape of the grain also influences the boundary area. In our calculations, the shape of each grain is represented with the same ellipsoid and this effect is not considered. In addition, the adopted time increment also affects the nucleation probability. In what follows, the scaling of the nucleation probability with the volume fraction and the time increment is derived.

First, the effect of the time increment on the nucleation probability is examined. We consider one grain during the time increment Δt^{ref}. The probability, $P(\Delta t^{ref})$, that this grain will nucleate during this increment in time is defined by the stored strain energy. Next, let us subdivide the time increment into a sequence of n subincrements, $dt = \Delta t^{ref}/n$. Since the subincrements dt are very small, during each subincrement i the grain may nucleate only one nucleus, with a nucleation probability given by dP^i. Therefore, each subincrement represents a Bernoulli trial [64]. It is assumed that the grain state does not change during the time increment Δt^{ref}. Furthermore, outcome of each subincrement is assumed to be independent on the outcomes of all the other subincrements. Consequently, the nucleation probability of each subincrement is the same: $dP^i = dP$. A finite or an infinite sequence of independent Bernoulli trials is a Bernoulli process. Consequently, the probability that at least one nucleus forms during

the time increment Δt^{ref} is equal to the probability that at least one successful Bernoulli trial occurs:

$$P(\Delta t^{ref}) = 1 - \binom{n}{0}(1 - dP)^n = 1 - \frac{n!}{0!n!}(1 - dP)^n = 1 - (1 - dP)^n. \tag{21}$$

Let us consider the nucleation probability of the same grain during different time increment, Δt, subdivided into m subincrements of the same length as before, $\Delta t = m \times dt$. Under the adopted assumptions, the change of the length of the time increment is equivalent to the change of the number of trials in the Bernoulli process. The probability that at least one nucleus forms during the time increment Δt is given by:

$$P(\Delta t) = 1 - (1 - dP)^m. \tag{22}$$

From Eq. (18) and (19) the nucleation probability during the time increment Δt is given by:

$$P(\Delta t) = 1 - \left(1 - P(\Delta t^{ref})\right)^{\frac{m}{n}} = 1 - \left(1 - P(\Delta t^{ref})\right)^{\frac{\Delta t}{\Delta t^{ref}}}. \tag{23}$$

By applying similar argument for the change of area the following expression can be derived:

$$P(\Delta t, w) = 1 - \left(1 - P(\Delta t^{ref}, w^{ref})\right)^{\frac{\Delta t}{\Delta t^{ref}}\left(\frac{w}{w^{ref}}\right)^{\frac{2}{3}}}. \tag{24}$$

Note that the ratio of weights is raised to the exponent 2/3 due to the square-cube law. Same expression can be derived by considering nucleation process as a Poisson distribution.

As stated before, as the time increment increases, the number of Bernoulli trials increases. Consequently, the probability of two or more successful Bernoulli trials during the Bernoulli process also increases. In the model, the time increment is always set to a value resulting in the nucleation probability less than 0.1, because in this case the probability of two or more

successful Bernoulli trials is relatively small. Therefore, we can assume that if nucleation occurs only one nucleus is formed.

2.2.4 Boundary migration

During annealing, high angle boundaries become mobile with the boundary velocity given by:

$$v = MP, \tag{25}$$

where M is the boundary mobility and P is the pressure acting on the boundary [1]. The driving pressure is caused by the difference in the stored energy between the two sides of the high angle boundary. Therefore, the grains with the lower strain energy grow while the grains with the higher strain energy shrink. We adopt a mean field approach and assume each grain is surrounded by the homogeneous effective medium [37, 43]. The boundary velocity of each grain is thus proportional to the difference between the stored energy of the grain, $E^{(r)}$, and the stored energy of the effective medium, E^{avg} [37]:

$$v^{(r)} = M\left(E^{avg} - E^{(r)}\right), \tag{26}$$

where the stored energy of the effective medium is the average for the polycrystal, $E^{avg} = \sum_r w^{(r)} E^{(r)}$. The change of the grain weight due to the boundary migration with the velocity $v^{(r)}$ during the time increment Δt is given by [37]:

$$w^{(r),t+\Delta t} = w^{(r),t} + 3M \left(\frac{4\pi}{3}\right)^{\frac{1}{3}} \left(w^{(r),t}\right)^{\frac{2}{3}} \left(E^{avg} - E^{(r)}\right) \Delta t. \tag{27}$$

After updating the weight of each grain, the normalization of grain weights is performed to ensure that $\sum_r w^{(r),t+\Delta t} = 1$.

2.2.5   Algorithm

Summarizing, the algorithm of the proposed recrystallization model is as follows:

Calculate the average local neighbor misorientation angle, $\langle\delta\theta\rangle^{(r)}$, and strain energy, $E^{(r)}$, for each grain after deformation. For each recrystallization time increment:

1) Calculate the average strain energy E^{avg}.

2) Grain boundary nucleation:

    For each grain r:

    if $E^{(r)} > E_{th}^{gb} \wedge \langle\delta\theta\rangle^{(r)} > \delta\theta_{th}^{gb}$:

        a) Calculate nucleation probability $P_{gb}^{(r)}\left(\Delta t, w^{(r)}\right)$

        b) Draw a random number $0 < rand < 1$

        c) **if** $rand < P_{gb}^{(r)}$:

            Create a new grain with zero strain energy, initial slip resistance and

            randomly sampled grain boundary orientation.

3) Transition band nucleation:

    For each bi-modal grain r:

    if $E^{(r)} > E_{th}^{tb} \wedge \langle\delta\theta\rangle^{(r)} > \delta\theta_{th}^{tb}$:

        a) Calculate nucleation probability $P_{tb}^{(r)}\left(\Delta t, w^{(r)}\right)$

        b) Draw a random number $0 < rand < 1$

        c) **if** $rand < P_{tb}^{(r)}$:

Create a new grain with zero strain energy, initial slip resistance and

randomly sampled transition band orientation.

4) Weight update:

For each grain r update the weight:

$$w^{(r),t+\Delta t} = w^{(r),t} + 3M \left(\frac{4\pi}{3}\right)^{\frac{1}{3}} \left(w^{(r),t}\right)^{\frac{2}{3}} \left(E^{avg} - E^{(r)}\right)\Delta t.$$

5) Renormalize the grain weights.

3   Results

We apply the developed model to several case studies of coupled deformation and static recrystallization modeling. Dynamic recrystallization can be performed simply by calling the recrystallization model after each or several deformation steps [37, 43].

3.1   *Annealing of cold drawn copper wire*

We simulate cold drawing of copper wire to 90% area reduction and subsequent annealing at 700 °C reported in [74]. The central region of the wire is subjected to the uniaxial tension while regions closer to the surface of the wire undergo additional shearing [74]. The applied boundary conditions in the model correspond to the central region of the wire and the predictions are compared to the measurements taken at the central region. The initial texture of the sample is represented by 400 randomly oriented spherical grains. The grains are assumed to deform by $\{111\}\langle1\bar{1}0\rangle$ slip and linear hardening given by Eq. 4.

Fig. 2a and 2c compare the measured deformation texture and the predicted deformation texture in the central region of the wire after 90% area reduction. The measured texture consists of major [111] (the intensity of 26.7) and minor [100] (the intensity of 7.6) components. The

predicted intensity of the [001] component is considerably higher than the experimentally measured intensity. This discrepancy is attributed to the very slow evolution of intragranular misorientation spreads for grains close to [001] in simulations [47]. Consequently, the orientations are more clustered around the [001] resulting in the higher intensity. On the other hand, the predicted total fraction of orientations with tension directions within 15° of [001] is 0.4, while the orientations with tension directions within 15° of [111] total 0.6. These predictions for the fractions of [111] and [001] components are in very good agreement with [75, 76], where for copper the ratio of [001] to [001]+[111] is estimated to be around 0.37.

After 90% drawing, the mean orientations of grains have clustered around the stable components and the intensity of the texture is predominantly determined by the magnitudes of the grain orientation spreads, which have also reached their stable states. On one hand, the orientation spreads of grains that have reached stable components tend to shrink because the stable regions are convergent and all the orientations within them reorient toward the stable component. On the other hand, the stress fluctuations caused by the variation of grain properties within the polycrystal increase the orientation spreads. These two effects eventually balance each other and the orientation spreads of grains that have reached stable components stop evolving with further deformation. The stable spread magnitude determines the intensity of the stable components in the deformation texture. Therefore, because the model overpredicts the [001] intensity, we conclude that the model tends to under predict the magnitudes of orientation spreads for grains with tension direction close to [001]. A possible reason is the absence of neighborhood effects on the grain's stress distribution in the GF-VPSC model. In an actual polycrystal, the intragranular stress distribution of each grain is affected by stress states of neighboring grains. During tension of fcc polycrystals, grains clustered around [001] will likely

be surrounded by grains with tension direction close to [111] because the majority of the grains in the polycrystal are close to [111]. Since the stress state is predominantly determined by the grain's orientation, the [001] grains are likely to be surrounded by grains with quite different stress states. Consequently, the effect of the neighborhood on the grain's stress state will be fairly strong for [001] grains. On the other hand, the [111] grains are likely surrounded by grains with similar orientation and thus similar stress state resulting in weaker effect of the neighborhood on the grain's stress distribution. The neighborhood effects are missing in the GF-VPSC model and the stress distribution of each grain is affected equally by all the other grains in the polycrystal. The averaged effect of all the other grains on the grain's stress distribution seems to be weaker than the actual effect of the local neighborhood for the grains in the [001] region. Consequently, the orientation spreads of grains with tension direction close to [001] might be inaccurately predicted.

Fig. 2b and 2d compare the predicted and measured recrystallization textures. The experimental recrystallization texture was measured at the central region of the 90% drawn wire after annealing at 700 °C for 1h using electron backscatter diffraction (EBSD). The central region was not fully recrystallized and no extensive abnormal grain growth was observed. The experimental recrystallization texture consists of [001], [111] and [112] components. It is noted that the component [112] is not strong in the deformation texture. In the recrystallization model, the nucleation and growth constants were adjusted to favor nucleation at transition bands (Table 1) and the material was fully recrystallized. The model predicts well the [001], [111] and [112] components in the recrystallized texture. On one hand, [001] and [111] components are a result of the nucleation at grain boundaries within [001] and [111] grains in the deformed texture. The GF-VPSC model predicts transition band orientations clustered around [112], and thus the

transition band nucleation is responsible for the [112] recrystallization texture component in the simulation. We note that the [112] component is practically absent from the predicted deformation textures in both the simulation and experiment, and only emerges after recrystallization. Similar behavior is observed in rolled fcc where a strong cube recrystallization component is observed after recrystallization, and not after deformation. We believe that the same transition band nucleation process is responsible for both of these phenomena [48].
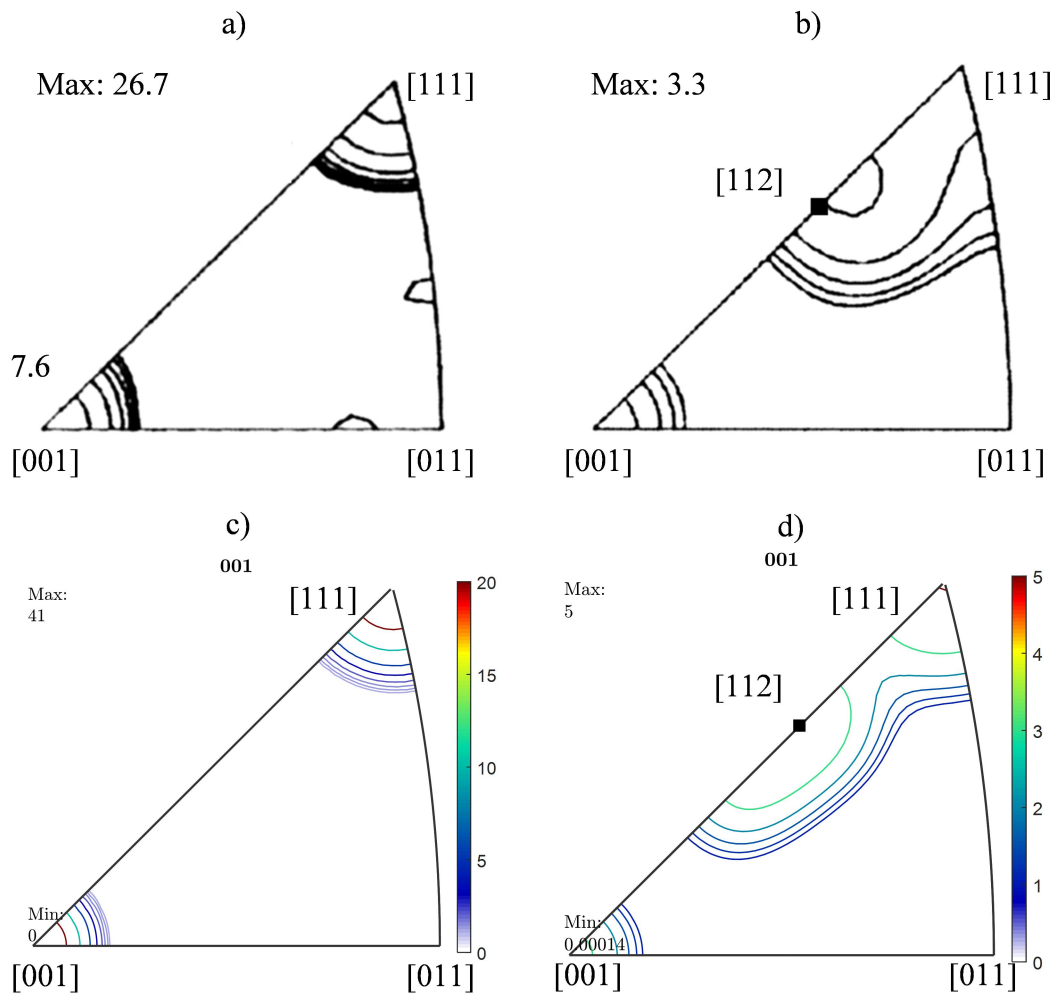
Level lines: 1.0, 1.2, 1.5, 2.0, 3.0, 5.0, 10.0, 20.0

Figure 2 Inverse pole figures showing deformation and recrystallization textures of 90% drawn copper wire: a) measured deformation texture at the central region of the wire; b) measured recrystallized texture at the central region of the wire; c) predicted deformation texture; d) predicted recrystallization texture.

Fig. 3 shows the evolution of recrystallized volume, X_V, as a function of time, $\log t$. The plot shows characteristic sigmodal shape [1]. At the beginning of the recrystallization, a typical incubation period is observed followed by increased rate of recrystallization and a linear region. As the recrystallized volume increases, the impingement of newly formed grains occurs reducing the rate of recrystallization. In the model, the impingement of the defect free grains is captured through the reduction of the average strain energy of the effective medium due to increase of the recrystallized material, which results in a lower recrystallization rate.
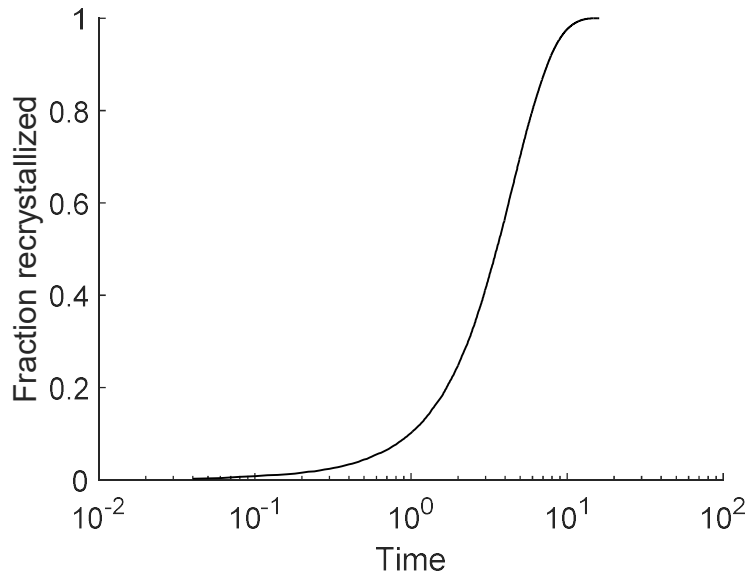

Figure 3 Predicted evolution of the volume fraction of recrystallized material during recrystallization of 90% drawn copper wire.

3.2 Annealing of 95% rolled copper

Next, we simulated rolling of copper to 95% reduction and subsequent annealing [77]. The rolling process was modelled by imposing plane strain compression (PSC) boundary conditions. This approximation is valid for the central region of the rolled plate, away from the rolls. Initial texture of the sample is represented by 400 randomly oriented spherical grains deforming by $\{111\}\langle 1\bar{1}0\rangle$ slip and linear hardening (Eq. 4).

234

The predicted and measured deformation textures are compared in Fig. 4a and 4c. The main components of the deformation texture are predicted well. However, the simulated texture is noticeably weaker than the measured one. The likely cause for discrepancy is the over prediction of intragranular orientation spreads of grains at stable regions.

Level lines: 1.0, 2.0, 4.0, 6.0, 8.0, 10.0
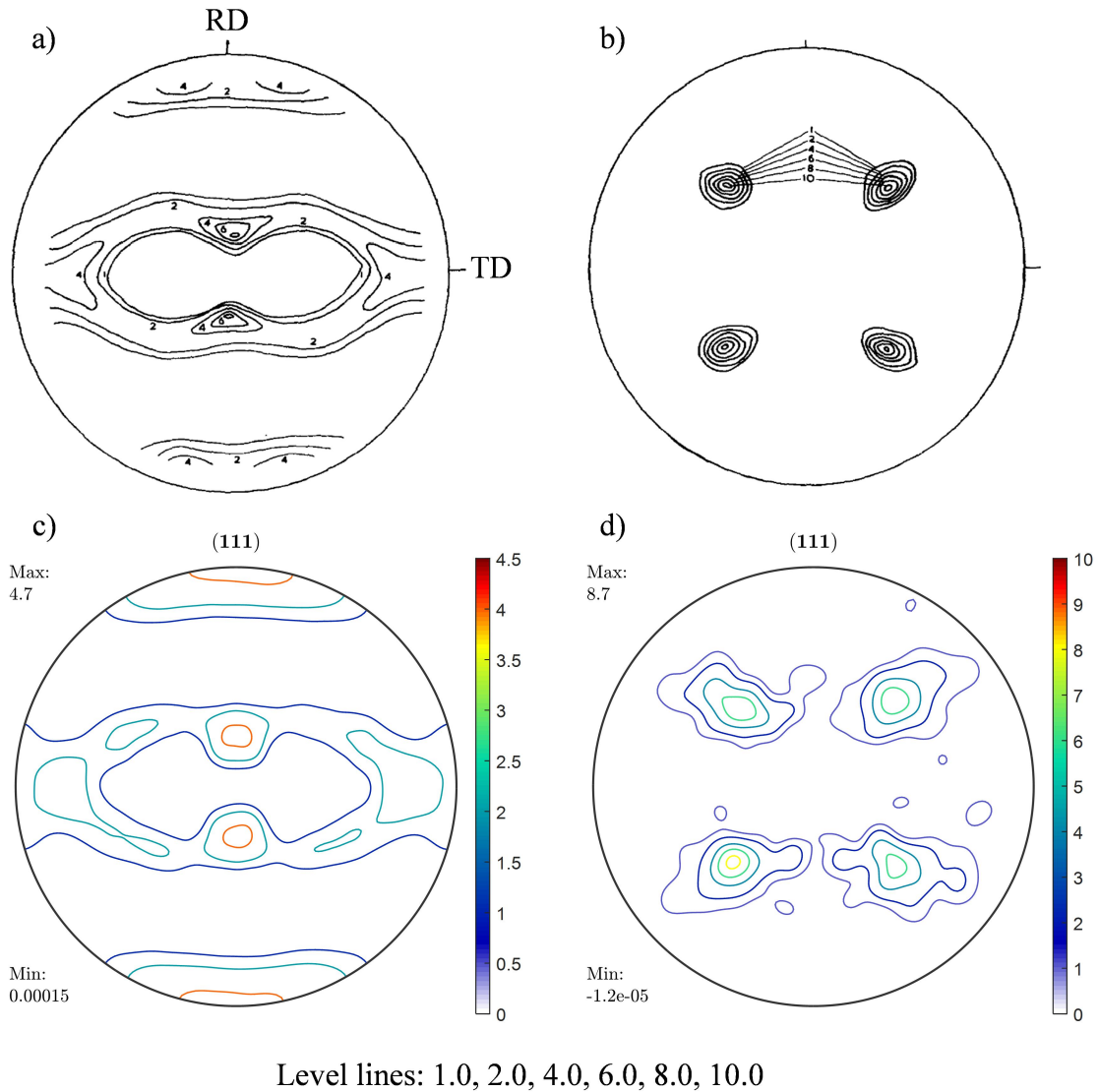
Figure 4 {111} pole figures showing deformation and recrystallization textures of 95% rolled copper: a) measured deformation texture; b) measured recrystallized texture; c) predicted deformation texture; d) predicted recrystallization texture.

Fig. 4b and 4d show the predicted and measured recrystallization textures. Well-known cube recrystallization texture is observed both in the simulation and experiment. It is widely accepted

that the cube recrystallization texture is caused by the nucleation at the transition bands with the cube orientation in the center of the band [9, 11, 72]. The model predicts that approximately 25% of the initial grains form transition bands at the end of deformation. Fig. 5 shows all the transition band orientations (one orientation per each transition band) color-coded according to the average local neighbor misorientation angle. A majority of the predicted crystallographic orientations of transition bands are concentrated around the cube orientation, in good agreement with experimental observations. In addition, the grains with the cube-oriented transition bands possess the highest intragranular misorientation. The remaining transition band orientations are concentrated around the Goss, 45°ND rotated cube and $(011)[21\bar{1}]$ orientations. Dillamore and Katoh predicted that Goss is also likely to develop transition bands [72]. It is noted that at lower reductions (~80%), the model predicts predominantly cube-oriented transition bands. In the recrystallization simulation, only transition band nucleation is allowed and only the transition bands with the highest misorientation are allowed to nucleate (Table 1). The predicted cube recrystallization texture is thus directly caused by the nucleation in the cube-oriented transition bands, which possess the highest intragranular orientation gradient.
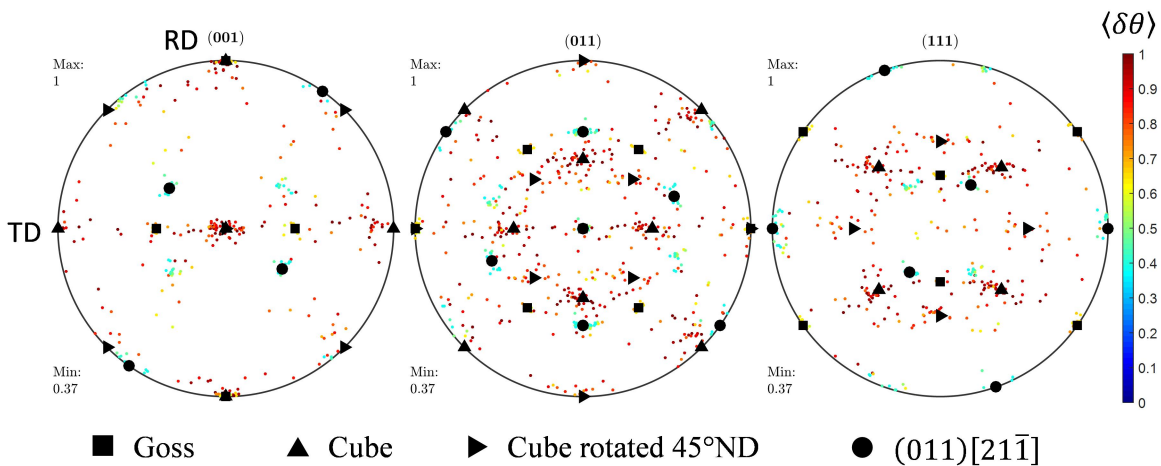
Figure 5 Predicted transition band orientations (one orientation per transition band) after 95% plane strain compression of copper, color-coded according to the average local neighbor misorientation angle within the corresponding grain, $\langle\delta\theta\rangle^{(r)}$.
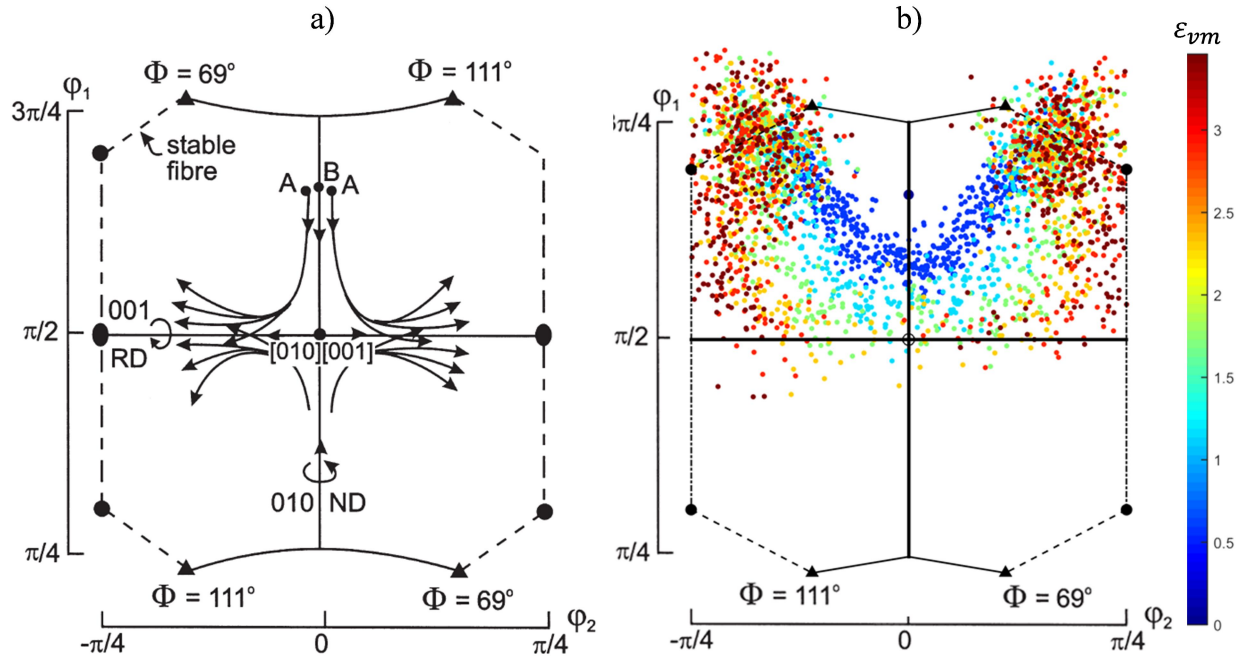
Figure 6 Formation of the cube transition band during rolling of copper illustrated on the section $\Phi = 90°$ of Euler space; a) evolution of the orientation spread of a grain with [010]‖ND initial orientation (Dillamore and Katoh, 1974; Humphreys and Hatherly, 2004); b) predicted evolution of the orientation spread of a grain with [010]‖ND initial orientation using GF-VPSC as a function of strain. The spread was represented by a set of discrete orientations and color-coded according to the strain level.

Fig. 6 shows the process of formation of cube transition bands during rolling of copper. Evolution of a grain with [010]‖ND and small initial orientation spread is considered in the $\Phi = 90°$ section of Euler space during rolling. Schematic on the left shows analysis by Dillamore and Katoh, obtained using a Taylor iso-strain approach for calculation of reorientation tendencies in Euler space [1, 72]. As the grain approaches the cube orientation along the [010]‖ND line, portions of the orientation spread that are not on the [010]‖ND line diverge by rotation around the RD, while the portion on the [010]‖ND converges to the cube orientation. Therefore, the grain subdivides into two fragments and the transition band forms with the cube orientation in the center. The plot on the right shows evolution of the orientation spread of the grain with [010]‖ND predicted by the GF-VPSC model. The orientation spread is represented by

500 discrete points and plotted for 7 strain levels and color-coded according to the strain level. Model predicts that the portions of the orientation spread away from the [010]‖ND line quickly converge to different stable fibers, while the portion of the spread on the [010]‖ND line reorients to the cube orientation and subsequently diverges by rotation around the RD as it approaches the cube. Therefore, the model predicts formation of cube-oriented transition band in a similar manner as described by Dillamore and Katoh.

3.3 Annealing of 88% compressed iron-carbon alloy

Compression of Fe-0.02%C to 88% strain and subsequent annealing reported in [78] is simulated using GF-VPSC furnished with the recrystallization model. The initial texture is represented by 400 randomly oriented spherical grains deforming by {110}⟨111⟩ and {112}⟨111⟩ slip and linear hardening. Initial slip resistance and hardening are assumed to be the same for each mode (Eq. 4).

Fig. 7a and 7c compare the predicted and measured deformation textures. The measured texture consists of a strong [111] component and a weaker [001] component. Similar texture is obtained during tension of fcc polycrystals. For the same applied boundary conditions, the reorientation caused by {110}⟨111⟩ slip in bcc materials has the same magnitude as the reorientation caused by {111}⟨110⟩ slip in fcc materials but in the opposite direction. Consequently, tension of an fcc polycrystal and compression of a bcc polycrystal result in very similar reorientations, if only {111}⟨110⟩ and {110}⟨111⟩ slip are considered, respectively [72]. Similar to the case of tension of copper, the model over-predicts the intensity of the [001] component because the misorientation spreads in the [001] region are under-predicted. The total weights of orientations with compression direction within 15° of [001] and [111] are 0.35 and 0.6, respectively.
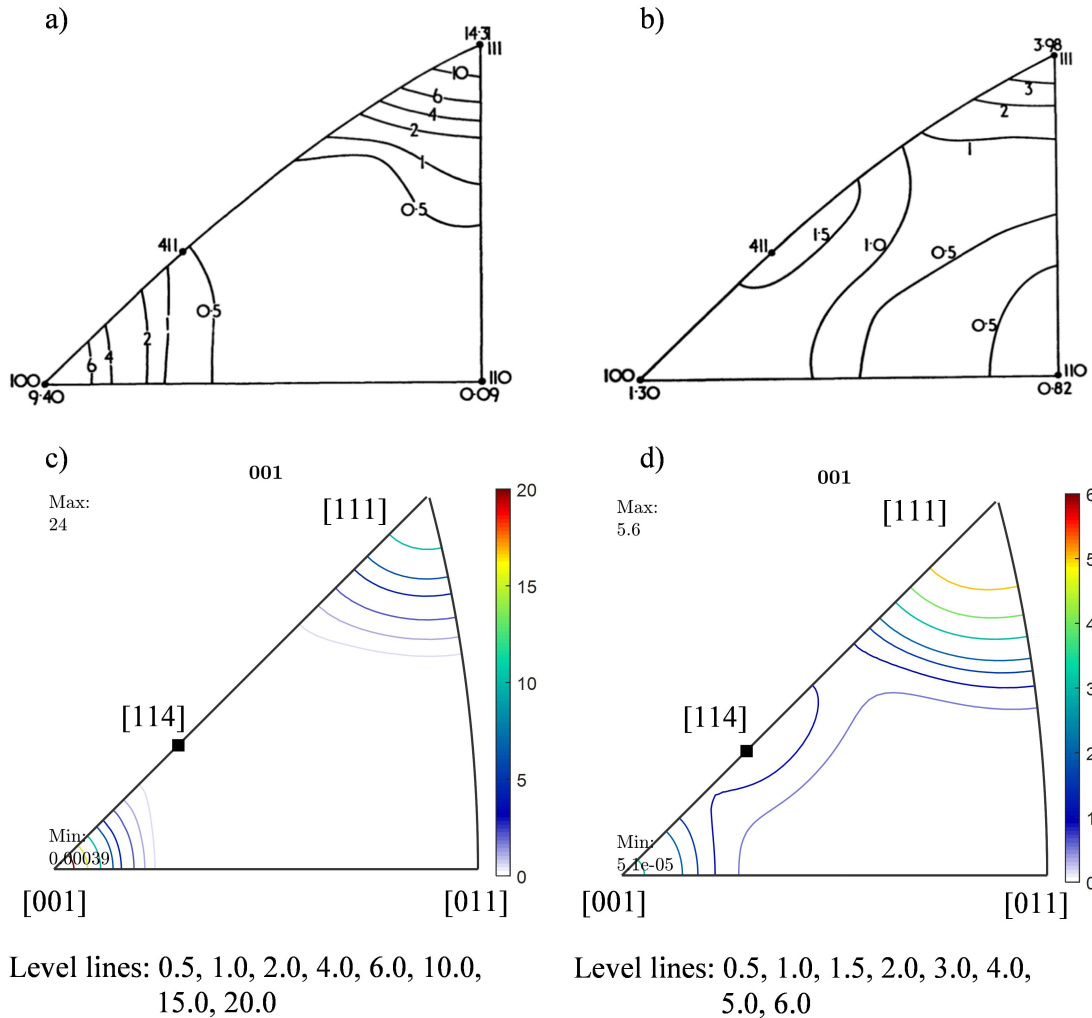
Figure 7 Inverse pole figures showing deformation and recrystallization textures of 88% compressed iron: a) measured deformation texture; b) measured recrystallized texture; c) predicted deformation texture; d) predicted recrystallization texture.

Fig. 7b and 7d show the measured and predicted recrystallization textures. The major [111] and minor [001] components present in the deformation texture are also present in the measured recrystallization texture. In addition, the [114] and the weak [011] components, which are nearly absent in the deformation texture, emerge during recrystallization. Both components are attributed to transition band nucleation. Orientations on the [114]-[110] line tend to develop transition bands because portions of grains' orientation spreads above the [114]-[110] line converge to the [111] stable component while the portions of grains' orientation spreads below

239

this line converge to [001] stable component [10, 72, 78]. The transition band orientations consequently converge toward the [114] component. In the predicted recrystallization texture, the [111] and [001] components are formed by the grain boundary nucleation mechanism, while the [114] component is a consequence of the transition band nucleation [48]. Parameters for the recrystallization model are given in Table 1. The [011] component is absent from the predicted recrystallization texture because only a few grains developed transition bands with these orientations. At lower strain (50% compression) the majority of predicted transition band orientations would be in the [011] region. During further straining to 88% compression these transition bands converge to the [114] component.

3.4   Annealing of 85% rolled Ti-Nb IF steel

Rolling and recrystallization of 85% rolled Ti-Nb IF steel is simulated and the predicted textures are compared with the experimental measurements [79, 80]. We represent the initial texture with 400 randomly oriented spherical grains deforming by {110}⟨111⟩ and {112}⟨111⟩ and linear hardening (Eq. 4). Initial slip resistance and hardening parameters are assumed to be the same for each mode.

Fig. 8a and 8c show the $\varphi_2 = 45°$ section of Euler space for the measured and predicted rolling textures [79, 80]. A majority of the grains in the experimental texture are concentrated around the γ-fiber and a portion of the α-fiber [62, 81, 82]. Note that the intensities of those two fibers have been reduced due to the ghost correction applied to the experimental data [79]. The predicted texture qualitatively matches the experimental results, but it is considerably sharper than the measured texture. Again, the likely reason for the discrepancy in the intensities is the under-prediction of misorientation spreads of grains in the stable region.
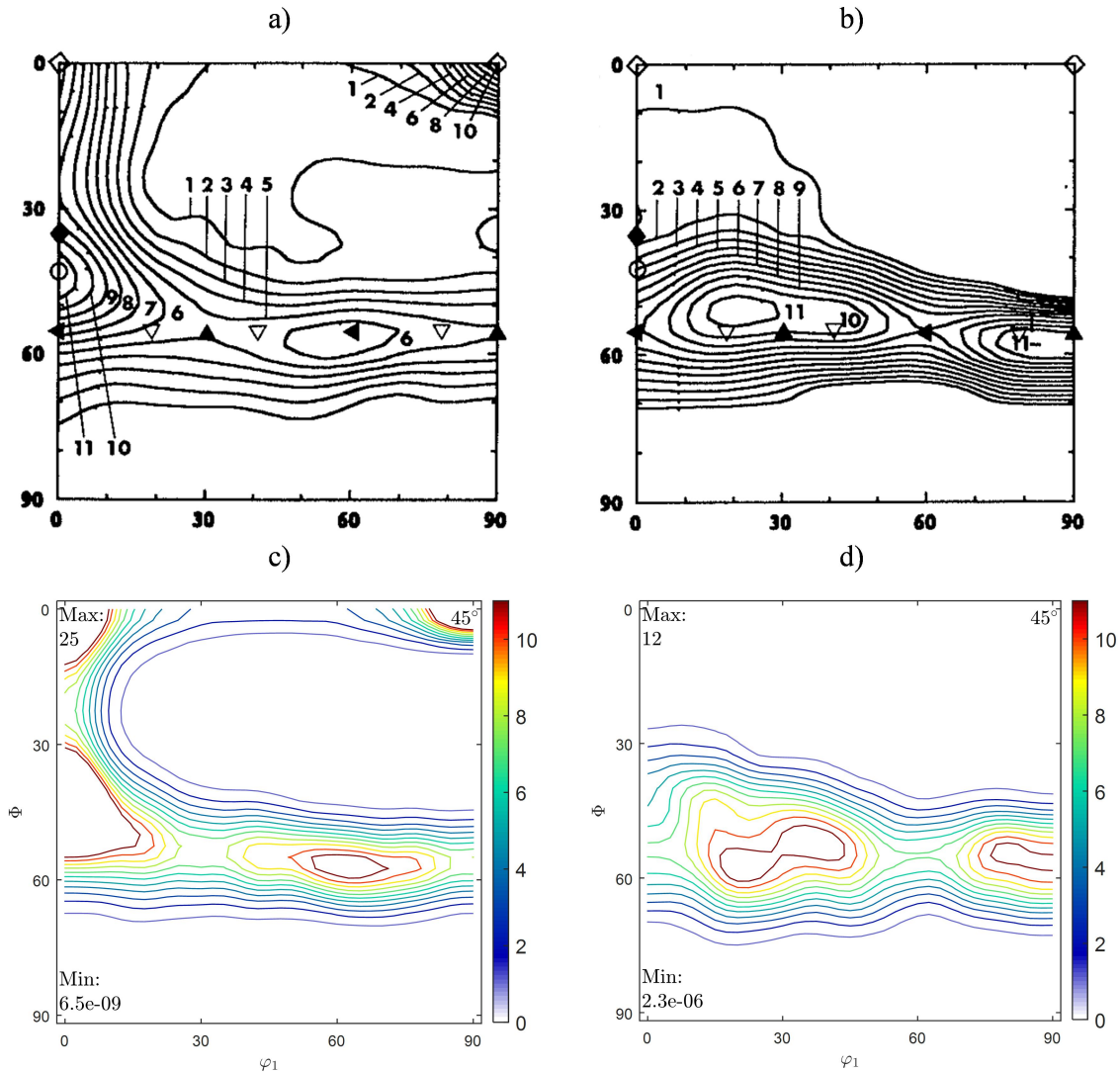
Level lines: 1.0, 2.0, 3.0, 4.0, 5.0, 6.0, 7.0, 8.0, 9.0. 10.0, 11.0

Figure 8 $\varphi_2 = 45°$ ODF section of deformation and recrystallization textures of 85% rolled IF steel: a) measured deformation texture; b) measured recrystallized texture; c) predicted deformation texture; d) predicted recrystallization texture.

The $\varphi_2 = 45°$ section of Euler space for the measured and predicted recrystallization textures are given on Fig. 8b and 8d. Comparison of the measured recrystallization texture with the deformation texture indicates that the γ-fiber strengthens during recrystallization, while the α- fiber weakens [62, 82-84]. The grains on the γ-fiber possess higher stored energy and are thus favorable nucleation sites [84, 85]. The nuclei are commonly observed in the vicinity of grain

boundaries [80, 86]. Inokuti and Doherty showed that intragranular nucleation at transition bands occurs only sporadically as opposed to the nucleation in compressed iron where majority of the nuclei formed at the transition bands [10, 87]. Considering the experimental observations, in the setup of the recrystallization model, only grain boundary nucleation was allowed in the grains with the highest stored energy (Table 1). The predicted recrystallization texture agrees well with the experimental texture, and the model corroborates the experimental observations.

Table 1 Recrystallization model parameters.

	Grain boundary nucleation				Transition band nucleation			Growth
	E_{th}^{gb}	$\delta\theta_{th}^{gb}$	A_{gb}	c	E_{th}^{tb}	$\delta\theta_{th}^{gb}$	A_{tb}	M
90% drawn copper	0.0	0.0	3.0×10^5	2.0	0.0	0.0	3.0×10^3	1.5×10^{-5}
95% rolled copper	$N\backslash A$	$N\backslash A$	$N\backslash A$	$N\backslash A$	0.0	0.867	2.15×10^5	1.5×10^{-5}
88% compressed iron	0.0	0.14	6.0×10^3	2.0	1.32×10^2	0.0	1.0×10^2	8.5×10^{-5}
85% rolled IF steel	7.38×10^2	0.0	1.8×10^5	1.0	$N\backslash A$	$N\backslash A$	$N\backslash A$	2.0×10^{-5}

4   Conclusions

We developed a coupled deformation and recrystallization model that utilizes intragranular orientation distributions and strain energy fields predicted by the GF-VPSC model. The new formulation incorporates nucleation at grain boundaries and transition bands. The fitting parameters of the recrystallization model are determined based on the experimental observations to appropriately weight the probability of nucleation events. Deformation and recrystallization textures of fcc and bcc materials were simulated and reasonable agreement with experiments was achieved. It was found that nucleation at transition bands is responsible for development of the

recrystallization texture components that are largely absent from deformation texture. A drastic example is the recrystallization of 95% rolled copper, where the strong cube recrystallization texture was found to be predominantly a consequence of transition band nucleation, which is in good agreement with experimental observations. Furthermore, transition band nucleation was also found to be the cause of the [114] recrystallization texture component of compressed iron and the [112] recrystallization texture component of drawn copper wire. On the other hand, the recrystallization texture of rolled IF steel was found to be caused by grain boundary nucleation occurring in the grains with highest strain energy, which is experimentally observed. The main deformation texture components were predicted well, but the sharpness of certain components was either under- or over-predicted. The likely reason is the inaccurate evolution of intragranular orientation spreads around those components caused by the inherent limitations of the present mean-field modeling approach.

Acknowledgments

Appendix

Orientations of nuclei originating at grain boundaries

The Cholesky decomposition of the second moment of the grain's misorientation spread is $\langle \delta \mathbf{r} \otimes \delta \mathbf{r} \rangle^{(r)} = \mathbf{L}\mathbf{L}^T$. The lower triangular matrix $\mathbf{L}$ transforms random vectors, $\mathbf{x}$, with zero mean and unit variance to random vectors, $\delta \mathbf{r}^{(r),rand}$, with zero mean and second moment $\langle \delta \mathbf{r} \otimes \delta \mathbf{r} \rangle^{(r)}$:

$$\delta \mathbf{r}^{(r),rand} = \mathbf{L}\mathbf{x}. \tag{A1}$$

Therefore, the inverse matrix, $\mathbf{L}^{-1}$, transforms random vectors $\delta \mathbf{r}^{(r),rand}$ to random vectors $\mathbf{x}$.

In the model, the orientation of the grain boundary nucleus is randomly chosen using a rejection method. First, the distribution of misorientation vectors $\delta \mathbf{r}$ is assumed to be multivariate Gaussian and a random misorientation vector, $\delta \mathbf{r}^{(r),rand}$, is sampled from the grain's misorientation distribution. The sampled random misorientation vector, $\delta \mathbf{r}^{(r),rand}$, is mapped to the random vector, $\mathbf{x}$, with zero mean and unit variance using the matrix $\mathbf{L}^{-1}$. If the length of the vector $\mathbf{x}$ is larger than the constant c, then the length of the vector $\delta \mathbf{r}^{(r),rand}$ is larger than $c \times SD\left(\delta \mathbf{r}^{(r),rand}/\left|\delta \mathbf{r}^{(r),rand}\right|\right)$ and the vector $\delta \mathbf{r}^{(r),rand}$ is accepted. $SD\left(\delta \mathbf{r}^{(r),rand}/\left|\delta \mathbf{r}^{(r),rand}\right|\right)$ is the standard deviation along the direction of the vector $\delta \mathbf{r}^{(r),rand}$. The constant c defines the magnitude of misorientation of grain boundary orientation with respect to the mean orientation of the grain. If the length of the vector $\mathbf{x}$ is smaller than c, the random vector $\delta \mathbf{r}^{(r),rand}$ is rejected and a new random vector is sampled. The orientation of the nucleus is obtained by composing the randomly sampled misorientation and the mean orientation of the grain.

The transition band orientations correspond to the orientations in the region between the modes of the bi-modal orientation distribution. The transition band region of the misorientation spread can be identified by the projections of the misorientation vectors to the dominant rotation axis. For transition band regions, these projections have to belong to an interval between the modes of a probability density function (pdf) along the dominant rotation axis. The orientation of the transition band nucleus is randomly sampled from the transition band region using the rejection method. A random misorientation vector, $\delta\mathbf{r}^{(r),rand}$, is sampled from the grain's misorientation distribution and then projected to the dominant rotation axis, $\mathbf{v}^{1,(r)}$. If the projection $\delta\mathbf{r}^{(r),rand} \cdot \mathbf{v}^{1,(r)}$ does not belong to the defined transition band region a new random misorientation vector is sampled from the spread until the transition band misorientation vector is sampled. The orientation of the nucleus is obtained by composing the randomly sampled misorientation and the mean orientation of the grain.

References

[1]   F. Humphreys, M. Hatherly. Recrystallization and related annealing phenomena, 2004. Elsevier, 2004.

[2]   B. Verlinden, J. Driver, I. Samajdar, R.D. Doherty. Thermo-mechanical processing of metallic materials, Elsevier, 2007.

[3]   P.A. Beck, P.R. Sperry. Strain induced grain boundary migration in high purity aluminum, Journal of applied physics 21 (1950) 150-152.

[4]   G. Gottstein, L.S. Shvindlerman. Grain boundary migration in metals: thermodynamics, kinetics, applications, CRC press, 2009.

[5]   H. Hu. Recrystallization by subgrain coalescence, Electron Microscopy and Strength of Crystals. Interscience, New York (1963) 564-573.

[6]   J. Walter, E. Koch. Substructures and recrystallization of deformed (100)[001]-oriented crystals of high-purity silicon-iron, Acta Metallurgica 11 (1963) 923-938.

[7]   I. Dillamore, P. Morris, C. Smith, W. Hutchinson. Transition bands and recrystallization in metals, Proc. R. Soc. Lond. A 329 (1972) 405-420.

[8]   S.P. Bellier, R.D. Doherty. The Structure of Deformed Aluminum and Its Recrystallization--Investigations With Transmission Kossel Diffraction, Acta Metall. Mater. 25 (1977) 521-538.

[9]   J. Hjelen, R. Ørsund, E. Nes. On the origin of recrystallization textures in aluminium, Acta metallurgica et materialia 39 (1991) 1377-1404.

[10]   Y. Inokuti, R. Doherty. Transmission Kossel study of the structure of compressed iron and its recrystallization behaviour, Acta Metallurgica 26 (1978) 61-80.

[11]   A. Ridha, W. Hutchinson. Recrystallisation mechanisms and the origin of cube texture in copper, Acta metallurgica 30 (1982) 1929-1939.

[12]   F. Adcock. The internal mechanism of cold-work and recrystallization in Cupro-Nickel, J INST MET 27 (1922) 73-92.

[13]   B. Duggan, M. Hatherly, W. Hutchinson, P. Wakefield. Deformation structures and textures in cold-rolled 70: 30 brass, Metal Science 12 (1978) 343-351.

[14]   T. Haratani, W. Hutchinson, I. Dillamore, P. Bate. Contribution of shear banding to origin of Goss texture in silicon iron, Metal Science 18 (1984) 57-66.

[15]   M. Ardeljan, M. Knezevic, T. Nizolek, I.J. Beyerlein, N.A. Mara, T.M. Pollock. A study of microstructure-driven strain localizations in two-phase polycrystalline HCP/BCC composites using a multi-scale model, Int. J. Plast. 74 (2015) 35-57.

[16]   R.A. Lebensohn, R. Brenner, O. Castelnau, A.D. Rollett. Orientation image-based micromechanical modelling of subgrain texture evolution in polycrystalline copper, Acta Materialia 56 (2008) 3914-3926.

[17]   R.A. Lebensohn. N-site modeling of a 3D viscoplastic polycrystal using Fast Fourier Transform, Acta Materialia 49 (2001) 2723-2737.

[18]   S.R. Kalidindi, C.A. Bronkhorst, L. Anand. Crystallographic texture evolution in bulk deformation processing of FCC metals, J. Mech. Phys. Solids 40 (1992) 537-569.

[19]   M. Knezevic, B. Drach, M. Ardeljan, I.J. Beyerlein. Three dimensional predictions of grain scale plasticity and grain boundaries using crystal plasticity finite element models, Computer Methods in Applied Mechanics and Engineering 277 (2014) 239-259.

[20]   M. Ardeljan, I.J. Beyerlein, M. Knezevic. A dislocation density based crystal plasticity finite element model: Application to a two-phase polycrystalline HCP/BCC composites, J. Mech. Phys. Solids 66 (2014) 16-31.

[21]   D.J. Srolovitz, M.P. Anderson, P.S. Sahni, G.S. Grest. Computer-Simulation of Grain-Growth .2. Grain-Size Distribution, Topology, and Local Dynamics, Acta Metallurgica 32 (1984) 793-802.

[22]   D.J. Srolovitz, M.P. Anderson, G.S. Grest, P.S. Sahni. Computer-Simulation of Grain-Growth .3. Influence of a Particle Dispersion, Acta Metallurgica 32 (1984) 1429-1438.

[23]   M.P. Anderson, D.J. Srolovitz, G.S. Grest, P.S. Sahni. Computer-Simulation of Grain-Growth .1. Kinetics, Acta Metallurgica 32 (1984) 783-791.

[24]   A. Rollett. Overview of modeling and simulation of recrystallization, Progress in materials science 42 (1997) 79-99.

[25]   M.A. Steiner, R.J. McCabe, E. Garlea, S.R. Agnew. Monte Carlo modeling of recrystallization processes in α-uranium, Journal of Nuclear Materials 492 (2017) 74-87.

[26]   D. Raabe. Cellular automata in materials science with particular reference to recrystallization simulation, Annual review of materials research 32 (2002) 53-76.

[27]   D. Raabe. Introduction of a scalable three-dimensional cellular automaton with a probabilistic switching rule for the discrete mesoscale simulation of recrystallization phenomena, Philosophical Magazine A 79 (1999) 2339-2358.

[28]   H. Hallberg. Approaches to modeling of recrystallization, Metals 1 (2011) 16-48.

[29]   A. Molinari, G.R. Canova, S. Ahzi. Self consistent approach of the large deformation polycrystal viscoplasticity, Acta Metall. Mater. 35 (1987) 2983-2994.

[30]   R.A. Lebensohn, C.N. Tomé. A self-consistent anisotropic approach for the simulation of plastic deformation and texture development of polycrystals: Application to zirconium alloys, Acta Metall. Mater. 41 (1993) 2611-2624.

[31]   J.W. Hutchinson. Proceedings of the Royal Society of London A319 (1970) 247.

[32]   H. Bunge, U. Köhler. Model calculations of primary recrystallization textures, Scripta metallurgica et materialia 27 (1992) 1539-1543.

[33]   O. Engler. A simulation of recrystallization textures of Al-alloys with consideration of the probabilities of nucleation and growth, Texture, Stress, and Microstructure 32 (1999) 197-219.

[34]   L. Kestens, J. Jonas. Modeling texture change during the static recrystallization of interstitial free steels, Metallurgical and Materials Transactions A 27 (1996) 155-164.

[35]   C. Tomé, R.A. Lebensohn, U. Kocks. A model for texture development dominated by deformation twinning: application to zirconium alloys, Acta metallurgica et materialia 39 (1991) 2667-2680.

[36]   A. Hildenbrand, L. Tóth, A. Molinari, J. Baczynski, J. Jonas. Self-consistent polycrystal modelling of dynamic recrystallization during the shear deformation of a Ti IF steel, Acta materialia 47 (1999) 447-460.

[37]   H.-R. Wenk, G. Canova, Y. Brechet, L. Flandin. A deformation-based model for recrystallization of anisotropic materials, Acta Materialia 45 (1997) 3283-3296.

[38]   R. Lebensohn, H.-R. Wenk, C. Tomé. Modelling deformation and recrystallization textures in calcite, Acta Materialia 46 (1998) 2683-2693.

[39]   H.R. Wenk, C. Tomé. Modeling dynamic recrystallization of olivine aggregates deformed in simple shear, Journal of Geophysical Research: Solid Earth 104 (1999) 25513-25527.

[40]   R.E. Bolmaro, A. Roatta, A.L. Fourty, J.W. Signorelli. Recrystallization textures in fcc materials: A simulation based on micromechanical modeling data, Scripta Materialia 53 (2005) 147-152.

[41]   O. Bouaziz, P. Buessler. Iso-work Increment Assumption for Heterogeneous Material Behaviour Modelling, Advanced Engineering Materials 6 (2004) 79-83.

[42]   H. Zurob, Y. Brechet, J. Dunlop. Quantitative criterion for recrystallization nucleation in single-phase alloys: Prediction of critical strains and incubation times, Acta materialia 54 (2006) 3983-3990.

[43]   D. Cram, H. Zurob, Y. Brechet, C. Hutchinson. Modelling discontinuous dynamic recrystallization using a physically based model for nucleation, Acta Materialia 57 (2009) 5218-5228.

[44]   F. Humphreys. A unified theory of recovery, recrystallization and grain growth, based on the stability and growth of cellular microstructures—II. The effect of second-phase particles, Acta materialia 45 (1997) 5031-5039.

[45]   F. Han, B. Tang, H. Kou, L. Cheng, J. Li, Y. Feng. Static recrystallization simulations by coupling cellular automata and crystal plasticity finite element method using a physically based model for nucleation, Journal of materials science 49 (2014) 3253-3267.

[46]   R. Sebald, G. Gottstein. Modeling of recrystallization textures:: interaction of nucleation and growth, Acta materialia 50 (2002) 1587-1598.

[47]   M. Zecevic, W. Pantleon, R.A. Lebensohn, R.J. McCabe, M. Knezevic. Predicting intragranular misorientation distributions in polycrystalline metals using the viscoplastic self-consistent formulation, Acta Materialia 140 (2017) 398-410.

[48]   R.A. Lebensohn, M. Zecevic, M. Knezevic, R.J. McCabe. Average intragranular misorientation trends in polycrystalline materials predicted by a viscoplastic self-consistent approach, Acta Materialia 104 (2016) 228-236.

248

[49]   M. Zecevic, R.A. Lebensohn, R.J. McCabe, M. Knezevic. Modeling of intragranular misorientation and grain fragmentation in polycrystalline materials using the viscoplastic self-consistent formulation International Journal of Plasticity (2018).

[50]   R.A. Lebensohn, C.N. Tome, P.P. Castaneda. Self-consistent modelling of the mechanical behaviour of viscoplastic polycrystals incorporating intragranular field fluctuations, Philosophical Magazine 87 (2007) 4287-4322.

[51]   R. Masson, M. Bornert, P. Suquet, A. Zaoui. An affine formulation for the prediction of the effective properties of nonlinear composites and polycrystals, J. Mech. Phys. Solids 48 (2000) 1203-1227.

[52]   J.D. Eshelby. The determination of the elastic field of an ellipsoidal inclusion, and related problems, Proc R. Soc. Lond. A 241 (1957) 376-396.

[53]   O. Castelnau, R. Brenner, R. Lebensohn. The effect of strain heterogeneity on the work hardening of polycrystals predicted by mean-field approaches, Acta materialia 54 (2006) 2745-2756.

[54]   M. Bobeth, G. Diener. Field fluctuations in multicomponent mixtures, Journal of the Mechanics and Physics of Solids 34 (1986) 1-17.

[55]   R.A. Lebensohn, Y. Liu, P.P. Castaneda. On the accuracy of the self-consistent approximation for polycrystals: comparison with full-field numerical simulations, Acta Materialia 52 (2004) 5347-5361.

[56]   M. Bobeth, G. Diener. Static elastic and thermoelastic field fluctuations in multiphase composites, Journal of the Mechanics and Physics of Solids 35 (1987) 137-149.

[57]   W. Kreher. Residual stresses and stored elastic energy of composites and polycrystals, Journal of the Mechanics and Physics of Solids 38 (1990) 115-128.

[58]   R. Doherty, D. Hughes, F. Humphreys, J. Jonas, D.J. Jensen, M. Kassner, W. King, T. McNelley, H. McQueen, A. Rollett. Current issues in recrystallization: a review, Materials Science and Engineering: A 238 (1997) 219-274.

[59]   O. Engler. Nucleation and growth during recrystallisation of aluminium alloys investigated by local texture analysis, Materials Science and Technology 12 (1996) 859-872.

[60]   P. Bromiley. Products and convolutions of Gaussian probability density functions, Tina-Vision Memo 3 (2003) 1.

[61]   J. Pospiech, K. Lücke, K. Sztwiertnia. Orientation distribution and orientation correlation functions for description of microstructures, Acta metallurgica et materialia 41 (1993) 305-321.

[62]   V. Randle, O. Engler. Introduction to Texture Analysis. Macrotexture, Microstructure & Orientation Mapping, Gordon and Breach Science Publishers, 2000.

[63]   V. Sadovskii Michael. Statistical Physics, 2012.

[64]   A. Papoulis. Probability, Random Variables and Stochastic Processes, McGraw-Hill, Inc., New York, 1991.

[65]   D. Hughes, N. Hansen. High angle boundaries formed by grain subdivision mechanisms, Acta materialia 45 (1997) 3871-3886.

[66]   W. Pantleon, N. Hansen. Dislocation boundaries—the distribution function of disorientation angles, Acta materialia 49 (2001) 1479-1493.

[67]   D. Hull, D.J. Bacon. Introduction to dislocations, Butterworth-Heinemann, 2001.

[68]   J.P. Hirth, J. Lothe. Theory of dislocations, (1982).

[69]   S. Mishra, P. Pant, K. Narasimhan, A. Rollett, I. Samajdar. On the widths of orientation gradient zones adjacent to grain boundaries, Scripta materialia 61 (2009) 273-276.

[70]   R.J. McCabe, A.W. Richards, D.R. Coughlin, K.D. Clarke, I.J. Beyerlein, M. Knezevic. Microstructure effects on the recrystallization of low-symmetry alpha-uranium, Journal of Nuclear Materials 465 (2015) 189-195.

[71]   N. Hansen, D.J. Jensen. Development of microstructure in FCC metals during cold work, Philosophical Transactions of the Royal Society of London A: Mathematical, Physical and Engineering Sciences 357 (1999) 1447-1469.

[72]   I. Dillamore, H. Katoh. Mechanisms of recrystallization in cubic metals with particular reference to their orientation-dependence., Metal Science 8 (1974) 73-83.

[73]   W. Pantleon. Retrieving orientation correlations in deformation structures from orientation maps, Materials Science and Technology 21 (2005) 1392-1396.

[74]   H. Park, D.N. Lee. The evolution of annealing textures in 90 pct drawn copper wire, Metallurgical and materials transactions A 34 (2003) 531.

[75]   A. English, G. Chin. On the variation of wire texture with stacking fault energy in fcc metals and alloys, Acta metallurgica 13 (1965) 1013-1016.

[76]   K. Rajan, R. Petkie. Microtexture and anisotropy in wire drawn copper, Materials Science and Engineering: A 257 (1998) 185-197.

[77]   I. Dillamore. Factors affecting the rolling recrystallisation textures in FCC metals, Acta Metallurgica 12 (1964) 1005-1014.

[78]   I. Dillamore, H. Katoh, K. Haslam. The nucleation of recrystallisation and the development of textures in heavily compressed iron-carbon alloys, Texture, Stress, and Microstructure 1 (1974) 151-156.

[79]   T. Urabe, J.J. Jonas. Modeling texture change during the recrystallization of an IF steel, ISIJ international 34 (1994) 435-442.

[80]   R. Ray, J.J. Jonas, R. Hook. Cold rolling and annealing textures in low carbon and extra low carbon steels, International materials reviews 39 (1994) 129-172.

[81]   U. Von Schlippenbach, F. Emren, K. Lücke. Investigation of the development of the cold rolling texture in deep drawing steels by ODF-analysis, Acta metallurgica 34 (1986) 1289-1301.

[82]   K. Lücke, M. Hölscher. Rolling and recrystallization textures of BCC steels, Texture, Stress, and Microstructure 14 (1991) 585-596.

[83]   F. Emren, U. Von Schlippenbach, K. Lücke. Investigation of the development of the recrystallization textures in deep drawing steels by ODF analysis, Acta Metallurgica 34 (1986) 2105-2117.

[84]   I. Samajdar, B. Verlinden, P. Van Houtte, D. Vanderschueren. γ-Fibre recrystallization texture in IF-steel: an investigation on the recrystallization mechanisms, Materials Science and Engineering: A 238 (1997) 343-350.

[85]   N. Rajmohan, Y. Hayakawa, J. Szpunar, J. Root. Neutron diffraction method for stored energy measurement in interstitial free steel, Acta Materialia 45 (1997) 2485-2494.

[86]   W. Hutchinson. Recrystallisation textures in iron resulting from nucleation at grain boundaries, Acta Metallurgica 37 (1989) 1047-1056.

[87]   Y. Inokuti, R. Doherty. Transmission Kossel Study of the Structure of Cold-Rolled Iron and its Nucleation Behaviour, Texture, Stress, and Microstructure 2 (1977) 143-168.

SUMMARY AND FUTURE WORK

In Chapter 1, a novel numerical approach for solution of the macroscopic coupling between the VPSC and elasticity is explored. The proposed numerical approach calls the VPSC model with imposed strain rate boundary conditions which is found to be more stable than calling the VPSC with applied stress boundary conditions. In addition, solving the macroscopic equation for strain rate enables us to achieve higher precision of the numerical solution, at lower computational cost. In the future work, the numerical method used for solution of the macroscopic constitutive equation could be further improved. Currently, Newton's method is used for iterative correction of the visco-plastic strain rate. For each guess for the visco-plastic strain rate the residual of the macroscopic constitutive equation has to be evaluated which requires one call to the VPSC model. Out of all the calls to the VPSC model, only the call with the converged visco-plastic strain rate will actually be used for calculation of the macroscopic stress which will be returned to the FEA solver. Consequently, majority of the calls to the VPSC will only be used for calculation of the residual and Jacobian of the macroscopic constitutive equation required by the Newton's method. By combining the iterative loop for the solution of the macroscopic constitutive equation and the outer iteration loop over grain stresses of the VPSC model, the visco-plastic strain rate will be iteratively adjusted in the same loop as the grain stresses. Consequently, each new guess for the visco-plastic strain rate will be generated based on the current guess for the grain stresses and we would no longer need to solve the VPSC model in order to obtain a new guess for the visco-plastic strain rate. As a result the computational time required to solve the macroscopic constitutive equation should significantly reduce.

In Chapters 1 and 2, two methods for accurate representation of rate sensitivity within the finite element implementation of VPSC are proposed. Both methods are applied to Taylor impact simulations and reasonable agreement is achieved. As part of the future work, the phenomenological power-law constitutive equation at the slip system level used in VPSC could be replaced by Orowan's equation. In the power law constitutive equation, the rate sensitivity of stress is defined by a constant rate exponent fitted to the experimental data. Consequently, the rate sensitivity in the model does not change with strain rate, strain or temperature and is thus accurate only for a limited range of test conditions. On the other hand, the Orowan's equation relates the shear rate on a slip system with the average density and velocity of mobile dislocations. The rate sensitivity of stress is defined by the adopted expression for the average velocity of mobile dislocations which is rate and temperature dependent. Therefore, the rate sensitivity of stress is described in a physical way and is accurate for a wide range of test conditions.

In Chapters 3 and 4, an approach for calculation of intragranular misorientation distributions within VPSC is developed. Predictions of intragranular misorientation distributions in VPSC achieve reasonable agreement with full-field simulations and experimental measurements. In the future work, similar approach could be employed for calculation of intragranular distributions of other grain state variables like total accumulated shear, dislocation density, slip resistance etc. First, the intragranular distributions of particular state variable at low strain could be calculated directly from the intragranular stress distributions, by neglecting the effects of the fluctuations of other state variables. After verification of these predictions, the calculation of the intragranular distributions of particular state variable could be extended to include the joint effects of the intragranular distributions of stress and intragranular distributions of other state variables. In

addition, the calculated fluctuations of grain state variables could be further used for improvements of the twinning and hardening models. For example, the intragranular stress distributions could be used for calculation of the maximal resolved shear stress values on the twin systems, which would then be used within the improved twin nucleation model. In addition, the intragranular fluctuations of strain allow calculation of strain gradients within the grains which in turn govern the evolution of the densities of geometrically necessary dislocations. The density of geometrically necessary dislocations can next be utilized for calculation of the corresponding increase in slip resistance within the hardening model.

Finally, in Chapter 5 a deformation based mean-field static recrystallization model utilizing the calculated intragranular misorientation distributions is proposed. The model is capable of reproducing the experimentally measured recrystallization textures for fcc and bcc materials after different deformations. The intragranular misorientation distributions were found to be crucial for the formulation of the transition band nucleation rule. In future, the developed mean-field recrystallization model could be improved to include the neighborhood effects. To this end, each grain and each nucleus would be paired with their spatial neighbors. Consequently, the grains and nuclei would grow into their actual neighbors and not into the effective medium. In addition, the mobility of each grain boundary would be calculated based on the boundary misorientation angle. The fluctuations of grain state variables could also be utilized for calculation of the fluctuations of strain energy which could improve the grain boundary nucleation criterion and the growth model. Finally, introduction of the temperature dependence of the mobility and nucleation would facilitate the extension of the recrystallization model to include the dynamic recrystallization.

In conclusion, the improvements to the VPSC model and its finite element implementation described in this dissertation enable simulation of an arbitrary thermo-mechanical process. Each improvement has been validated separately by comparison with the full-field simulations and experimental measurements. As part of the future work, the proposed improvements could be merged into one version capable of simulating the whole thermo-mechanical process. The unified model could be validated through comparison of the microstructural predictions after each operation of the process with the corresponding experimental measurements.